Simulating sea breeze type climatologies: Implications for wind energy, weather forecasting and sailing in the southern North Sea

A thesis submitted to the School of Environmental Sciences of the University of East Anglia in partial fulfilment of the requirements for the degree of Doctor of Philosophy

By Christopher Steele

July 2013

Abstract

The energy industry is currently undergoing a revolution. In the southern North Sea, renewable energy production targets, set by European governments to counter growing concerns over climate change, have sparked an initiative to rapidly construct a large number of offshore wind farms. To meet the targets, the industry must overcome many challenges, one of which is to capitalize on the coastal and offshore wind resource. One particular relative component of the sea breeze system, including the contrasting individual sea breeze types, in the offshore environment and requires further study. Here it is shown through idealized model simulations, that each sea breeze type has distinctive characteristics and that the scales involved have the potential to influence opposing coastlines at length scales equivalent to the southern North Sea. It is revealed, through model sensitivity experiments, that variations due to the choice of model boundary layer scheme significantly alter the characteristics of the sea breeze and verification against onshore and offshore measurement data is conducted in order to quantify model performance. A unique simulated climatology of sea breezes is constructed for 5 different coastlines in the southern North Sea spanning from 2002-2012 using an identification method created to distinguish between the sea breeze types. Crucially, it is found that the frequency of sea breezes is highly dependant on coastal orientation with respect to the gradient wind and that total sea breeze frequency varies by more than a factor of two between coastlines. Furthermore, sea breezes forming on one coastline are shown to directly influence those on another. In order to quantify the impact of each sea breeze on wind energy, the climatology is used to assess wind power production on both spatial and temporal scales. It is found that sea breezes do have the potential to significantly impact offshore wind energy production, including the proposed round 3 farms which are further offshore. Furthermore, the precise impact is dependant on sea breeze type. Pure sea breezes reduce power output through the generation of offshore calm zones, whilst corkscrew sea breezes can add to the wind resource through the formation of coastal jets. The lesser known corkscrew sea breeze is attributed to 70% of the total power contribution of all sea breeze events. As turbines increase both in size and power capabilities, it is also demonstrated that the impact of sea breezes on wind turbine output will be greater in the future.

Acknowledgements

Firstly, I would like to thank my funders, NERC and Weatherquest for providing the financing to make this research possible. Thanks to Phil English at Siemens for going through the pain to help secure the release of wind farm data. Special thanks to Karin van der Wiel for pointing me in the direction of the Dutch surface network, Egmond aan Zee and Cabauw masts and for helping me with interpretation of Dutch text. Thanks also to Sander Tijm for providing information on sea breeze events at Cabauw. A special thank you to Sarah Louise Newberry, Jenny Graham, Amy Binner, Chris Walker Brown and my family for helping me to get through the especially difficult times, when completion of the PhD looked a million miles away. Thanks also to Nick Earl for his expertise in interpretation of data and for putting up with me in our collaborative efforts.

Thanks also go to Céline Heuzé, for supplying me with coffee during the final stages of the PhD and for threatening me with violence whenever I stopped writing. Thanks to Honza Chylik for providing a wide variety of real ales, toasties, and Weissbier at happy hour on a Friday after a long hard week at work. Thanks again to Nick Earl (personal communication) for his balding shiny head being a light for me when all other lights went out. For Dan Holley and Theo Gkousarov, for their continual asking of questions to really make sure I knew what I was talking about. Thanks to Chris Bell, for his supply of pizza and for giving me a storm chasing holiday to look forward to once I hand in. Thanks to Rhiannon Davies and Karin van der Wiel for shouting and throwing things at me whenever I went on facebook or whenever I was distracted by snooker. Thanks again to my flatmate Sarah Louise Newberry for putting up with my incessant whining, especially during the closing stages of writing up. Thanks to Andrew Elvidge for generally being disruptive, thus preventing me from working too hard. Thank you also to David Steele, who provided me with the best motivational speech during the last few days of writing up.

Finally, none of this would have been possible if it wasn't for my supervisors: Steve Dorling, Roland von Glasow, Jim Bacon and earlier on John Bacon. Thanks to Roland, who without, we would of never thought about using idealized simulations, which resulted in the paper. Thanks to Jim Bacon for providing a weather forecasters perspective and for giving me guidance for interpreting results. Finally, a huge thank you goes to Steve

Dorling, who not only was a brilliant supervisor, but frequently went above and beyond to make sure I stayed on the right track and was coping well. I am indebted to you all.

Acronyms

UK United Kingdom

EU European Union

NWP Numerical Weather Prediction

WRF Weather Research and Forecasting

ANN Artificial Neural Network

SBS Sea Breeze System

SBC Sea Breeze Circulation

SST Sea Surface Temperature

NAO North Atlantic Oscillation

WeMO Western Mediterranean Oscillation

SBF Sea Breeze Front

PBL Planetary Boundary Layer

NCEP National Centers for Environmental Prediction

MYJ Mellor-Yamada-Janjic

YSU Yonsei State University

MRF Medium Range Forecast

ACM2 Asymmetric Convective Model Version 2

MYNN Mellor-Yamada-Nakinishi-Niino

QNSE Quasi-Normal Scale Elimination

KNMI Royal Netherlands Meteorological Institute

HIRLAM High Resolution Limited Area Model

WMO World Meteorological Organization

SIAM KNMI Sensor Interface

CESAR Cabauw Experimental Site for Atmospheric Research

MODIS Moderate Resolution Imaging Spectroradiometer

AVHRR Advanced Very High Resolution Radiometer

EOS Earth Orbiting System

GFS Global Forecasting System

NMM Non-hydrostatic Mesoscale Model

Contents

List of tables

List of figures

Chapter 1

The rapidly evolving wind energy industry and the need to simulate coastal meteorological phenomena

A revolution in the energy industry is currently under way. Many countries across the globe are working towards switching from the use of fossil fuels to renewable forms of energy. In Europe, the European Union (EU) has set member state targets for 20% of all forms of energy by 2020 to be produced by renewable sources. For the most part, the response of member states has been through the encouragement of wind energy, both in onshore and offshore environments. In particular, the UK has begun a rapid plan to construct offshore wind farms especially in the southern North Sea. Such a plan presents many challenges in terms of offshore engineering, connecting the turbines to the National Grid and developing an efficient method of predicting and monitoring power levels. A poor understanding of coastal meteorological phenomena, such as sea breezes and coastal jets, within the offshore environment, presents an important challenge. This Chapter explores the wind energy industry both in terms of history and its current state in the southern North Sea. Current methods of wind power prediction are also explored on a variety of temporal scales. In Section 2, the literature on coastal meteorological phenomena, in particular the sea breeze, is examined, including knowledge on its structure, scales, types, interactions and identification methods. Finally, Section 3 explores relevant modelling studies with particular focus on the planetary boundary layer, the region of the atmosphere

most relevant for modelling sea breezes and wind power potential.

1.1 Offshore wind power: The primary UK response to renewable energy targets

For a number of years, it has been known that anthropogenic greenhouse gas emissions have been accelerating climate change (eg. Matthews *et al.*, 2009; Allen *et al.*, 2009). In Europe, particular changes in weather and climate patterns have been noted, such as an increase in length of European heat waves (eg. Della-Marta *et al.*, 2007), changes in flooding frequency and severity (eg. Kundzewicz *et al.*, 2005) and changes in wind climate (eg. Dorland *et al.*, 1999; Earl *et al.*, 2013). Such changes not only present a potential threat to public health, but have also been held accountable for the extinction of animal species and the destruction of habitats (eg. Thomas *et al.*, 2004). It is not surprising, therefore, that many countries around the world are trending towards using renewable forms of energy in an effort to curb greenhouse gas emissions.

The southern North Sea is a region where a large scale effort is being made to construct a number of offshore wind farms, many of which are likely to be completed by 2020 (RenewableUK, 2013). This Section explores the subject of wind energy, beginning with the history of wind power in Section 1.1. Subsequently, the renewable energy targets and the projects in the southern North Sea are examined. Advances in turbine development and future trends are discussed in Section 1.3 and issues related to turbine positioning are examined in Section 1.4. A discussion relating to modern challenges in wind power forecasting concludes this section.

1.1.1 History of wind power and the current renewable energy obligations

A wind energy system is a structure that harnesses the kinetic energy of the wind and converts it into mechanical or electrical energy (Bilgili *et al.*, 2011). As early as 5000BC, wind turbines were used to transport the ancient Egyptians along the Nile in wind propelled boats (Kaldellis, 2012). Much later, in the 12th century, the earliest working wind machines were developed to mill grain in the form of windmills. These remained the main function of the wind energy system until the 19th century when wind machines, for the

purposes of pumping water, were used in the USA (Kaldellis, 2012). It was not until 1891 when the first wind turbine was created for the purposes of generating electricity (Bilgili *et al.*, 2011).

During the early 20th century, wind turbines were only very small and not used on an industrial scale. The popularity of such devices became directly tied to the cost of fossil fuels and so after the second world war, when fuel prices began to fall, the popularity of the wind turbine dwindled (Bilgili *et al.*, 2011). By the early 1970's, however, nations began to relate wind energy with issues surrounding meteorology and climate change (Peterson *et al.*, 1998a). The results of this renewed interest were the first national wind resource surveys, such as the American Wind Energy Resource Atlas and the Danish Wind Atlas (Peterson *et al.*, 1998a).

The first wave of rapid wind turbine development began in the 1980's, in California, where the first wind farm was constructed. These farms, however, were not permanent sites. They were mostly used for demonstration purposes and many were dismantled after one or two years due to unsuccessful designs (Peterson *et al.*, 1998a). Coupled with an economic crisis, many of the Californian wind energy companies went bankrupt, and consequently wind farm production rates declined just as rapidly as they had begun. Concurrently, smaller companies progressed more slowly in Europe. Progression was based on knowledge of the wind resource and the planning phases, rather than the rapid construction and testing ideology used in California.

The first British wind farm was constructed in 1991 in Delabole, Cornwall. At the time of construction, the farm consisted of ten 400kW wind turbines giving a combined power of 4MW. Also in 1991, Vindeby, the first offshore wind farm was constructed 2.5km off the coast of Denmark, consisting of eleven 450kW turbines (Barthelmie *et al.*, 1996). For a time, countries were not bound by targets of renewable energy production.

The first of the renewable obligations for the UK was set in 2002, where electricity suppliers committed to ensuring that at least 3% of their energy production were from renewable resources by 2003. If this target was not achieved, then the supplier would face a fee which was proportional to the magnitude of the shortfall. Internationally, the 20-20 targets were set in place by the EU in 2007 (EC, 2009). The 20-20 targets state that 20% of energy produced by EU member states is to be produced by renewable methods by 2020.

In Britain, this is equivalent to having 29GW of installed capacity (Huhne *et al.*, 2011) . These targets have sparked an unprecedented venture for production of wind farms across Europe both on land and offshore.

1.1.2 The current status of the UK and European wind energy industry

By the end of 2012, the total wind power capacity, including onshore sites, for the EU member states was 106GW (EWEA, 2013a). Wind energy alone constructed in 2012 accounted for 26%, or 11.9GW of installed capacity, costing between 12.8 billion to 17.2 billion Euros (EWEA, 2013b). The leading country in the EU for wind power is Denmark, where 27% of energy consumption is accounted for by wind energy, making Denmark the first country to achieve the 20-20 targets. Since October 2008, however, the UK has become the world leader in installed offshore wind power capacity (RenewableUK, 2013).

In 2012, the UK installed 1.9GW of capacity, bringing the total to 8.4GW, where 3.3GW is from offshore wind farms. This is equivalent to 413 total operational farms with 19 in the offshore environment. At the time of writing, a further 3.8GW capacity is either in construction or awaiting planning approval offshore (RenewableUK, 2013).

Construction of the offshore wind farms around the waters of the UK has taken place in a series of rounds (Fig. 1.1; Table 1.1). Round one began with the construction of Blyth in 2001, and is currently near completion. It consists of 18 sites amounting to a capacity of 1.5GW (Table 1.1). Only one Round 1 site, Teeside, remains under construction. Round 2 was commissioned in 2003. With improvements in turbine design and siting efficiency, these were located in deeper waters, such as The Wash and the Thames Estuary. Once complete, Round 2 sites will contribute a further 7GW to the renewable energy target of 29GW. At the time of writing, 7 of the 17 Round 2 sites are now operational (Table 1.1).

The final round, Round 3, is by far the largest and is scheduled to begin in 2014. In 2010, nine different areas were identified for construction of particularly large wind farms, as denoted by the shaded regions in Fig. 1.1. On its own, the largest site, Dogger Bank, has the potential to generate 13GW of power. Note that this is greater than both the capacities of Round 1 and Round 2 combined. In total, the Round 3 developments are expected to produce around 31GW.

Table 1.1: List of wind farms by development round. For locations of the sites, refer to Fig. 1.1

Round 1 - 2001		
site	Capacity (MW)	Status of site
Barrow	90	Operational
Beatrice Demo	10	Operational
Blythe	4	Operational
Burbo Bank	90	Operational
Gunfleet Sands I and II	173	Operational
Lynn and Inner Dowsing	194	Operational
Kentish flats	90	Operational
North Hoyle	60	Operational
Rhyl Flats	90	Operational
Robin Rigg	180	Operational
Scroby Sands	60	Operational
Teeside	62	Under Construction
Round 2 - 2002		
Thanet	300	Operational
Walney 1	183.6	Operational
Waleny 2	183.6	Operational
Greater Gabbard	504	Operational
Ormonde	150	Operational
Sheringham Shoal	317	Operational
Gwynt Y Mor	576	Under construction
Lincs	270	Under construction
London Array 1	630	Operational
Humber Gateway	300	Approved
West of Duddon Sands	389	Approved
Westernmost Rough	240	Approved
Dudgeon	560	Approved
Race Bank	580	Approved
London Array II	370	Approved
Triton Knoll	900-1200	Submitted
Round 3: 2010		
Morray Firth	1300	Submitted
Firth of Forth	3465	Submitted
Dogger Bank	9000-12800	Site Awarded
Hornsea	4000	Site Awarded
East Anglia	7200	Submitted
Rampion	665	Site Awarded
Navitas Bay Wind Park	900-1200	Site Awarded
Bristol Channel	1500	Site Awarded
Celtic Array	4185	Site Awarded

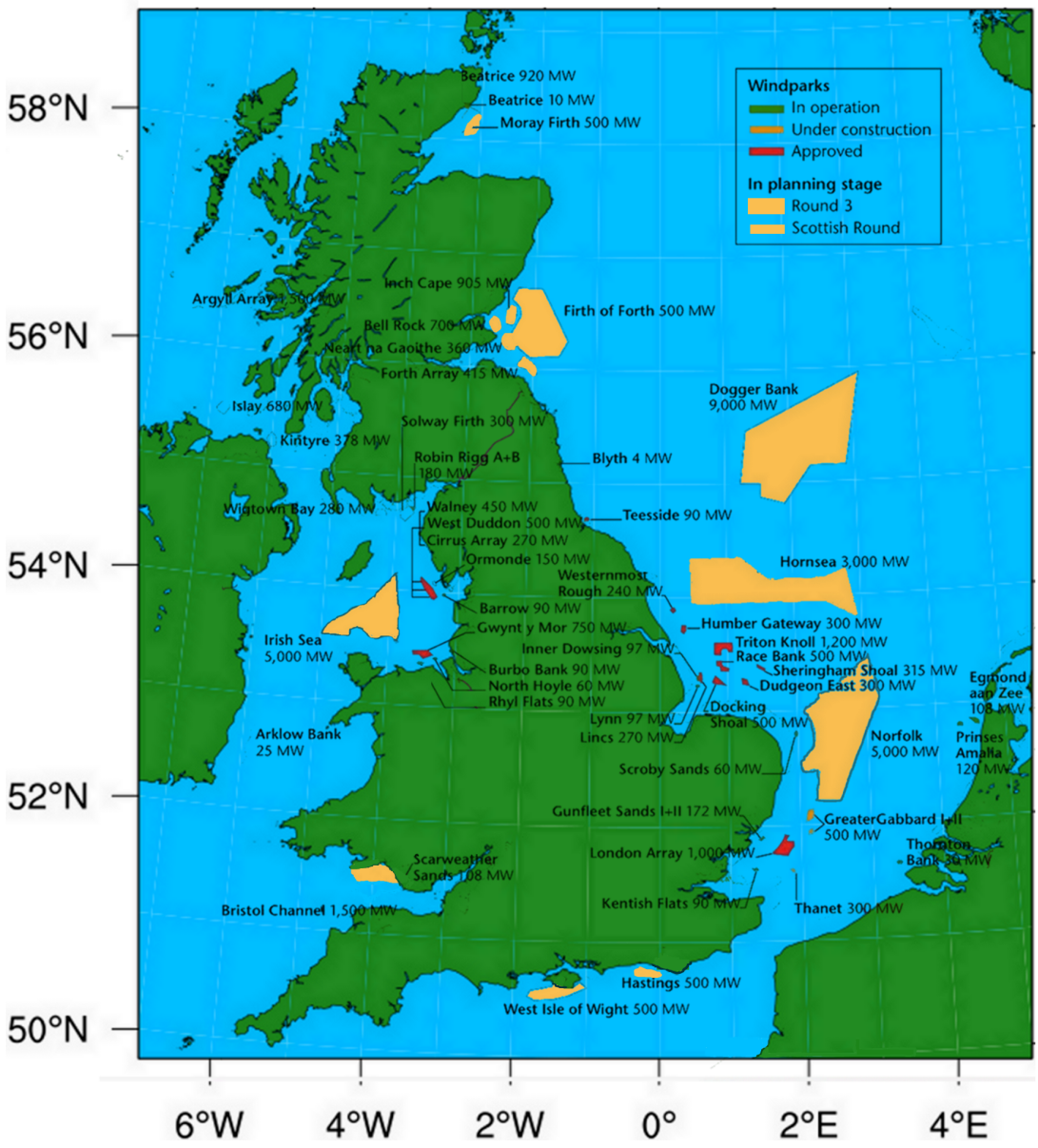

Figure 1.1: The locations of constructed or planned offshore wind farms in the UK (adapted from Cleantech (2010)).

1.1.2.1 Turbine advancements

Apart from the difference in spatial scale of each Round, the technology behind each generation of wind turbines is also improving at a similar rate to farm planning and construction (Breton and Moe, 2009). As noted in Section 1.1, the first offshore wind farm consisted of eleven 450kW turbines with a hub height of 38m and rotor diameter of 35m. Current Round 1 wind farms, for example Lynn and Inner Dowsing off the Lincolnshire coast, are much larger. The power rating of each turbine at Lynn and Inner Dowsing is 3.6MW, with a hub height of 80m and a rotor diameter of 107m (4COffshore, 2013). The

distance from shore is also larger. To the centre of the farm it is approximately 6.2km to the nearest coastline compared with a distance of only 1.8km at Vindeby.

Predictions suggest that these trends of increasing hub height and blade diameter will continue (Bilgili *et al.*, 2011). Indeed, turbine power ratings of 8-10MW with blade diameter of 160m are not totally beyond reason (Snyder and Kaiser, 2009; Breton and Moe, 2009; Bilgili *et al.*, 2011). Furthermore, in order to create the Round 3 sites, it is also necessary to manufacture wind turbines that can be stable in deep water. In the UK, the demonstration wind farm Beatrice was constructed in 2007 in water depth of 45m off the Eastern coast of Scotland and is currently the deepest offshore wind farm in the world (Breton and Moe, 2009). However, the effect of increasing hub height has a large impact on costing of the turbine, and so it is more likely that future turbines will not increase in size any more than is necessary to support the blade diameter (Islam *et al.*, 2013).

Relatively deep water presents several challenges not only in covering the costs of cables and maintenance, but in the method of securing the turbine to the seabed (Breton and Moe, 2009). Existing methods include monopile, gravity based or suction approaches. The method used is both dependant on water depth and soil type. However, at some depth, it is no longer technologically or economically achievable to use the seabed to support the wind turbine. Consequently, this has led to the design of floating wind turbines (Breton and Moe, 2009). The first floating wind turbine was constructed at a test site 20km offshore from Brindisi in Italy. The turbine itself was only rated 80kW, however, the floating design enabled the turbine to operate over a water depth of 108m.

Improvements in the speed and efficiency with which wind turbines are being designed, manufactured and constructed is occurring at an exceptional rate. In the following section, wind power prediction is described and some of the potential issues highlighted.

1.1.3 Wind power prediction and potential issues

The power generated by a wind turbine is proportional to the area swept by the blades, and the volume of air passing through. Consequently, wind power is derived by the following relation:

$$P = \frac{1}{2} C_p \rho A u^3 \tag{1.1}$$

where C_p is the power co-efficient, A is the wind swept area, ρ is the density of air and u is the wind speed. There are several things to consider here. Firstly, note the cubic relationship between wind speed and wind power. In terms of predicting power output, even the slightest error in the wind speed can have a serious effect on the power output. This error could become very costly for the energy industry, since, without an efficient method of storage, the power supply must be balanced with the demand of the consumer. Errors in this regard are both economically damaging to the energy provider and a problem to the consumer.

It has been reported by Sinden (2005) in an assessment of the UK wind resource, that despite this sensitivity to wind speed, the potential power from a typical diurnal wind speed cycle also follows demand for electricity. For example, the typical rise in wind speed in the hours after the evening rush hour coincide well with the increase in demand. Furthermore, the seasonal cycle of wind speed also follows increased demand. In Winter, due to less daylight hours and colder air temperatures, requirements for energy are high. Wind speeds in Winter are also higher in North West Europe, due to an increased frequency of eastern Atlantic storms and a more southerly storm-track.

The second thing to consider from Equation 1.1 is the power coefficient constant C_p. The purpose of this constant is to take into account the efficiency of the wind turbine, whereby energy is lost to heat and sound emissions. Theoretically, the maximum efficiency at which a turbine can operate, known as the Betz-limit, is 0.593. The true value of C_p can be empirically determined from an individual turbine to make the power estimates more accurate. The efficiency of a turbine will vary on an individual basis according to interference with other external structures, or general deterioration over time (eg. Christiansen and Hasager, 2005; Peterson *et al.*, 1998a; Barthelmie *et al.*, 1996)

Thirdly, much of the increase in capacity in recent years has been due to the increase in blade diameter which contributes to the rotor swept area, A. For example, a 100m diameter turbine would have a rated power of 3MW, whereas a turbine with blades of 70m would only be sufficient to produce 1.5MW (EWEA, 2013a).

Equation 1.1 does not hold true for all wind speeds, it is in fact tied to both the power rating of the particular turbine and the so-called cut in speed (Sinden, 2005). Fig. 1.2 shows a typical power curve of a 3.6MW turbine (currently the most common offshore

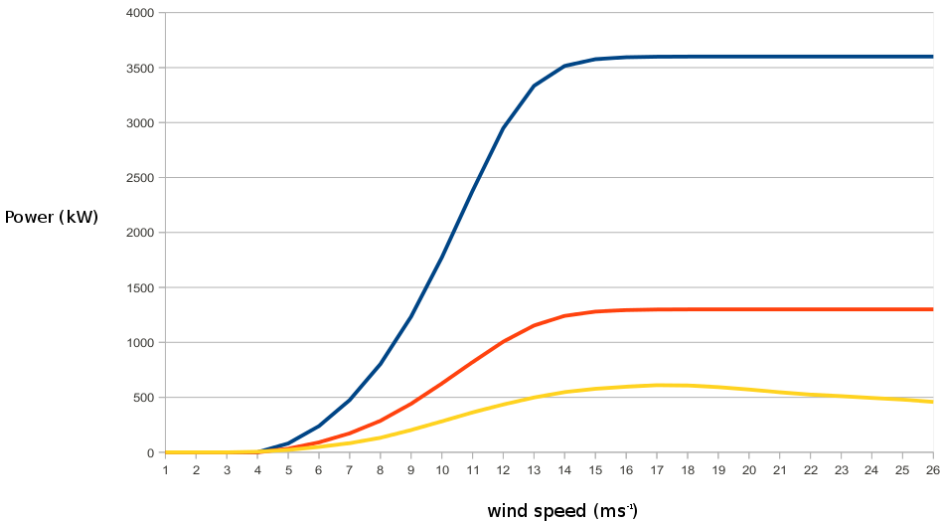

Figure 1.2: Turbine power curves for 600kW (orange), 1.3MW (red) and 3.6MW (blue) wind turbines.

turbine size) and two smaller turbines (EWEA, 2013a). For all turbines, wind speeds under 4ms^{-1} are not sufficient to produce power, and so in this case, 4ms^{-1} is the cut-in speed. More recent turbine designs, however, such as the vertical axis wind turbine, have cut-in wind speeds of 2ms^{-1}, although use of these vertical designs is currently restricted to the onshore environment (Islam *et al.*, 2013). All turbines in Fig. 1.2 reach maximum rated power between hub height wind speeds of 14-17ms^{-1}. Above these speeds, the power production remains constant, except for the 600kW turbine which decreases slightly, until the cut-out wind speed of 26ms^{-1}.

Sinden (2005) remarked that, between 1970-2003, on no occasion was all of the UK below the cut-in threshold of 4ms^{-1}. Furthermore, periods when 90% of the country experienced low wind speeds only constituted 1 hour in every year. Sinden (2005) also stated that wind speeds above a cut-out speed of 25ms^{-1} occurred at one site for 0.1% of an hour every year. This is, in principal, due to the localized nature of wind storms.

A closer examination of Fig. 1.2 highlights the trend of increased efficiency with increased turbine power. Between the cut-in and the rated wind speed, the minimum wind speed required to produce maximum power, the power curve approaches Equation 1.1 and therefore the Betz-limit. In summation of these factors, in any given time period, power can fluctuate rapidly (Fig. 1.3). Sudden changes in power output are either called *ramp-up* or *ramp-down* periods, depending on the sign of the change (Maddaloni *et al.*, 2009). Ramp-up and ramp-down periods can occur on many time scales, from the passing of a

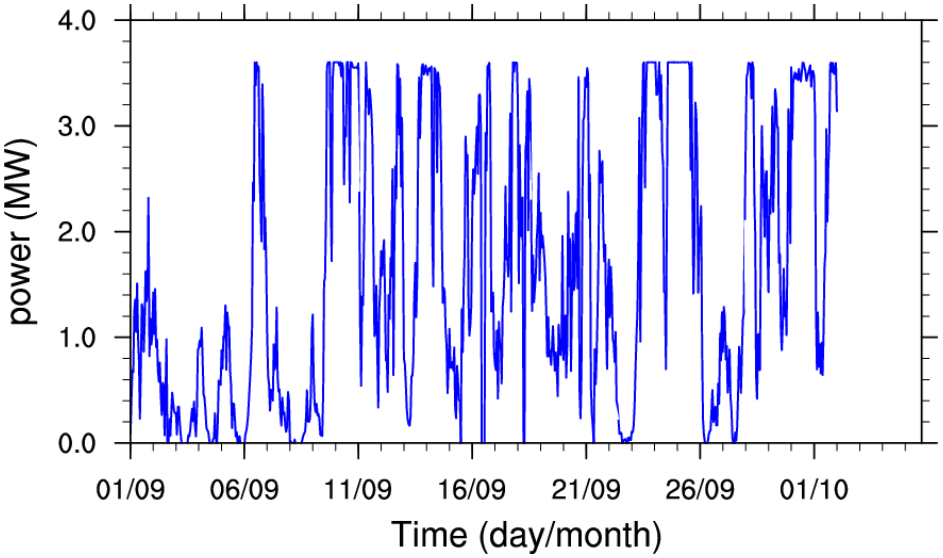

Figure 1.3: A typical 3.6MW wind turbine power output from Lynn wind farm for the period 1st - 2nd October 2012.

frontal system over a matter of hours, to seconds where turbulent gusts cause short-term rapid fluctuations. In turbulent flow, the efficiency of the turbine is hampered, due to the delay of response of the turbine to wind gusts.

1.1.3.1 Wind power forecasting methods

The process of forecasting for wind power can typically can be split into three distinct forecasting time periods (Costa *et al.*, 2008). Each of these forecast time scales are used for different purposes:

1. **Weeks.** Decisions regarding undertaking maintenance on turbines and farm siting.
2. **Days.** Determining the load scheduling strategy for specific farms.
3. **Hours to minutes.** Making small scale refinements on capacity transfers and turbine load.

As a result, various different techniques have evolved in order to predict power output, such as using Numerical Weather Prediction (NWP) models, statistical models and artificial neural networks. There are also hybrid approaches which adopt both statistical methods and NWP to determine power output. A summary of the current wind energy models can be found in Foley *et al.* (2012). In terms of locating suitable sites for wind farms, statistical models are often used (Peterson *et al.*, 1998a,b). A long time series of

observational data is required, typically in the form of a temporary meteorological mast which is established for 1 year or more before construction of the farm (Peterson *et al.*, 1998a). A statistical wind power model, such as the Alea wind model, developed in Spain, is then applied to the data in order to determine long term averages in wind speed. Statistical models rely on large amounts of data to determine an empirical relationship between wind speeds and power production at a given site and do not involve weather dynamics. Further examples of statistical models include the Garrad Hassan Forecaster model and the Danish WPPT model.

For shorter time frames, from 1 or 2 days to 2 weeks, atmospheric dynamics play a critical role and so statistical methods therefore break down (Foley *et al.*, 2012). Wind power models therefore require the use of NWP models to formulate predictions of wind speed, which the wind power model then converts into power production using a theoretical power curve. Examples of the so-called physical models include Prediktor and SOWIE. The choice of NWP model is critical to these wind power models in terms of the geographical location, horizontal resolution and time frame required. Meso-scale models, such as COSMO, ALADIN, HIRLAM and WRF offer the advantage of being able to resolve local features and are frequently used in wind power prediction.

As it is computationally expensive and often time consuming to estimate power output for every farm, prediction data can be regionally averaged in a process called either upscaling or downscaling, depending of the model resolution. Furthermore, if the numerical weather prediction model is of coarse resolution then a downscaling approach is adopted. This can be either dynamically based, for example the Weather Research and Forecasting (WRF) model is capable of dynamically downscaling to a higher resolution from a global model resolution, or through statistical means. In the case of the WRF model, the downscaling is dynamic as it takes place during the simulation as a nested structure, whilst full model physics are being implemented (Skamarock and Klemp, 2008). Statistical models again use data observed from wind farms to create a transfer function between the observations and the coarser numerical weather prediction model. Examples of wind power models which include both atmospheric dynamics and statistical down or upscaling include the Danish Zephyr and the WEPROG models.

NWP models will always contain errors, due to inaccuracies in initial and boundary conditions required to initialize the model and computational limitations involved in forecasting at finer resolutions (Sweeney *et al.*, 2013). To reduce systematic errors, statistical post processing methods are applied to NWP models such as Model Output Statistics (MOS), Kalman filtering and Artificial Neural Networks (ANNs). Sweeney *et al.* (2013) tested 7 post-processing methods, including techniques in short-term bias correction, diurnal cycle forecast correction, linear-least square correction, the Kalman filter, mean and variance correction, directional bias and an ANN. All techniques were effective at reducing bias errors. Additionally, combining techniques by applying a weighting to each method's recent performance and applying that weighting to an average of all post-processing skill scores reduced the overall Root Mean Square Error (RMSE).

At very short time scales of the order of minutes to 1 hour, numerical weather prediction models are less computationally viable or accurate for reliable wind power estimates (Potter and Negnevitsky, 2006). Therefore, the most common method employed here is again a statistical approach. Such approaches often use ANNs and fuzzy systems in which large amounts of observational data are used. These methods, a form of artificial intelligence, use historical relationships between model predictions and forecast power output to predict future power production. These methods are deemed artificial intelligence methods as the model learns from historical relationships to predict power output.

The challenges of wind energy forecasting are similar to those of numerical weather prediction with the additional complexity of the cubic relationship to wind power at both short and long temporal scales. Furthermore, the degree of speed in which turbines are being designed, manufactured and constructed at new wind farm sites places added pressure on research into improving forecasting methods. The degree of sensitivity of wind power to wind speeds and the costs involved, both in terms of monetary value and in terms of balancing power for the National Grid if forecasts fail, are particularly high. Currently, many of the constraints on turbine design are related to engineering and economic feasibility. Shallow coastal regions, such as the Wash and the Thames estuary, are particularly complex and present challenges to numerical weather prediction models. Not only does the model require sufficient resolution to represent the coastline, it also needs to represent meso-scale features, such as sea breezes and coastal jets correctly. These features are now

described.

1.2 The Sea Breeze: behaviour, structure, dimensions and gaps in the literature

Modern understanding dictates that the sea breeze system consists of a circulation cell formed as the result of the build up of a temperature differential between the land and sea (Simpson, 1994; Miller *et al.*, 2003; Crosman and Horel, 2010). During the day, the land surface heats to a greater degree than the sea due to heat capacity differences. An onshore thermal pressure gradient establishes, causing air at the surface to flow landward and air aloft to return back towards the sea. Knowledge of the sea breeze can be traced back 2500 years, before the time of Aristotle, and yet gaps still exist in our understanding of this complex meso-scale phenomena (Goodwin, 1906; Simpson, 1994).

In the following, Sections 1.2.1 and 1.2.2 describe the evolution of the Ancient theory to modern understanding. Section 1.2.3 describes in detail relevant modelling studies, with a primary focus on the offshore environment. Section 2.1.4 examines existing sea breeze identification methods, highlighting advantages and disadvantages of each before the discussion is summarized in the Section 2.1.5.

1.2.1 Ancient History

The earliest reference to a sea breeze arguably came during the Persian war, in the battle of Salamis, where Thermistocles, commander of the Greek army made a decisive victory against the Persians (Goodwin, 1906). Prior to the attack, he noted that the waters were often more difficult to cross in the afternoon, owing to the presence of a regular diurnal wind regime. Combined with the knowledge that the Persian vessels were inadequately equipped to deal with rough waters, he timed his attack with the arrival of this wind and, as a result, was able to make short work of his Persian enemy. With the application of hindsight, it could be suggested that the regular winds were the result of a sea breeze flowing across the Strait of Salamis and that Thermistocles was using the onshore component to his advantage (Simpson, 1994).

According to several authors, the first correct descriptive account of the sea breeze

system came from William Dampier in *Voyages* during the beginning of the eighteenth century (Abbs and Physick, 1992; Simpson, 1994). Dampier describes the sea breeze from a sailing perspective, giving reference to the dependency of the system on synoptic forcing by quoting variations in the timing and directly attributing these to variations in the *weather*. Crucially, Dampier also refers to the calming of the winds prior to sea breeze onset where the sea is like *glass*. As the sea breeze develops, the wind speed increases to a brisk gale before succession during mid to late afternoon.

Evidence for knowledge of the return flow of the circulation cell can also be found in historical texts. During the American civil war, John La Fountain flew the world's first reconnaissance flights over confederate territory (Haydon, 1941; Simpson, 1994). Throughout the campaign, he flew in at low levels into the enemy domain, conducted his observations, then released ballast to catch an opposing flow aloft. This can be viewed as clear evidence that a full circulation cell was known to have existed. However, the ability to take advantage of a feature's presence does not necessarily mean that there is an adequate scientific understanding of how such a feature forms.

Indeed, despite an obvious knowledge of its presence very few attempts were actually made to provide an explanation (Simpson, 1994). Aristotle, 150 years after Thermistocles in *Meteorolologica*, attempted one of the first theories (Webster, 2013). He stated that all winds were the result of a dry exhalation from the land, and consequently sea breezes could be created by a reflection from offshore barriers, such as islands or coastal hills. Unfortunately, a lack of knowledge of the influence of differential heating prevented a more accurate description.

Theophratus, in *De Ventis*, 30 years after *Meteorologica* discussed the importance of the Sun in forcing the wind. He also gave a description of a coastal system opposing the gradient flow not unlike that of a sea breeze. Unfortunately, very few scientific advancements were made between the times of Theophratus and Dampier. However, especially during the last 50 years, thanks largely to advances in computational power and the increases in population pressures in coastal areas, there is a strong motivation and capability to study sea breezes (Arritt, 1987). Consequently, the physics are now reasonably well known and there exists a huge array of observational and computational studies available in the literature. Section 1.2.2 now examines modern theory.

1.2.2 Physics and observations

1.2.2.1 Basic mechanism

When describing the sea breeze system, there are many different views which can be adopted. Which standpoint to take will depend on the scale that is being described. At the most basic conceptual level, the sea breeze system can be described as a meso-scale circulation cell, formed as a result of differential heating between the sea and the land (Fig. 1.4; Atkinson, 1981). The way in which the cell is formed, however, is subject to debate and consequently three competing theories exist offering different explanations.

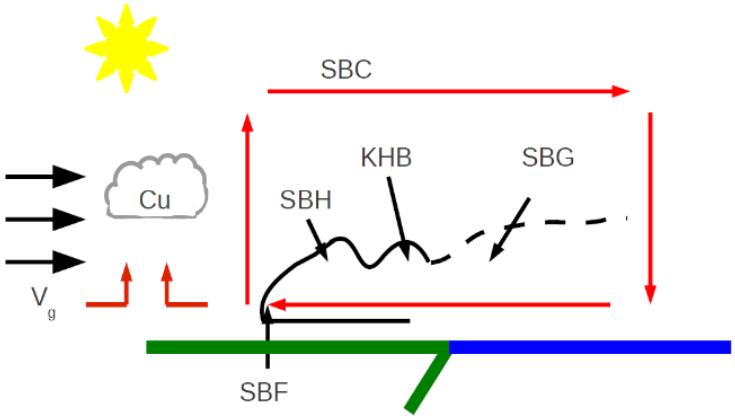

Figure 1.4: Schematic representation of the Sea Breeze System (SBS) adapted from Miller *et al.* (2003). Abbreviations have the following meanings: SBC - Sea Breeze Circulation, SBF - Sea Breeze Front, KHB - Kelvin-Helmholtz Bellow, SBH - Sea Breeze Head, SBG - Sea Breeze Gravity Current, Cu - Cumulus cloud.

To begin, take the assumption of a uniformly straight coastline, during daylight, with negligible friction and zero background flow. Solar radiation initially creates a thermal gradient between the land and sea, owing to differing heat capacities. Consequently, the air heats up more rapidly over the land, resulting in a difference in the rate of vertical thermal expansion. At all levels, apart from at the surface, the pressure becomes higher over the land, resulting in a pressure gradient flow towards the sea. This forms the upper limb of the circulation cell. At the surface, divergence of air away from the land and similarly convergence at sea, creates another low-level pressure gradient, but its direction is reversed. This onshore surface flow is what constitutes the sea breeze. The processes of differential heating, vertical expansion, upper and lower pressure gradient formations describe the *upward* theory of sea breeze development (Fig. 1.5a; Atkinson, 1981)

An alternate, known as the *sideways* expansion theory (Fig. 1.5b; Simpson, 1994),

assumes that there is a height above the land in which the thermal influence of the surface is negligible, thus forcing the air below to expand horizontally. This creates a region of low pressure over the land surface, rather than high pressure above the land as per the upward theory. A surface pressure gradient is established and the sea breeze forms before the onset of the return flow.

In the *mixed* hypothesis (Fig. 1.5c), the processes of horizontal and vertical thermal expansion occur simultaneously. So far, *upward*, *sideways* and *mixed* theories have neglected the process of hydrostatic adjustment which is quantified by looking at the differences between hydrostatic and non-hydrostatic models (Tijm *et al.*, 1999). When an air parcel is heated diabatically, it expands producing a series of sound, or compression, waves in all directions. In the case of the sea breeze cell, the production of sound waves facilitates both the horizontal and the vertical pressure gradients. In essence, this is still the mixed theory, but with a more complete description, including hydrostatic adjustment (Miller *et al.*, 2003; Tijm *et al.*, 1999).

The depth of the sea breeze and feeder flow can be defined as the height of zero onshore motion (Miller *et al.*, 2003). It follows naturally therefore that depths would vary depending upon the degree of solar insulation and therefore latitude of the forming sea breeze. Typical depths of the lateral flows in the UK are around a maximum of 700m for a sea breeze in the UK and about 1400m for the return flow (Simpson, 1994).

During the course of a day, solar heating increases the temperature differential between what is known as the sea breeze front, or the landward limb of the circulation cell, and the stationary air further inland. The result, enhanced by continental effects, is an increase in strength of the thermal gradient and consequently the sea breeze front advances inland. Similarly, the seaward component of the return flow will advance out to sea, but at a faster rate than the sea breeze front, due to reduced friction (Abbs and Physick, 1992). Simpson (1994) found the expected rate of landward advancement to be approximately 6-7ms^{-1}for tropical climates, and around 4ms^{-1} for temperate regions.

The progression of the sea breeze component of the circulation cell behaves more, but not always, as a density current, containing both turbulent and laminar flows (Fig. 1.6 Simpson, 1969, 1972; Abbs and Physick, 1992). The feeder flow of dense sea air travels towards the frontal boundary and is swept up and backwards, forming a raised head.

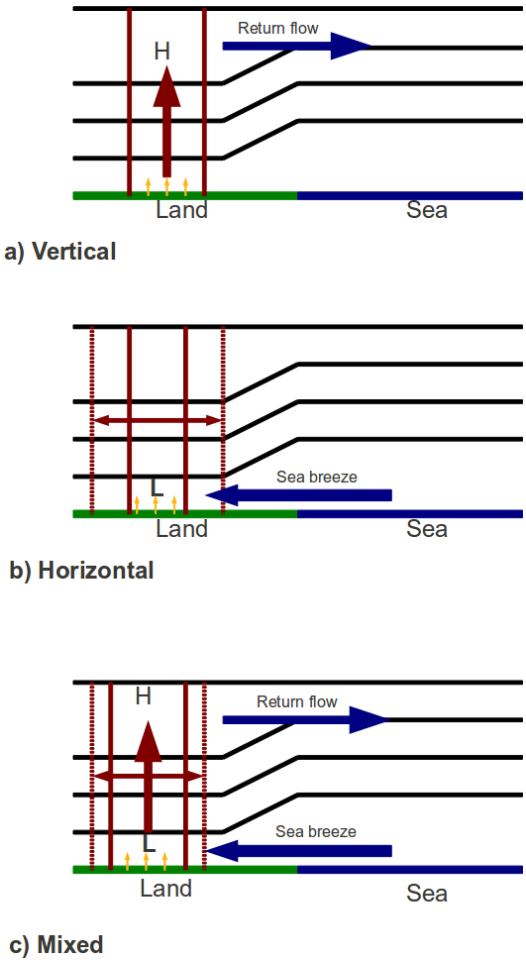

Figure 1.5: Schematic representations of the vertical (a), horizontal (b) and mixed (c) sea breeze initiation theories at the moment of onset. In all cases, the black lines are isobars, the yellow arrows indicate relative land surface heating compared to the sea, solid red lines indicate a vertical column of air and the red arrows the direction in which the column expands. Dashed red lines in (b) and (c) show the horizontal expansion of the air column. The component of the sea breeze which forms first in each theory is also shown by the blue arrow and the locations of local pressure anomalies indicated

Behind it, the Kelvin-Helmholtz shear instability mechanism causes the formation of turbulent breaking billows. This is where the opposing flow has greater velocity, but less density, than the incoming sea air (Simpson, 1994). The density difference required to induce this form of instability can be as low as 1% and flows of this nature have successfully been recreated in water tank experiments (Simpson, 1969).

As the sea breeze advances inland, the Kelvin-Helmholtz billows act to increase frictional drag between the sea breeze and the gradient wind. The sea breeze consequently slows its rate of onshore advancement over time. The billows form the turbulent component of the density current, causing mixing with the surrounding air in a layer up to half the depth of the sea breeze. The air below the turbulent flow is laminar and consists of

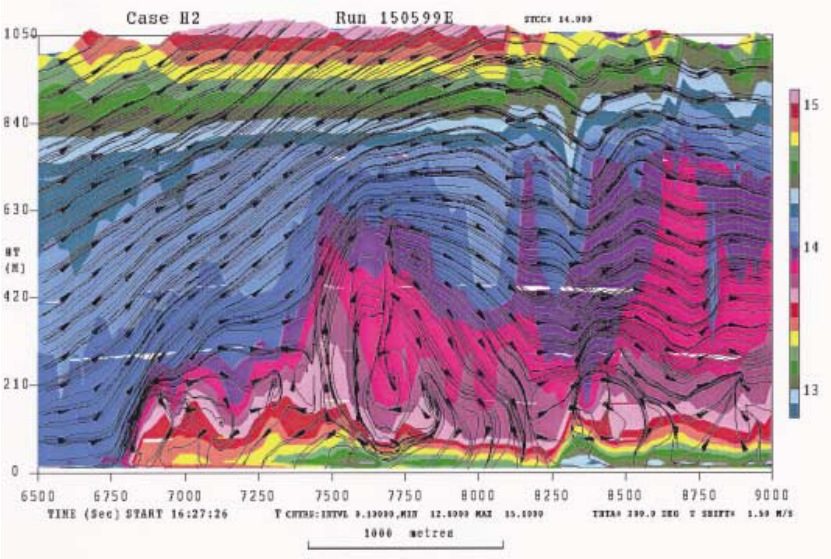

Figure 1.6: The passing of a sea breeze in south Wales, after Lapworth (2005a). The measurements were taken from a tethered kite measuring station during May 15th 1999. Using Taylor's frozen turbulence hypothesis, the time series can be thought of as a two-dimensional section through the sea breeze gravity current. In this case, this procedure enabled the identification of an undular bore superimposed on the sea breeze, which came from a collision between another weaker breeze from the Thames estuary.

pure unmixed sea air. Unless an internal boundary layer is formed from the heating of the sea air by the land surface, pollutants will be mixed with the Kelvin-Helmholtz billows but carried out to sea. In the former case, fumigation can occur, causing turbulent mixing of pollutants to the surface.

Once the magnitude of the solar heating decreases, the billows break down and the sea breeze accelerates due to the smoothing out of the interface between the sea breeze and the gradient wind. Upon sunset, the solar insolation drops to zero and the land-sea thermal contrast is substantially weakened, preventing the sea breeze head from being supplied with new marine air. The lack of surface heating eventually cuts off the sea breeze head entirely and it continues to advance inland as an undular bore (Simpson, 1996; Sha *et al.*, 1993). The bore continues to advance inland until either the circulation dissipates or Coriolis force rotates the bore so that it is moving in a shore-parallel direction.

It follows that the life-cycle of the sea breeze from genesis to dissipation can be summarised in 5 key stages, according to Miller *et al.* (2003). These include:

1. **Immature.** A region of divergence develops in response to the local thermally induced pressure gradient and the sea breeze develops typical density current characteristics in the onshore direction. At the sea breeze head, a front is formed.

2. **Early mature.** Solar insolation declines and the Kelvin-Helmholtz billows break down, causing the sea breeze to surge forward due to reduced friction.

3. **Late mature.** Solar insolation stops and the supply of marine air is cut off from the sea breeze head.

4. **Early degenerate.** The sea breeze head is entirely separated from the feeder flow and moves inland independently.

5. **Late degenerate.** The circulation is no longer closed within the sea breeze head and the rotation due to Coriolis prevents further inland penetration.

1.2.2.2 The addition of gradient winds and sea breeze types

If a large scale gradient flow is introduced, the simple view of the sea breeze cell becomes somewhat distorted. For an offshore gradient flow, the land-sea pressure gradient associated with sea breeze development directly opposes the large scale pressure gradient. The land-sea pressure gradient must therefore first overcome the large scale pressure gradient in order to produce a sea breeze. Consequently, the effect of an offshore gradient wind is to delay the onset time of the sea breeze and to reduce the degree of inland penetration. However, increasing the offshore gradient wind speed also intensifies the sea breeze front as low level convergence acts to both intensify the thermal contrast and to sharpen the temperature gradient across the front, increasing frontogenesis. The result of increasing frontogenesis by increasing offshore gradient wind speed is to create sea breezes with stronger vertical and horizontal winds. A typical observed vertical velocity of around $1ms^{-1}$can be doubled in opposing synoptic flow because of this intensification (Miller *et al.*, 2003). Furthermore, increasing the strength of the offshore gradient wind causes the sea breeze onshore flow thickness to be reduced (Arritt, 1993). If an offshore gradient flow is added into a water tank, the sea breeze head flattens and the density current advances in a similar way to both numerical and observational studies (Simpson, 1994; Simpson *et al.*, 1977).

If the offshore gradient wind is of moderate strength, then the development of the sea breeze is restricted to the offshore environment. Consequently the convergence zone lies within a region which is statically stable and so vertical motions are suppressed. However,

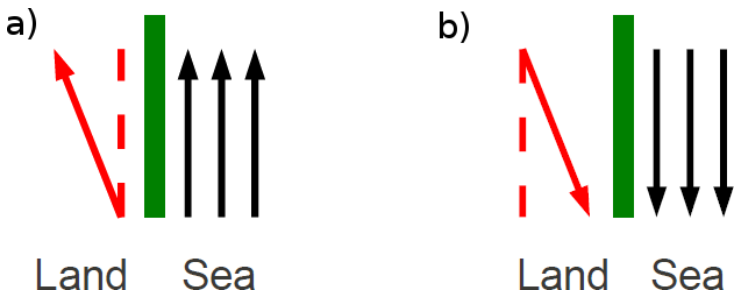

Figure 1.7: Plan views of *corkscrew* (a) and *backdoor* (b) sea breeze generating scenarios depicting the effect of shore parallel gradient winds on a coastline (green). The black arrows depict the unaltered gradient wind direction. The red arrows portray frictional effects on the gradient flow at the coastline.

for sufficiently strong offshore gradient winds the land-sea thermally induced pressure gradient is not strong enough to overcome the pressure gradient and a sea breeze fails to form. The precise magnitudes of these critical thresholds vary between studies. In their review of numerical studies, Crosman and Horel (2010) note that the threshold where the offshore gradient wind speed overcomes the land-sea pressure gradient preventing sea breeze formation varies between 6-11ms^{-1} and that the sea breeze is held in the offshore environment between 6-10ms^{-1}. Their justification for these simulated differences in thresholds lies within variations in the strength of the land-sea thermal contrast.

In the context of wind energy, if a sea breeze is formed in opposing gradient flow, then the resultant wind speed is likely to be less since the sea breeze is acting in the opposite direction to the gradient wind. This therefore implies that the sea breeze will be detrimental to wind power production unless the initial gradient wind is sufficiently weaker than the sea breeze.

The orientation of the gradient wind causes the sea breeze to take on different characteristics and has led to the classification of different sea breeze types (Fig. 1.7; Adams, 2006; Miller *et al.*, 2003). If the gradient flow is offshore and is not too strong compared with the land-sea thermal contrast, then it is classified as a *pure* sea breeze event and it behaves in the way that has been described previously. If, however, there is an along shore component to the ambient wind in a northward direction (to an east coast in the northern hemisphere), then an entirely different type of sea breeze is formed. At the surface, as air crosses the coastline, the frictional differences between land and sea cause the air to change speed. This change in speed causes the magnitude of the Coriolis acceleration to

change, depending on whether the surface roughness increases (reduction of Coriolis acceleration) or decreases (strengthening of Coriolis acceleration) at the coastline Typically, the land surface roughness is greater than the sea (Stull, 1988) and so if, for example, a shore-parallel wind with an offshore wind component crosses a coastline, the acceleration in wind speed does not occur instantaneously across the streamlines. In this case, the southern-most streamlines cross the coast and accelerate first, therefore increasing Coriolis acceleration before the northern-most streamlines and creating a region of divergence at the coast. Since the thermally induced pressure gradient force and the synoptic are not in the same orientation, a *corkscrew* breeze is able to penetrate inland with a weaker thermal contrast than the *pure* type. The along shore component distorts the cell structure of the sea breeze system in such a way that it takes on a helical, or corkscrew, shape (Adams, 2006).

The *backdoor* type is similar to the *corkscrew* in that it there is an along shore component to the ambient flow but it is in the opposite direction (Fig. 1.7b). The presence of the contrast in friction on the coast and Coriolis rotation creates a region of convergence at the coast. This prevents the air above from sinking and inhibits the progress of the sea breeze, making it necessary to have a stronger thermal contrast than the *pure* type to initiate the sea breeze system. Once more the circulation is helical shaped, but in the opposite sense to the *corkscrew* type. Adams (2006) coined the term *backdoor* sea breeze to describe the relative difficulty in forming compared to the *corkscrew* (or *frontdoor*) type.

The final type described by Miller *et al.* (2003) is *pure synoptic*. This is the transport of sea air inland by synoptic scale flow. It will not be considered any further as it effectively includes any onshore wind, stretching the definition of a sea breeze to beyond a thermally induced flow.

The *pure* type is the most intensely studied type of sea breeze (eg. Crosman and Horel, 2010; Finkele, 1998; Azorin-Molina and Chen, 2009). Primarily, this is due to the ease of creation of an identification method relying on the winds reversing from offshore to onshore (eg. Azorin-Molina *et al.* (2011)). Diagnosing the offshore extent of a sea breeze is also simpler with the *pure* type, since a distance offshore can be defined where the wind speed exceeds a particular threshold (Arritt, 1989).

The behaviour of *corkscrew* and *backdoor* sea breezes is largely under-studied. References to the types, as described by Miller *et al.* (2003), are usually implicit. For example, Gahmberg *et al.* (2010) studied the effects of incrementally varying wind direction and found that the sea breeze is stronger for geostrophic flows 45-90° left of perpendicular from a Northern Hemisphere coastline (approaching from the sea), indicative of a *corkscrew* sea breeze. This implies that the effect of a *corkscrew* sea breeze on wind energy is likely to be beneficial in terms of producing power, highlighting the need to be able to distinguish between the different types.

1.2.2.3 Fine-scale structure

Typically, the arrival of a sea breeze will be accompanied by an increase in humidity and a decrease in dry bulb temperature (Simpson, 1994). At the sea breeze front, additional features can develop (Fig. 1.6). Away from the frictional drag of the surface, air travels faster and consequently overruns, trapping the warmer land air into unstable pockets called clefts (Simpson *et al.*, 1977). Between these, lobes are created, which contain ducts of trapped warm air travelling laterally towards the clefts with the overrunning sea air above. These are only present during the day as radiative cooling at night rapidly cools the overlying air, causing an increase in stability (Abbs and Physick, 1992). Typical length scales of lobes and clefts are of the order 1km and so only the highest resolution models are able to distinguish them (Simpson, 1994).

At the interface between the sea breeze inflow and the return flow above, no mixing occurs (Abbs and Physick, 1992). This is important in air pollution studies, as it means that any pollutants released within the sea breeze will be transported further inland as it advances. Importantly, pollutants do not mix in the Kelvin-Helmholtz bellows either, instead, they become trapped in a convective internal boundary layer (Miller *et al.*, 2003). This region forms due to thermal modification of the sea air as it advances over land. If, in the converse case, pollutants are released in air preceding a sea breeze, they will be picked up and removed by the advancing front (Abbs and Physick, 1992). The gravity current will therefore act to purge the air of pollutants (Simpson, 1994). Many studies therefore exist relating sea breezes to air pollution, particularly in the large coastal cities such as Tokyo, Adelaide and those around the Gulf Coast of the USA (eg. Yerramilli *et al.*, 2009;

Tsunematsu *et al.*, 2009; Simpson, 1994)

Heralding the arrival of the sea breeze gravity current, are prefrontal, or forerunner waves (Miller *et al.*, 2003). These waves are generated when the front is directly above the land-sea interface. To an observer, the arrival of such waves would be associated with a landward wind that consists of continental air passing through before the passing of the sea breeze front. Forerunner waves are also produced during the late evening when the front interacts with the nocturnal stable boundary layer. Physically however, these are different to their earlier counterparts. They appear as overturning cells with wavelengths of approximately 10km, moving at much slower speeds of aRound 3.5ms^{-1} and rapidly dissipate in the surrounding flow (Miller *et al.*, 2003). Note this is at approximately the same speed as the advancing gravity current. Early forerunner waves travel much faster and can travel as deep as 60km inland (Miller *et al.*, 2003).

After approximately 6hrs into formation, the Coriolis force begins to play an increasingly important role. Indeed, Coriolis rotation causes the advancement of a *pure* breeze to veer over time (in the northern hemisphere) so that often a sea breeze that initially began at right angles to the coastline will finish at sunset blowing parallel to it (Simpson, 1994). Combining this with the nocturnal rotation of the land breeze, a complete 360° change of wind direction in a 24 hour period can often be found in hodographs (Fig. 1.8; Simpson, 1994). These effects are, however, dependent on the type of the sea breeze. A *backdoor* breeze will follow the same pattern as a *pure* breeze, but a corkscrew will show gradual backing over time. If, in the case of the *pure* breeze, Coriolis causes veering to the extent that there is shore parallel flow, by definition, it has now become a *corkscrew* flow (Miller *et al.*, 2003). However, the effects of local winds from terrain can distort, and sometimes reverse this picture.

1.2.2.4 Complex terrain

Many studies only consider sea breezes in regions with relatively flat terrain and simplistic coastlines to avoid complications with other topographical induced effects (eg. Bigot and Planchon, 2003; Damato *et al.*, 2003; Fichet *et al.*, 2010). The result is that individual features can be analysed and the effects on the sea breeze system documented, so that it can be used to help explain sea breeze behaviour in more complex terrain (Simpson,

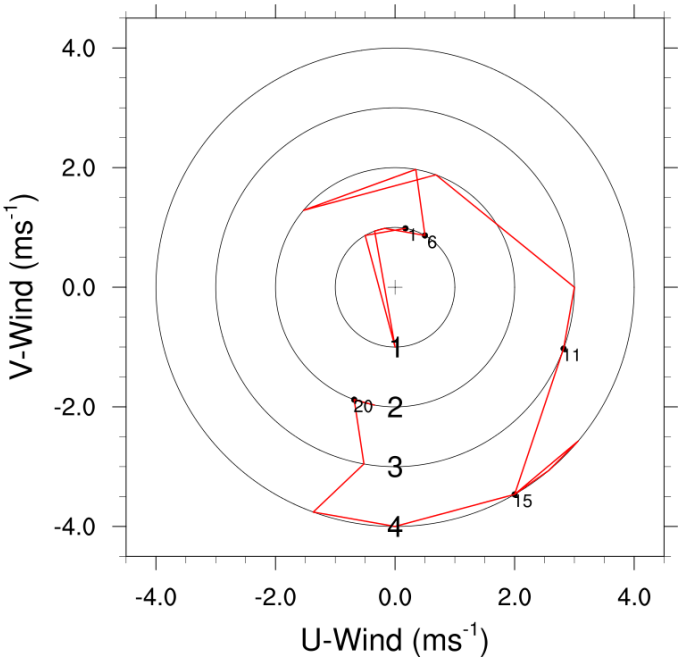

Figure 1.8: Observed hodograph at Valkenburg meteorological station on the western coast of the Netherlands for a *pure* sea breeze event on the 19th June 2012. North westerly winds correspond to winds in the onshore direction and south easterly winds are offshore.

1994).

So far, the coastline has been assumed to be straight, but if either a concave or convex structure is added, as when the flow is over a bay or headland, then the behaviour of the sea breeze system is altered. For a convex coast, the sea breeze converges, creating strong updrafts and sometimes convective storms (Abbs and Physick, 1992; Golding *et al.*, 2005; Simpson, 1994). Conversely, for concave coastlines, sea breezes experience divergence (Abbs and Physick, 1992). The picture becomes more distorted for coastlines with multiple bays and headlands.

Abbs and Physick (1992), in a review of sea breeze model and observational studies, examine the effects of more complex coastlines and introduce the notion of bay and ocean breezes. Bay breezes are essentially small scale sea breezes acting on the temperature differential between the land and the bay waters. Ocean breezes act on the much larger scale, behaving as though acting on the more generic shape of the coastline. Also noted was that there are differences in composition between bay and ocean breezes. Usually the bay temperature will be cooler than inland, due to continental effects, and therefore the ocean breeze is warmed from below at a greater rate than the bay breeze. This results in a ocean breeze of less density, therefore allowing it to penetrate inland above the bay breeze

(Abbs and Physick, 1992).

As it is possible to generate more than one sea breeze on a coastline, it is often the case that a physical reaction will occur if the breezes collide. Usually, at the point of collision, a line of deep cumuloform type clouds develop, often triggering thunderstorms as a result of the enhanced uplift (Simpson, 1994). Clarke (1984) carried out numerical experiments involving two parallel coasts, in what was to become known as the double coast model. The simulation involved a lateral gradient wind, so that one of the sea breezes would be enhanced and the other suppressed by the flow. Eventually, the two circulations collided, producing a sharp vertical protrusion of cold air, closer to one of the coastlines which collapsed. The result was the production of undular bore waves, which propagate at a similar speed to the sea breeze, but underwent no advection of mass (Abbs and Physick, 1992).

The formation of undular bores can occur on any peninsula, though, one of the most famous examples is the 'morning glory' in the Gulf of Carpentaria, Australia (Clarke, 1983, 1989; Clarke *et al.*, 1981). Visually, the morning glory is a wind squall, or succession of squalls, that produce roll clouds in the early hours of a spring morning (Clarke *et al.*, 1981). Two sea breezes, one from the east coast of Cape York Peninsula, and a weaker one from the west, interact to produce a bore that propagates on the nocturnal, or maritime, inversion (Abbs and Physick, 1992). The effect of the stronger sea breeze is to modify the atmosphere over a coastal strip, producing a suitable boundary layer for the bores to propagate (Clarke, 1983).

A relatively recent example of bore generation in the UK (South Wales) was observed by Lapworth (2005a), where originally intending to observe a single event, using tethered kites, a wave-like structure was discovered superimposed onto the structure (Fig. 1.6). It soon became apparent that a second breeze had developed from the Severn estuary and collided with the larger sea breeze, producing the bore.

Bores can also be produced without the need of a collision (Miller *et al.*, 2003). During the late evening, the late degenerate sea breeze front and head can separate themselves from the feeder flow and propagate along the nocturnal temperature inversion as an undular bore. It is the interaction with the nocturnal boundary layer itself that triggers the

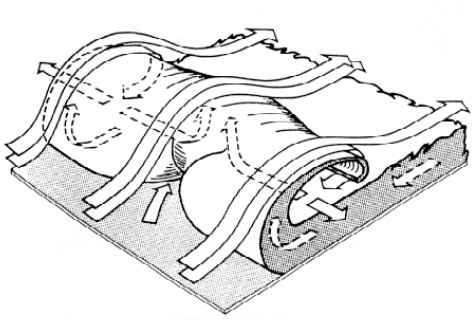

Figure 1.9: Diagrammatic representation of lobes and clefts from Simpson *et al.* (1977). Note the presence of vertical motion in the centre of the lobe. Warm air that is trapped by the collapsing overlying sea air becomes unstable and is forced to rise, forming a lobe.

detachment. The bore then travels further inland, acting as transport for pollutants, eventually dissipating due to inertial damping and radiative energy loss (Miller *et al.*, 2003).

When flowing over elevated terrain, the effects of mountain valleys and winds must also be considered, as both the positioning and the height of the terrain have an effect on the flow patterns of a sea breeze (Simpson, 1994). The primary effect of mountain winds is to enhance the circulation of the sea breeze, however, the precise effect depends strongly on both the location of the range (Abbs and Physick, 1992). Abbs and Physick (1992) state that if a coastal valley runs parallel to the shore, and has an opening out to sea, then the sea breeze will either flow up the valley, or flow over the hills and spill into it, depending on the orientation of the gradient wind. However, if either the height of the mountain range, or the stability of the atmosphere is increased, the sea breeze can become blocked. Furthermore, if the mountains, or hills, are positioned close to the coastline, the cell splits into one entirely over the ocean, and another on the windward side of the mountain (Abbs and Physick, 1992).

Mountain winds can also mask the observed reversal of the winds seen in hodographs. Simpson (1994) gave the examples of Aberdeen and Kinloss, Scotland, to explain this effect. The diurnal cycle of winds in Kinloss is, as you would expect in a *pure* sea breeze, a complete 360° clockwise rotation, but at Aberdeen the rotation is anti-clockwise. It is the presence of the Cairngorms that both enhance and suppress the circulations at the respective settlements.

1.2.2.5 Inland and offshore extents

During one of the more intensely studied sea breeze episodes in southern England on 14th June 1973, Simpson *et al.* (1977) was able to show and describe the typical passage of a sea breeze front with the aid of both numerical simulations and a climatology. The advance of the sea breeze was found to be directly related to the local density differences across the front and the authors were able to successfully describe the changes in the rate of inland penetration during the course of a day.

Typically, as the sea air starts to flow inland, its temperature becomes modified by the land surface. As the inflow of sea air is usually a lot shallower than the air over land, its temperature rises more rapidly and consequently the temperature gradient across the front becomes significantly reduced, slowing the speed of advancement. This tends to occur around midday, when the sea breeze is still immature (Abbs and Physick, 1992). This continues until late afternoon when the rate of solar heating decreases. Despite reduction, the land surface still gradually warms, but the advancing sea air is still arriving from offshore. The net result, is an increase in thermal gradient across the front and an acceleration of the sea breeze in the evening.

There have been numerous observational studies of sea breezes specifically focusing on the degree of inland penetration (eg. Damato *et al.*, 2003; Simpson *et al.*, 1977; Bigot and Planchon, 2003). Typically, they agree that for mid latitude environments they tend to penetrate between 30-50km inland, however it is also possible for a front to travel over distances greater than 100km if the conditions allow. For example, in Europe, of the 76 *pure* sea breezes that were identified by Simpson *et al.* (1977), 6 were observed to have travelled over 100km inland. Similarly, Tijm *et al.* (1999) conducted both a model and observational study for May 1989 over the the Netherlands and concluded that approximately 60% of sea breeze days during this month advanced over 100km inland. Tijm *et al.* (1999) also noted that the degree of inland penetration is not significantly affected by surface roughness, by initial boundary layer depth or by increasing the sensible heat flux behind the sea breeze front as the sea breeze advances over a relatively warm surface layer. Instead, the magnitude of onshore advancement is dictated by the large scale flow and the temperature contrast.

Sea breeze onshore extents have also been intensively studied through the use of

numerical models. These range from 2-dimensional idealized hydrostatic models to 3-dimensional non-hydrostatic simulations with full physics parameterization and high resolution coastlines.

The purpose of idealized simulations is to simplify the problem to its essential elements and progressively build in complexity so a theory or dependency of a parameter can be tested. Scaling laws can then be constructed in order to calculate various parameters such as horizontal and vertical length scales. Scaling laws have been derived from various forms, including observations (Steyn, 2003), Large Eddy Simulations (Antonelli and Rotunno, 2007) and linear theory (Rotunno, 1983). Table 2 in Crosman and Horel (2010) shows a detailed summary of examples of the various scaling laws developed. One such method is based on the linear theory of Rotunno (1983). This assumes that the Earth's atmosphere can be simplified as a rotating stratified fluid which is therefore dependant on the Coriolis parameter, *f*, and vertical stability, *N*. The diurnal cycle is represented as a stationary wave with frequency ω. Through the linear theory of wave motion, the horizontal length scale, *L*, of the sea breeze is as follows:

$$L = \frac{Nh}{(\omega^2 - f^2)^{0.5}} \tag{1.2}$$

where *h* is the vertical scale of the surface heating. Rotunno (1983) noted that for low latitudes, the sea breeze response takes the form of inertia-gravity waves but for higher latitudes, the response of the sea breeze is to produce a localized circulation. Note that in this case, there is no dependency on background flow. Qian *et al.* (2009) expanded this theory to include background wind speed but for equatorial cases where $f = 0$, and produced another set of gravity waves which were produced by the addition of the gradient wind. Jiang (2012) further extended this theory still by investigating coastal geometry on sea breeze onshore advancement.

Unlike inland penetration, and importantly for offshore wind energy generation, there have been very few studies looking at the offshore extent of a sea breeze. This is primarily due to a lack of offshore observational data and therefore studies are mostly model based. Furthermore, there is a much stronger motivation to study sea breezes in the onshore environment because of the sea breeze effects on public health, such as air pollution in coastal cities, the cooling effect during warm weather and flash flooding associated with strong

sea breeze convergence (Borge *et al.*, 2008; Simpson, 1994; Golding *et al.*, 2005). With the construction of offshore wind farms, there is now a more pressing need to understand sea breeze behaviour and frequencies in the offshore environment.

Crosman and Horel (2010) note that there are both a lack of studies focusing on the offshore sea breeze environment and a deficiency looking at sea breeze sensitivity to the extent of the water body. Indeed, in a review of over 50 years of sea breeze modelling studies they highlight only two influential papers focusing entirely on the offshore component. In the first study by Arritt (1989), 2- and 3-dimensional model simulations were performed to determine the environmental controls on the offshore extent of sea breezes. Arritt (1989) defined the offshore extent to be the region where the winds towards the shore were greater than 1ms^{-1}. Latitude and synoptic forcing were found to have the most significant effect; both higher latitudes and offshore gradient flows greatly reduced the offshore extent. For example, increasing the latitude from 0°N to 40°N reduced the offshore extent of the sea breeze from 160km to 113km. It was also determined that if the (SST) was sufficiently warm to produce a convective boundary layer, then the sea breeze was weakened. However, if the water was already sufficiently cold to produce a stable surface layer, any further cooling did not have an additional effect. Decreasing the SST from 293K to 283K, increased the sea breeze offshore extent by 25km, however, a further reduction in SST to 273K only caused a further 6km loss in offshore horizontal extension.

More recently, in the second study, Finkele (1998) used a 3-dimensional hydrostatic model to ascertain offshore propagation speeds, with the help of airborne measurements. Principally, in contrast to Arritt (1989), it was found that the offshore extent was similar for both light (2.5ms^{-1}) and moderate (5ms^{-1}) offshore gradient wind conditions. The propagation speeds for both onshore and offshore development were non-uniform at these wind speeds. Finkele (1998) also suggested that the onshore extent was more sensitive to gradient wind speed than the offshore, though it was added that during periods when wind speeds were greater than 7.5ms^{-1} the sea breeze had become entirely detached and so it was no longer possible to confirm. Both studies report, however, that the offshore extent can be several times that of the onshore, and can reach distances ranging from 75-150km. In the southern North Sea, the length of the water body ranges from 100-250km. therefore it is entirely plausible that any sea breeze forming off the coast of the UK could interact

with another forming off mainland Europe.

Unfortunately, interactions of two sea breezes in the offshore environment is a process that is also under-studied; Savijarvi and Alestalo (1988) addressed the issue of a smaller scale water body, even so, their primary focus remained on the inland component. Their approach was to use a 2-dimensional meso-scale model to simulate sea breezes across a channel 80km wide with SST, land surface temperature and roughness length variations representative of the Gulf of Finland. Both wind speed and direction were varied to examine the behaviour of the sea breeze in this situation. In particular, Savijarvi and Alestalo (1988) note that the sea breeze was insensitive to the strength of along-shore gradient winds, however offshore winds generated a low level jet along the coast and suppressed sea breeze inland penetration.

More recently, Crosman and Horel (2012) performed idealized large eddy simulations of both sea and lake breezes. Sensitivity tests were performed on lakes of varying size, up to 100km. However the focus of the study was once again in the onshore environment. The effect of varying the width of the water source produced sea/lake breezes which did not conform to sea breeze scaling parameters, suggesting that lake breezes should be treated differently. For a 100km lake, however, the lake breeze characteristics matched those of a sea breeze in terms of sensitivity to heat flux and vertical stability.

1.2.3 Existing sea breeze identification methods

Sea breezes are truly multi-scalar features. As a starting condition, they require a series of synoptic situations, or triggers, to be satisfied before they can develop. Methodologies have therefore needed to include these, whilst simultaneously involving techniques to work on the local scale. Furthermore, there is no perfect solution. Additional complexities such as mountainous terrain or island effects have all created problems, leading to what is now a myriad of available methods.

1.2.3.1 Surface observational and automated techniques

One of the notable earlier studies, conducted by Simpson *et al.* (1977), focussed on the inland penetration of breezes in the south east of England. A climatology was constructed

using several different data sources. These included meteorological stations, pilot balloons, instrumented gliders and radar observations. Sea breezes were identified using thermohygrographs. The position of the rise in dew point, associated with the arrival of the front, highlighted the presence of a sea breeze. These results were checked against the timing of the reversal of the winds to provide confirmation. Stations were oriented so that the progress of the front could be tracked. The pilot balloons were used in conjunction with the glider and radar observations in order to determine the fine scale structure of individual sea breezes. In all, Simpson *et al.* (1977) identified 76 different sea breeze events in a 12 year period, with the vast majority of breeze systems penetrating between 30-40km inland. The results from this study are consistent with several other studies in Britain and in Europe (Simpson, 1994; Damato *et al.*, 2003; Bigot and Planchon, 2003).

In spite of this, it must be noted that this method is subjective and extremely expensive in terms of labour. In short, all days during the months of April to September were studied where the addition of some form of synoptic, or temperature gradient, filter could have negated the need. Also, the size of the necessary a rise in dew point temperature associated with the sea breeze is not mentioned. The passing of a synoptic front could also generate a rise and so there needs to be some way of eliminating this effect.

One of the ways to streamline the approach is to introduce a fully automated method involving filters. One such example was used by Borne *et al.* (1998), whereby the primary focus was the complete reversal of the surface wind in 24hrs. The method, originally developed for application to the Swedish west coast, comprised six different filters:

1. The gradient wind speed shift was less than 90° in 24hrs
2. The gradient wind speed changed less than 6ms^{-1} over the 24hr period
3. The gradient wind speed was less than 11ms^{-1}
4. The temperature difference between land and sea was greater than 3°C
5. The surface winds after the onset of the sea breeze rotate by more than 30°
6. The ratio of peak change of wind direction to the mean change in the proceeding 5hrs is greater than 6

The filters create a conservative selection method that could be applied to any coastline without the need to take into account complex terrain. However, the strict definition of a sea breeze from this method means that some days are likely to be missed. One critical assumption of the method is that the change in wind direction is purely associated with a sea breeze and not orographically induced. This must be taken into account in particularly mountainous terrain. During the course of their study, Borne *et al.* (1998) compared the results to an independently developed method at the University of Lund, Sweden. The procedure, known as the Lund method, involved using observations of surface wind speed, upper air winds and surface air temperature in order to divide the days into either sea breeze, possible sea breeze or non-sea breeze day. Sea breeze days were classified if there was a distinct change in wind direction during the day and a reversal at night. There must also be an increase in wind speed that is entirely due to the change in wind direction. If this is not the case, then the day was classified as a possible sea breeze day. Finally, there must be a temperature difference between the land and sea. All other cases were classified as a non-sea breeze day. The results of the analysis indicated that the method operated with an expected 75% accuracy and that the most important filter was filter 5, though all were significant in the selection process.

A similar filter method was used by Furberg *et al.* (2002) to construct a climatology of sea breezes in Sardinia. The method was an amalgamation of an earlier method by Steyn and Faulkner (1986) and Borne *et al.* (1998), its main focus being on the wind reversal. It comprised of 3 main filters and filter 4 from Borne *et al.* (1998). These were:

1. The vast majority of hourly wind speeds must be offshore during 6 hours before and 2 hours after sunrise

2. The surface wind must be blowing onshore for at least 2 consecutive hours between 2 hours after sunrise and 2 hours after sunset

3. The vast majority of the winds between 2 and 8 hours after sunset must not be in an onshore direction

These filters were the same as Steyn and Faulkner (1986) except for the timings in order to compensate for the change in latitude. Also, instead of using sea surface temperature, as in Borne *et al.* (1998), the air temperature over water was used and the temperature

difference required to pass the filter reduced to 0°C. The key findings of the study were that sea breezes on Sardinia could occur at any time of the year, but were more common in the summer months, especially June. This is in-keeping with other studies, though in the western European winter the thermal temperature gradient between the land and sea is often reversed and so sea breeze formation is not likely (Simpson *et al.*, 1977; Simpson, 1994; Borne *et al.*, 1998). Once more, this study does not discriminate between the effects of mountain winds, despite being located in much more mountainous terrain than the Swedish archipelago. Also, no considerations are given to the possibility of strong and rapidly changing synoptic scale flow producing the effects sought by the filters, though this is less applicable in the Mediterranean climate.

One technique created by Azorin-Molina and Chen (2009) for use with the Mediterranean involves making use of a recently discovered teleconnection pattern, the Western Mediterranean Oscillation (WeMO). This barometric dipole is measured by using differences in pressure between stations in Spain and Italy (San Fernando and Padua respectively). Similar in nature to the North Atlantic Oscillation (NAO), the WeMO has three distinct phases. The positive phase; strong pressure gradients and westerly or northwesterly flow, the negative phase; strong pressure gradients and easterly or southeasterly flow and the neutral phase involving weak pressure gradients. The neutral phase is logically the most supportive for the development for sea breezes. In their study, Azorin-Molina and Chen (2009) tested different thresholds of the index against a manual selection method and found a range of values between ± 1 as the most ideal range for a first filter in selecting sea breezes. They also suggest that this method is adaptable for any region where a barometric dipole exists. Theoretically, this means that this could be applied to the NAO, although the dipole does not dissect the region of interest as is the case with WeMO.

1.2.3.2 Satellites and geostatistical techniques

Initially, satellites were used as nothing more than an illustration to back up observations rather than as data to be processed (Damato *et al.*, 2003). However, since the imagery can reveal the presence of a sea breeze front, through the line of cumulus cloud streets forming parallel to the coast, a study of inland penetration is possible (Simpson, 1994). Damato *et al.* (2003) conducted such a study using the Advanced Very High Resolution

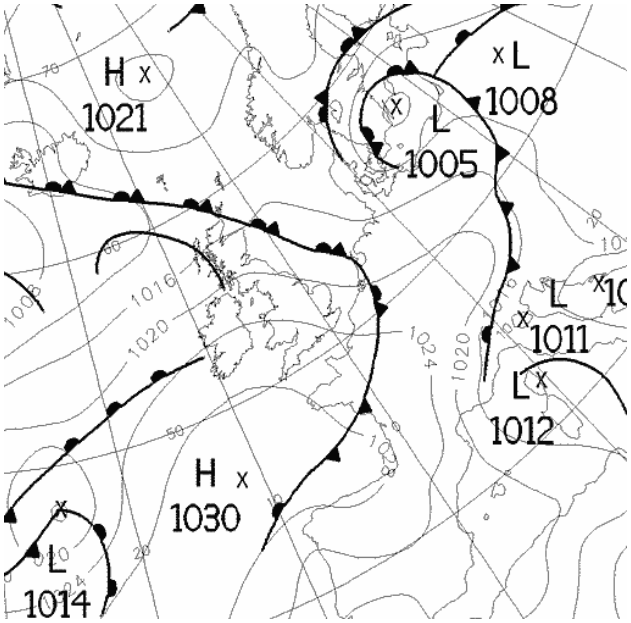

Figure 1.10: Surface pressure chart valid for 00:00 UTC on the 7th June 2000. The surface pressure pattern is representative of the Northern European Anticyclone (NEA) as classified by the *Bulletins Hebdomadaires d'Etudes et de Renseignements* (BHER). The NEA weather type was dominant when sea breezes were formed on the south coast of England in the study of Damato *et al.* (2003)

Radiometer (AVHRR) visible imagery from May to September 2000 in the English channel area. Sea breeze fronts were assumed by the presence of the cumulus next to cloudless coastal skies. The boundaries were marked and composited to construct a climatology for inland penetration. On comparison with the *Bulletins Hebdomadaires d'Etudes et de Renseignements* (BHER), a catalogue of synoptic maps from Météo-France, it was found that the number of sea breezes observed were sensitive to the prevailing anticyclonic situation. Damato *et al.* (2003) identified three distinct patterns that produced sea breezes which depended on the position of the dominating anticyclone. Far more sea breezes were formed by the Northern European Anticyclone (NEA) than any other classification (Fig. 1.10). Damato *et al.* (2003) point out, however, that this method is highly subjective and does not include days with sea breezes that form no cumulus frontal boundary. These situations often occur when the air is too dry to induce convection (Galvin, 2006). Also, if an onshore synoptic flow were present, it would be difficult to determine whether the cloud streets were indeed caused by a sea breeze. Meteorological data from observational stations are needed to confirm.

Such a study was adopted by Bigot and Planchon (2003). A climatology of sea breezes was constructed using AVHRR in northern France for June and July 2000 and a new

geostatistical technique called Singular Value Decomposition (SVD) tested. SVD is a method that summarizes the multi-spectral output of the AVHRR into a few components and allows comparison with a climatic database; in this case, a network of 22 meteorological stations. This technique also allows discrimination of different weather systems and thermo-topographic winds. There are, however, several constraints on this type of analysis. Firstly, studies are always restricted by the number of images and the time of the satellite pass. The images used in this study were limited to 1400 UTC, thus the maximum penetration of the Sea Breeze Front (SBF) was not studied (Bigot and Planchon, 2003). The process also relies on having a dense network of meteorological stations so that the statistical analysis can be undertaken. The study was also subject to the same constraints as Damato *et al.* (2003), in that sea breezes which formed on cloudless days were missed by the method. Furthermore, the results of such a statistical analysis are subjective and computationally expensive (the resolution had to be constrained to 8km) and so will only be applicable if resources are adequate. However, despite these constraints, SVD did produce a meaningful climatology, with results that were inkeeping with other studies at similar latitudes.

As well as studies using either surface observational or remotely sensed methods (or both), some works make use of some form of additional synoptic archive. As previously mentioned in the study by Damato *et al.* (2003), the BHER archive was used to identify the most common synoptic situations responsible for producing sea breezes. Additionally, in a more recent study, Fichet *et al.* (2010) made use of the Objective Grosswetterlagen (OGWL) catalogue to produce a climatology in the Caen region, France. The OGWL consists of 29 different weather regimes for Europe and the North Eastern Atlantic, constructed from ECMWF ERA-40 reanalysis from 1947 to present (James, 2007). Fichet *et al.* (2010) found that all sea breezes but one formed in anticyclonic conditions, the most frequent being anticyclonic easterly or northeasterly types. Once again, Fichet *et al.* (2010) used the sea and land temperature difference to pose as the *breeze trigger*. Finally, on a local scale, a series of temporary meteorological stations were used to perform statistical analysis in order to quantify the effect of the terrain on sea breeze development. The statistical technique used, known as agglomerate hierarchical clustering, relies on a dense network of measuring stations in order to be effective. It involves selecting categories,

in this case the varying rate of sea breeze progression and its spatial extent, and progressively merging them with the nearest neighbour until only a single category, or cluster, remains. The result is a hierarchy of different combinations of stations that eventually merge into a combination of all. Each cluster produced will have its own typical features associated with it. For example, for the cluster selected by Fichet *et al.* (2010) that is designated a fast sea breeze with large spatial extent, the location of the system as it crossed different stations at different times can be mapped. The result of the study was a detailed description of the aereology of the region for different progressions of sea breezes.

1.2.3.3 Sea breeze indices

The final technique to be considered revolves around the use of dimensional analysis to represent the key forces involved. Initially, this method was devised for the formation of a lake breeze but has since been adapted for use as a sea breeze index (Biggs and Graves, 1962; Porson *et al.*, 2007a). The forces to consider are inertia and buoyancy. They are controlled by wind speed and temperature difference and are given by the following respective relations:

$$\frac{U^2}{C_p T} \tag{1.3}$$

$$\frac{\Delta T}{T} \tag{1.4}$$

where U is a characteristic velocity, C_p the specific heat capacity of air, T a characteristic temperature and ΔT the temperature difference between the land and water surface (Biggs and Graves, 1962). If (1.3) is divided by (1.4), then the result is the formation of a lake breeze index that is dependent on wind speed and temperature difference only (1.5).

$$\frac{U^2}{C_p \Delta T} \tag{1.5}$$

If the value of the index is large, then the gradient winds are too strong. Similarly if it is small, then the buoyancy forcing is assumed sufficient to induce a lake breeze. The precise critical value given by Biggs and Graves (1962) was 3, although when used for a sea breeze index, it has been found to be rather varied (Miller *et al.*, 2003). Porson *et al.*

(2007a) modified this index to use surface heat flux, rather than temperature difference, since the index is dependent on the ability of the air to transport heat rather than the magnitude of the thermal forcing. This relation includes velocity scaling law where $u_{sbscale}$ is the scaled velocity of a sea breeze, H is the time averaged integrated surface heat flux taken near to the coastline, $\frac{g}{T}$ is the buoyancy parameter and ω is the diurnal rotational frequency of the Earth (Porson *et al.*, 2007b).

$$u_{sbscale} = \left(\frac{gH}{T\omega}\right)^{1/2} \tag{1.6}$$

This was then used to form the index

$$I_{sb} = \frac{U_{gcrit}}{0.953 u_{sbscale}} \tag{1.7}$$

where U_{gcrit} is defined as the critical opposing geostrophic wind speed for which the sea breeze circulation does not reach the coastline. The value 0.953 was empirically derived from simulations with the Topographic Vorticity Model (TVM). For $I_{sb} > 0$ the forcing is deemed sufficient to induce a circulation.

1.2.4 A note on coastal jets

In addition to sea breezes, a lesser documented meso-scale phenomena, the coastal jet, is a feature which could potentially affect offshore wind farms in conditions where the large scale flow is in geostrophic balance (Orr *et al.*, 2005; Hunt *et al.*, 2004). Jets are defined as a local wind speed maxima within a distance of 1km from the coast (Hunt *et al.*, 2004). Their influence, however, can extend between 30-300km offshore; well within range of the proposed Round 3 wind farms (Fig. 1.1 Orr *et al.*, 2005). They have several possible triggers, but all occur in the presence of a neutral layer when capped by an overlying stable layer (Hunt *et al.*, 2004):

1. When the large scale flow is shore-parallel to the coast Coriolis force induces a jet which is parallel to the coast.

2. If there is a coastal discontinuity present, such as a headland, a *detached* jet is formed downstream.

3. If there is a sharp change in elevation at the coast. A *positive* jet is formed in the Northern Hemisphere when the coast is on the right hand side (looking downwind), and a *negative* jet is formed which reduces the effective wind speed when the coast is on the left.

Known examples of jets include the Greenland tip jet and barrier winds which form as a result of flow interactions with the large topographic barrier of Greenland (Moore and Renfrew, 2005). More relevant to offshore developments in the southern North Sea, wind jets form off the Dover Straits (Capon, 2003). Again, observations of such features are limited, and so experiments are often limited to either simulations or water tanks (Orr *et al.*, 2005).

Coastal jets are predominantly associated with stronger wind speeds than sea breezes and do not require a thermal contrast to form them. However, for *corkscrew* and *back-door* sea breezes, there is a shore-parallel component and so there exists the possibility to produce coastal jets.

1.2.5 Numerical simulations of sea breezes and the planetary boundary layer

The Planetary Boundary Layer (PBL) consists of the region of the atmosphere which is affected by the surface (Garratt, 1994). Heat, momentum and moisture fluxes are mixed vertically within the PBL by turbulent eddies, many of which have a length scale which is less than the model horizontal resolution (Stensrud, 2007). In terms of forecasting, this means that the PBL must be parametrized to represent the sub-grid scale processes. Both from a wind energy and a sea breeze perspective, accurate representation of the PBL is vital.

Highlighting the importance of PBL representation, Shimada and Ohsawa (2011) conducted a simulation using WRF in order to calculate energy density off the coast of Japan and found that year long simulations nested to 2km horizontal resolution represent energy densities less accurately than the 1° National Centers for Environmental Prediction (NCEP) final analysis. Much of the model error was associated with a strong wind speed bias of 47% near the surface, which Shimada and Ohsawa (2011) attributed to the Mellor-Yamada-Janjic (MYJ) PBL scheme.

There are many different forms of PBL scheme in which small scale turbulence is represented. Vertical mixing can either be simulated by a local scheme, in which only the top layer within the PBL and the layer above are represented, or using a non-local scheme in which all vertical levels are examined. Examples of local and non-local schemes include the MYJ and Yonsei State University (YSU) respectively (Mellor and Yamada, 1982; Hong *et al.*, 2006).

The effect of PBL sensitivity for different case studies has been thoroughly examined (Table 1.2 Borge *et al.*, 2008; Berg and Zhong, 2005; Shin and Hong, 2011). Borge *et al.* (2008) conducted an extensive sensitivity study over the Iberian Peninsula using the WRF model under 23 different configurations. The study primarily focussed on air quality in the region, applying the WRF model configuration which statistically compared best with observations to two air quality models. The PBL schemes examined were the local Medium Range Forecast (MRF), the YSU and the MYJ. Of the 3 options, the YSU agreed best with observations, also giving good agreement with PBL height estimates.

Table 1.2: Selected PBL sensitivity studies.

Study	Location	Motivation	Duration	PBL schemes	Notes
Cheng *et al.* (2012)	Taiwan	air quality	7 days continuous	YSU, MYJ	sea breeze strengths varied on/offshore
Krogsaeter *et al.* (2011)	North Sea	wind energy	1 year continuous	YSU, MYJ, ACM2, MYNN, QNSE	Accuracy depends on time of year
Xie *et al.* (2012)	Hong Kong	air quality	22 days 16hrs (Winter), 28 days 16hrs (Summer)	YSU, ACM2, MYJ, Boulac	ACM2 overall superior, local schemes shallower PBL
Hu *et al.* (2010)	Texas, USA	air quality	96 36hr simulations spanning 3 months	MYJ, YSU, ACM2	Non-local schemes more accurate
Borge *et al.* (2008)	Iberian Peninsula	air quality	8 days (Winter), 8 days (Summer)	MRF, YSU, MYJ	YSU best fit results
Shimada and Ohsawa (2011)	Japan	wind energy	1 year	MYJ	MYJ scheme responsible for large biases

In another air quality study, this time for the coastal city of Hong Kong, Xie *et al.* (2012) used the WRF model to examine different local and non-local schemes at horizontal resolutions to 1km. The non-local schemes tested were again the YSU and the Asymmetric Convective Model Version 2 (ACM2). The local options were the MYJ and the Boulac schemes. Each scheme was extensively compared against observations of 2m temperature, 10m wind speed and vertical profiles of horizontal velocity, potential temperature, bulk Richardson number and mixing ratio. The bulk Richardson number is a measure of stability and is defined by the ratio of buoyancy and shear:

$$Ri = \frac{\frac{g}{\bar{\theta}}\frac{\partial \bar{\theta}}{\partial z}}{\left[\left(\frac{\partial \bar{u}}{\partial z}\right)^2 + \left(\frac{\partial \bar{v}}{\partial z}^2\right)\right]} \tag{1.8}$$

where g is acceleration due to gravity, $\bar{\theta}$ is the layer averaged potential temperature, z is the height above the ground and $\bar{u}$ and $\bar{v}$ are the layer averaged zonal and meridional wind components respectively. As each method determines the PBL height differently, Xie *et al.* (2012) adopted a unified method to determine PBL height and found that local schemes simulated a shallower boundary layer. Overall performance was best in this case for the ACM2 scheme.

In the offshore environment, Krogsaeter *et al.* (2011) compared 5 different PBL schemes with the FINO1 platform in the eastern North Sea. Each simulation was a year in length where, in all cases, wind speed was compared to observations for the purposes of wind energy assessment. The different PBL schemes used were the YSU, ACM2, MYJ, Mellor-Yamada-Nakinishi-Niino (MYNN) and Quasi-Normal Scale Elimination (QNSE). The results indicate that the non-local ACM2 and MYJ agree better with observations although there was a high degree of temporal variability from month to month.

Cheng *et al.* (2012) compared the MYJ and YSU PBL schemes for two different aerosol flow regimes, including one which induced sea breezes. It was found that the YSU PBL simulated a weaker land breeze but a stronger sea breeze in the offshore environment then the MYJ. In the onshore environment, however, the YSU sea breeze was weaker than the MYJ.

It is noticeable from several case studies that PBL schemes show a high degree of variability in terms of accuracy for different spatial and temporal scales; different PBL schemes perform better under different conditions or PBL types. Both sea breeze and

offshore wind power forecasting suffer from a lack of observations in the offshore environment. Additional complexities may also arise in particularly complex coastal environments, such as those where some offshore wind farms are situated.

1.3 Summary and research aims

In the southern North Sea, a large scale campaign is currently under way to construct a number of offshore wind farms. This presents many challenges in terms of power prediction, turbine design and management of infrastructure. The high degree of sensitivity of power generation to wind speed requires that model predictions are accurate on a variety of different temporal scales. There is therefore a need to examine model simulations of coastal phenomena in an offshore environment.

The sea breeze is a coastal feature which is well observed and documented in the onshore environment, but is poorly understood offshore. Furthermore, studies which focus on the offshore environment are restricted to numerical experiments as data is not as readily available. Little is also known about the different sea breeze types, where the type refers to the orientation of the gradient wind relative to the coastline. No sea breeze climatology, or selection method exists for determining the frequency of different sea breeze types for coastlines in the southern North Sea.

In terms of simulating events, PBL schemes can vary widely in accuracy depending on the location and type of PBL being simulated. Sensitivity of sea breeze types to PBL scheme have not been studied in an idealized environment and little is known about the effect of another coastline, at scales typical of the North Sea, on the production of sea breezes. Therefore, the following research aims are adopted which ultimately lead to the goal of quantifying the effect of different sea breeze types on wind energy:

1. To perform a series of idealized experiments of the different sea breeze types
   (a) To diagnose dimensions and differences between sea breeze types
   (b) To determine the effect of an additional coastline
   (c) To test sensitivity of the idealized cases to the choice of PBL scheme
2. To identify the most accurate PBL scheme

3. To construct a sea breeze identification method based on the results of the idealized simulations

4. To construct a sea breeze climatology for different coastlines in the southern North Sea

5. To determine the effect of each sea breeze type on wind energy in the offshore environment both in a spatial sense and during a typical sea breeze day

From the achievement of these aims, several hypotheses can be deduced:

1. **Sea breeze types each have distinct characteristics of their own.**

2. **There is a minimum horizontal resolution required to simulate the sea breeze.**

3. **Sea breeze systems can interact on coastlines across the southern North Sea.**

4. **A sea breeze identification method can be designed which produces a coherent composite of events with realistic characteristics.**

5. **Sea breeze climatology is independent of coastal orientation in a given region.**

6. **Sea breezes have an important impact on wind energy generation in the southern North Sea.**

Chapter 2

Methodology

This chapter discusses the methods involved in achieving the research aims, as first described in Section 1.3. Section 3.1 discusses the use of idealized WRF experiments to simulate the different sea breeze types, on both a single coastline and using a second for a scaled representation of the southern North Sea. Section 3.2 describes the WRF verification experiments and Section 3.3 discusses the details of the sea breeze identification method and how it is implemented on a selection of 5 different coastlines. Finally, in Section 3.4, the methods used to determine the sea breeze contribution to wind energy are outlined. Where possible, reference is made to the relevant section where the results are described.

2.1 Idealized WRF experiments

The purpose of using 2-dimensional idealized WRF sea breeze experiments is to firstly determine whether each sea breeze type have their own distinctive characteristics (Hypothesis 1 in Section 1.3). Secondly, to determine the spatial scales involved in simulating sea breezes and to assess whether there is potential for one sea breeze type to interact with another in spatial scales equivalent to the southern North Sea. This is achieved through a combination of *single* and *dual-coast* experiments (Fig. 2.1) which are described subsequently. The results of the idealized experiments are presented in Chapter 3.

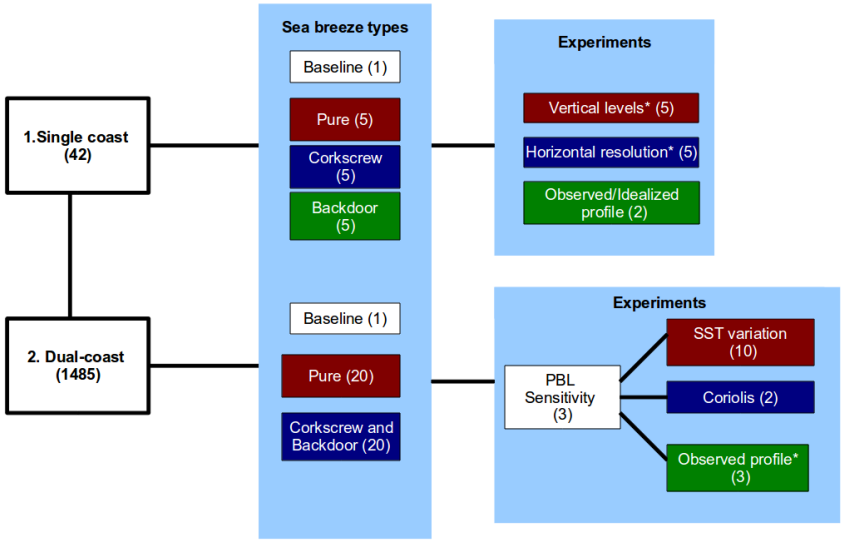

Figure 2.1: Summary schematic of all of the idealized experiments undertaken. The number in brackets indicate the number of tests performed.

2.1.1 Single coast experiments

During all single coast experiments, the model domain is divided so that 100 grid points occupy land and 100 represent sea (Fig. 2.2a). The model horizontal resolution is 3km and 35 vertical layers are distributed so that 8 layers are in the lowest 1km and the remainder distributed to a height of 15km. The first five η levels in the model are 0.999, 0.997, 0.994, 0.987, 972 and 0.959, equivalent to 4, 10, 16, 40, 87, 170m heights, on average, respectively. Model scalar variables are located on the η levels and vector quantities reside on half levels. Vector quantities are interpolated to the scalar, or mass, points using adjacent half levels.

Coriolis acceleration is enabled for a latitude of 52° for these experiments to best represent the southern North Sea. Initialization is achieved using an observed midnight sounding from Herstmonceux radiosonde station without the inclusion of the observed wind profile (Fig. 2.3; Section 2.1.7) and is applied to the whole model domain. The model is then integrated forward through time, from midnight, for a period of 24 h, with a time step of 10 seconds and with output recorded every 15 minutes. The simulations are restricted to 24 h as the definition of sea breeze type is strongly dependant on the preceding wind direction. When the simulations were extended to 48 h during preliminary

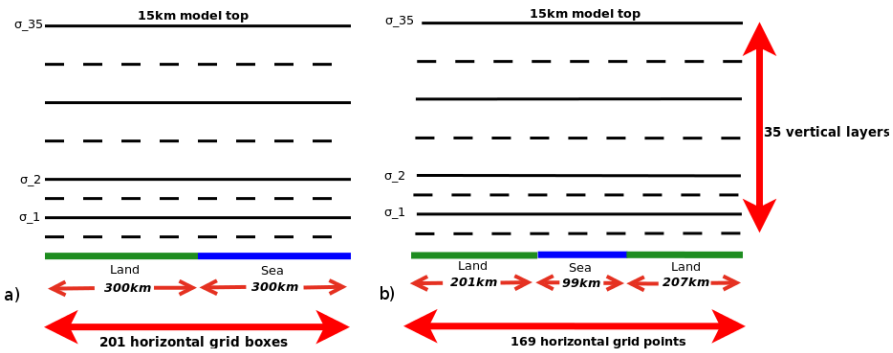

Figure 2.2: Model configuration for single (a) and dual-coast (b) idealized experiments. Dashed lines indicate half levels on the Arakawa C-staggered grid used in the WRF model.

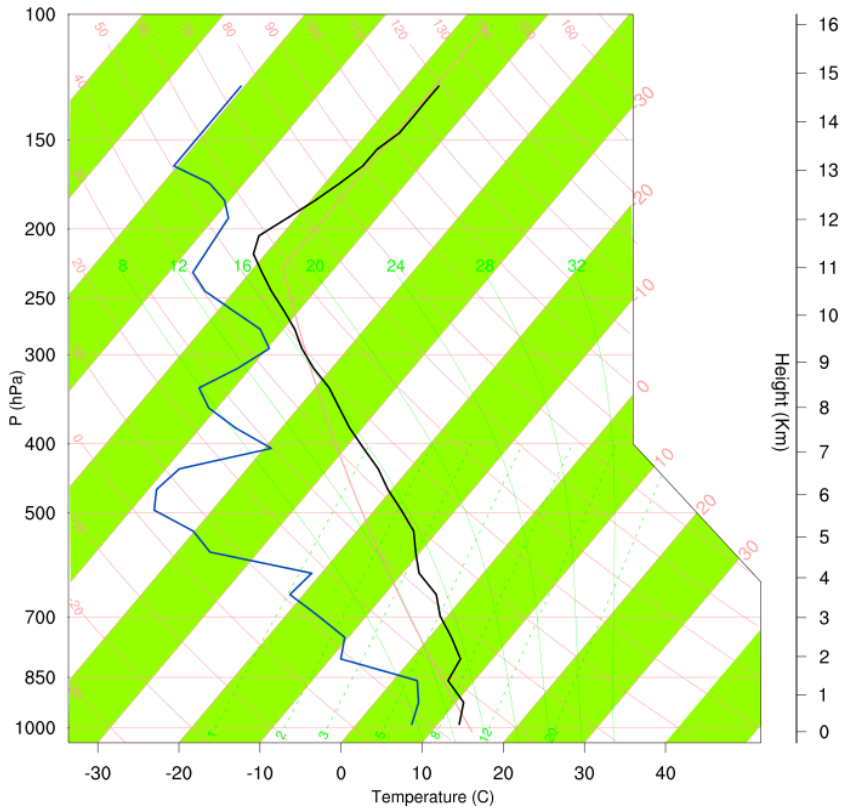

Figure 2.3: The initialization vertical dry bulb (black) and dewpoint temperature (blue) skew-T profiles applied to the single coast domain. The profile was originally observed at Herstmonceux at 0000 UTC 4th June 2006.

testing, the type of sea breeze forming on the second day is a function of both the previous day's sea breeze type and the initial gradient wind forcing. Consequently, the sea breeze simulated on the second day is not necessarily of the same type as the original gradient wind forcing would dictate. The land use category is selected as *dryland, cropland and pasture* to best represent the eastern United Kingdom. The initial land and sea skin temperatures are 280K and 287K respectively.

Table 2.1: WRF model and physics specifications used for the single coast baseline experiments.

WRF Setting and physics options	**Value**
Horizontal resolution (km)	3
Long wave physics	RRTM
Short wave physics	Monin-Obukhov similarity
Model top (hPa)	50
Ground physics	Noah land surface
PBL scheme	YSU
Vertical levels	35
Cumulus scheme	None
Microphysics	WSM-3-class
Coriolis (s^{-1})	1.15x10^{-4}

Model simulations consist of varying the along-shore and offshore gradient winds from 2 to 10ms^{-1} in steps of 2ms^{-1} so as to generate the different types of sea breeze. In all idealized simulations, the u-wind component is described as positive in the offshore direction and orientated perpendicular to the coastline. The v-wind component is orientated shore parallel and positive with the land to the left. The offshore extent for all idealized simulations is defined using the method of Arritt (1989), that is where the strength of the onshore flow breaches 1ms^{-1}, anything smaller than this threshold is not considered to be part of the sea breeze. A single simulation is also run without gradient winds so that a baseline could be established for comparison with the other sea breeze types. This is referred to hereafter as the baseline experiment for which the model physics and settings are described in Table 3.1. Additional simulations are also undertaken to test the sensitivity to two alternative initializing thermodynamic profiles (Fig. 2.4).

2.1.2 Dual-coast experiments

For these simulations, a second coastline is added so that a central sea channel occupies the central 99km of the model domain (Fig. 2.2). Once again, the land use category is categorized as *dryland, cropland* and *pasture* to best represent the UK and mainland Europe. Simulations are run to test the effect of varying gradient wind strengths, Sea Surface Temperature (SST) and Coriolis on three different PBL schemes: The YSU, the MYJ and the MYNN schemes (Table 3.2). SST variations match those typically experienced in the southern North Sea during June and are varied between 280-290K in steps of 1K. Simulations are also carried out with and without Coriolis acceleration for a latitude of 52°, since

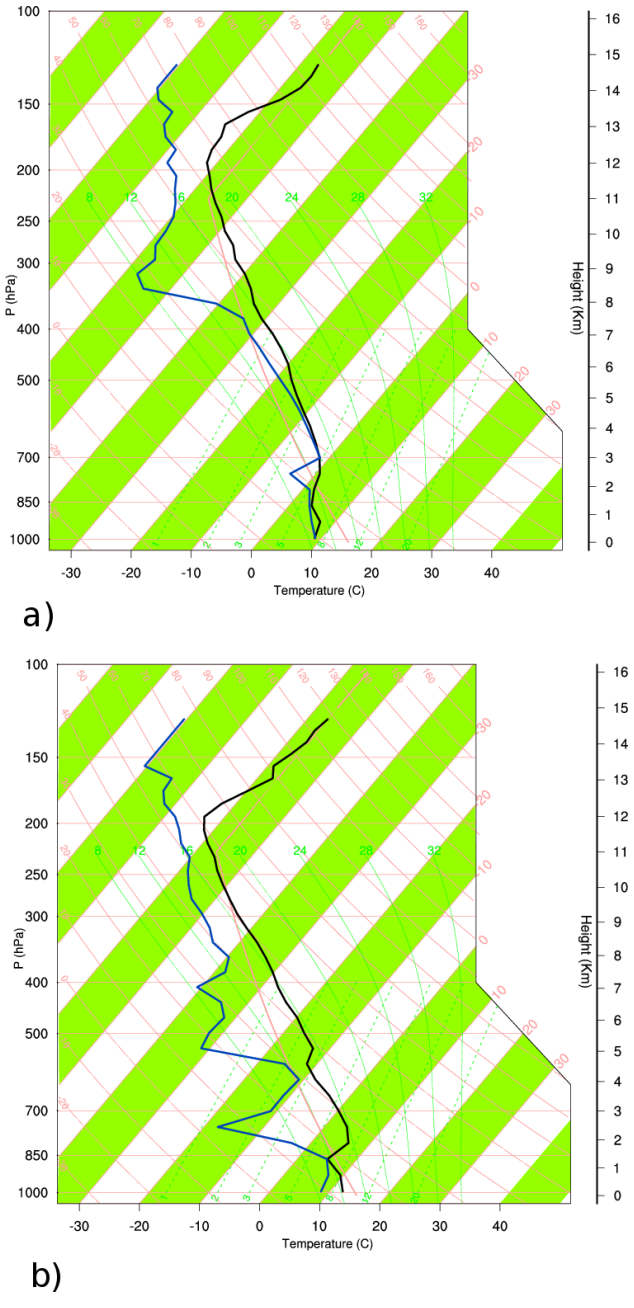

Figure 2.4: Skew-T profiles from Herstmonceux station at a) 0000 UTC 2^{nd} June 2006 and b) 0000 UTC 3^{rd} June 2006

the effect of Coriolis variations with latitude on the sea breeze is rarely studied (Crosman and Horel, 2010). Finally, another baseline simulation is run without gradient winds for the dual-coast cases.

Table 2.2: Sensitivity tests for the dual-coast experiments. The u-wind is orientated shore perpendicular and positive in the offshore direction and the v-wind is shore parallel and positive with land to the left. In all experiments the MYNN level 2.5 scheme is used.

Parameter	Sensitivity test
u-wind (ms^{-1})	0 to 20, steps of 1
v-wind (ms^{-1})	-20 to 20, steps of 1
SST (K)	280 to 290, steps of 1
PBL Schemes	YSU, MYNN (level 2.5), MYJ
Coriolis (s^{-1})	0, 1.15x10^{-4}

Table 2.3: WRF model and physics specifications used for the climatological simulations. Note that for domain 4 (d04) the cumulus scheme is no longer present.

WRF Setting and physics options	**Value**
Horizontal resolution (km)	d01: 27, d02: 9 d03: 3 d04: 1
Long wave physics	RRTM
Short wave physics	Monin-Obukhov similarity
Model top (hPa)	50
Ground physics	Noah land surface
PBL scheme	YSU
Vertical levels	35
Cumulus scheme	Kain-Fritsch
Microphysics	WSM-3-class
Coriolis (s^{-1})	1.15x10^{-4}

2.2 WRF model verification

Due to superior data coverage and availability of offshore measurements, when compared to East England, much of the verification is carried out using surface and mast data from the Netherlands (Fig. A.1). Two sets of simulations are carried out. First, a single case study of a sea breeze event is conducted testing sensitivity to model resolution (Section 1.3; Hypothesis 2), lead time and PBL sensitivity. Second, simulations are extended to span a 5 month sea breeze season so that the performance of each PBL scheme can be evaluated over a long time period. The results of both the case study and the longer monthly simulations are presented in Chapter 4.

2.2.1 Case study: 19th June 2012

Several WRF simulations are conducted for a sea breeze case study on the 19th June 2012, in order to test sensitivity of the 3 PBL schemes used in the idealized simulations on lead time and horizontal resolution. The model domain is shown in Fig. 2.5. The baseline

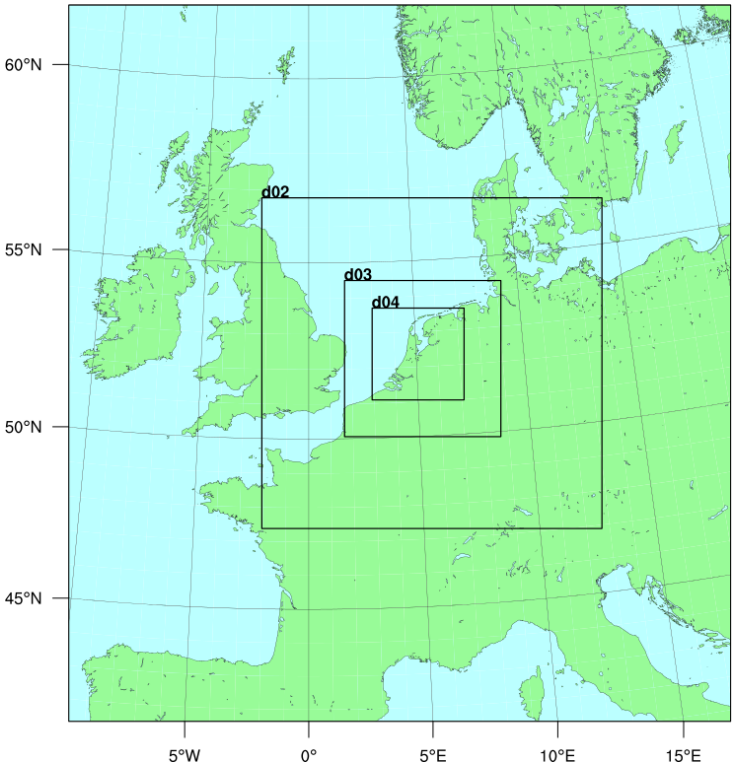

Figure 2.5: WRF model domain used for the sea breeze case study on the 19th June 2012. The horizontal resolutions for d01,d02,d03,d04 are 27,9,3 and 1km respectively.

Table 2.4: Sensitivity tests of the WRF case study simulations for the 19th June 2012.

Sensitivity test	Values
PBL scheme	YSU, MYJ, MYNN
Lead time (hrs)	0,6,12,18,24
Resolution (km)	27,9,3,1

simulation follows Table 2.3. The horizontal resolution of each domain is 27,9,3 and 1km, where the domains are 2-way interactively nested.

Each baseline simulation initializes with 1° GFS FNL Analysis (described in Section 2.2.1) at 00:00 UTC and runs for a period of 24 hrs. Every 6 hours, the SST is updated using interpolated daily 0.5° NCEP Real-Time Analysis (in Section 2.2.2). The lead time is varied by 6, 12, 18 and 24 hrs and each resolution is independently simulated using 1, 2, 3 and 4 2-way nested domains. Both the lead time and the horizontal resolution experiments are repeated for the YSU, MYJ and the MYNN PBL schemes. A summary of the simulations is given in Table 2.4.

Each simulation is compared to the Dutch surface network (Fig. **??**) where statistical scores of BIAS, MAE and RMSE are applied to 2m temperature, 10m wind speed and

dew point temperature to ascertain which PBL scheme reproduces the sea breeze most faithfully. In particular, the minimum horizontal resolution required to simulate the sea breeze is examined (Section 1.4, Hypothesis 2). Furthermore, the results are compared against each level of the Cabauw tower, where the WRF model data are interpolated to the height of the tower before comparison. The nearest land model grid point is used for the comparison with observations.

Since the verification applied is for a single case study only, there are limitations to the validity of any conclusions. For this reason, the WRF model simulations are extended.

2.2.2 WRF climatology verification

The sea breeze climatology is constructed from WRF simulations. Before conducting the simulations, it is necessary to test the ability of the WRF model to simulate over longer time periods. The period chosen to conduct these simulations is May to September 2006, with the duration of each simulation lasting 1 month. Again, the model is initialized with 1° GFS FNL Analysis and updated every 6 hours with interpolated daily 0.5° NCEP SST analysis. In addition, to prevent model drift, analysis nudging is enabled every 6 hours. The period is chosen as it was particularly warm and anticyclonic, and so, on a simple level, should promote the establishment of sea breezes.

The model domain, shown in Fig. 2.6, contains 2 nests, each configured for 2-way interactive nesting of resolution 9km and 3km. The outer domain has a horizontal resolution of 27km, as per the sea breeze case study. Model physics schemes again follows those in Table 2.3 with exception of the PBL schemes which are the subject of the sensitivity study.

The model is run every month between May to September 2006 using the YSU, MYJ and MYNN, PBL schemes and their respective surface layer schemes and compared against both the Cabauw tower and the Egmond aan Zee mast 18km offshore. Again, model verification statistics include MAE, RMSE and BIAS error where wind speed, temperature and dew point temperature are verified. In addition, at the Cabauw tower, additional variables such as solar insulation, sensible and latent heat fluxes are compared against observations in order to qualitatively determine the cause of any differences in the simulations. The results from the model verification will be used to determine the model

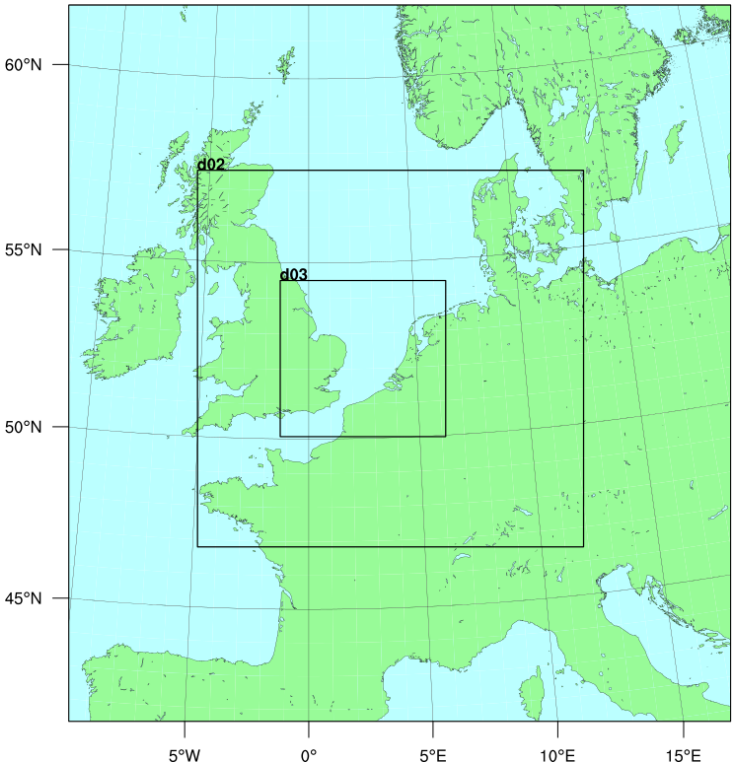

Figure 2.6: WRF model domain used for both simulating the sea breeze climatology and for the extended verification simulations for the months May to September 2006. The horizontal resolutions for d01,d02,d03 are 27,9 and 3km respectively.

configuration for the construction of the sea breeze climatology.

2.3 Development of the sea breeze selection method

A single method does not exist for identifying all existing types of sea breeze so a universal sea breeze selection method is needed in order to create a sea breeze climatology for coastlines in the southern North Sea (Section 1.3, Hypothesis 4.). The method involves different spatial scales in a multi-filter process, rather than an index or the use of a remote sensing methodology.

Sea breeze indices are typically based on the ratio of wind speed to land-sea thermal contrast (eg. Biggs and Graves, 1962) and do provide a good indication as to the potential of sea breeze development. However, they have not been tested for *corkscrew* and *backdoor* type circulations and also suffer a high degree of sensitivity to the thresholds set, which change according to location (Miller *et al.*, 2003). Remote sensing methods rely on the formation of cloud streets to denote the location of the sea breeze front, though as cloud streets are not always formed in sea breeze events this method cannot be applied

universally.

The use of a filter method will allow for the systematic determination of days in which sea breeze favouring conditions on a variety of different spatial scales. The filter method can also be made to be much more generic than the other techniques, encompassing a wide range of possible scenarios to give days where sea breeze formation is plausible rather than explicitly resolved. This is therefore the preferred method as each filter can be refined to varying sensitivity and the performance of each individual filter can easily be analysed.

The method begins at the synoptic level and progressively decreases in scale with each filter so that eventually local parameters relative to the target coastline are examined. Data are used from both the GFS FNL analysis and WRF climatology simulations but the method could be applied to any model forecasts.

The two fundamental constraints on the likelihood of sea breeze formation are the strength of the gradient wind and the land-sea thermal contrast (Biggs and Graves, 1962; Simpson, 1994). Therefore the selection method begins by first looking at the large scale flow, identifying those days where either the flow direction rapidly changes or the gradient flow is too strong. Depending on the flow direction and strength relative to the coastline, the predicted sea breeze type is then determined. Finally, the strength of the local land-sea thermal contrast is examined. The result is a selection method which is both adaptable for both location, orientation of the coastline, and distinguishes between different sea breeze types (Fig. 2.7). The different types of sea breeze can then be incorporated into the assessment of wind energy contributions.

2.3.1 Filters 1 and 2: The Jenkinson-Collison method

Jones *et al.* (1993) created an objective weather type classification scheme for the UK based on the original subjective method of (Jenkinson and Collison, 1977). The procedure involves using midday sea level pressure for 16 grid points as shown in Fig. 2.8. The weather types are classified into Anticyclonic (A), Cyclonic (C), or purely a directional flow in any of the 8 compass directions. The A and C types can either be pure or a hybrid with the directional types, depending on the position of the relative weather system. There are therefore 26 main types of flow regime in the method. These are:

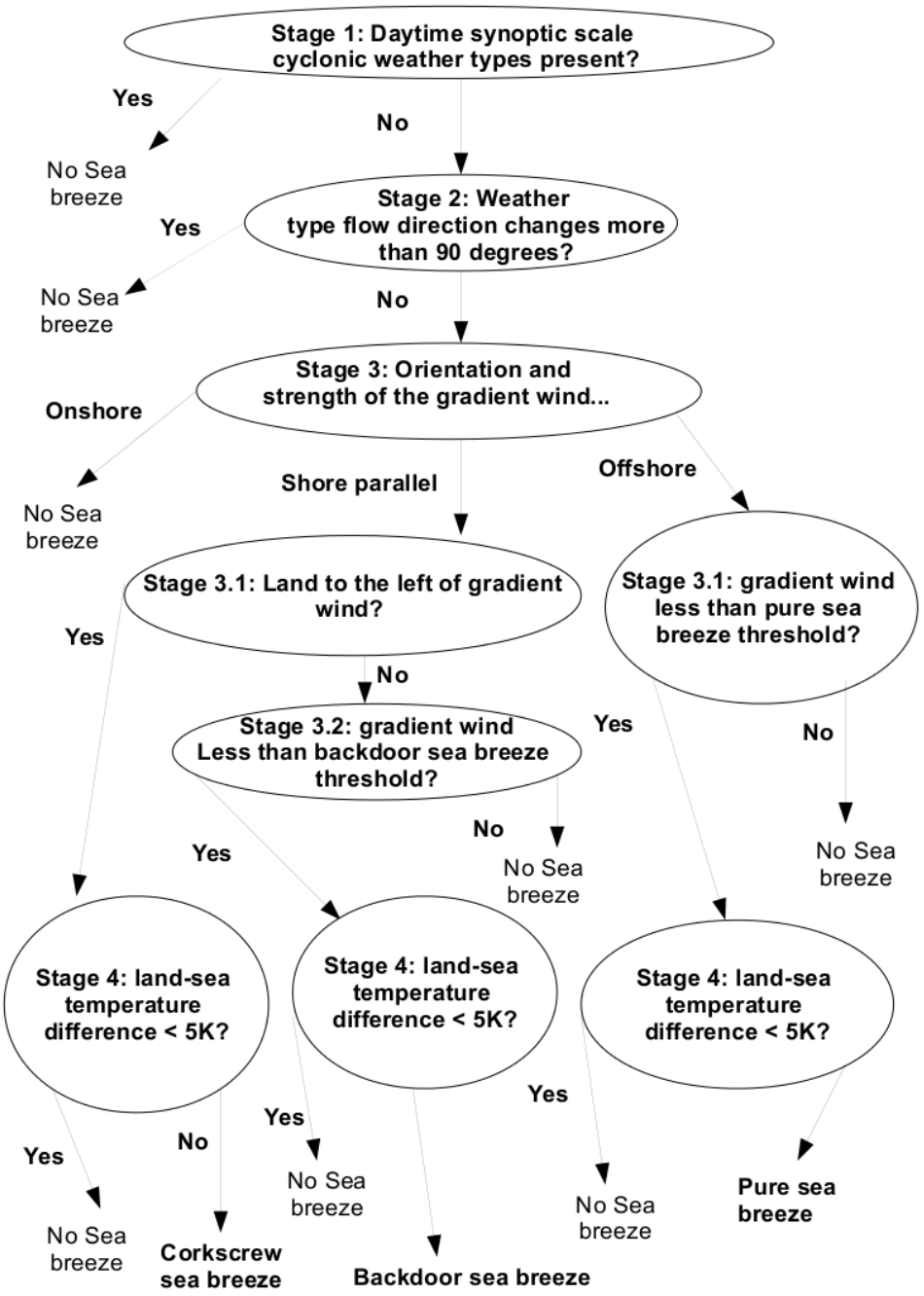

Figure 2.7: Flow chart of the generalized sea breeze selection method showing the various filters and sub-filters.

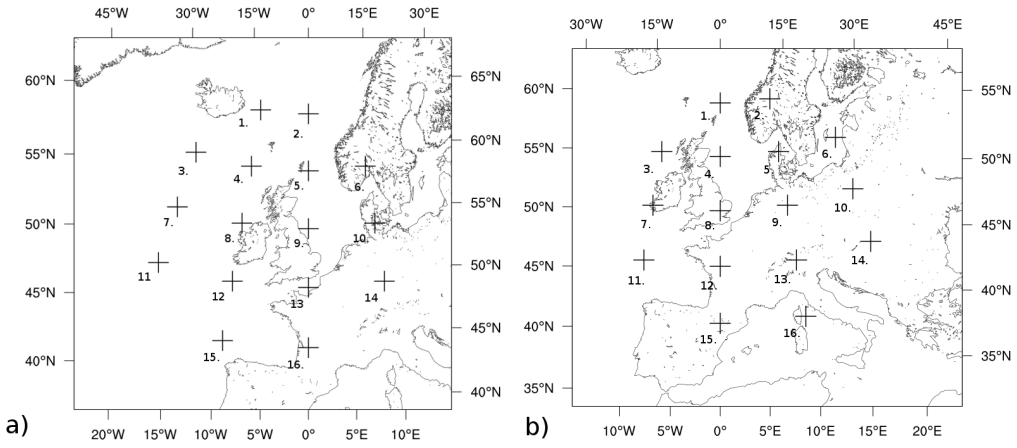

Figure 2.8: The 16 positions used for the Lamb weather typing method both for classifying Lamb weather types over the UK (a) and over the Netherlands (b).

- **Anticyclonic**. Pure (AA), Northerly (AN), Northeasterly (ANE), Easterly (AE), Southeasterly (ASE), Southerly (AS), Southwesterly (ASW), Westerly (AW) and Northwesterly (ANW)

- **Cyclonic**. Pure (CC), Northerly (CN), Northeasterly (CNE), Easterly (CE), Southeasterly (CSE), Southerly (CS), Southwesterly (CSW), Westerly (CW) and Northwesterly (CNW)

- **Pure directional**. Northerly (NN), Northeasterly (NE), Easterly (EE), Southeasterly (SE), Southerly (SS), Southwesterly (SW), Westerly (WW) and Northwesterly (NW)

The weather type is determined from both calculations of the zonal and meridional components of the gradient wind speed and the degree of vorticity over the domain. This is achieved by dividing the domain into 16 points as shown in Fig. 2.8 The magnitude of Westerly (W), Southerly (S) and resultant (F) geostrophic flows are calculated by:

$$W = \frac{1}{2}(12 + 13) - \frac{1}{2}(4 + 5) \tag{2.1}$$

$$S = 1.74[\frac{1}{4}(5 + 2 \times 9 + 13) - \frac{1}{4}(4 + 2 \times 8 + 12)] \tag{2.2}$$

$$F = (S^2 + W^2)^{1/2} \tag{2.3}$$

where the units are expressed as hPa per 10° latitude at 55N and the numbers represent the respective locations on Fig. 2.8. A single unit is equivalent to 1.2 knots. The westerly

(ZW) sotherly (ZS) and total (Z) shear vorticities are calculated by:

$$ZW = 1.07[\frac{1}{2}(15+16) - \frac{1}{2}(8+9)] - 0.95[\frac{1}{2}(1+2)] \tag{2.4}$$

$$ZS = 1.52[\frac{1}{4}(6+2\times10+14) - \frac{1}{4}(5+2\times9+13) - \frac{1}{4}(4+2\times8+12) + \frac{1}{4}(3+2\times7+11)] \tag{2.5}$$

$$Z = ZW + ZS \tag{2.6}$$

where the units of vorticity are expressed as hPa per 10° latitude at 55N. Each flow regime is then determined by the following criteria:

- If $|Z| < F$ then the flow is of pure directional type
- If $|Z| > 2F$ then the type is of either AA or CC for $Z > 0$ and $Z < 0$ respectively
- if $F < |Z| < 2F$ the flow is a hybrid anticyclonic or cyclonic type for $Z > 0$ and $Z < 0$ respectively. The direction is determined by $\arctan W/S$
- If both F and $|Z| < 6$, then the flow is light and intermediate and is therefore Unclassified (U)

2.3.2 Filters 3 and 4: Gradient wind speed thresholds and land-sea thermal contrast

The Jenkinson-Collison methodology is used in the first two filters, the role of which are to eliminate large scale flow regimes that are not conducive to the formation of sea breezes. To achieve this, using only the midday analyses will not be sufficient to rule out fast moving depressions or flow regimes. The Jenkinson-Collison method is therefore used on the 6 hourly GFS FNL analyses. If any of the 6, 12 and 18Z outputs are classified as cyclonic, the day is rejected.

The second filter eliminates days where the type is changes rapidly, which would otherwise make the classification of a sea breeze difficult. Therefore, if the gradient wind direction of the weather type changes overall by more than 90°, then the day is rejected.

The third stage of the selection method involves the use of WRF simulations to eliminate days where the wind speed locally is greater than some pre-defined threshold. WRF model output is interpolated to gradient wind height and averaged over a pre-defined

gridbox. The height where the gradient wind is averaged is calculated at 925hPa, but an additional sensitivity test is conducted at 850hPa.

The fourth and final step of the method is to examine the strength of the land-sea thermal contrast. The 2m temperature is a WRF model output variable whilst the SST are from the NCEP real-time archive, but are ingested by the WRF model as surface boundary conditions. The minimum threshold required for sea breeze generation was determined by Simpson (1994) to be 5K. This is used as a basis for this step, however additional sensitivity tests included using skin temperature and SST or 2m temperature and SST to calculate the magnitude of the land-sea thermal contrast.

In the sensitivity results, the test involving the same variables used in the construction of the sea breeze climatology, that is using 2m temperature for the land-sea thermal contrast and calculating the gradient wind at 925hPa, is designated CLIM. The test involving changing the gradient wind height to 850hPa is designated GRAD. Similarly for the thermal contrast sensitivity, the experiments using SST and skin temperature, and SST and 2m temperature are designated SSTTSK and SSTT2 respectively.

2.4 Using and testing the sea breeze selection method

2.4.1 Outlining the coastlines

All the sea breeze climatology and associated sensitivity results are presented in Chapter 5. Five different coastlines are identified for using the identification method, which vary in complexity, length and orientation (Fig. 2.9). These are: northern Norfolk, eastern Norfolk, Suffolk and Essex, the Netherlands and Kent. Each of these have their own unique complexities which are discussed below.

2.4.1.1 North Norfolk

The first coast is North Norfolk. In itself it is not particularly complex; the coastline is orientated west-east and is relatively straight. The boxes used for averaging gradient wind speed, land and sea temperatures are depicted in Fig. 2.10. Adjacent to north Norfolk lies the coast of Lincolnshire, so there exists the strong possibility of interference when examining the behaviour of sea breezes offshore. Furthermore, directly to the east lies the

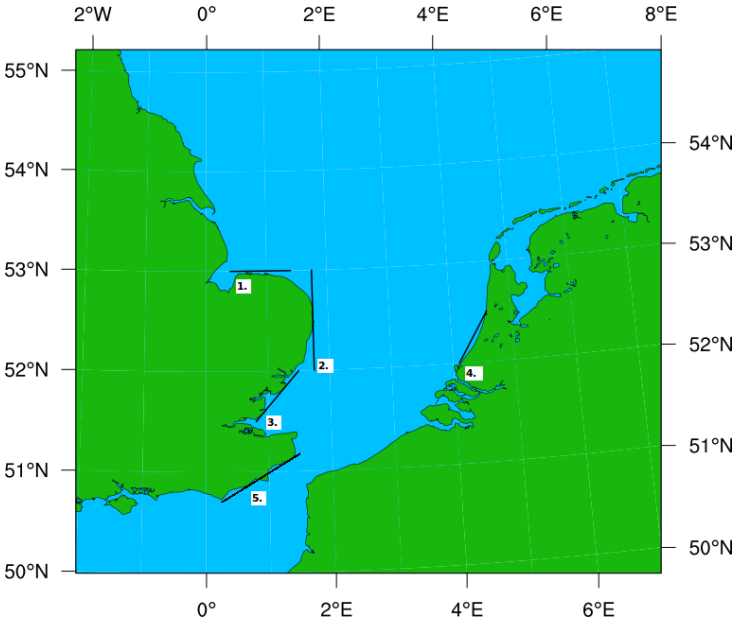

Figure 2.9: Lambert conformal projection indicating the locations of the coastlines considered for the sea breeze selection method

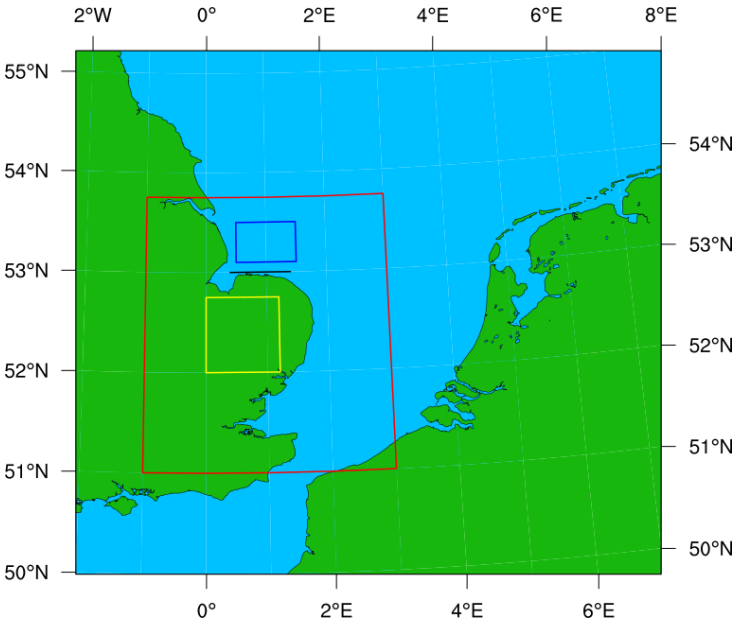

Figure 2.10: Lambert conformal map projection denoting the positions of the grid boxes required for the sea breeze selection method operating on the north Norfolk coast. The red box is for the 850hPa wind speed. The blue and yellow boxes denote the spatial extents of the averaged sea and land temperatures respectively

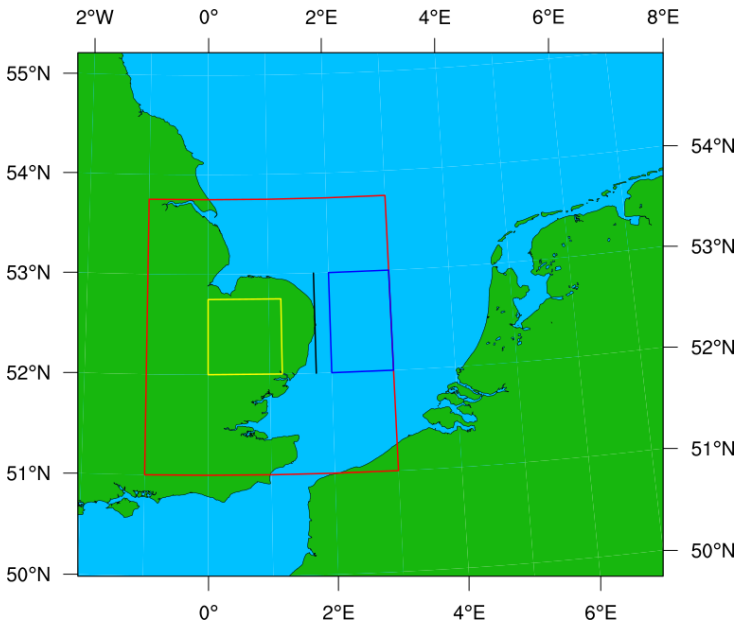

Figure 2.11: Lambert conformal map projection denoting the positions of the grid boxes required for the sea breeze selection method operating on the eastern Norfolk coast. The red box is for the 850hPa wind speed. The blue and yellow boxes denote the spatial extents of the averaged sea and land temperatures respectively

Wash, a relatively shallow body of water, surrounded on three sides by coastline with an opening to the north into the southern North Sea. Within this particularly complex region lies the Lynn and Inner Dowsing wind farm, situated approximately 15km off the coast of Lincolnshire (Fig. A.1; Number 32). There is therefore a greater need to be able to examine the wind climate in this region and so it has been chosen for the first site.

2.4.1.2 Eastern Norfolk

East Norfolk is orientated north-south and is also relatively straight, although at it's southern extremity, in northern Suffolk, it begins to take a more concave shape (Fig. 2.11). Approximately 250km to the east of Eastern Norfolk lies the Netherlands and so in a similar manner to the dual coast idealized experiments, sea breezes forming off eastern Norfolk may be affected by those forming over the Netherlands. However, considering this is 100km greater than the idealized simulations, it may be the case that the values chosen for the thresholds in the selection method will need to be adjusted specifically to this coastline.

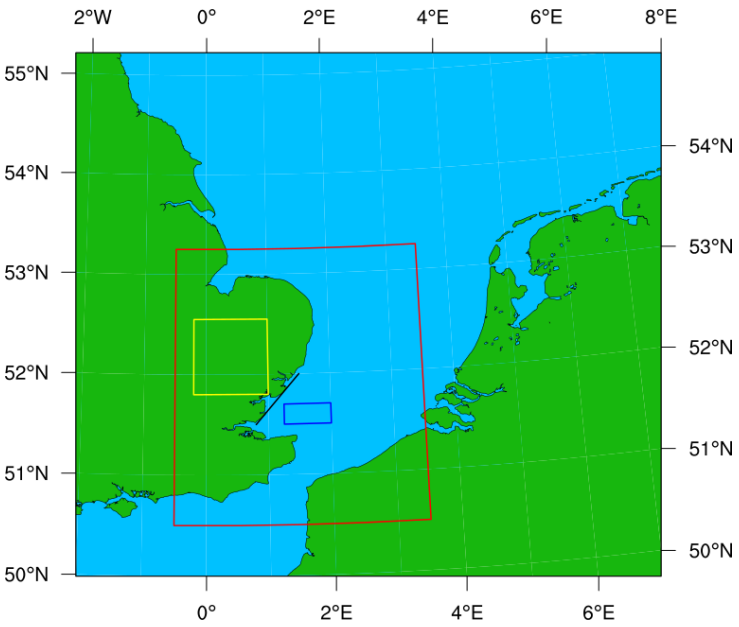

Figure 2.12: Lambert conformal map projection denoting the positions of the grid boxes required for the sea breeze selection method operating on the Suffolk and Essex coastlines. The red box is for the 850hPa wind speed. The blue and yellow boxes denote the spatial extents of the averaged sea and land temperatures respectively

2.4.1.3 Suffolk and Essex

This particular stretch of coastline is the most complex of all of the coastlines tested (Fig. 2.12). It is also the site for which several wind farms are being either planned or have already been constructed and so it is well worth consideration (Fig. 1.1). The coast itself is orientated SW-NE and consists of many intricate bays, headlands and river mouths. Approximately 50km to the south east, the extreme eastern edge of Kent protrudes just enough so that the fetch of the southern portion of this coast is reduced. Furthermore 100km directly south east from the northern sector lies the coast of France. Potentially therefore there is the possibility that this coastline will be affected by sea breezes forming on a variety of other coasts as well as those smaller bay breezes forming individually.

2.4.1.4 The Netherlands

The Dutch is the only continental coast considered by the method. The coast of the Netherlands is concave and is orientated SE-NW, 250km east of eastern Norfolk (Fig. 2.13). Its position when compared to eastern Norfolk could allow a comparison to see whether a *corkscrew* sea breeze on one coastline corresponds with a *backdoor* sea breeze

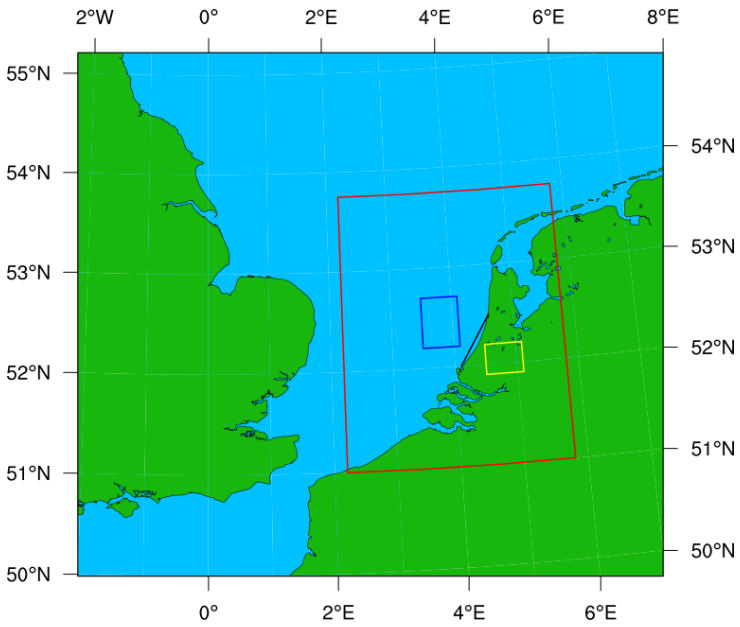

Figure 2.13: Lambert conformal map projection denoting the positions of the grid boxes required for the sea breeze selection method operating on the coast of the Netherlands. The red box is for the 850hPa wind speed. The blue and yellow boxes denote the spatial extents of the averaged sea and land temperatures respectively

on the other. However, the coastlines are not directly facing each other so it is not necessarily a direct comparison. Furthermore, the continental effect could allow for a higher land-sea thermal contrast and so the number and strength of the simulated sea breezes could be affected. The coast is comparatively simple, however much more complexity is introduced on either side in the form of islands, bays and headlands. Also, in the onshore environment, the presence of the inland body of water of Markermeer adds further complexity.

2.4.1.5 The Kentish coast

The Kentish coast has the smallest body of water to generate sea breezes compared with all of the others (Fig. 2.14). At this point, the northern reaches of the English channel separate Kent from northern France by only 50km. The land surface is also significantly smaller than the others as Kent protrudes from south eastern England to form a peninsula. The coastline itself is orientated ENE-WSW and is comparatively straight, save for a large headland in it's centre. There will also likely be sea breezes forming on the northern Kentish coast which will compete with those forming to the south. Furthermore, because

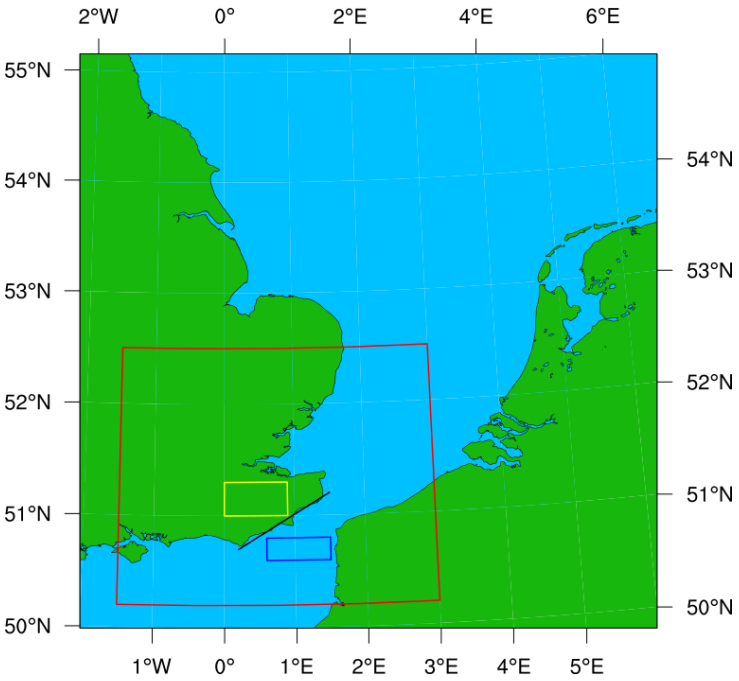

Figure 2.14: Lambert conformal map projection denoting the positions of the grid boxes required for the sea breeze selection method operating on the southern coast of Kent. The red box is for the 850hPa wind speed. The blue and yellow boxes denote the spatial extents of the averaged sea and land temperatures respectively

of the narrow gap between the straits of Dover and France, there is also the issue of coastal jets which form in shore-parallel winds (Capon, 2003; Orr *et al.*, 2005). Fundamentally, these could be resolved from the selection method when attempting to identify *corkscrew* and *backdoor* sea breezes.

2.4.2 Generation of a sea breeze climatology for 2002-2012

The method is used for each coast, following Fig. 2.7. The land-sea thermal contrast calculated using 2m temperature and the height of the gradient wind calculated at 925hPa. From the idealized simulations, the thresholds used for determining the cut off speeds of each sea breeze are used for *pure* and *backdoor* sea breezes respectively. Sensitivity tests were carried out on the height of the gradient wind and the measure of the land-sea thermal contrast.

2.4.3 Quantifying the sea breeze contribution to wind energy

The contribution of each sea breeze type to wind energy is assessed on both spatial and temporal scales. Firstly, hub height wind speed is converted into wind power by:

$$P = \frac{1}{2} C_p \rho A u^3 \tag{2.7}$$

where C_p is the power co-efficient set at it's theoretical maximum value of 0.593, ρ is air density and *A* is the rotor swept area. For spatial relationships, the 4$^{\text{th}}$ model level, at approximately 90m is used for hub height. Cut-in and cut-out wind speeds are imposed on the model wind speeds of 4ms^{-1} and 25ms^{-1} respectively. A power rating is also applied to the turbine of 3.6MW unless stated otherwise, giving the power curve in Fig. 2.15.

Composite diurnal cycles of wind speed and wind power are compared against the Egmond aan Zee mast for each sea breeze type. Also, to determine the spatial contribution of each sea breeze type to offshore wind energy, model output from the 3km domain is differenced from the 27km, where the 27km domain is interpolated onto a 3km grid before differencing. This assumes that sea breezes are not well simulated at 27km horizontal resolution and is inferred from the results of Chapter 4.

Before differencing, the power output is converted into capacity factor, where capacity factor is the ratio of actual power output to the theoretical maximum power output for a given time period, t:

$$c_f = \frac{Pt}{p_r t} \tag{2.8}$$

where p_r is the power rating of the hypothetical turbine.

2.4.3.1 Sea breeze impact on the 2009 season

From the sea breeze climatology, wind turbine data from Lynn wind farm are used in conjunction with mast data from Egmond aan Zee for the 2009 sea breeze season to determine the percentage relative contribution of the sea breeze during a single season. Furthermore, the results from the differencing method pointed to a significant contribution from the 2-way nesting (Section 6.2) and so additional WRF simulations to 27km horizontal resolution were conducted for the 2009 season to quantify the impact of the

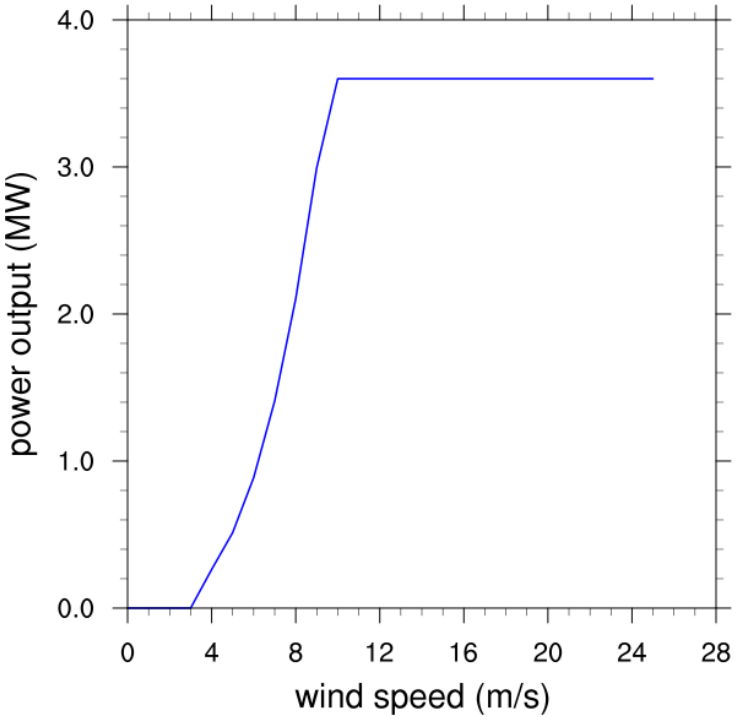

Figure 2.15: Theoretical 3.6MW wind turbine power curve with a hub height of 80m, blade radius of 60m and a cut-in wind speed of 3ms^{-1}

nesting method.

2.4.3.2 Quantifying impact against non-sea breeze days

Finally, the impact of each sea breeze type is assessed against those days which fail the identification method purely as the result of an insufficient land-sea thermal contrast. This allows a direct comparison against non-sea breeze days at equal resolution and avoids the problems associated with different coastal resolutions in the previous differencing method.

Chapter 3

Idealized simulation results

This chapter comprises of work published in *Atmospheric Chemistry and Physics* (Steele *et al.*, 2013) with some additional material. The results consist of both single and dual-coast idealized WRF experiments, testing the sensitivity of the different sea breeze types to the choice of PBL scheme, gradient wind strength and SST as described in Chapter 2. The work is organised so that the results of the single coast simulations are described first, followed by the more complex dual-coast sensitivity simulations, whereby specific thresholds are found so that they can be later used in the sea breeze identification method.

3.1 Single coast experiments

3.1.1 Baseline case (no gradient wind)

150km onshore, the baseline case produces a boundary layer which reaches a maximum height of approximately 1550m over the land surface (Fig. 3.1). This height is reached at approximately 1400 UTC and lasts until 1845 UTC where upon the boundary layer collapses. Similarly, the background specific humidity steadily rises to 13.5gkg^{-1}, reaching its peak approximately 15 minutes before the maximum height in the PBL (Fig. 3.1).

The maximum 2m land temperature is approximately 303K, giving a maximum land-sea temperature difference 270km inland of 16K (Fig. 3.2). The diurnal cycle, without the influence of the sea breeze, is affected by the development of clouds at 850hPa which causes the local minimum at 1300 UTC. The formation of cloud is specific sounding used to initialize the model (Section 3.3). Regardless of the effects of the initializing vertical

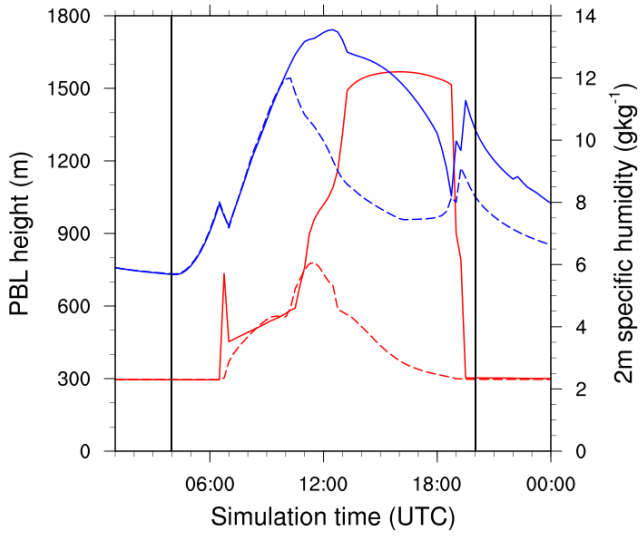

Figure 3.1: Daytime evolution of PBL height (red) and 2m specific humidity (blue) for the baseline single coast simulation using the YSU PBL scheme and an SST of 287K. Solid lines indicate values 150km onshore and dashed lines are at the coastline. Sunrise and sunset times are represented by the solid vertical black lines.

thermodynamic profile, the amplitude of the diurnal cycle 270km inland from sunrise at 0400 UTC to sunset at 2000 UTC is 23K.

From approximately 0200 - 0900 UTC, a light shallow circulation near the surface is established over the coastline, indicative of a land breeze (Fig. 3.3). This breaks down and a very weak sea breeze with return flow emerges simultaneously, but it is not until after 1200 UTC, that the sea breeze strength breaches the 1ms^{-1} threshold set by Arritt (1989) and continues to intensify to 2.5ms^{-1} by 1800 UTC (Fig. 3.3).

The effect of the onset of the sea breeze on the PBL is to prevent entrainment and the consequent development of the convective boundary layer. Since the determination of the PBL height is, in this case, based on the bulk Richardson number, an increase in the strength of shear turbulence brought about by the formation of the sea breeze, suppresses the buoyancy instability over the land surface and therefore stabilizes the PBL. The arrival of the sea breeze also causes the specific humidity to drop (Fig. 3.1) in agreement with observations by Finkele (1998).

The overall depth of the sea breeze landward component is approximately 700m, with a seaward return flow depth which is approximately twice this magnitude (Fig. 3.4). The depths found are consistent with observations presented by Simpson (1994) of sea breezes along the south coast of England, and with the numerical experiments by Finkele

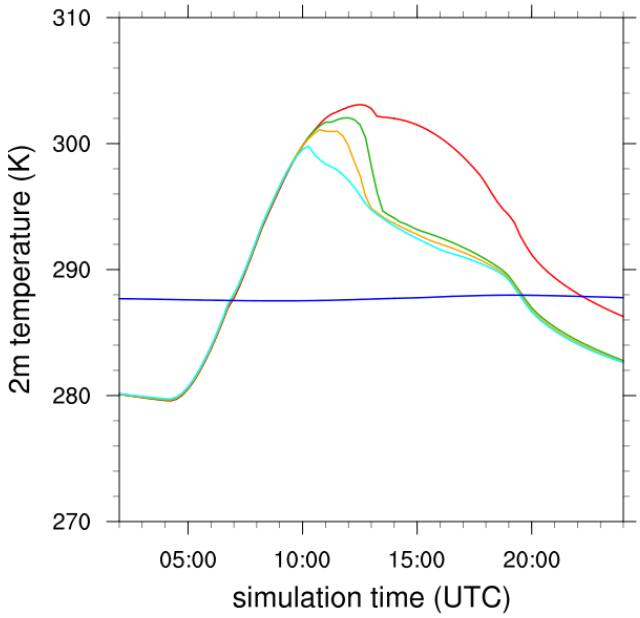

Figure 3.2: Time series of 2m temperature at 270km (red), 15km (green), 9km (orange) and 3km (cyan) onshore from the coastline. The solid blue line is the 2m temperature 60km offshore for the single coast baseline case. Based on the YSU PBL scheme and a SST of 287K.

(1998) and Arritt (1989). Ahead of the sea breeze onshore, a region of calm ($<1\text{ms}^{-1}$) onshore flow of approximately the same length, but double the thickness of the sea breeze onshore flow, persists for the duration of the simulation. This is indicative of continental air moving inland as the sea breeze advances (Miller *et al.*, 2003). The continental air is deeper than the incoming sea breeze due to surface heating ahead of the sea breeze front (Crosman and Horel, 2012). A vertically propagating wave develops as shown in Fig. 3.4, and reaches a maximum height of 12km by the end of the simulation. To our knowledge, there have been no observations of the vertically propagating wave in a sea breeze circulation, but they are frequently seen in simulations of mountain winds and other sea breeze numerical studies (eg. Klemp and Lilly, 1978; Qian *et al.*, 2009). Further study into this is beyond the scope of this study since our primary focus remains on the offshore environment.

Applying the wind speed threshold criteria defined by Arritt (1989) over the modelled sea, the sea breeze is more than capable of reaching over 250km offshore. However, the scale of offshore advancement is sensitive to the speed threshold set for defining a sea breeze. For example, increasing the threshold to 1.5ms^{-1} results in a reduction of approximately a third less offshore advancement. Even at this threshold of 1.5ms^{-1}, the

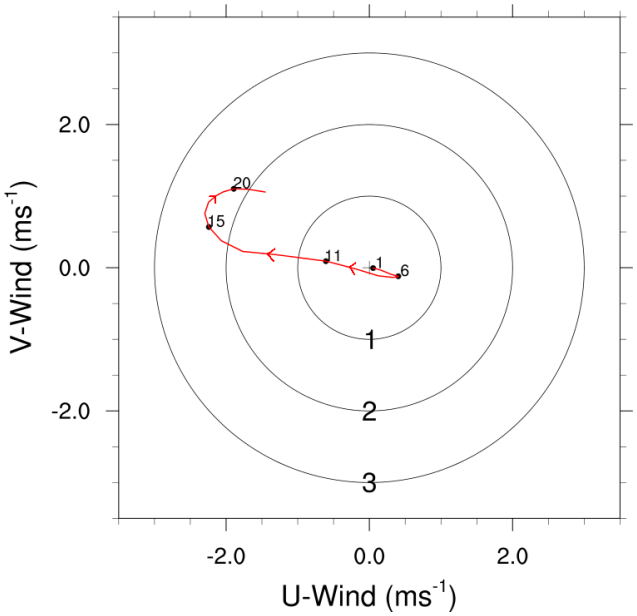

Figure 3.3: Hodograph of the single coast baseline simulation at the coastline using the YSU PBL scheme and an SST of 287K. Numbers labelled on the curve represent the simulation hour in UTC and concentric circles portray the magnitude of the 10m vector wind. The negative u-wind component represents onshore flow and the negative v-wind component represents shore parallel flow with the land mass to the right.

sea breeze still reaches 170km offshore, well above the typical length scale of the southern North Sea (Fig. 3.5).

3.1.2 *Pure* sea breeze

For a *pure* type sea breeze with an offshore gradient wind of 2ms^{-1} the return flow component first establishes over the coast at 1100 UTC, two hours before the development of the low level onshore flow (Table 3.1), unlike the baseline case where they are coincident. There is, however evidence of a weakening of the gradient wind at low levels, due to the establishment of a temperature gradient. The offshore extent becomes approximately equal to the baseline case for this gradient wind speed, extending to a maximum of 270km offshore (Fig. 3.6a). East of the seaward end of the sea breeze a calm zone (10m wind speed $<1\text{ms}^{-1}$) rapidly expands, so that by 1900 UTC, the influence of the *pure* sea breeze extends across the entire offshore domain. The presence of a calm zone offshore has been observed in the southern North Sea by Lapworth (2005b) though only extending between 20-40km during offshore gradient wind flow.

Increasing the gradient offshore wind speed results in a delay in the establishment of

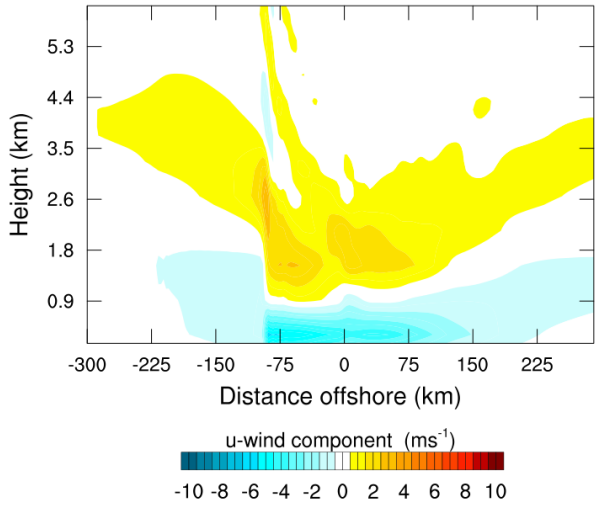

Figure 3.4: The u-wind component (ms^{-1}) of a mature sea breeze at 1900 UTC for the baseline single coast case using the YSU PBL scheme and a SST of 287K. Negative values indicate onshore flow.

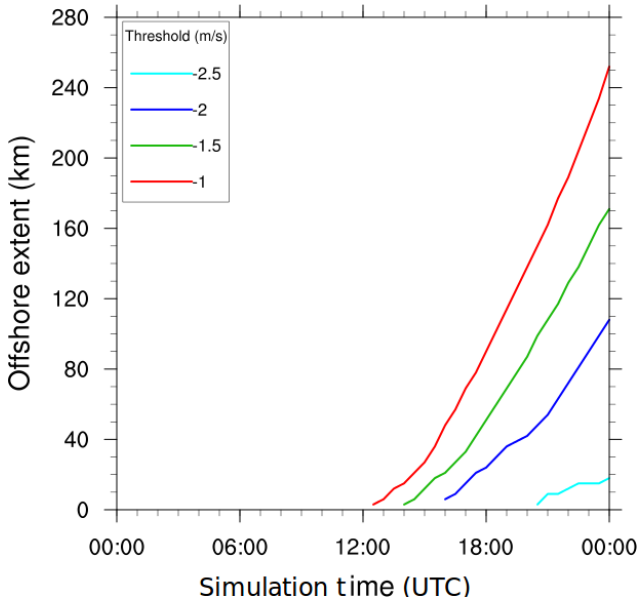

Figure 3.5: The sensitivity of the single coast baseline sea breeze offshore extent to the choice of 10m u-wind sea breeze definition threshold. Based on the YSU PBL scheme and a SST of 287K.

the full sea breeze circulation. For example, increasing the offshore gradient wind from the baseline to $4ms^{-1}$ results in a delay of 2 hours (Fig. 3.6b). The onshore component also weakens with increasing gradient wind speed to the extent that once the gradient speed becomes equal to $8ms^{-1}$, the onshore component does not breach the $1ms^{-1}$ threshold used by Arritt (1989) and a sea breeze is not formed (Figs. 3.6 and 3.7). However,

weak onshore flow below the $1ms^{-1}$ threshold is simulated at $8ms^{-1}$ offshore gradient wind speed which does reach the coastline at 1700 UTC. The onshore flow then weakens and does not penetrate inland (Fig. 3.7).

The PBL height development is not substantially different from the baseline case with increasing wind speed, although the delay with the formation of the sea breeze results in the PBL at the coast becoming deeper before the onset. Increasing the gradient wind speed results in the formation of a front, denoted by a sharp rise in specific humidity at the onset of the sea breeze which is not present in the baseline case (Fig. 3.8). This peak becomes more pronounced with increasing gradient wind speed until it reaches $8ms^{-1}$ when the onshore 10m wind speed is of insufficient strength to form a sea breeze.

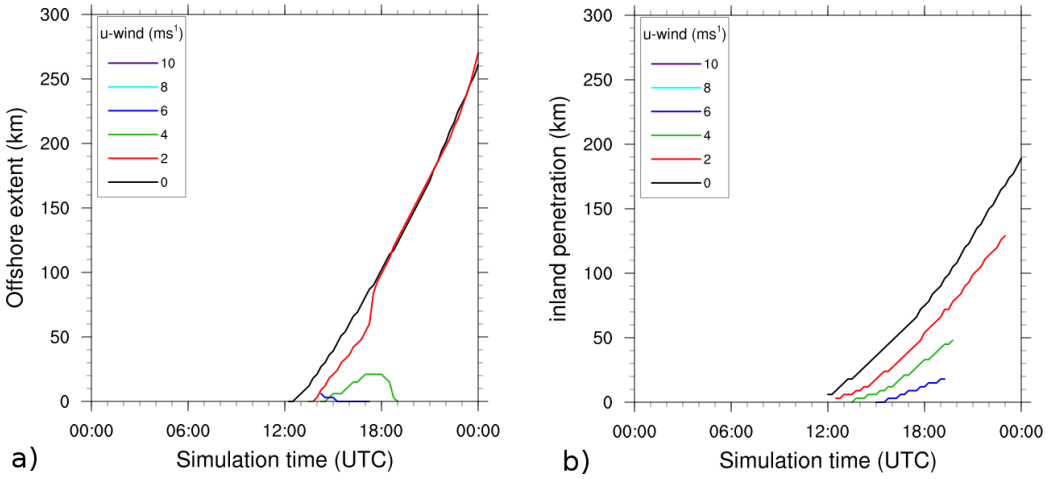

Figure 3.6: Simulated offshore (a) and onshore (b) extents through time of pure sea breezes under various offshore gradient wind strengths. Calculation of the respective lengths is achieved following the method of Arritt (1989). Based on the YSU PBL scheme and a SST of 287K.

Table 3.1: Summary characteristics of different sea breeze type characteristics for single coast experiments using gradient wind speeds of 2ms^{-1} and 6ms^{-1} orientated offshore (*pure*), along shore with land to the left (*corkscrew*) and along shore with land to the right (*backdoor*). All simulations are based on the YSU PBL scheme and a SST of 287K.

Parameter	Pure		Corkscrew		Backdoor	
Gradient wind speed (ms^{-1})	2	6	2	6	2	6
Onset (UTC)	1300	1415	1130	1100	1200	1100
Onshore thickness (m)	700	450	750	650	600	600
Max wind speed (ms^{-1})	3.75	1.13	4.47	3.76	4.25	3.88
Offshore advancement (ms^{-1})	5.55	-	6.48	8.33	4.63	3.47
Onshore advancement (ms^{-1})	2.89	1.39	4.11	4.86	4.36	3.57
Onshore extent (km)	132	21	111	162	111	90
Offshore extent (km)	270	12	300	300	171	102

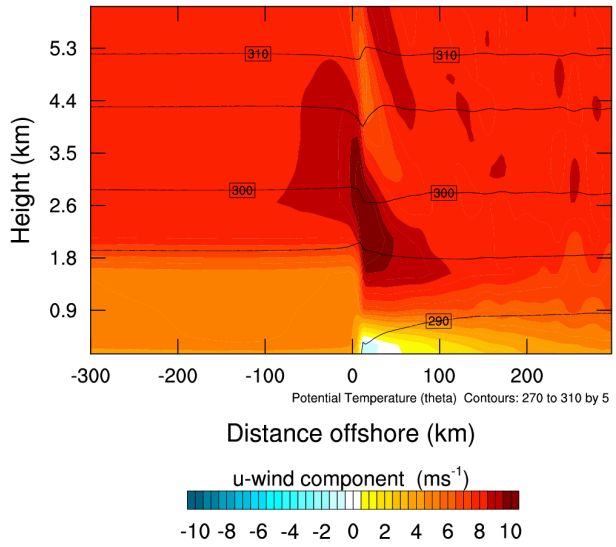

Figure 3.7: Vertical cross-section at 1600 UTC of the u-wind component for a single coast baseline simulation with an offshore gradient wind of 8ms^{-1}. Distances and wind speeds are positive in the offshore direction. Solid contours denote potential temperature. Based on the YSU PBL scheme and a SST of 287K .

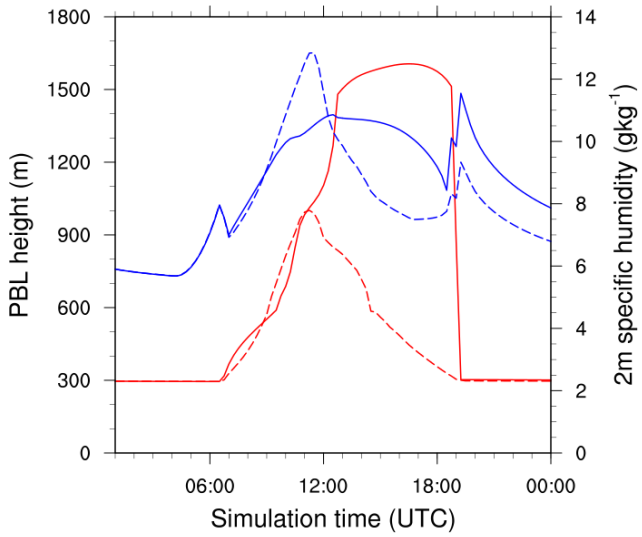

Figure 3.8: Time series of PBL height (red) and 2m specific humidity (blue) for a single coast simulation with 2ms^{-1} offshore gradient winds. Dashed lines represent the values at the coast and solid lines are 150km onshore. Based on the YSU PBL scheme and a SST of 287K .

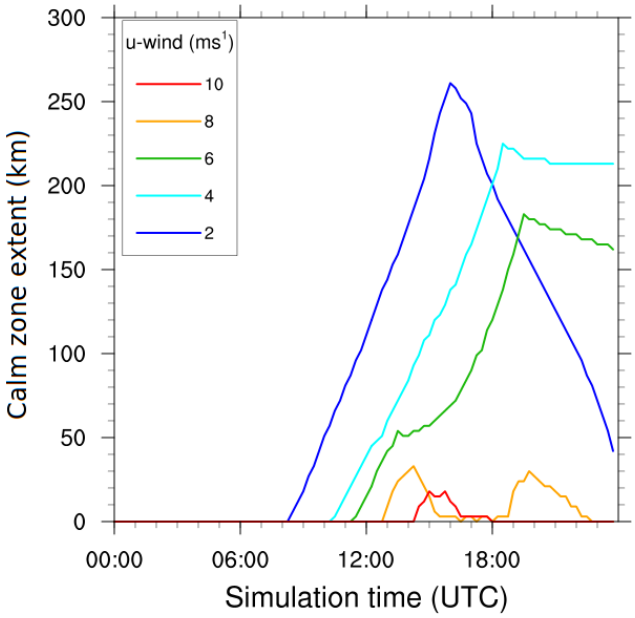

Figure 3.9: Length of the single coast calm zone (10m wind speed ¡ $1ms^{-1}$) for varying offshore gradient wind strengths. Based on the YSU PBL scheme and a SST of 287K.

Offshore, the horizontal extent of the sea breeze is sensitive to the strength of the gradient wind above $2ms^{-1}$ to the degree that raising the gradient wind strength to $4ms^{-1}$ reduces the maximum offshore extent to 21km (Fig. 3.6a). Calm zones (10m wind speed $< 1ms^{-1}$), however, persist in all experiments, reaching a maximum length of 21km for an offshore gradient wind speed of $10ms^{-1}$ (Fig. 3.9).

In context, a typical 100m offshore wind turbine has a hub height cut-in speed of $4ms^{-1}$, whereby at wind speeds below this threshold the turbine does not operate (Sinden, 2005). Therefore it is entirely possible for a *pure* sea breeze, incorporating adjustment for wind speed to hub height, to have a negative influence on wind power production. Once above this threshold, the power produced is proportional to the cube of the wind speed, so at higher gradient wind speeds the sea breeze, acting in the opposite direction, can significantly reduce power output. In cases where the land-sea thermal contrast is of insufficient strength to produce a sea breeze, or where the offshore gradient wind is too strong, there is still a significant reduction in wind speed offshore which, for a period, is below the turbine cut-in speed (Fig. 3.10).

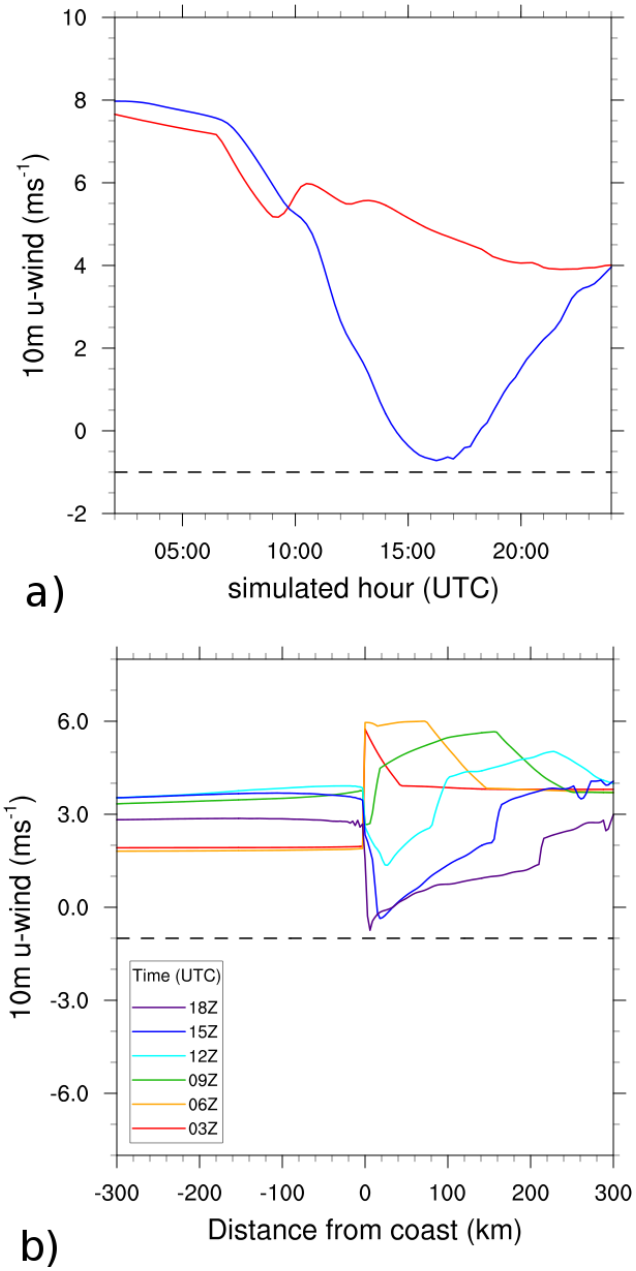

Figure 3.10: a) 10m u-wind speed for locations on the coastline (red) and 30km offshore (blue) for a single coast *pure* sea breeze simulated with 8ms^{-1} offshore gradient wind. b) 10m u-wind speed across the model domain at 0300 (red), 0600 (orange), 0900 (green), 1200 (cyan), 1500 (blue) and 1800 (purple) UTC. The dashed line represents the 1ms^{-1} onshore wind speed threshold required for diagnosing a sea breeze. In all simulations, the YSU PBL scheme was used in conjunction with a SST of 287K.

3.1.3 *Corkscrew* and *backdoor* sea breezes

As with the *pure* case, the formation of a *corkscrew* sea breeze in 2ms^{-1} shore-parallel winds involves the establishment of the return flow circulation before the onset of the low-level onshore flow. This develops at 0900 UTC, rather than at 1000 UTC, as with

the *pure* case, supporting the theory that a *corkscrew* type sea breeze requires a weaker thermal contrast to initialize (Section 1.2.2.2). The earlier onset time prevented the PBL height at the coast from reaching a height above 750m before the arrival of the sea breeze (Fig. 3.11). Consequently the PBL height drop on arrival was not as sharp as with the equivalent *pure* case and by 1600 UTC it had lowered to 300m, the height of the PBL over the sea. This pattern was replicated for specific humidity (Fig. 3.11).

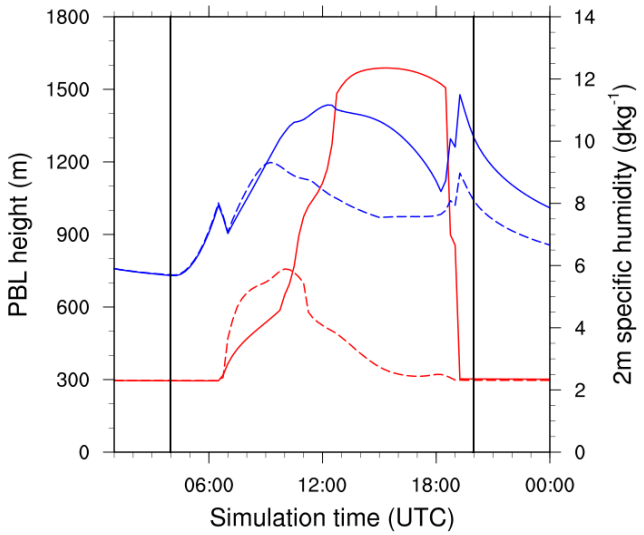

Figure 3.11: 2m specific humidity (blue) and PBL height (red) for a single coast *corkscrew* simulation with 2ms^{-1} along-shore gradient winds. Solid and dashed lines represent values at 150km onshore and at the coast, respectively. Sunrise and sunset are marked by the vertical black lines. The YSU PBL scheme was used in conjunction with a SST of 287K.

Increasing the strength of the shore-parallel gradient flow results in both an increase in the onshore horizontal extent and an earlier onset time, unlike the *pure* sea breeze which does not establish for offshore gradient wind speeds over 6ms^{-1} (Figs. 3.6 and 3.12). Also unlike the *pure* sea breeze, all gradient wind strengths produce a *corkscrew* sea breeze which has sufficient offshore extent to cross the entire offshore domain (Fig. 3.12a). The increase in shore-parallel gradient wind speed enhances the degree of divergence from friction at the surface, consequently allowing the *corkscrew* sea breeze to expand more rapidly than the *pure* type sea breeze.

The vertical thickness of the *corkscrew* sea breeze is approximately 750m (Fig. 3.13) and this does not deviate substantially for increasing along-shore gradient flow. However, the depth of the return flow appears to increase substantially with increasing along-shore gradient wind speed, though the true degree is masked by rotation of the gradient winds

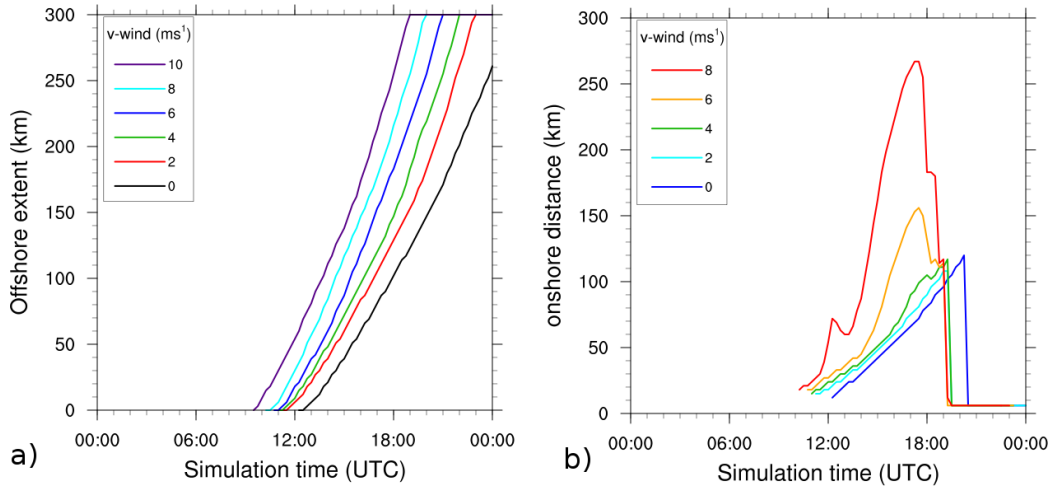

Figure 3.12: Offshore (a) and onshore (b) extents of single coast corkscrew sea breezes for different v-wind strengths defined using the method of Arritt (1989). Based on the YSU PBL scheme and a SST of 287K.

by Coriolis acceleration.

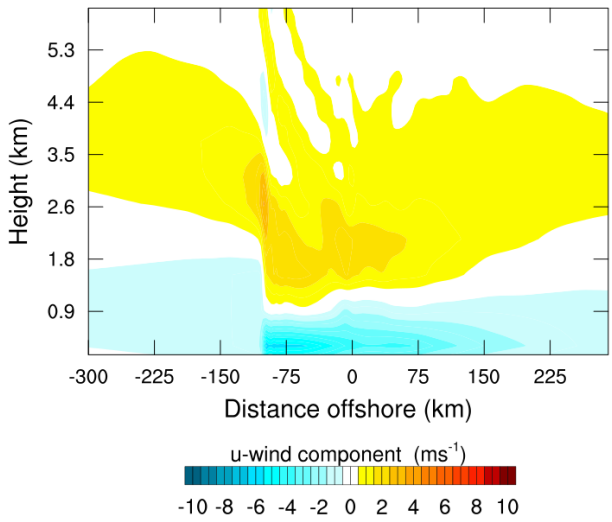

Figure 3.13: Cross-section of a mature *corkscrew* sea breeze at 1900 UTC developing in 2ms^{-1} along shore gradient flow for the single coast case. The PBL used was the YSU scheme and the SST was 287K. The u-wind component is positive in the offshore direction.

The *backdoor* sea breeze, generated by shore parallel flow with land to the right, is less sensitive to increasing gradient wind speed than the *pure* type sea breeze and, like the *corkscrew* sea breeze, establishes at an earlier time than the *pure* type (Table 3.1). However, the circulation is weaker, advancing only 111km at an average offshore rate of 4.63ms^{-1} for a shore parallel gradient wind speed of 2ms^{-1}. The weaker circulation is due to the combination of Coriolis acceleration and surface friction acting to create a

region of convergence at the surface. Like the *corkscrew* sea breeze, the thickness of the onshore flow does not deviate substantially for increasing shore parallel gradient wind speed (Fig. 3.14).

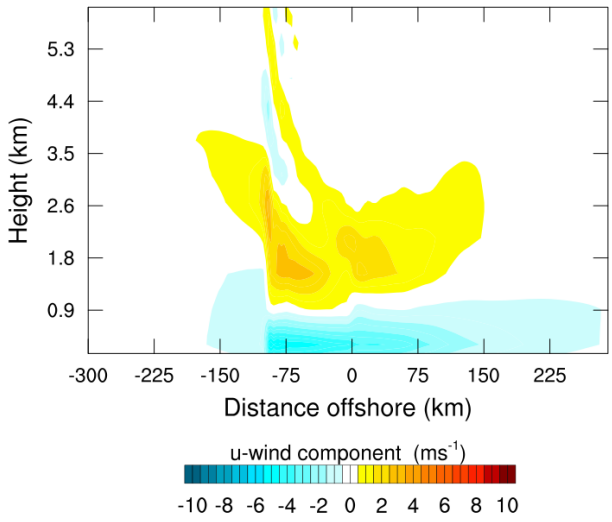

Figure 3.14: Cross-section of a *backdoor* type sea breeze at 1900 UTC generated with shore-parallel gradient winds of -2ms^{-1} for the single coast case. The YSU PBL scheme was used in conjunction with a SST of 287K.

Both the *corkscrew* and the *backdoor* sea breezes, produce stronger vector wind speeds offshore than at the coast unlike the *pure* sea breeze simulations (eg. Fig. 3.15). Whilst the results are for 10m wind speeds, the differences in wind speed offshore between different sea breeze types has potential implications for offshore wind energy. Significant deviations from predicted wind speeds are costly to the wind energy sector and so knowing the different effects of the sea breeze types is important.

3.1.4 Sensitivity to thermodynamic profile

In order to test the extent to which the results of the simulations were dependant on the initial thermodynamic profile, two further profiles were used for model initialization (Section 3.1.2.1). Both profiles were from the same period of early June 2006 as the original but contrasted in terms of both stability and moisture availability. Profile 2 (Fig. 3.3a) is from 0000 UTC at Herstmonceux on the 2nd June 2006 when the dominance of the anticyclone first established. The profile is saturated, or close to saturation, to 750hPa with a weak temperature inversion and relatively dry air above. This is indicative of low

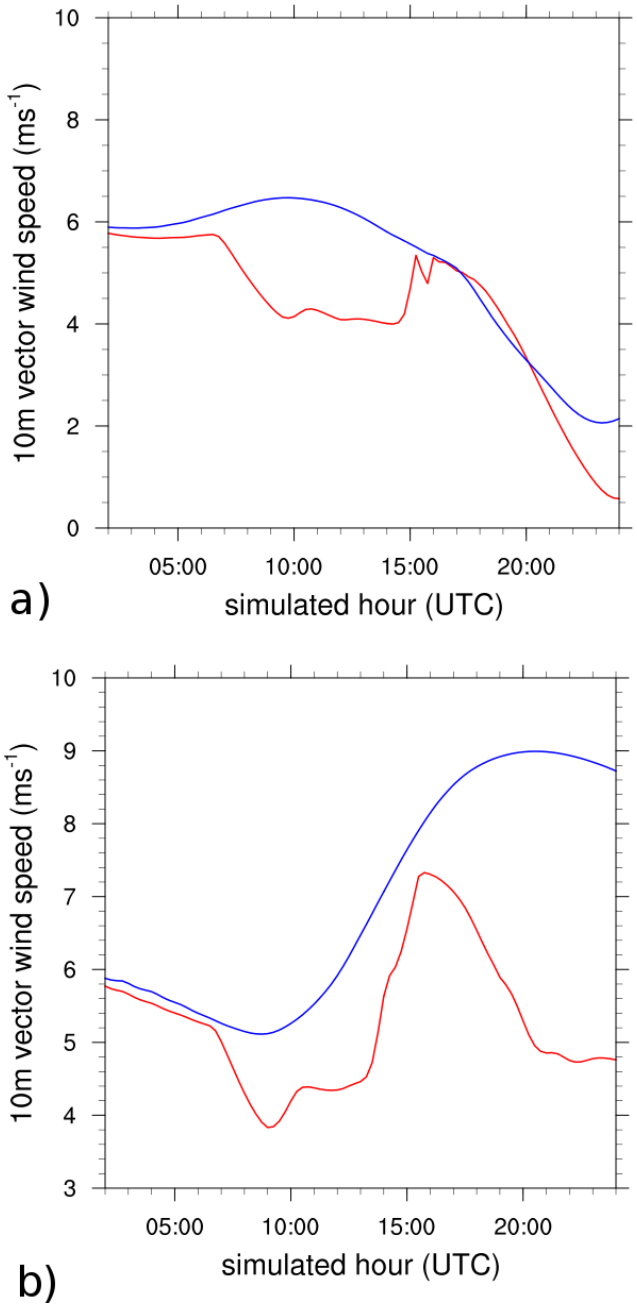

Figure 3.15: The evolution of 10m vector wind speed for *backdoor* (a) and *corkscrew* (b) sea breezes at the coast (red) and 30km offshore (blue) in the single coast case. Shore-parallel gradient winds for both cases are of magnitude 6ms^{-1}. The YSU PBL scheme was selected for both cases along with a SST of 287K.

level cloud during nocturnal cooling of the PBL. A dry layer exists between 750-700hPa, with another cloud layer to 500hPa. The second cloud layer is indicative of the remnants of a decaying frontal system to the north. This feature quickly decays and moves to the east and a sea breeze forms. Profile 3 was observed at Herstmonceux at 0000 UTC on the 3rd June 2006 and contains a much sharper temperature inversion at 860hPa and dryer air

aloft

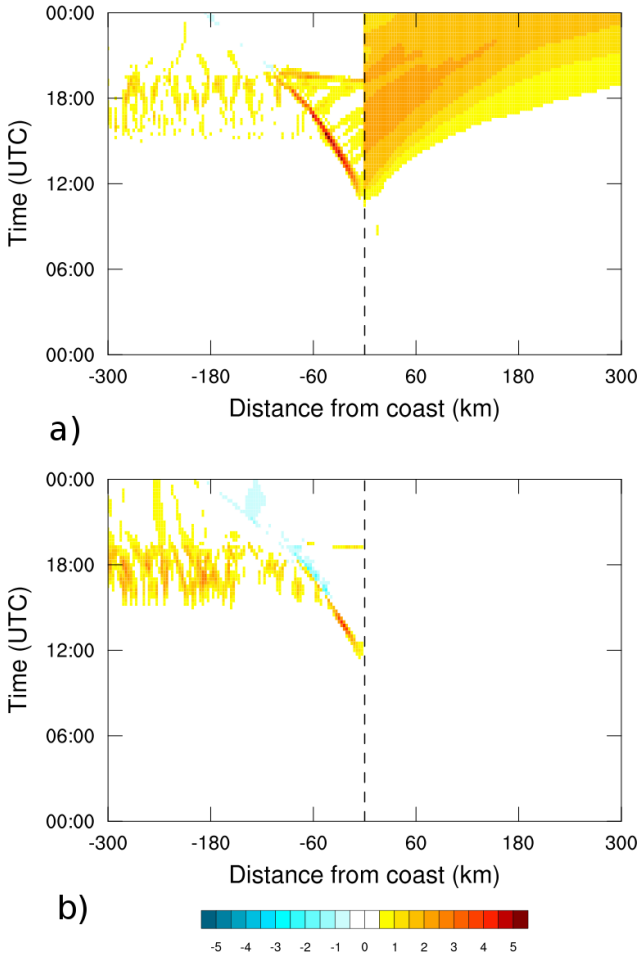

Figure 3.16: Differences in u-wind speed (ms^{-1}) between two single coast simulations using alternative initial profiles. Results based on 0000 UTC profiles for the 4^{th} June 2006 (Fig. 4) subtracted from the results for a) 3rd and b) 2nd June 2006. In all cases, the YSU PBL and an SST of 287K were used.

The results of these baseline simulations show that only profile 2 produced any significant deviations offshore (Fig. 3.16) relative to those associated with the original profile shown in Fig. 3.1. Profile 2 formed a sea breeze with onshore winds of approximately $5ms^{-1}$ and was the only single coast baseline experiment to extend to the edge of the 300km offshore domain (Fig. 3.17a) . In contrast, profile 3 (Fig. 3.2) forms a sea breeze which is weaker and only extends 222km offshore, compared to profile 1 which extended 261km offshore (Fig. 3.17b). The presence of the initial cloud cover in profile 2 kept temperatures over land higher overnight, thereby intensified the land-sea air temperature contrast which subsequently developed during the daytime and consequently intensifying the sea breeze. Other differences occurred over land and concerned the varying strength

of the sea breeze front and the degree of convection ahead of the sea breeze. These differences are associated with any thermodynamic instabilities in the profiles.

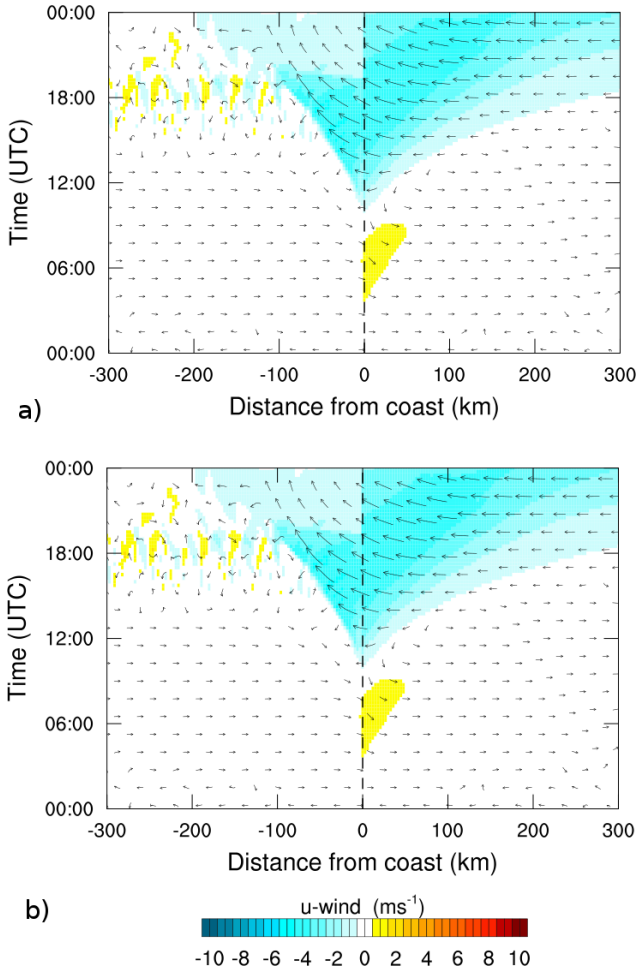

Figure 3.17: Single coast baseline experiments using vertical profiles a) 2 and b) 3 for initialization. Filled contours denote 10m u-wind component with positive values in the offshore direction. Arrows represent 10m wind vectors. The PBL choice for both simulations was YSU and the SST set at 287K.

In contrast to the baseline simulations, the *pure*, *corkscrew* and *backdoor* sea breeze simulations offshore all simulate a wide range of differences in wind velocities when compared to the simulations initialized with profile 1 (Figs. 3.18 to 3.19). The strong inversion in profile 3 intensifies the region of divergence at the coast at approximately 0615 UTC, when the land-sea thermal air temperature difference was zero. Overall offshore, the differing profiles produce only minor differences once the sea breeze had formed, unless the initial thermodynamic profile is close to saturation at night where the land-sea thermal contrast is intensified and the sea breeze is strengthened.

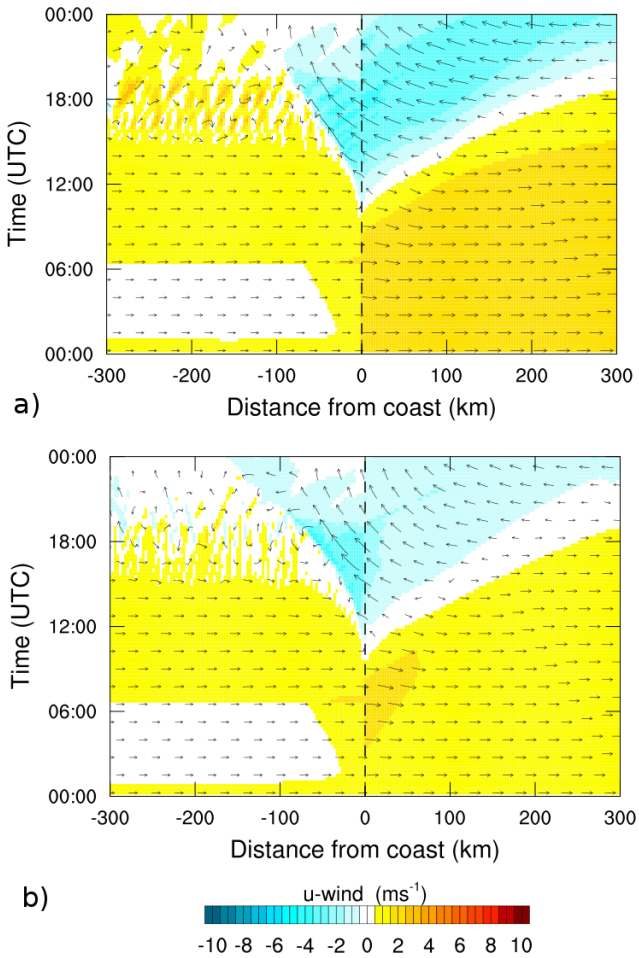

Figure 3.18: Single coast simulations using vertical profiles a) 2 and b) 3 for initialization in a 2ms^{-1} offshore gradient wind. Filled contours denote 10m u-wind component with positive values in the offshore direction. Arrows represent 10m wind vectors. The PBL scheme for both simulations was YSU and the SST set at 287K.

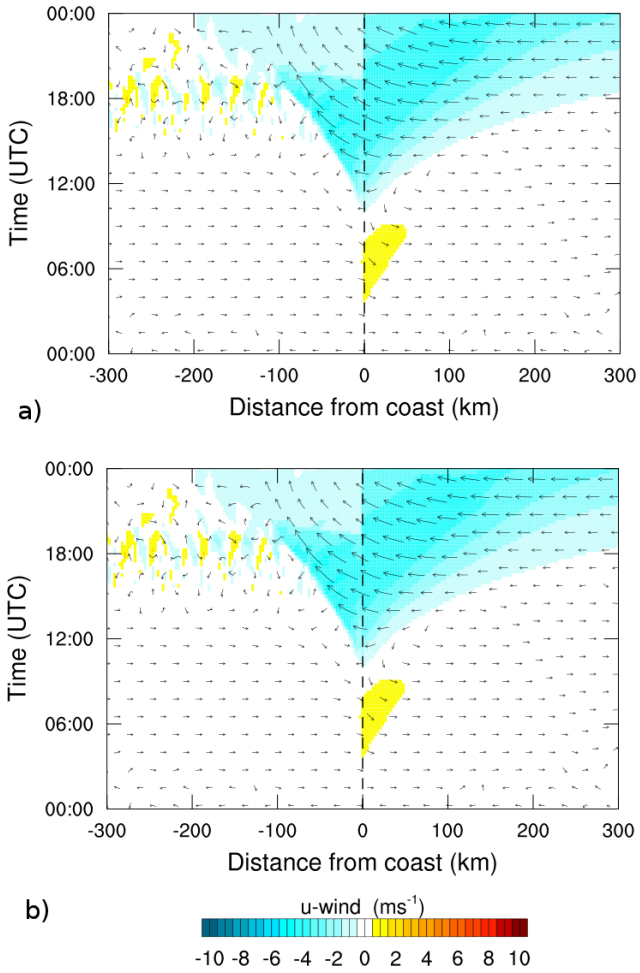

Figure 3.19: Single coast simulations using vertical profiles a) 2 and b) 3 for initialization in 2ms^{-1} shore parallel gradient wind. Filled contours denote 10m u-wind component with positive values in the offshore direction. Arrows represent 10m wind vectors. The PBL scheme for both simulations was YSU and the SST set at 287K.

3.1.5 Summary of single coast experiments

In summary, there are notable differences between the types of sea breeze which warrant consideration. *Corkscrew* sea breezes are stronger circulations than *pure* types and can be produced under gradient wind speeds which are too high for a *pure* type to establish (Table 4.1). They also potentially have a much larger offshore extent and increase the wind speed offshore, unlike the *pure* type which acts to reduce the wind speed offshore. *Backdoor* sea breezes establish earlier than *pure*, however, surface convergence restricts the horizontal extent and strength of the *backdoor*. Potentially, the offshore extents of the different sea breeze types and related calm zones could therefore affect offshore wind farms in regions such as the southern North Sea. However the coastline of mainland Europe could modulate this and so we now move on to investigate the effect of an additional coastline in dual-coast simulations.

3.2 Dual-coast

3.2.1 Baseline cases (no gradient wind)

Similar to the previous single coastline example, a single simulation with no gradient winds superimposed was run this time for the YSU, MYJ and MYNN boundary layer schemes (Section 3.1.2.2; See Appendix A for descriptions). layer schemes. The simulation for the YSU scheme produced two symmetrical sea breezes on each coastline each with a peak offshore extent of 42km at 1700 UTC (Fig. 3.20). After this, the sea breeze retreats towards the coast until 1900 UTC when no sea breeze was present offshore. The maximum strength of the onshore flow occurrs approximately 30km inland at 1500 UTC with a speed of 4ms^{-1}. Eventually the onshore extent reaches 60km, when the sea breeze subsides after 1700 UTC. Onshore flow inland remained present although it was not continuous from the coast after this time. The PBL height and 2m specific humidity simulated were comparable to the single coast simulation, reaching maxima of 1550m and 13.5gkg^{-1} respectively, 150km onshore from the western coast (Fig. 3.21).

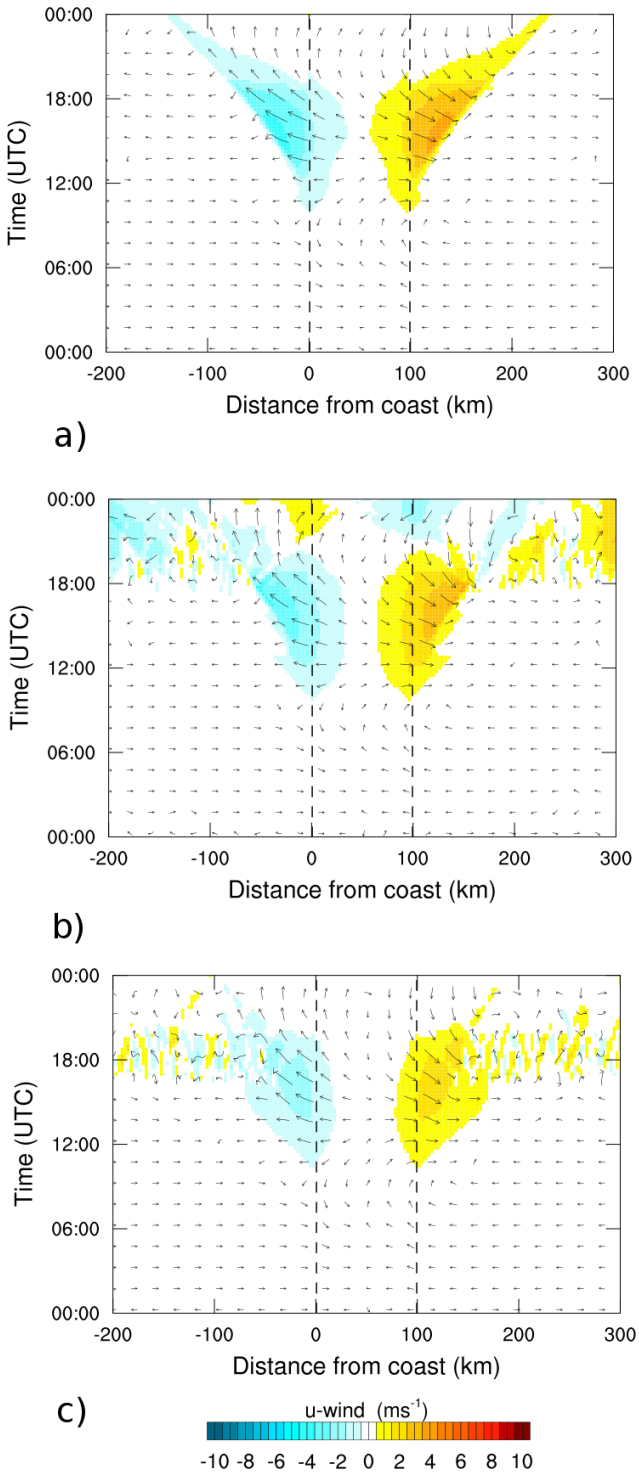

Figure 3.20: Baseline windfield cases (no gradient wind) for dual-coast simulations using (a) YSU, (b) MYJ and (c) MYNN boundary layer schemes. Dashed lines represent each coastal boundary and distances are expressed as seaward from the western coastline. The SST for all simulations was 287K.

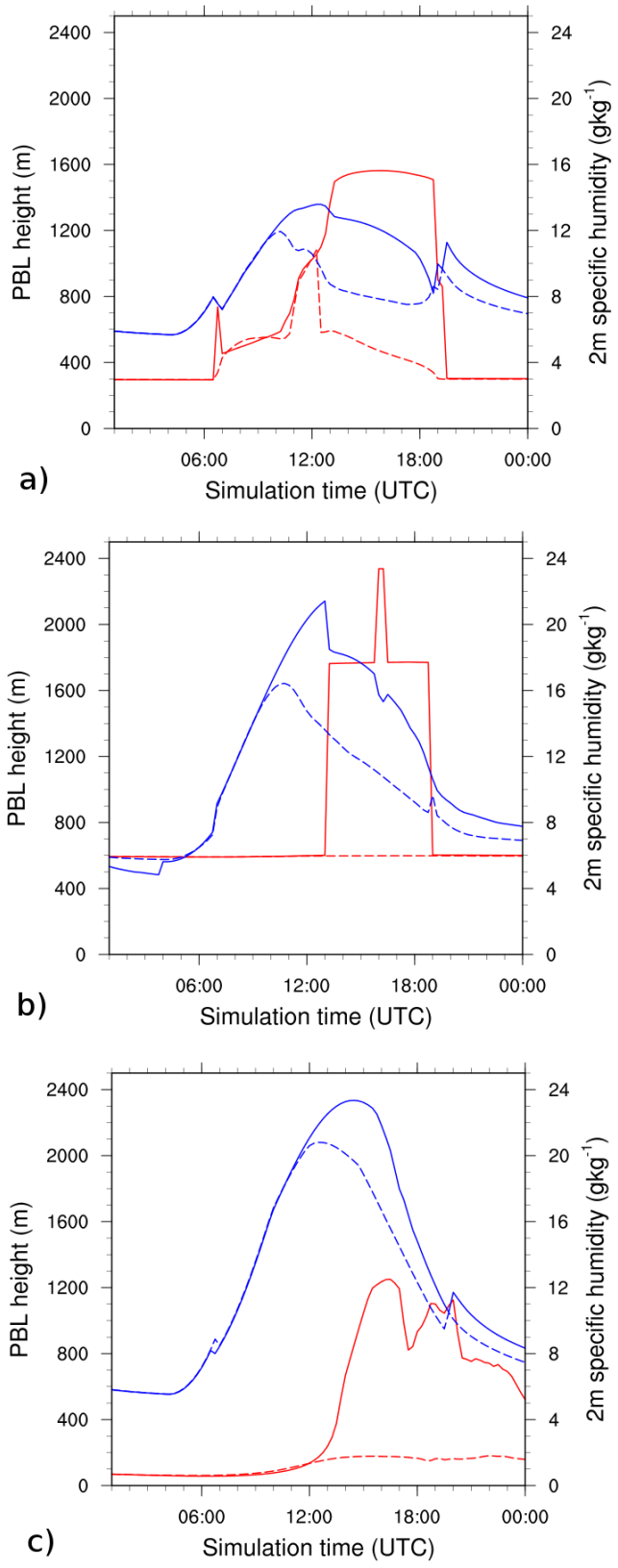

Figure 3.21: Evolution of 2m specific humidity (blue) and PBL height (red) for the baseline dual-coast simulations using a) YSU, b) MYJ and c) MYNN PBL schemes. Solid lines indicate values at 150km inland and dashed lines indicate the values at the coast. The SST in all cases was 287K.

Both the MYJ and MYNN PBL schemes produce different baseline states (Figs. 3.20b and 3.20c). At 1800 UTC both cases form convection ahead of the sea breeze . Furthermore, the MYJ scheme produces a much deeper PBL than the YSU baseline simulation, reaching 2300m, and with 2m specific humidity of $21 gkg^{-1}$ at 1300 UTC, 150km onshore. The MYNN scheme formes a shallower PBL than the YSU, reaching a maximum depth of 1300m, however, it also simulated the highest 2m specific humidities of $23 gkg^{-1}$ (Fig. 3.21).

3.2.2 *Pure* Sea Breeze

Without the inclusion of Coriolis forcing in the simulation, increasing the strength of the offshore gradient wind results in the western sea breeze retreating towards the sea. Indeed, for the YSU PBL scheme, the sea breeze does not reach the coastline at gradient wind speeds between 11-14ms^{-1} (Fig. 3.22). The offshore extent of the sea breeze was insensitive to gradient wind speed below $11 ms^{-1}$, reaching 42km offshore.

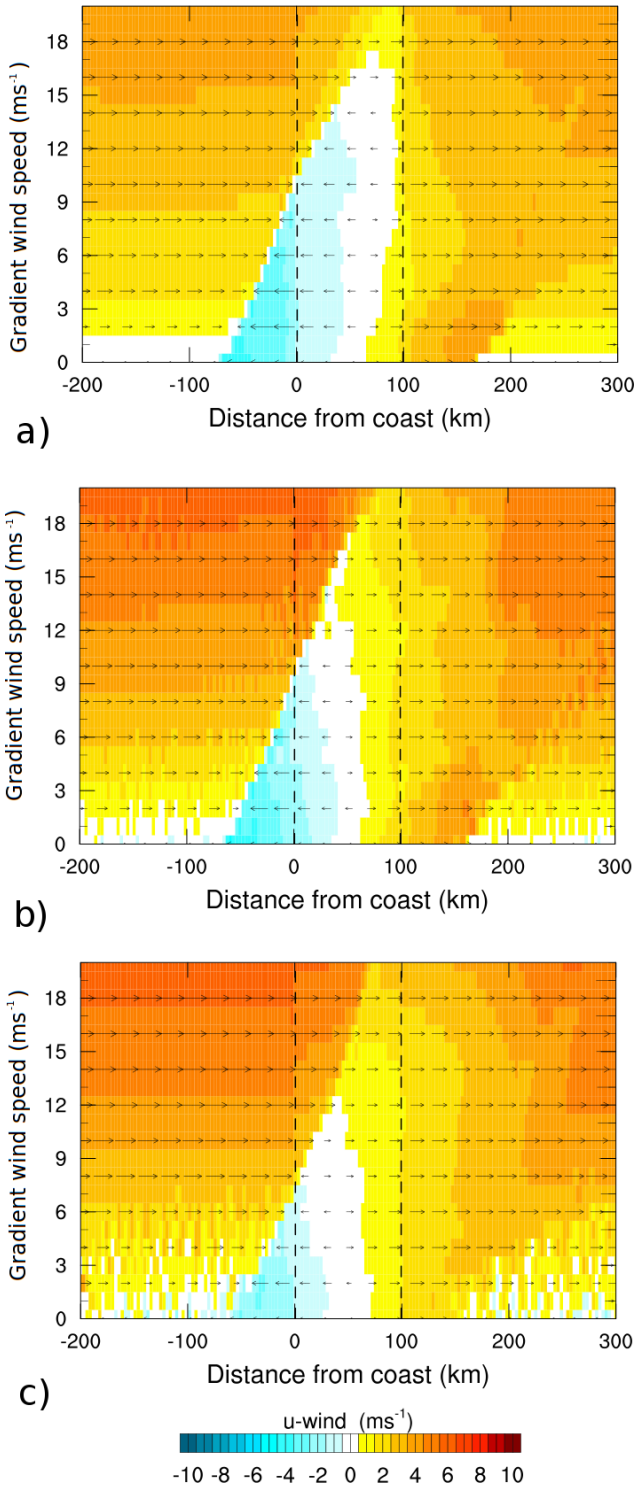

Figure 3.22: Variations of the 10m u-wind component (color) and vector wind speeds (arrows) with increasing west-east gradient wind strength (*pure* type sea breeze) at 1700 UTC using the (a) YSU, (b) MYJ and (c) MYNN PBL schemes without Coriolis acceleration. Distances are measured from the western coastal boundary with each coastline being depicted by the dashed lines. In all cases, the SST was 287K.

With increasing gradient wind speed, both the MYJ and MYNN PBL schemes produce weaker onshore wind speeds in the offshore environment than the YSU scheme without the inclusion of Coriolis acceleration (Fig. 3.23). As a result, the maximum offshore gradient wind speed that forms a *pure* sea breeze circulation is 13ms^{-1} for the YSU PBL scheme, compared to 10ms^{-1} and 7ms^{-1} for the MYJ and MYNN PBL scheme simulations respectively. This is also a higher threshold than the previous single coast experiments using the YSU scheme. The confined sea in the dual-coast simulations is of insufficient length for the offshore gradient winds to fully adjust to the change in roughness length at the coast and is therefore more turbulent than with the single coast case. This means that the effective offshore gradient wind speed will be less than the single coast simulations and so the sea breeze will be able to form at higher gradient wind speeds for the dual-coast case.

The combination of the offshore calm zone (10m wind speed $<$1ms^{-1}) and the offshore limit of the sea breeze extends to a greater distance with the YSU PBL, reaching 90km offshore from the western coast compared with maxima of 70km for both the MYJ and MYNN schemes without Coriolis acceleration. The *pure* sea breeze offshore extent of the PBL schemes are comparable, extending to 30km, though the sensitivity of the MYNN PBL scheme is greater to increasing gradient wind speed.

The inclusion of Coriolis acceleration reduces the minimum offshore gradient wind required to prevent the *pure* sea breeze from reaching the western coast (Table 3.2). Sensitivity of the minimum offshore gradient wind speed to PBL scheme is also apparent (Table 3.2). These range from 5ms^{-1} with the MYNN PBL scheme to a maximum of 9ms^{-1} using the YSU PBL scheme, and are consistent with the relative strengths of the sea breezes produced by each PBL scheme.

The inclusion of Coriolis acceleration also increases the sensitivity of the offshore extent of the *pure* sea breeze to increasing gradient wind speed (Fig. 3.23). The MYNN PBL scheme, in particular, does not simulate an onshore flow over the sea once Coriolis acceleration is included. With the YSU and MYJ schemes, the offshore extent does not become negligible until gradient wind speeds are above 7ms^{-1} (Fig. 3.24).

Table 3.2: Summary of *pure* sea breeze dual-coast characteristics for varying offshore gradient wind speeds and PBL schemes. The detachment wind speed is the minimum offshore gradient wind speed required to prevent a sea breeze from reaching the coast. The maximum offshore extent is defined as the maximum continuous distance offshore that the u-wind component is less than -1ms^{-1}. The calm zone length is defined as a continuous region with wind speed below 1ms^{-1}. The flow retardation percentage is the percentage drop in 10m wind speed over the water surface due to the thermal contrast relative to the average value at 0300 UTC (Figs. 3.20 - 3.24).

Parameter					**Pure**				
PBL scheme		YSU			MYJ			MYNN	
Gradient wspd (ms^{-1})	3	9	15	3	9	15	3	9	15
detachment wspd (ms^{-1})		9			8			5	
Max. offshore extent (km)		18			15			0	
Calm zone length (km)	66	48	0	48	0	0	66	0	0
Flow retardation (%)	75	75	79	60	66	-	75	75	65
Max. onshore wspd (ms^{-1})	3.14	0.93	-	2.95	0.26	-	1.73	-	-

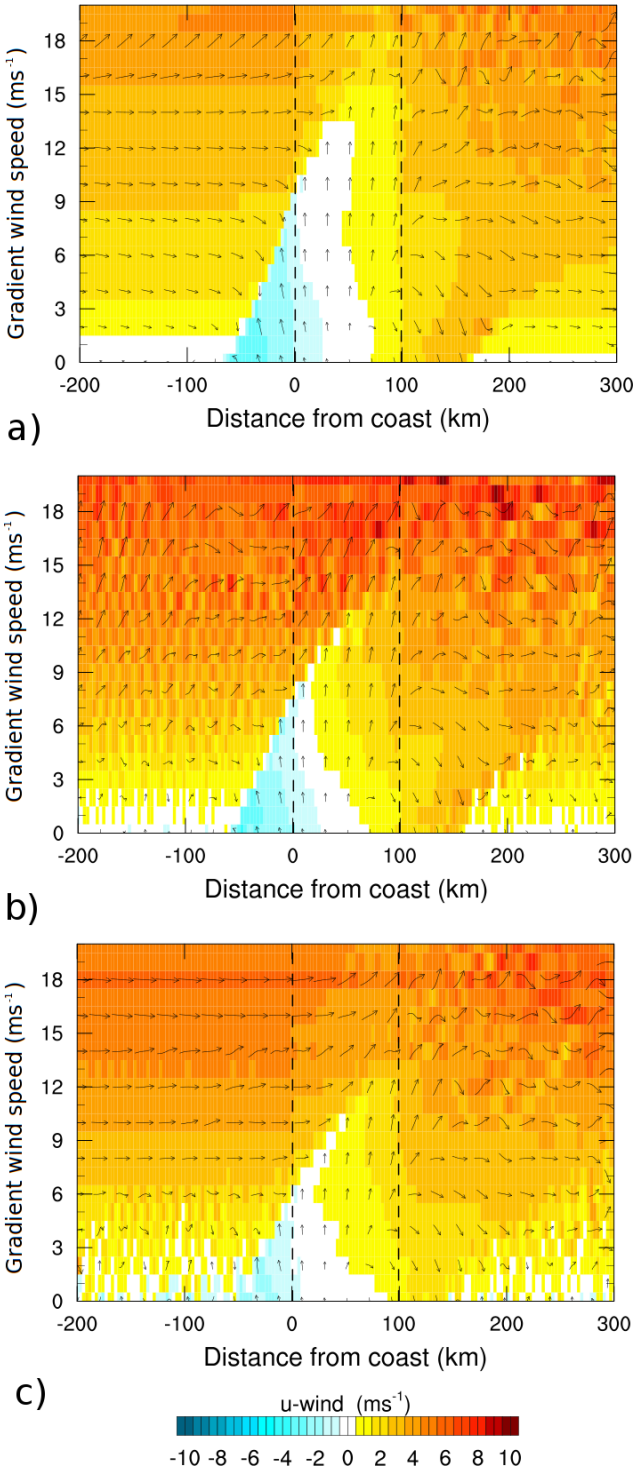

Figure 3.23: Variations of the 10m u-wind component (color) and vector wind speeds (arrows) with increasing west-east gradient wind strength (*pure* sea breeze type) at 1700 UTC using the (a) YSU, (b) MYJ and (c) MYNN PBL schemes with Coriolis acceleration. Distances are measured from the western coastal boundary with each coastline being depicted by the dashed lines. The SST was set to 287K for all simulations.

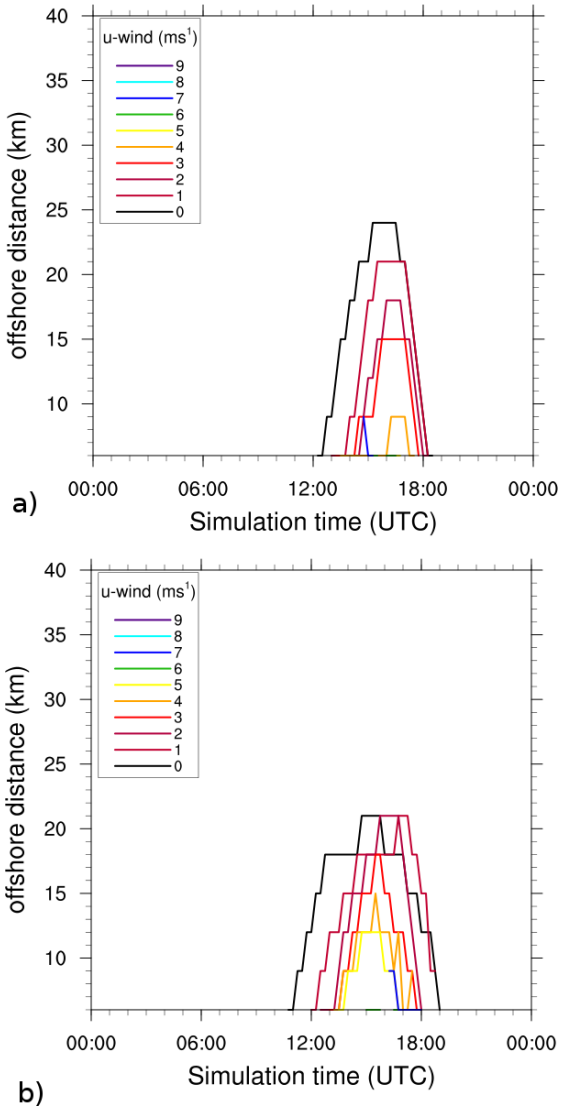

Figure 3.24: Dual-coast pure sea breeze offshore extents defined using the method of Arritt (1989) for different offshore gradient wind speeds using the a) YSU and b) MYJ PBL schemes. The SST was 287K for all simulations.

Similarly, the offshore calm zone is more sensitive to increasing gradient wind speed with the inclusion of Coriolis acceleration although this is not the case for the YSU PBL experiments (Fig. 3.25). The calm zones for the YSU simulations vary in length between approximately 50-70km and are still generated with an offshore gradient wind speed of 10ms^{-1}; when the sea breeze is not formed (Fig. 3.25). The MYJ and MYNN PBL simulations do not produce a calm zone for offshore gradient wind speeds above 6ms^{-1} (Fig. 3.25).

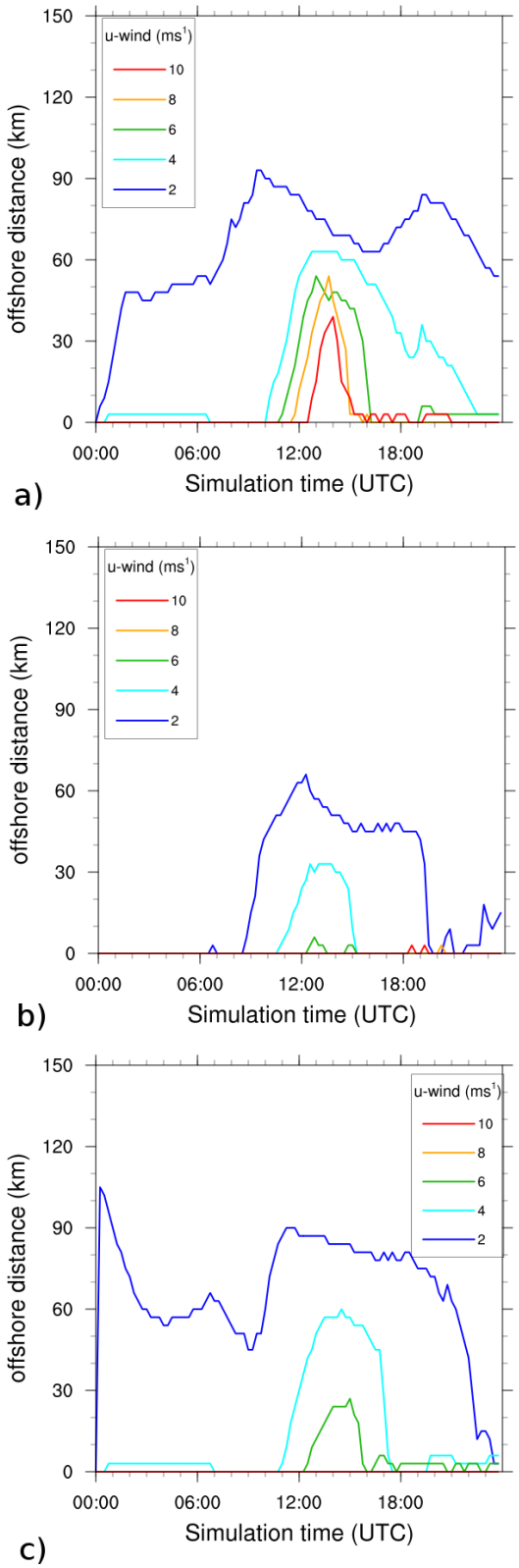

Figure 3.25: Horizontal extents of offshore calm zones (10m wind speed ¡ 1ms^{-1}-1) for different offshore gradient wind strengths using a) YSU, b) MYJ and c) MYNN PBL schemes. The SST was 287K for all simulations

In summary, the behaviour of the *pure* sea breeze offshore is strongly influenced by the choice of PBL scheme (Table 3.2). The two TKE schemes tested simulate a *pure* sea breeze that has less horizontal extent, is weaker and more sensitive to gradient wind speed changes than the non-local YSU scheme. The MYNN PBL scheme in particular does not simulate a sea breeze in the offshore environment that meets the definition given by Arritt (1989).

Furthermore, the inclusion of the second coastline also allows the formation of a sea breeze in higher gradient wind speeds than the single coast simulations, though the length of both the offshore extent of the sea breeze and the calm zones are restricted by the inclusion of the second coastline. In context, though these are only idealized experiments, both the offshore calm zones and the *pure* sea breeze would influence any offshore wind farms, bringing the wind resource below the cut in threshold required to operate a turbine.

3.2.3 *Corkscrew* and *backdoor* cases

For a shore-parallel gradient wind without Coriolis acceleration, two symmetrical *corkscrew* and *backdoor* sea breezes are formed on each coastline for all gradient wind speeds (Fig. 3.26). The inclusion of Coriolis acceleration however produces the asymmetry which allows the two sea breeze types to be distinguishable from each other (Fig. 3.27).

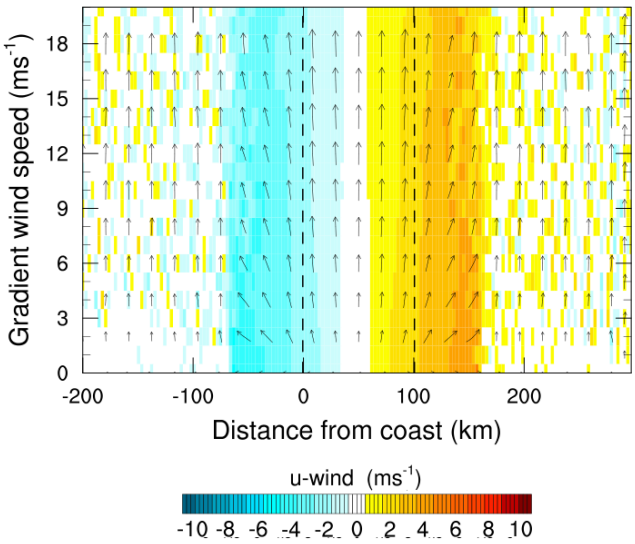

Figure 3.26: Variation of the 10m u-wind component of wind speed for dual coast simulations with increasing shore parallel gradient winds without Coriolis acceleration. Coastlines are marked as dashed black lines and the wind direction is represented as vectors. The selected PBL scheme is MYJ and SST set at 287K. Distances are measured from the western coastal boundary.

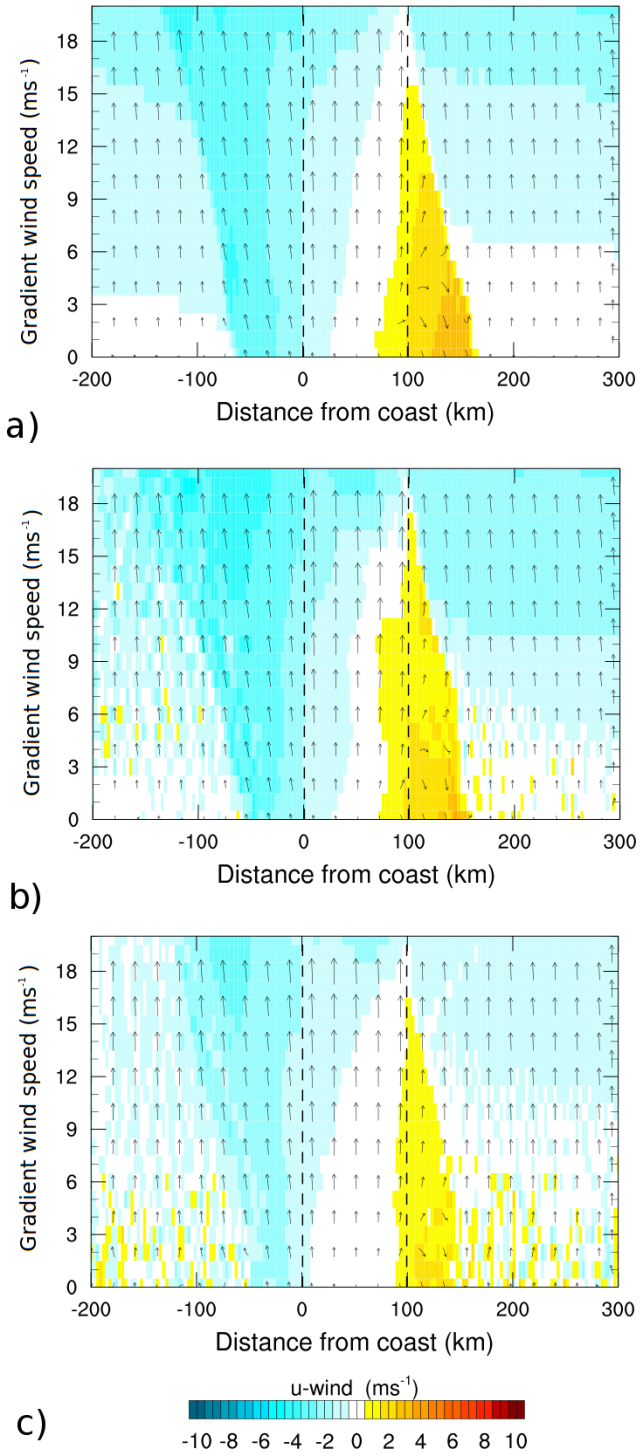

Figure 3.27: Variations of 10m u-wind component (colour) with 10m wind vectors (arrows) for increasing south-north gradient winds at 1700 UTC using the (a) YSU, (b) MYJ and (c) MYNN PBL schemes. Coriolis acceleration is enabled for a latitude of 52° and distances are measured from the western coast. The SST was set at 287K for all simulations.

For all PBL schemes, increasing the strength of the along-shore gradient wind speed increases the extent and strength of the *corkscrew* sea breeze both onshore and offshore on the western coast, as per the single coast results (Table 3.3 and Fig. 3.27). This implies that the enhancement of the *corkscrew* sea breeze by creation of the region of divergence at the coast becomes increasingly important with increasing gradient wind speed. The least sensitive PBL schemes to gradient wind speed changes are the YSU and MYJ schemes (Figs. 3.27b and 3.27c). As with the *pure* case, the MYNN scheme produces an offshore extent which is the smallest, reaching only 12km for shore-parallel gradient wind speeds between 1-8ms^{-1}. Above this speed, the *corkscrew* sea breeze offshore extension rapidly increases so that by 1700 UTC, a gradient wind speed of 9ms^{-1} is sufficient for the sea breeze to reach 96km offshore (Fig. 3.23c and Table 6).

Table 3.3: Summary of *corkscrew* sea breeze dual-coast characteristics for varying offshore gradient wind speeds and PBL schemes. The maximum offshore extent is defined as the maximum continuous distance offshore that the u-wind component is less than -1ms^{-1}. The calm zone length is defined as a continuous region with wind speed below 1ms^{-1}. The flow retardation percentage is the percentage drop in 10m wind speed over the water surface due to the thermal contrast relative to the average value at 0300 UTC. Negative values represent an increase in 10m wind speed.

Parameter					**Corkscrew**				
PBL scheme		YSU			MYJ			MYNN	
Gradient wspd (ms^{-1})	3	9	15	3	9	15	3	9	15
Max. offshore extent (km)		81			97			97	
Flow retardation (%)	-71	0	12	-70	-27	0	-57	9	22
Max. onshore wspd (ms^{-1})	3.34	3.23	3.39	2.83	3.38	4.23	1.83	2.37	3.12

In contrast to the *corkscrew*, the *backdoor* sea breeze on the eastern coast has both the largest horizontal extent and strength at the lowest gradient wind speeds for all PBL schemes. There is little fluctuation in offshore extent until the point where the *corkscrew* sea breeze on the western coast prevents the formation of the *backdoor* sea breeze on the eastern. This varies for each PBL scheme. For the YSU scheme both the maximum offshore extent and the strength of the gradient wind speed required to prevent sea breeze formation are the maximum between the different PBL schemes with values of 30km and 15ms^{-1} respectively (Fig. 3.27a).

Both the *corkscrew* and *backdoor* sea breezes do not suffer the degree of flow retardation as the *pure* sea breeze does by the formation of calm zones (compare Tables 3.2, 3.3 and 3.4). In some of the *corkscrew* sea breeze experiments, the sea breeze enhances

Table 3.4: Summary of *backdoor* sea breeze dual-coast characteristics for varying offshore gradient wind speeds and PBL schemes. The maximum offshore extent is defined as the maximum continuous distance offshore that the u-wind component is less than -1ms^{-1}. The *corkscrew* dominance is defined as the wind speed where the offshore influence of the *corkscrew* sea breeze, formed on the opposing coastline, suppresses the *backdoor* sea breeze offshore. The calm zone length is defined as a continuous region with wind speed below 1ms^{-1}. The flow retardation percentage is the percentage drop in 10m wind speed over the water surface due to the thermal contrast relative to the average value at 0300 UTC.

Parameter					**Backdoor**				
PBL scheme		YSU			MYJ			MYNN	
Gradient wspd (ms^{-1})	3	9	15	3	9	15	3	9	15
Cork. dominance (ms^{-1})		5			11			9	
Max. offshore extent (km)		24			27			24	
Flow retardation (%)	29	-	-	36	10	-	43	22	-
Max. onshore wspd (ms^{-1})	3.44	2.12	1.37	2.15	2.53	0.55	1.45	1.63	1.12

the gradient wind speed as shown by the negative values in Table 3.4.

In summary, the factor responsible for the development of the asymmetries which distinguish the sea breeze types in shore parallel flow is Coriolis acceleration when interacting with surface friction. For the *corkscrew* case, the creation of the region of divergence by Coriolis acceleration becomes increasingly important with increasing gradient wind speed to the degree that the *corkscrew* sea breeze restricts the development of the *backdoor* sea breeze on the eastern coastline. Also, for the wind speeds tested, increasing the strength of the along-shore gradient wind does not prevent the formation of a *backdoor* sea breeze, so this type is not restricted to low wind speeds, unlike the more intensely studied *pure* type.

3.2.4 SST variations

With the exception of the sea breeze front, varying the SST between 280-290K (a realistic SST range in southern North Sea temperatures for June) does not have a significant effect on the onshore environment for any type of sea breeze (Figs. 3.28- 3.29). Offshore, however, the result of increasing the sea surface skin temperature is to reduce the land-sea thermal contrast and therefore to weaken the sea breeze. In other words, the calm zone diminishes and the offshore wind speeds increase. For example, the magnitude of the increase in wind speed for sea surface skin temperatures between 280K and 290K is 1-2ms^{-1} for offshore gradient wind speeds below 4ms^{-1} (Fig. 3.30). At offshore gradient wind speeds above 4ms^{-1}, the change in offshore wind speed as a function of

SST diminishes, as the gradient flow dominates the thermal pressure gradient.

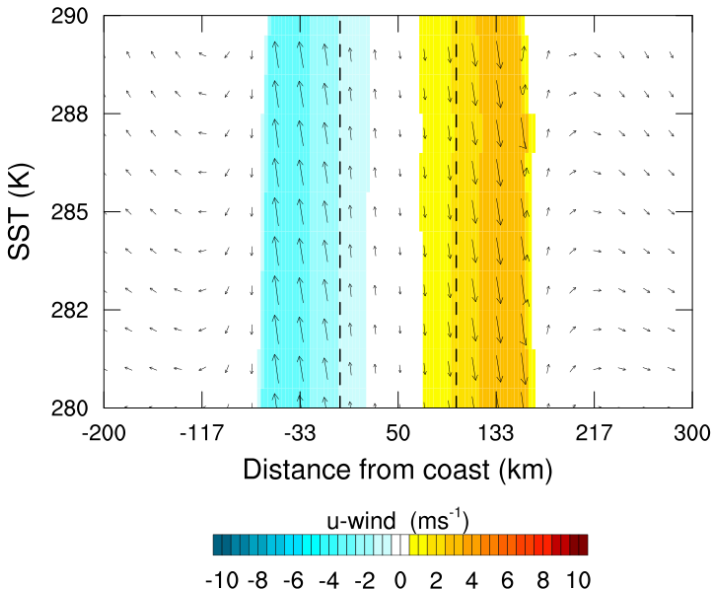

Figure 3.28: Sensitivity of the 10m u-wind component of wind speed (color) of the baseline (no gradient wind) dual coast simulations to SST using the YSU PBL scheme. Distances are positive offshore from the western coast. 10m wind speed vectors are shown by the arrows.

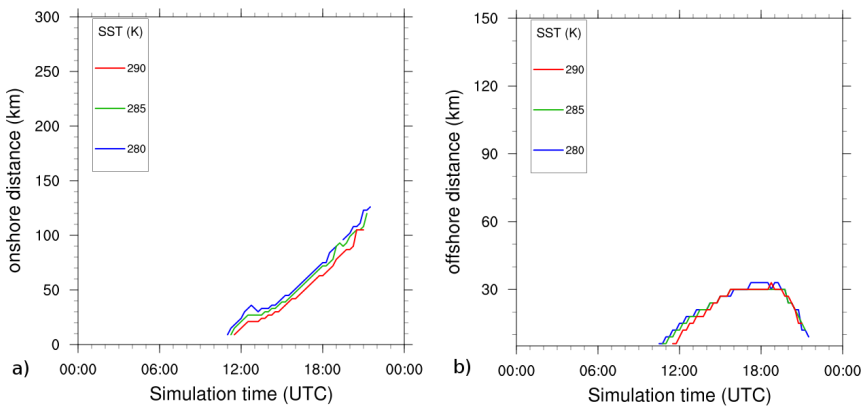

Figure 3.29: Sensitivity of a) onshore and b) offshore extent to SST for dual-coast simulations using the YSU PBL scheme.

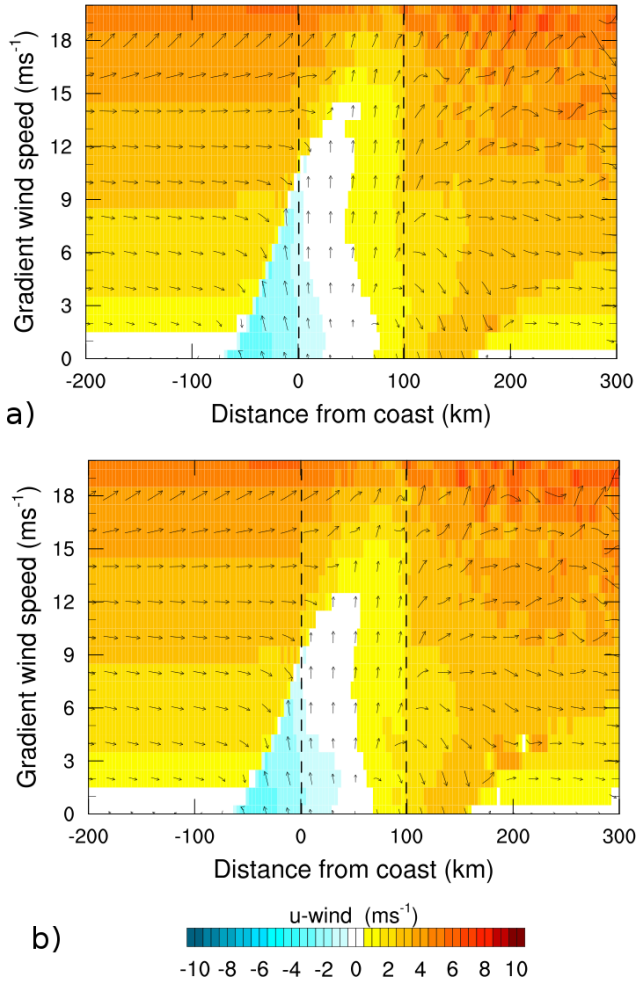

Figure 3.30: Effect of varying offshore gradient wind speed for SST's of a) 280K and b) 290K on the 10m u-wind component. Equivalent 10m wind speed vectors are also shown. The YSU PBL scheme was used for both cases. Distances and u-wind values are positive offshore from the western coastline. Both coastlines are shown as the dashed lines.

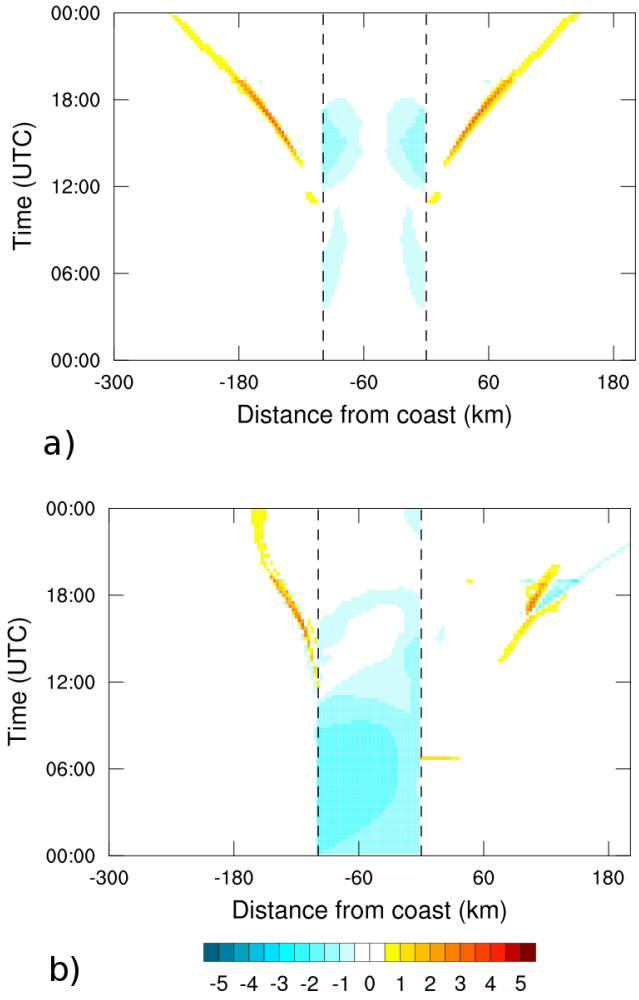

Figure 3.31: Differences in 10m u-wind component for a) the baseline case and for b) 4ms^{-1}. In each figure, the differences represent a simulation with sea surface skin temperature of 290K subtracted from a 280K simulation. In all cases, the YSU PBL was selected.

For *pure* sea breeze circulations, the increase in SST decreases the minimum wind speed required to prevent the sea breeze circulation from reaching the land (Fig. 3.30; Table 3.5). Fundamentally, this is to be expected and indeed several sea breeze prediction methods rely on the ratio of gradient winds to land-sea thermal contrast (eg. Biggs and Graves, 1962). Without the effect of advection cooling the land surface with increasing offshore gradient wind speed, the sea breeze horizontal length scales are insensitive to the SST's simulated (Figs. 3.29 and 3.30).

Additionally, a recent case study by Tang (2012) for an individual event has suggested that the effects of the diurnal cycle on shallow coastal water temperatures has significant impact on the sea breeze. To my knowledge, there has been no such idealized investigation into the effects of a shallow water diurnal cycle on the sea breeze. Adding such a cycle may reduce the land-sea thermal gradient and therefore lead to a weaker sea breeze.

Table 3.5: Dual-coast pure sea breeze response to varying SST. In both cases the YSU PBL scheme was selected and the simulations run with 2ms^{-1} offshore gradient winds.

Parameter	***Pure* sea breeze SST sensitivity**					
SST	280K			290K		
Gradient wspd (ms^{-1})	low	med	high	low	med	high
Detachment wspd (ms^{-1})		10			8	
Max. offshore extent (km)		15			33	
Calm zone length (km)	66	45	0	57	18	0
Flow retardation (%)	83	75	-	87	86	70
Max. onshore wspd (ms^{-1})	3.08	1.68	-	2.97	0.89	-

3.3 Summary and conclusions

A series of idealized numerical experiments of different sea breeze types have been performed and the additional constraint of a second coastal boundary has been tested. Of particular interest are the sea breeze characteristics and impact offshore, as extensive offshore wind farm development is currently underway in, for example, the southern North Sea. Sensitivity tests have also been performed regarding PBL physics schemes, initial thermodynamic profile, coriolis effect and realistic variations in sea surface skin temperature.

Principally, it is found that consideration must be given to the sea breeze type, if accurate prediction of the sea breeze characteristics is to be achieved. This is especially

important offshore, as both *corkscrew* and *backdoor* types produce higher wind speeds here than at the coast. In contrast to this, the *pure* sea breeze causes a reduction in wind speed offshore relative to the coastline.

The inclusion of the second coastline, more realistically representing the southern North Sea, enhances the effect of the offshore calm zones ($<$1ms^{-1}) which frequently span a large proportion of the modelled water surface, but are prevented from advancing as far as the single coast cases by the inclusion of the second coastline. Also, the *pure* sea breeze is able to form in higher offshore gradient wind speeds than in the single coast case; the smaller water surface does not allow the airflow to fully adjust before arrival at the second coastal boundary and so the airflow here is more turbulent, reducing the effective wind speed. Both the presence of the second coastline and the sea breeze type considered potentially have significant implications for offshore wind farms. This result is not particularly sensitive to realistic SST variations for the baseline case, however, for the *pure* type sea breeze, the effective thermal contrast is reduced for increasing offshore gradient wind speed and so consequently, the threshold gradient wind speed required to prevent the sea breeze from reaching the coastline is reduced. There are also important differences with regard to the PBL scheme used. In particular, the MYNN scheme simulates much weaker *pure* sea breezes offshore, extending to less than 10km for the majority of simulations, yet the extent of the simulated calm zone is comparable to other PBL schemes.

For all of the shore-parallel gradient wind simulations, a *corkscrew* sea breeze was formed on the western coast, and was intensified offshore relative to the baseline case (no gradient wind). Increasing the gradient wind speed further extended the *corkscrew* sea breeze offshore until it reached the opposite coastline. This occurred for all PBL schemes.

Since a *corkscrew* type sea breeze occurred on the opposite coastline to the *backdoor* sea breeze, the offshore extent of the *backdoor* sea breeze was restricted by the *corkscrew*. Consequently, the circulation was restricted to its own coastline. This, however, only occurred when Coriolis acceleration was enabled. Without Coriolis rotation, both coastlines produced identical sea breezes, and the distinct *corkscrew* and *backdoor* types were not generated. This implies that Coriolis acceleration plays an important role

in forming the different sea breeze types, and that in particular, the divergence associated with the *corkscrew* sea breeze becomes increasingly important with increasing gradient wind speed.

Whilst these results are purely idealized, they present an indication to the forecaster of the sea breeze dependence on both prognostic variables and physical model settings. Further research will be carried out through the modelling of real events coupled to realistic coastlines and combined with verification of the results against measurements from offshore wind farms in the southern North Sea to help determine the relative performance of the respective PBL schemes.

Chapter 4

WRF model verification

In chapter 3, it was noted through idealized sea breeze experiments that the fundamental length scales and strength of the sea breeze are significantly altered by the use of different PBL schemes. For example, the MYNN TKE PBL scheme forms the weakest sea breeze, which does not extend into the offshore environment according to the definition of Arritt (1989). Here, the simulations are extended to include more realistic coastlines and boundary conditions. An analysis of the performance of the model is provided against both surface and tower observations in the onshore and offshore environment. Verification assessments are discussed using temperature, wind speed and humidity in an effort to determine which PBL scheme gives the most realistic interpretation of a sea breeze. Additionally, longer hindcasts are performed, there the WRF model is run every month from May to September 2006, in order to ascertain PBL performance over longer time scales. Finally, through the analysis of radiation and heat fluxes, a plausible source of the errors in the PBL and surface physics is diagnosed.

4.1 Single case study: 19^{th} June 2012

The 19^{th} June 2012 was chosen as a single case study as the sea breeze which formed on this day in the Netherlands, is known to have reached the Cabauw tower, 50km inland (Tijm, pers. comm.). It therefore makes an ideal case study to verify the PBL schemes against both surface and mast data. A similar case study is not chosen from a UK coastline as the spatial coverage of observation stations in Eastern England is poor.

An elongated anticyclone dominates the weather of the Netherlands on the 19^{th} June

2012. Initially, the anticyclone is oriented south-west to north-east, centred over northern France, though by 12:00 UTC the centre has shifted north-eastward to Denmark. Relative to the Dutch coastline, the gradient winds are initially conducive to forming a *backdoor* sea breeze though by 12:00 UTC, the movement of the anticyclone centre has caused the gradient winds to become offshore. Temperatures, as shown in Fig. 4.1, reach approximately 295K over the Netherlands by 12:00 UTC and combined with sea surface temperatures of between 285-286K, the land-sea thermal contrast is sufficient to induce convection over the Netherlands, consequently forming a sea breeze. As noted be Miller *et al.* (2003), sea breezes take on the characteristics of the different types if the orientation of the gradient wind relative to the coastline changes during the day. In this case, the sea breeze can initially be classified as a *backdoor* sea breeze, but as the gradient winds rotate to the offshore direction, it takes on *pure* sea breeze type characteristics. In this case, the sea breeze was recorded to reach as far inland as the Cabauw tower, making it an ideal case study for examining the performance of the different PBL schemes, model resolution and spin up time as described in Table 3.5. The model is first analysed in terms of the baseline simulation and then through subsequent sensitivity tests such as increasing resolution and lead time. Model performance is evaluated against both onshore and offshore measurements.

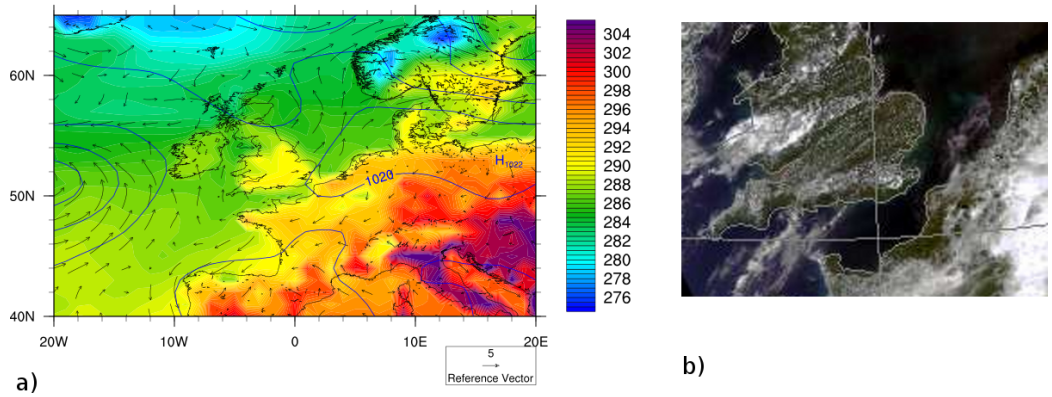

Figure 4.1: a) 12:00 UTC GFS FNL Analysis of sea level pressure (hPa) and 2m temperature (K), where 2m temperature is denoted by the filled contours. Vectors show 10m wind (ms^{-1}) b) MODIS RGB composite image of channels 1,4 and 3 at 12:14 UTC on the 19th June 2012.

4.1.1 Baseline simulation

Between 02:00-06:00 UTC (04:00-08:00 CEST), the 10m wind field is predominantly southerly. Over the Netherlands, the 10m wind is light and more variable than offshore,

with the vast majority of the country experiencing 10m wind speeds of less than 1ms^{-1}. Conversely, over the southern North Sea, the 10m wind speed is approximately 4.5ms^{-1} and is more uniform than over the land surface which naturally has more variations in surface roughness.

Initial signs of sea breeze development begin at 10:00 UTC. Onshore flow first develops in southern Holland extending approximately 10km offshore and a maximum of 5km onshore. A calm zone extending a further 20km, marking the boundary between the sea breeze and the offshore surface wind develops coincidently with the sea breeze. Travelling northward, a more rapid advancement onshore occurs, as the concave shape of the Dutch coastline allows the sea breeze to progressively benefit from an increasing onshore component as the orientation of the coastline changes. Further sea breezes also begin to develop off the coasts of Markermeer, Ijsselmeer and the Wadden sea.

By 12:00 UTC the sea breeze extends the length of the western coast of the Netherlands, reaching approximately 10km onshore and 15km offshore (Fig. 4.2). The onshore advancement is now more uniform along the western Dutch coast since by 12:00 UTC, the gradient wind has rotated so that the orientation relative to the western Dutch coast is now in the offshore direction. This allows the sea breeze forming off South Holland to take on *pure* sea breeze characteristics before the north. Furthermore, the sea breezes forming off Markermeer and Ijsselmeer advanced approximately 5km further onshore than the North Sea sea breeze on the opposing coastline. As the angle of the coast is oriented at an angle to the south easterly gradient wind, the sea breeze forming on the western coasts of Markermeer and Ijsselmeer is of *corkscrew* type. Notably, offshore to these coastlines there is a region of increased 10m wind speed, the most intense and largest of these spanning northern Ijsselmeer.

By 16:00 UTC, the sea breezes forming off the North sea, Markermeer and Ijsselmeer have collided (Fig. 4.3). The convergence line associated with the collision generates convection which is notably stronger than the convection purely formed by land surface heating. The stronger convection is sufficient to trigger rainfall in Northern Holland (Fig. 4.3b).

As the sea breeze advances, it does not do so at a linear rate. Instead, local regions advance more than others, giving the sea breeze a wave-like structure in which the areas

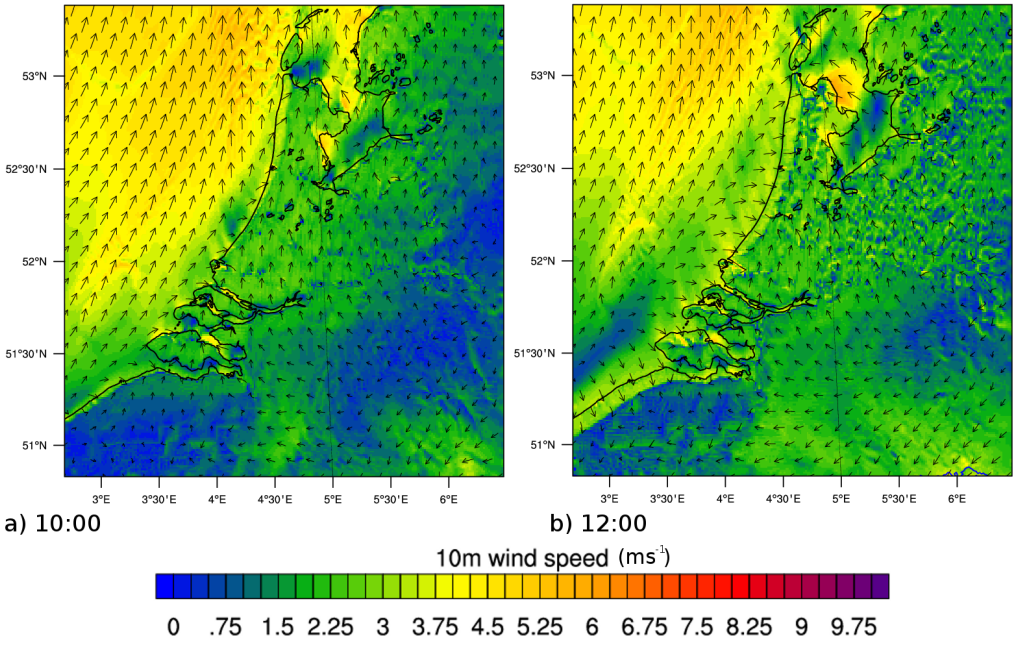

Figure 4.2: 10m vector wind speed (ms^{-1}) and direction at a) 10:00 UTC and b) 12:00 UTC of the baseline simulation on the 19^{th} June 2012.

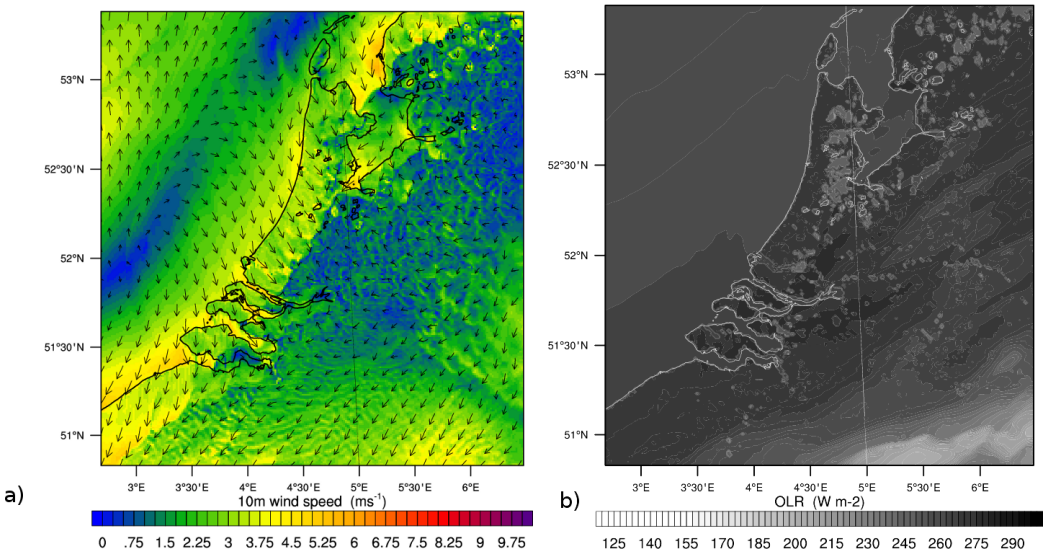

Figure 4.3: a) 10m vector wind speed (ms^{-1}) and direction at 16:00 UTC for the baseline simulation on the 19th June 2012. b) As *a* but for outgoing long-wave radiation.

which have extended the least onshore are associated with the higher 10m wind speeds. These features are similar to the lobes and clefts first described by Simpson *et al.* (1977) which are caused by the overrunning of the sea breeze air at height over the surface flow. However, Simpson *et al.* (1977) remarks that the spatial scale of these features are on the order of 1km; an order of magnitude smaller than the features simulated here. The thickness of the onshore flow is approximately 350m, with a return flow approximately

700m deep (Fig. 4.4). The offshore extent of the sea breeze continues to expand at a greater rate than in the onshore direction reaching a maximum distance of approximately 80km. Ahead of the sea breeze offshore advancement, the calm zone continues to travel seawards but does not expand to a greater spatial width of approximately 60km.

Despite evidence for the sea breeze front advancing approximately 100km inland by 20:00 UTC, the offshore structure of the sea breeze has broken down by 18:00 UTC. This is an indication that the collapse of the sea breeze circulation occurs prior to 20:00 UTC and the front continues to both advance inland and decay over time as an undular bore. Typically, this behaviour is associated with the *late mature* stage of sea breeze development (Miller *et al.*, 2003).

It is interesting to note that despite the increased complexity of both the coastline and the addition of a second dimension to the simulations in Chapter 3, the influence of the sea breeze still extends over 200km. The offshore advancement rate of this particular case study is faster than that of the land although the offshore structure is quicker to break down. As with the idealized simulations, however, there is likely a wide variation of simulation results with a different choice of PBL scheme and so the magnitude of these differences is now explored and verified against observations.

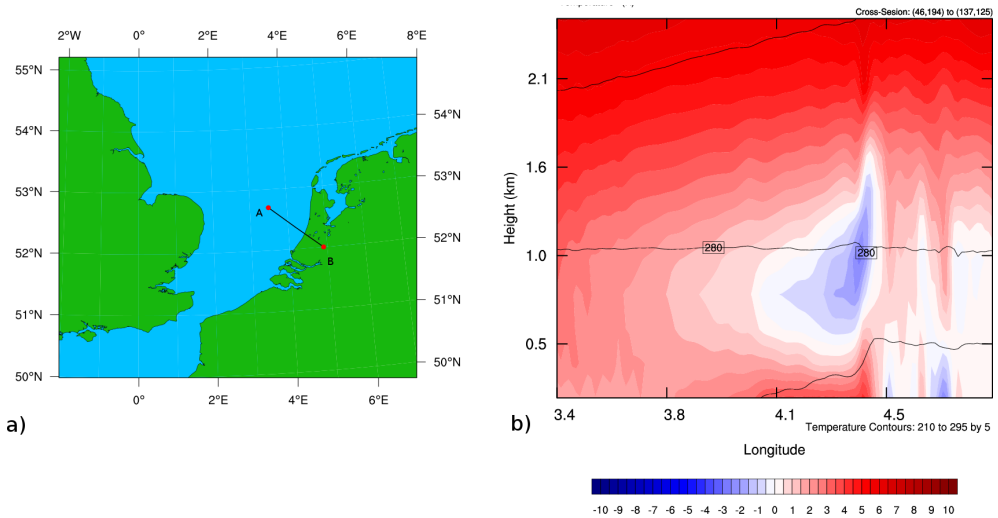

Figure 4.4: Location (a) and a cross-section (b) of onshore wind speed (filled contours) in ms^{-1} and temperature (solid lines) in K for the baseline simulation of the sea breeze occurring on the 19^{th} June 2012 at 12:00 UTC.

Table 4.1: Sea breeze statistics for WRF model simulations with different PBL physics options for the 19th June 2012.

Variable	YSU	MYJ	MYNN
Frontal speed (ms^{-1})	2.2	2.3	2.2
internal speed (ms^{-1})	3.5	5.0	5.0
onshore extent (km)	70	100	80
offshore extent (km)	80	70	60
duration (hrs)	9	12	10

4.1.2 Spatial differences between PBL schemes

As with the idealized simulations, there are several fundamental differences between simulations when different PBL options are used. The MYJ scheme, produces a circulation which is approximately $1.5ms^{-1}$ stronger, lasts 2 hours longer and advances 30km further inland than the baseline simulation involving the YSU scheme (Table 4.1). The differences between the YSU and MYNN PBL schemes are less well defined with the exception of the onshore flow strength of the sea breeze, shown in Table 4.1. The internal speed of the sea breeze is approximately equal between the two TKE schemes.

The maximum offshore extents for both the MYJ and MYNN are comparable to the YSU simulation, however, the scale of the sea breeze is more difficult to define. As with Chapter 3, the method adopted here is that of Arritt (1989), where an onshore flow of at least $1ms^{-1}$ defines the offshore sea breeze boundary. By 18:00 UTC in the YSU simulation, the 10m wind speed is northerly, coinciding with a breakdown of the land-sea thermal contrast, severing the supply of marine air to the sea breeze front. In all simulations, the maximum offshore extent is taken where the onshore feeder flow is cut off.

Both the offshore extent of the sea breeze and 10m wind speed within the onshore feeder flow are higher for the YSU scheme than for all other schemes in agreement with the results of Challa *et al.* (2009) and in support of the idealized simulations. The 10m wind speeds are more comparable when the YSU simulation is compared to the MYNN, though the calm zone is not as extensive in the YSU simulation.

The 10m wind speed of the sea breeze onshore is relatively uniform for both the TKE PBL schemes, producing speeds of between $4ms^{-1}$ and $5ms^{-1}$ (Fig. 4.5). In comparison, there are no banded structures with relatively higher wind speeds evident as with the YSU

PBL. The relative depths of each sea breeze are also comparable with the YSU scheme, however, the return flow is not as strong with the two TKE schemes as with the YSU PBL by approximately 1ms^{-1}.

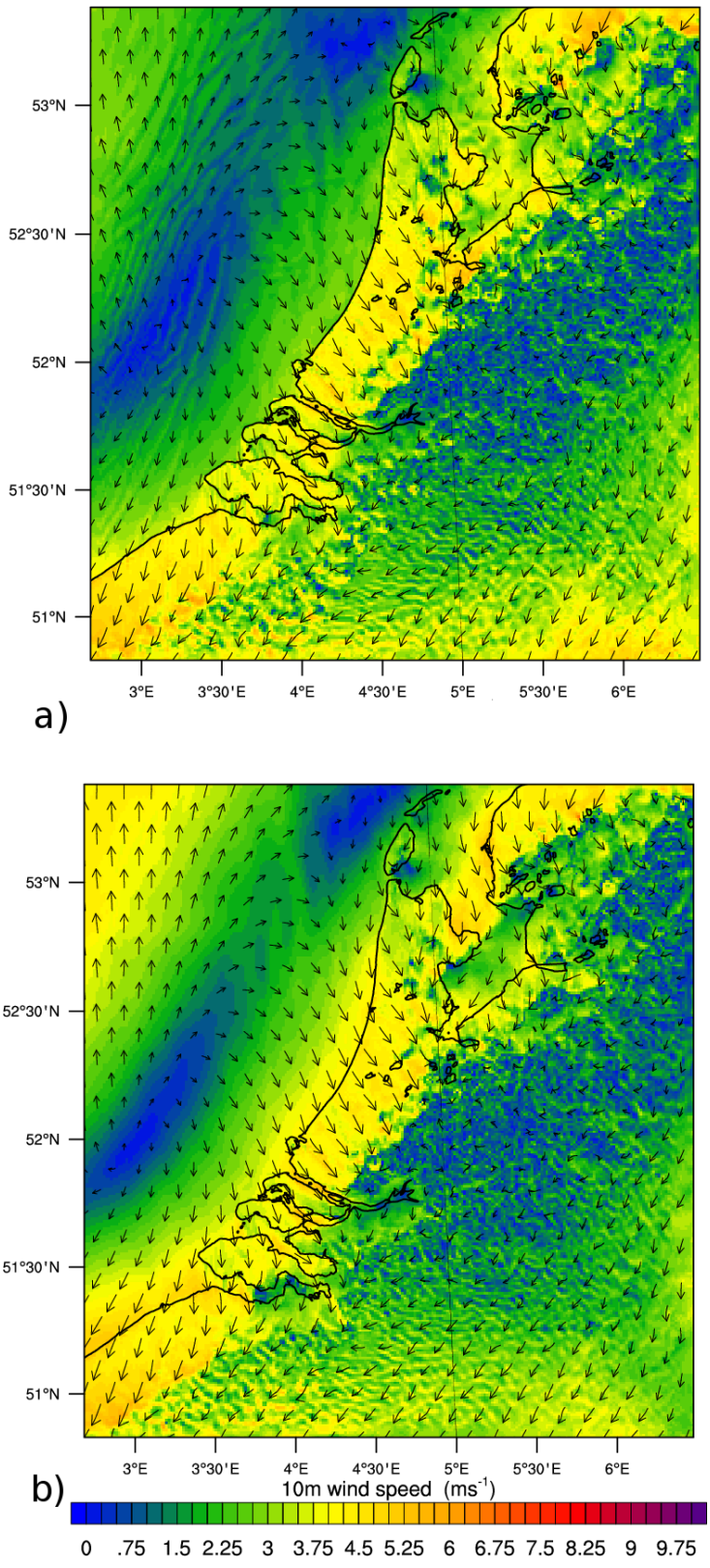

Figure 4.5: a) 10m vector wind speed (ms^{-1}) and direction at 16:00 UTC with the sea level isobars shown in blue on the 19th June 2012 for the baseline simulation of the MYJ PBL scheme. b) As *a* but for the MYNN PBL scheme.

Apart from differences within the PBL schemes themselves, the fundamental triggers for generating sea breezes are the strength of the land-sea thermal contrast and the gradient wind speed. Comparing the 925hPa height wind speed and direction for each of the PBL schemes, it is notable that by 12:00 UTC, the gradient wind is both stronger and orientated with a stronger shore parallel component indicative of a *backdoor* type sea breeze for the two TKE schemes (Fig. 4.6). The longer duration of the *backdoor* type gradient winds in the two TKE schemes partially explains the discrepancy between the sea breeze onset times.

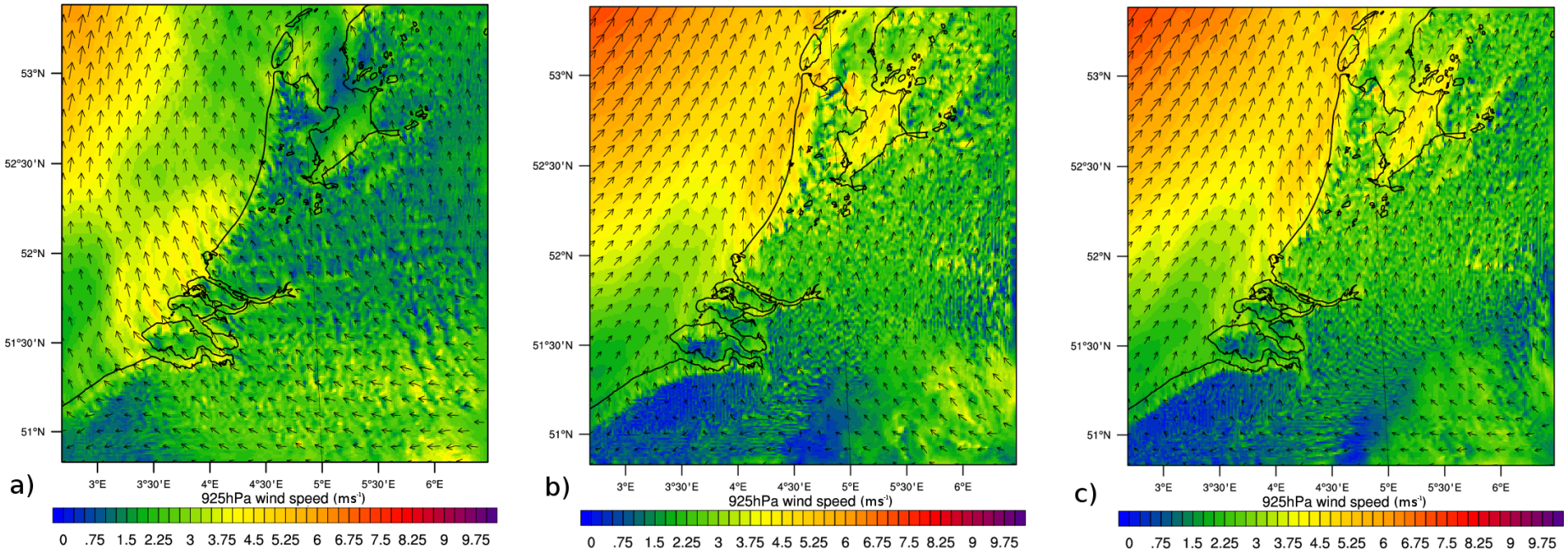

Figure 4.6: a) 925hPa vector wind (ms^{-1}) speed and direction at 12:00 UTC on the 19th June 2012 for the baseline simulation of the YSU PBL scheme. b) and c) As *a* but for the MYJ and MYNN PBL schemes respectively.

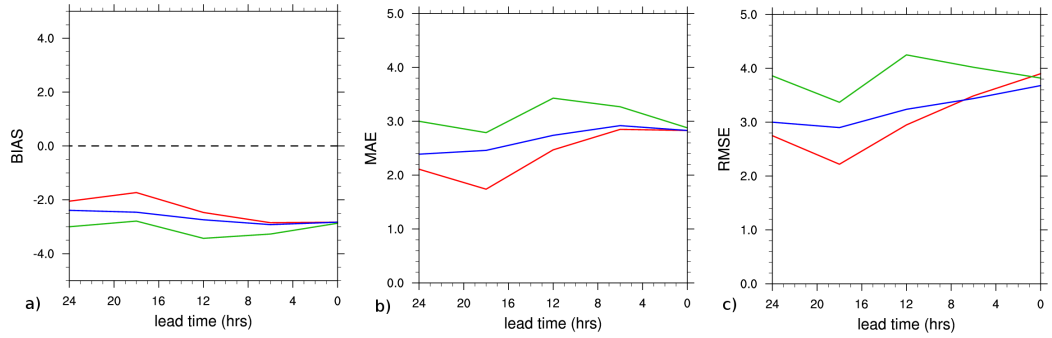

Figure 4.7: 2m temperature (K) error statistics averaged over the Dutch surface network for increasing lead time before 2012-06-19 00:00 UTC. The station locations are verified against the nearest land coordinate of the WRF domain. The red, blue and green lines represent the YSU, MYJ and MYNN PBL schemes respectively for a) BIAS, b) MAE and c) RMSE

There are also differences between the 2m temperature fields, especially in the convergence zones at the sea breeze front, and where the convergence occurs with the sea breezes from Markermeer and Ijsselmeer. Temperature contrasts within the convective regions can be as high as $\pm$3K (Fig. A.3).

4.1.2.1 Verification of the short range simulations

The error statistics for 2m temperature, averaged over all stations, using each PBL scheme under increasing lead time are shown in Fig. 4.8. According to the statistics, the amount of lead time which produces the least error for temperature across all schemes is 18 hours. In most cases, the YSU produces the most accurate simulation overall, although with decreasing lead time, the range of errors across each scheme is reduced to the extent that once the time for the baseline simulation is reached, there is very little difference between the PBL schemes. The only statistical measure where the YSU PBL scheme performs worse than the TKE is the RMSE, between the baseline and a lead time of 6 hours. This implies that, although the magnitude of the overall error using the YSU scheme is less than for the other schemes, the errors are less consistent across the surface station network.

All PBL schemes overall underestimate 2m temperature. Further examination of the station averaged diurnal cycle reveals that the majority of the temperature BIAS occurs during the nocturnal hours (Fig. 4.8). The maximum temperature is, however, simulated well by all schemes. Also, apparent during the nocturnal hours, the two TKE schemes perform significantly worse than the YSU. Hong and Kim (2008) modified the YSU scheme for stable boundary layers in the present model by increasing the value of the critical

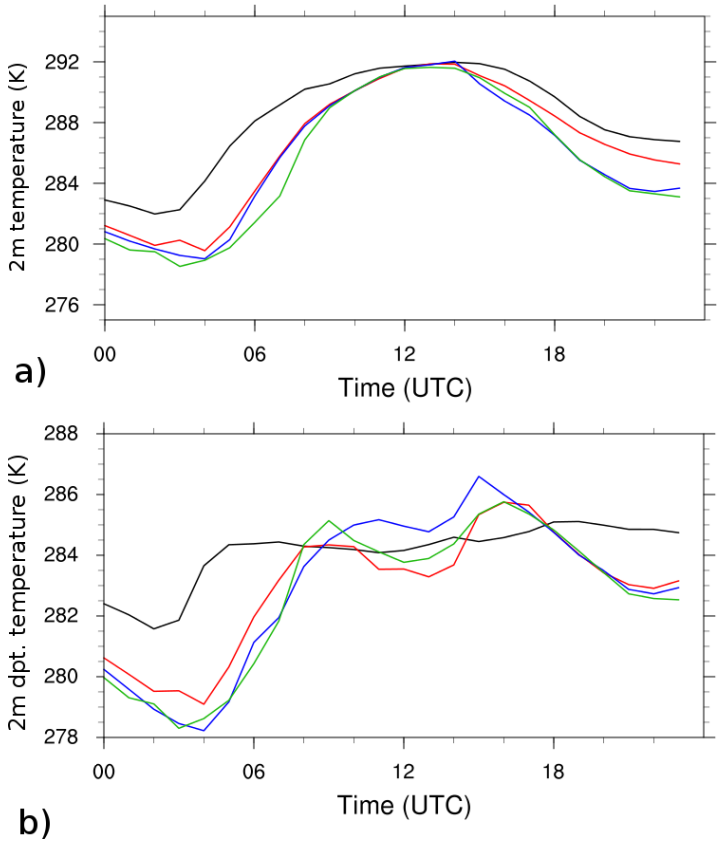

Figure 4.8: Station averaged a) 2m temperature (K) and b) 2m dew point temperature (K) time series for observations (black) and each of the three PBL schemes. Each simulation has a lead time of 18 hours and the YSU, MYJ and MYNN PBL schemes are represented by the red, blue and green lines respectively.

Richardson number from 0 to 0.25, thus increasing the degree of vertical mixing within the nocturnal boundary layer. It is plausible that the alteration of the Richardson number is the cause of this improvement, though further analysis of the nocturnal boundary layer is beyond the scope of this work.

In contrast to 2m temperature, the YSU PBL simulates 10m wind speed the least accurately of the PBL schemes tested (Fig. 4.9). The most accurate in this case study is the MYNN scheme. As with 2m temperature, however, the range of model error associated with the baseline simulations is the smallest when compared to the simulations with increasing lead time. Again in contrast to 2m temperature, each baseline simulation is also the most accurate in terms of MAE and RMSE across each station.

In terms of model BIAS, each scheme overestimates wind speed for all lead times and for each of the baseline simulations. The BIAS is particularly low between 6 and 12 hours of lead time. Much of the positive model BIAS comes from the nocturnal hours and late evening (Fig. 4.10). Between 09:00 UTC and 14:00 UTC all schemes underestimate

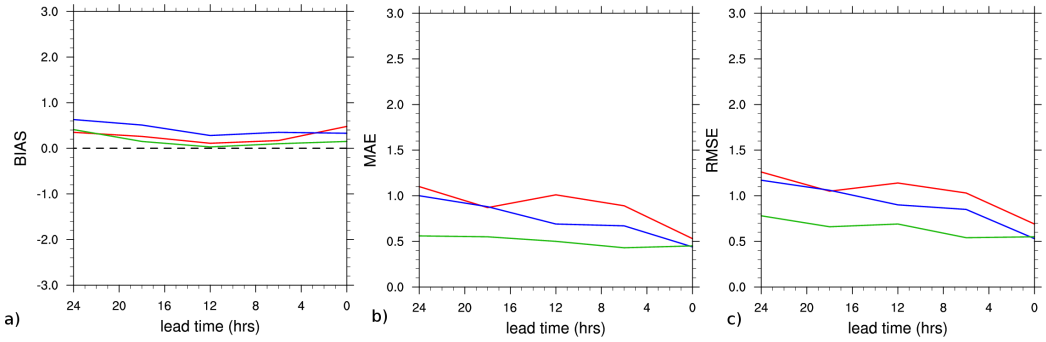

Figure 4.9: 10m wind speed error statistics averaged over 30 Dutch surface stations for increasing lead time before 2012-06-19 00:00 UTC. The red, blue and green lines represent the YSU, MYJ and MYNN PBL schemes respectively for a) BIAS, b) MAE and c) RMSE

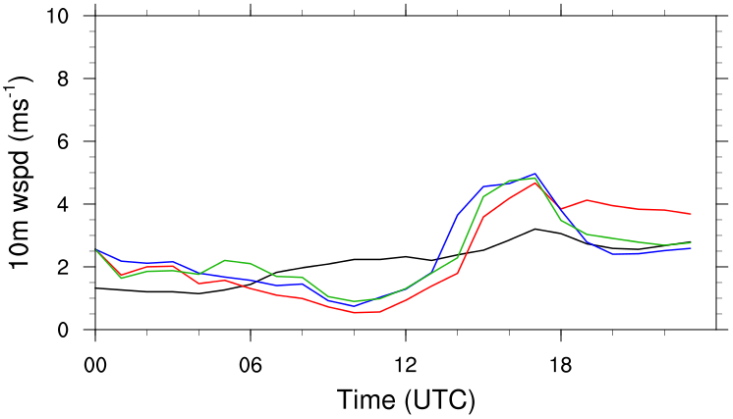

Figure 4.10: Station averaged 10m wind speed (ms^{-1} for the 19th June 2012. Observations are shown in black. Baseline simulations using the YSU, MYJ and MYNN PBL schemes are shown in red, blue and green respectively

the 10m model wind speed and considering that the majority of the stations are within 50km of a coastline, this implies that the strength of the sea breeze is underestimated in the model. Furthermore, after 14:00 UTC there is a notable sharp increase in 10m wind speed that is not as apparent in the observations, to the extent that between 14:00 UTC and 18:00 UTC, there is a positive 10m wind speed BIAS of approximately $2ms^{-1}$. The positive BIAS remains for the YSU and MYNN PBL schemes for the remainder of the simulation. The MYJ PBL, however, is much improved over this period of time.

Fig. 4.11 shows the effect of changing horizontal resolution on the error in 10m wind speed. Errors associated with a horizontal resolution of 27km are the largest in terms of BIAS, RMSE and MAE with magnitudes over $2ms^{-1}$ for each case. All horizontal resolutions tested for each PBL scheme have a positive BIAS for 10m wind speed. For horizontal resolutions of 9km and finer, the magnitude of the 10m wind speed BIAS does not vary significantly from between 0.1-0.2ms^{-1}. The largest improvement in terms of

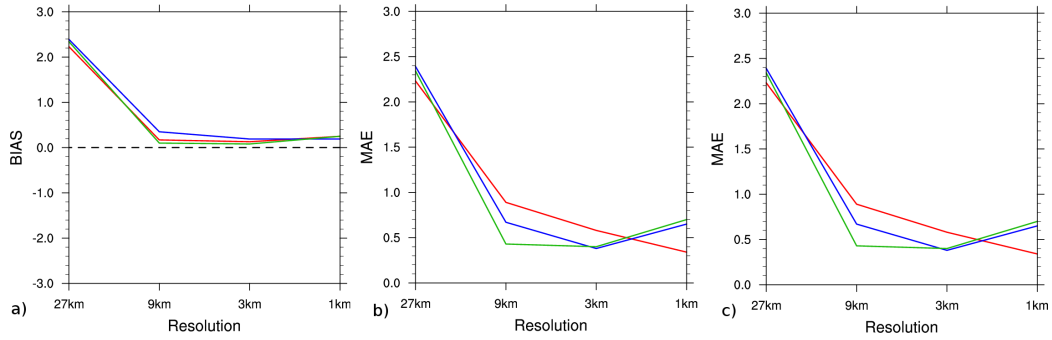

Figure 4.11: 10m wind speed error statistics (ms^{-1}) for changing horizontal resolution. Red indicates simulations using the YSU PBL scheme. Blue and green lines indicate simulations where the MYJ and MYNN PBL schemes are used. From a) to c) the statistical tests are BIAS error, MAE and RMSE.

the magnitude of both the RMSE and the MAE occurs between 27km and 9km horizontal resolution, however, it is between these resolutions that the similarity between PBL schemes ends. The YSU PBL shows a gradual improvement for all resolutions between 9km and 1km. Both the TKE schemes, however, show a deterioration between 3km and 1km, and very little change in skill between 9km and 3km.

Examining the spatial differences between 27km and 1km horizontal resolutions, it is noticeable that 27km resolution is insufficient to simulate either the sea breeze or the associated calm zones (Fig. 4.12). The sea breeze is however formed at 9km resolution and so differences between these horizontal resolutions are more based on resolved structures both in and out of the sea breeze. Furthermore, in terms of calculating the contribution of the sea breeze to wind energy, simply calculating the differences from the 27km and the 1km could be used, although differences would also result because of improved resolution at the coast and not just the sea breeze itself. Nevertheless, the difference between coarse and fine resolutions could make a first approximation and further analysis of this technique is presented in Chapter 6.

Similar to 2m temperature, 2m dew point temperature is underestimated for all simulations. Conversely, the PBL scheme with the weakest negative BIAS is the MYJ (Fig. 4.13. In terms of MAE and RMSE, the YSU is again most accurate for a lead time of 18hrs, however for all other times the MYJ scheme produces the least error. Of all the sensitivity tests, the YSU PBL with 18 hours of lead time produces the most accurate 2m dew point temperature when compared to the Dutch surface meteorological network with a BIAS error of 0.26K, a MAE of 0.87K and a RMSE of 1.05K.

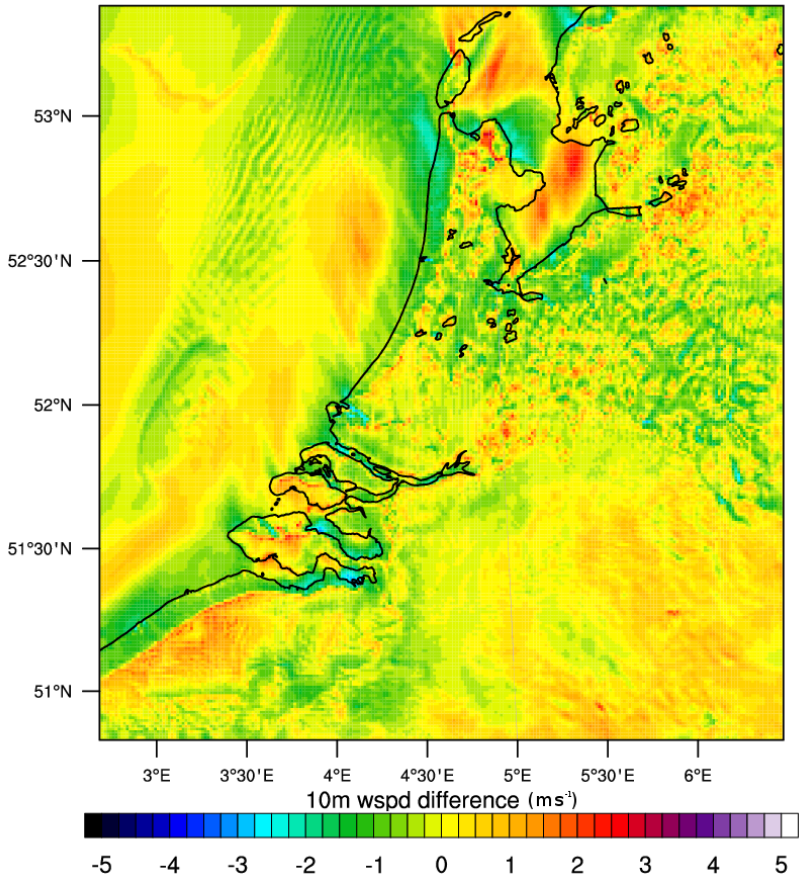

Figure 4.12: Difference between the 27km simulation and 1km baseline simulation 10m wind speed using the YSU PBL at 12:00 UTC. The 27km data were first interpolated onto the 1km grid so that the 1km data could be subtracted.

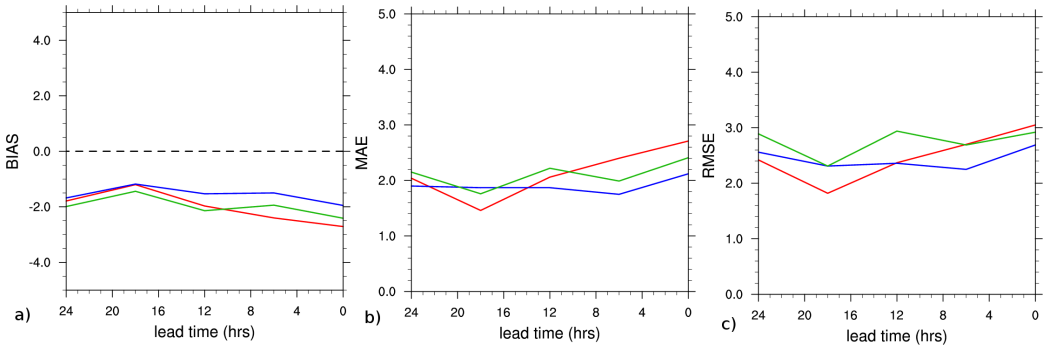

Figure 4.13: 2m dew point temperature (K) error statistics averaged over 30 Dutch surface stations for increasing lead time before 2012-06-19 00:00 UTC. The red, blue and green lines represent the YSU, MYJ and MYNN PBL schemes respectively for a) BIAS, b) MAE and c) RMSE

Again similar to 2m temperature, the first and last 6 hours of the simulation day are not simulated well in the model, with all PBL schemes underestimating 2m dew point temperature (Fig. 4.8). During the remaining hours however, it is noticeable that the MYJ PBL scheme overestimates 2m dew point temperature by approximately 1-1.5K. The other two schemes remain within $\pm$1K during this period.

The vast majority of the surface stations are located within a region which is affected by a sea breeze either formed off the North Sea coast or from Markermeer, IJesselmeer, the Wadden Sea or smaller inland lakes. Indeed, for the cross-section in Fig. 4.4, before the arrival of the North Sea sea breeze, a much weaker circulation establishes forming off one of the largest of the small inland lakes. The stations of Valkenburg, Cabauw and Herwijnen are in ideally positioned to examine the progress of the sea breeze as it penetrates inland.

The sea breeze first establishes in the observations at Valkenburg at 10:00 UTC, as depicted by the rapid change in wind direction in Fig. 4.14. Both the two TKE schemes form the sea breeze too early. In the case of the MYNN scheme, the onset of the sea breeze is at 09:00 UTC. The MYJ PBL simulates sea breeze onset at 08:00 UTC. This earlier onset is caused by the land surface warming at a faster rate than the other PBL schemes. However, there is still a cold temperature bias even with the MYJ PBL. Also apparent at Valkenburg, is a discrepancy in wind direction between the model and the observations after 17:00 UTC. The observations show a marked shift in wind direction to north easterly, whereas the simulations all maintain a north westerly component; an indication that the sea breeze is advancing too late in the evening in the model simulations.

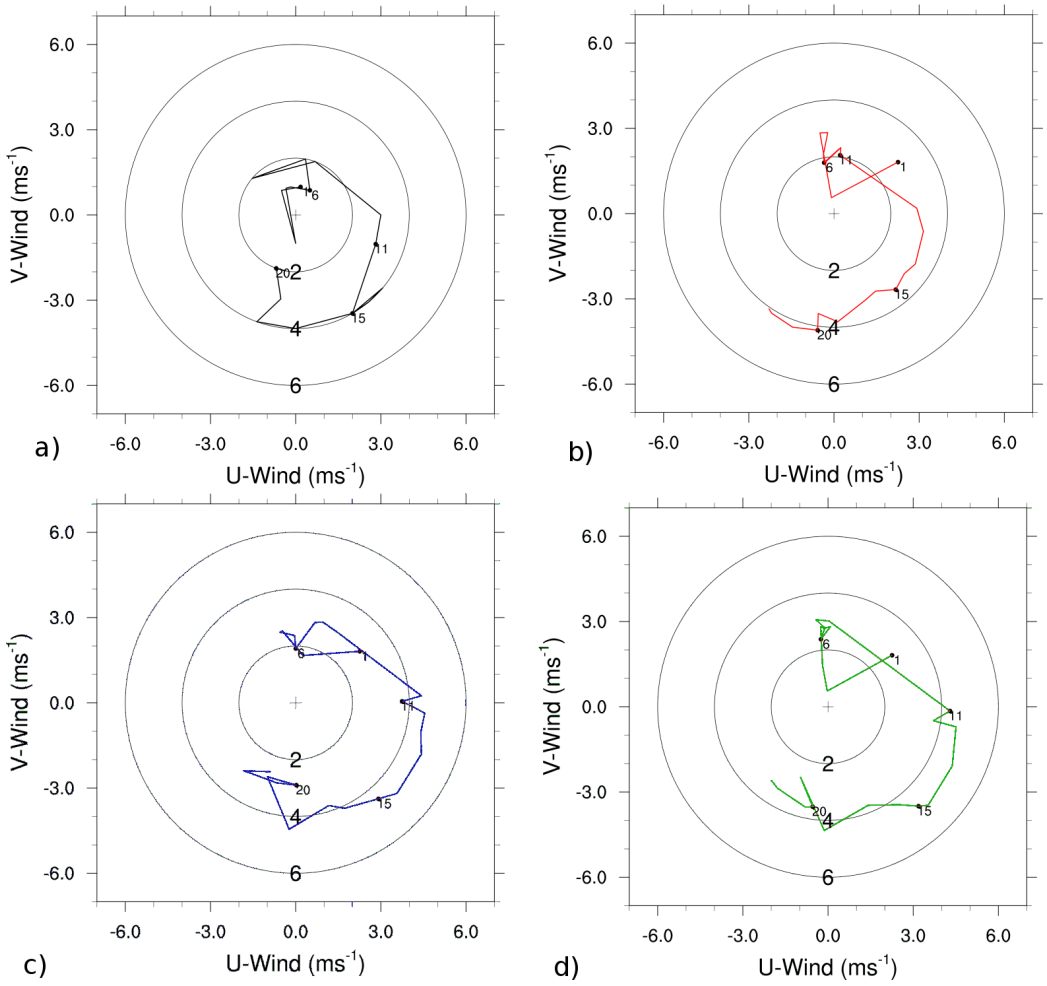

Figure 4.14: Hodographs for baseline 10m wind speed at Valkenburg (coastal). Observations are shown in a), the YSU, MYJ and MYNN PBL simulation results at Valkenburg are shown in b-d).

The sea breeze travels 50km inland to Cabauw by 17:00 UTC, travelling at an average speed of 2ms^{-1}. Shown in Fig. 4.15 are the profiles of temperature, wind speed and specific humidity for each of the PBL sensitivity simulations compared with those observed at the Cabauw tower. The strong early temperature bias is evident in the Cabauw observations, however, it is substantially reduced by 19:00 UTC, when the sea breeze in each simulation has reached the Cabauw tower. The YSU PBL matches the most closely to observations for temperature, although it is still 1K too cold throughout the profile.

It is also apparent from Fig. 4.15 that the wind speed profile is too weak before the onset of the sea breeze. The profiles are also more unstable than the observations, implying that either the surface roughness is too high or too rigorous convection is occurring in the model. The baseline simulation, however, does compare well with the vertical profile measurements at De Bilt, revealing a comparable degree of surface CAPE of 83J and 93J between observations and baseline simulation results respectively (Fig. A.4). Although a single point observation is insufficient to disprove the notion that profile instability is thermally driven, rather than mechanically, the combination of an underestimation of 2m temperature and a poorer model performance during nocturnal hours, where there is an absence of thermal forcing, supports the argument.

By 19:00 UTC, the sea breeze has travelled a further 25km inland and reached Herwijnen station, travelling at an estimated speed of 3.47ms^{-1}. This evening acceleration is associated with the decay of the Kelvin Helmholtz Billows and therefore reduced drag (Miller *et al.*, 2003). The YSU simulation, notably does not reach as far inland as Herwijnen. The other two TKE schemes, however surpass Herwijnen station at 19:00 and 20:00 UTC for the MYJ and the MYNN PBL schemes respectively, although in each case the front is difficult to distinguish.

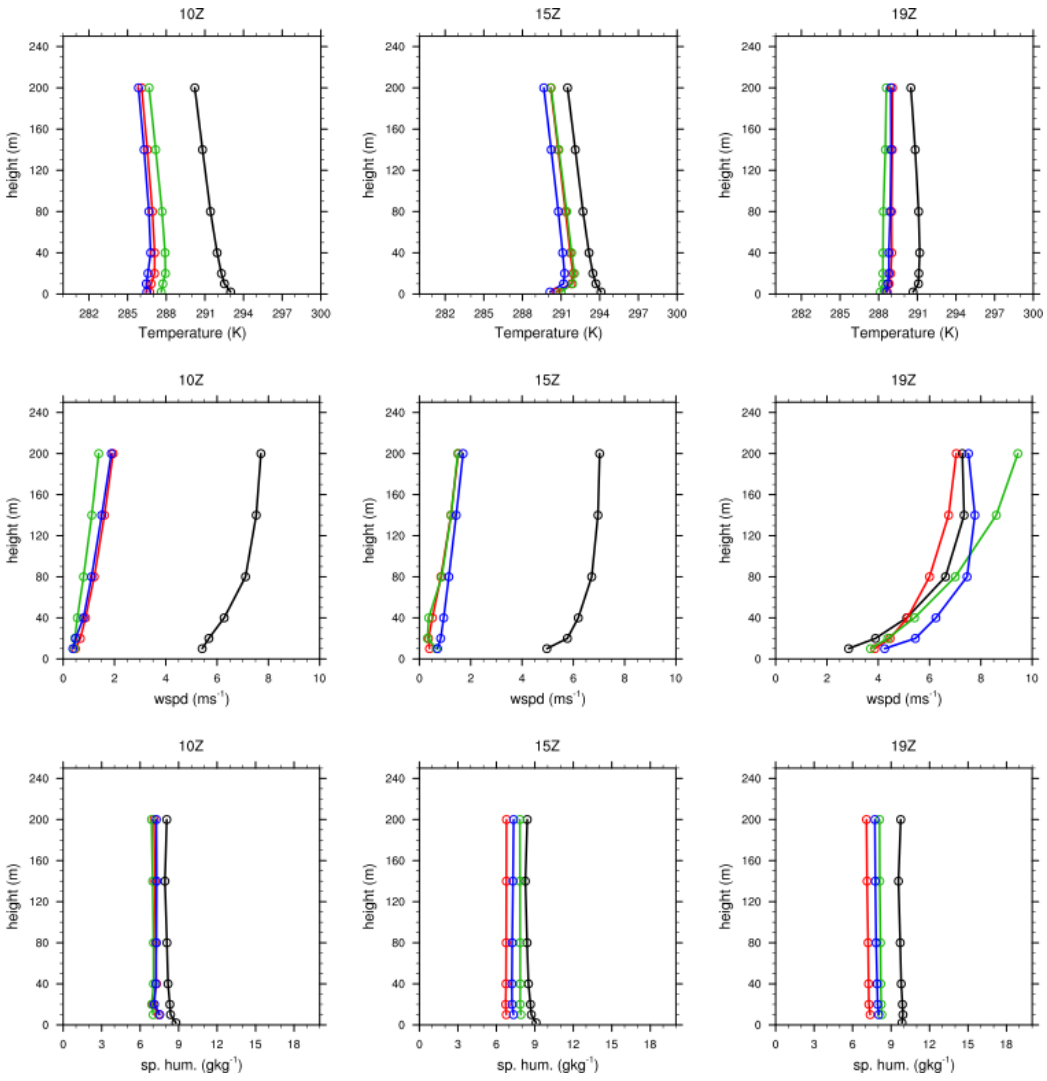

Figure 4.15: Vertical profiles of temperature wind speed and specific humidity at 10:00 UTC, 15:00 UTC and 19:00 UTC on the 19th June 2012 for the baseline simulation of YSU (red), MYJ (blue) and MYNN (green) PBL schemes. Observations are shown in black.

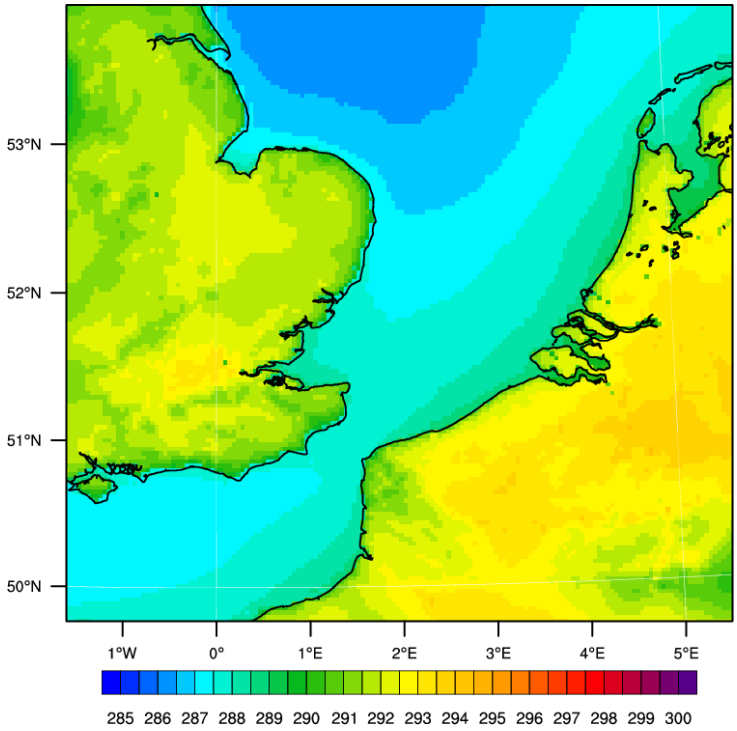

Figure 4.16: 12:00 UTC composite plot of 2m temperature (K) for the period May - September 2006 using the YSU PBL scheme.

The summary of this section can be divided into two parts; the general performance of each PBL scheme and the performance of the PBL schemes in simulating the sea breeze characteristics. The maximum 2m temperature is predicted well for all schemes, but in general the YSU PBL produces the best overall statistical scores at 18 hour lead time. Because of the underestimation of the 2m temperature, a sufficient land-sea thermal contrast to trigger sea breeze formation is reached later than in the observations. The sea breeze is also evident later in the model than in the observations and the YSU scheme does not advance the sea breeze a sufficient distance inland. Offshore, the performance of the model is more difficult to determine due to a lack of observations. The next section examines the performance of the WRF PBL schemes under longer time periods, specifically focussing on performance of the model in predicting parameters which are important for sea breeze development in both an onshore and offshore environment.

4.2 Extended simulations

4.2.1 Qualitative differences between simulations

As with the idealized simulations and single case study, there are significant differences between PBL schemes. Fig. 4.16 shows the composite simulated 2m temperature at 12:00 UTC over the period May to September 2006 using the YSU PBL. Clearly visible are the land-sea thermal contrast and the cooler coastal regions for both eastern England and mainland Europe. From north to south, the 2m temperature difference between the southern North Sea and the English Channel is approximately 2K, highlighting the coastlines which would be most susceptible to developing sea breezes.

Fig. 4.17 shows the differences between the PBL schemes in terms of 2m temperature at both 12:00 UTC. On average, the 12:00 UTC temperature is between 0.2-0.6K warmer using the YSU scheme, rather than the MYJ. However, the MYJ scheme produces warmer temperatures for urban areas, for low lying and for coastal regions than the YSU, especially for East Anglia, Lincolnshire and the south coast of England. This trend is much weaker for mainland Europe.

Offshore, there are notable biases in the YSU PBL towards warmer 2m temperatures in the Wash and the coast of North Norfolk, the Thames Estuary and to approximately 20km offshore from the coasts of the Netherlands, Belgium and France. The YSU is warmer for all sea locations but this is especially pronounced in these coastal regions, reaching warm biases of greater than 0.6K.

The composite 2m temperature differences between the YSU and the MYNN schemes are similar to between the YSU and the MYJ as overall the YSU scheme is warmer, with the exception of the urban areas and coastal regions. However, the pattern is much less pronounced and mainland Europe is approximately 0.6K warmer in the YSU scheme, reflecting a stronger temperature bias towards YSU than the MYJ PBL.

Furthermore, comparison with the two TKE schemes confirms that, for the most part, the MYJ scheme is on average warmer over the land surface than the MYNN, however, over sea the MYJ is 0.1-0.2K cooler than the MYNN. This is especially the case near to the coast, implying that, between the two TKE schemes, the MYJ PBL has on average the greater thermal contrast. It should be noted however, that Fig. 4.17 is a composite of all days and so has not been subjected to the sea breeze identification method. This

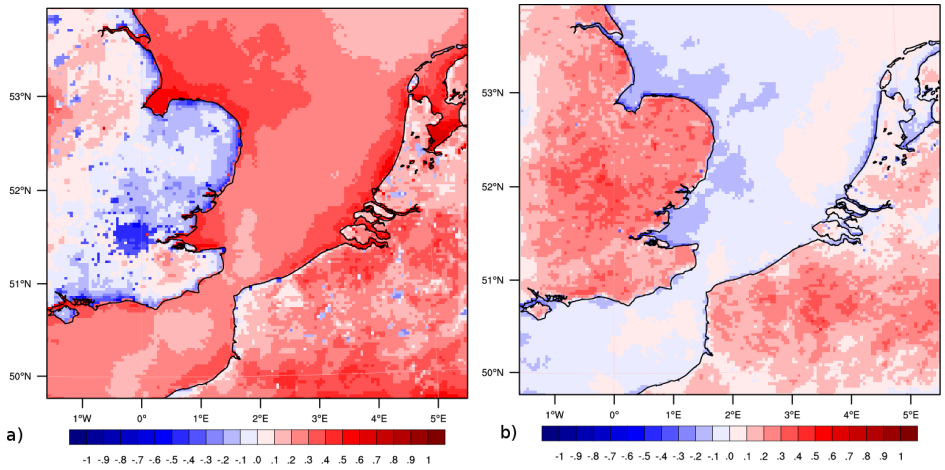

Figure 4.17: 12:00 UTC composite of the difference in 2m temperature (K) for the period May - September 2006 using the a) YSU - MYJ and b) YSU - MYNN PBL schemes.

implies that whilst identifying whether one PBL scheme produces a greater land-sea contrast can give an idea of the relative likelihood of sea breezes, the differences are not solely attributable to them.

The differences between different PBL schemes at 15:00 UTC reveal that the MYJ 2m dew point temperatures are approximately 1.5-2K higher when compared with the other schemes, both inland and over the sea (Figs. A.5b and A.5d). In comparison with the MYNN (Fig. A.5c), the YSU simulates higher dew points over the sea by approximately 1K. In contrast, over the land, the 2m dew points are approximately 1K higher.

At 00:00 UTC, the YSU PBL scheme is again warmer than the two TKE schemes. On average, the magnitude of the positive temperature bias for the YSU scheme is 1.6K over land and approximately 0.5K over the sea (Fig. 4.18). The bias is less positive in urban areas with an approximate magnitude of 0.5K. The two TKE schemes produce very similar 2m temperature though the MYJ does form average 2m temperatures that are approximately 0.5K warmer than the MYNN scheme over land. East Anglia and Lincolnshire are exceptions as the MYNN scheme is marginally ($<$1K) warmer.

4.2.2 Comparisons against mast data

To determine the performance of the PBL schemes it is not simply enough to compare against surface observations. In this section, the model results for the 2006 sea breeze season are compared with both the meteorological masts at Cabauw and at the Egmond aan Zee met mast. Standard prognostic variables are compared against model results for

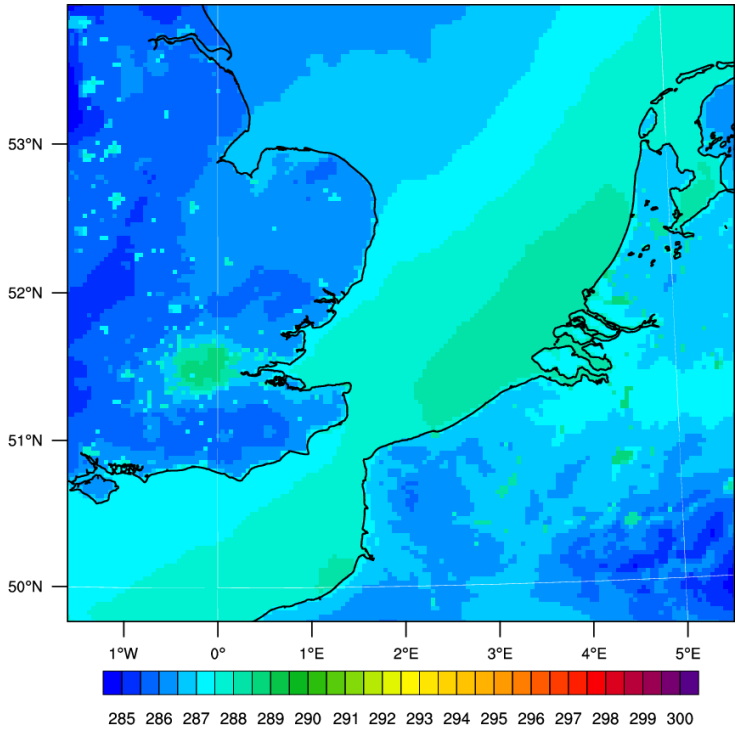

Figure 4.18: 00:00 UTC composite plot of 2m temperature (K) for the period May - September 2006 using the YSU PBL scheme.

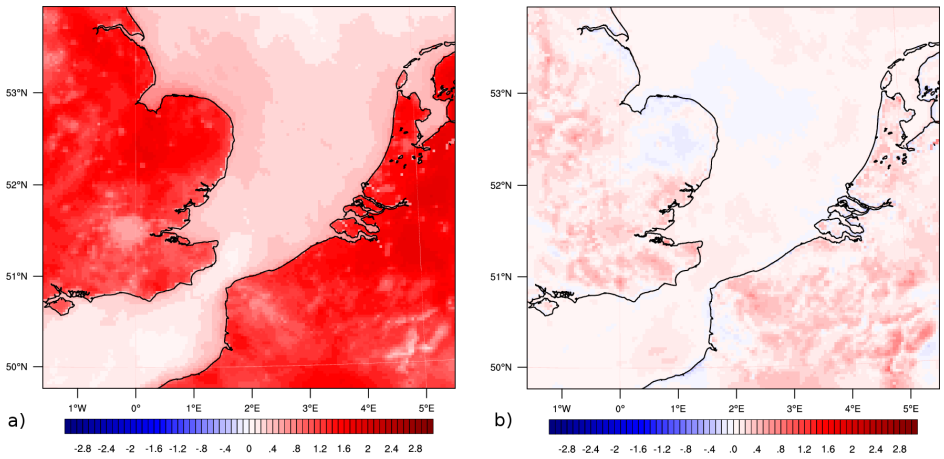

Figure 4.19: 00:00 UTC composite of the difference in 2m temperature (K) for the period May - September 2006 using the a) YSU - MYJ and b) YSU - MYNN PBL schemes.

both onshore and offshore sites before further examination takes place in order to diagnose reasons why there may be a discrepancy between boundary layer schemes.

4.2.2.1 Cabauw

Profiles for June 2006 and model verification statistics for the whole of the 2006 sea breeze season are shown in Fig. 4.21 and Tables 4.2-4.4. In all simulations, the WRF model underestimates temperature. Much of the negative temperature bias occurs during

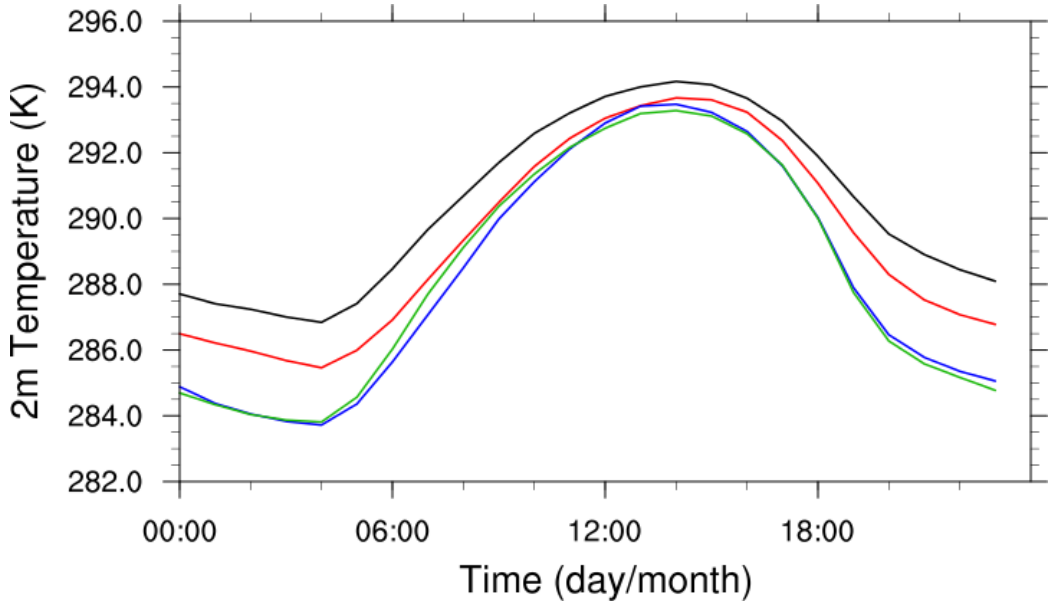

Figure 4.20: Average 2m temperature diurnal cycle for Cabauw during May to September 2006. The YSU, MYJ and MYNN PBL schemes for the nearest model grid point to the Cabauw tower are shown in red, blue and green respectively. Observations are shown in black.

the nocturnal hours though there is also a smaller negative temperature bias during the daylight hours (Fig. 4.20). The performance of the YSU PBL scheme is consistently better than the other PBL schemes for temperature for all other months in the verification period. This is especially notable at night in the lower 80m of the boundary layer. For stable boundary layers, the YSU PBL increases the critical Richardson number from 0 to 0.25, thus the degree of vertical mixing is increased within the boundary layer and so the surface is warmer (Hong and Kim, 2008),

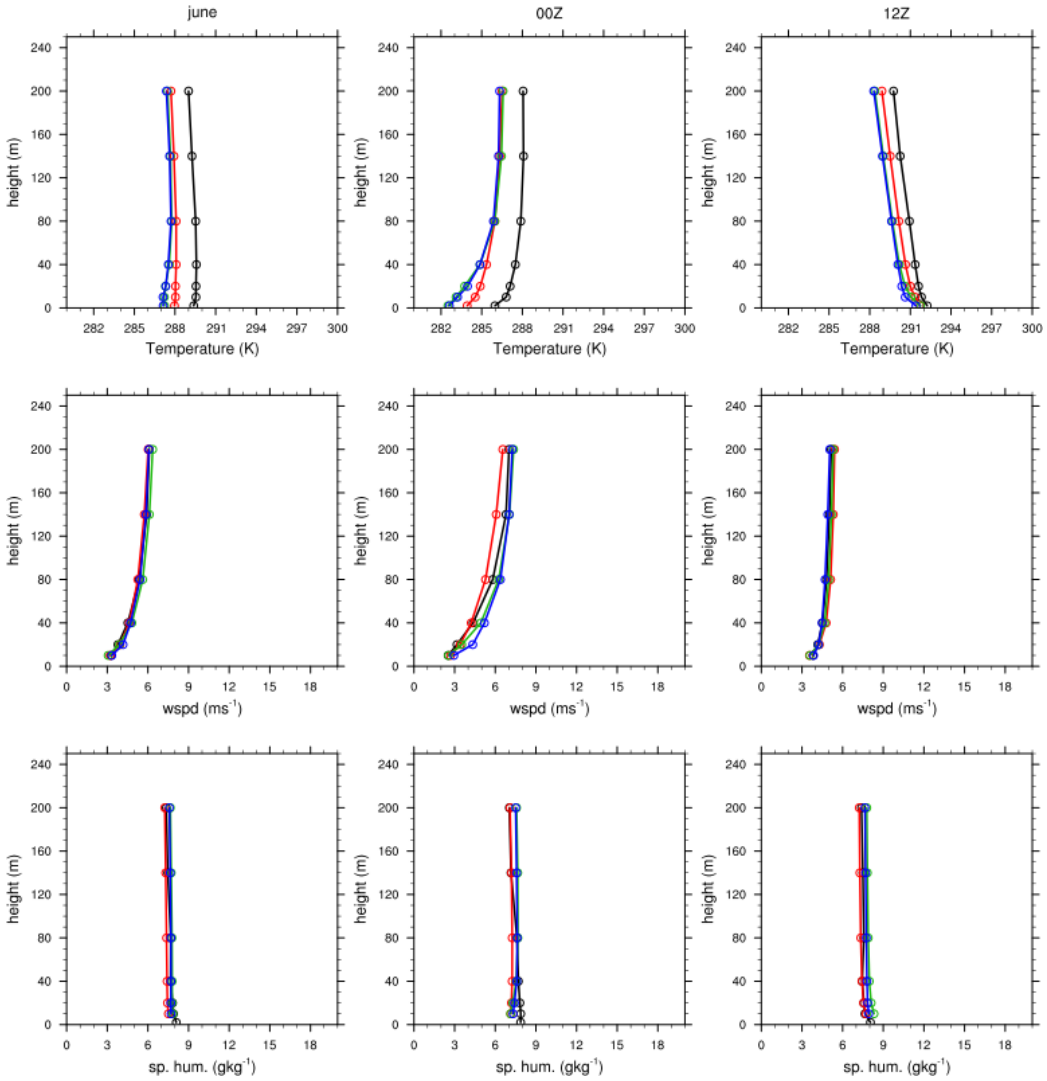

Figure 4.21: Vertical profiles of temperature, wind speed and specific humidity averaged for June 2006, at 00:00 UTC and at 12:00 UTC of YSU (red), MYJ (blue) and MYNN (green) PBL schemes for the nearest model grid point to the Cabauw tower. Observations are shown in black.

Table 4.2: Verification statistics for temperature measured at the Cabauw tower during May to September 2006.

Month	BIAS			MAE			RMSE		
	YSU	MYJ	MYNN	YSU	MYJ	MYNN	YSU	MYJ	MYNN
May	-0.98	-1.61	-1.39	1.31	1.77	1.55	1.72	2.32	2.01
June	-1.23	-1.64	-1.69	1.55	1.89	1.93	2.04	2.44	2.52
July	-1.78	-2.19	-2.15	2.10	2.41	2.39	2.66	3.00	2.95
August	-0.23	-0.95	-0.64	0.83	1.23	1.03	1.17	1.72	1.47
September	-1.23	2.37	-1.83	1.40	2.39	1.88	1.92	3.12	2.46

Table 4.3: Verification statistics for wind speed measured at the Cabauw tower during May to September 2006.

Month	BIAS			MAE			RMSE		
	YSU	MYJ	MYNN	YSU	MYJ	MYNN	YSU	MYJ	MYNN
May	0.30	0.14	0.25	1.31	1.22	1.24	1.92	1.76	1.80
June	-0.01	0.15	0.10	0.98	1.02	1.05	1.41	1.48	1.46
July	0.04	0.14	0.25	1.05	1.04	1.14	1.52	1.48	1.63
August	0.26	0.15	0.25	1.09	1.09	1.16	1.61	1.58	1.65
September	0.03	0.13	0.35	1.07	1.04	1.15	1.51	1.54	1.66

The vertical wind profiles, on average, match the observations at the Cabauw tower (Table 4.3; Fig. 4.21; Figs. A.7-A.10). The differences between boundary layer schemes is again most apparent during the nocturnal hours. The two TKE boundary layers produce a vertical profile that is too stable in comparison with the observations. The MYJ scheme here matches the observed wind profile on average better than the other schemes.

The BIAS in vertical specific humidity profile are less systematic and more varied between the PBL schemes for each month than for the other variables (Table 4.4). The YSU scheme, however, underestimates the specific humidity at all heights. During May, both the TKE schemes overestimate the specific humidity at all heights, however, during the remaining months, there is no coherent tendency for either of the PBL schemes to over or underestimate specific humidity. It is however apparent that the YSU scheme again performs better than with the other two schemes. The MYJ simulations, however, do not simulate specific humidity as well as the other variables.

In terms of use of the sea breeze selection method, the most important variables to consider are the maximum temperature and gradient wind strength. As stated in section 5.1, the gradient wind strength and direction is not significantly affected by changing the

Table 4.4: Verification statistics for specific humidity measured at the Cabauw tower during May to September 2006.

Month	BIAS			MAE			RMSE		
	YSU	MYJ	MYNN	YSU	MYJ	MYNN	YSU	MYJ	MYNN
May	-0.17	0.15	0.07	0.49	0.68	0.55	0.69	0.93	0.78
June	-0.23	0.10	0.02	0.68	0.80	0.71	0.94	1.16	1.04
July	-0.15	0.36	0.06	0.78	1.03	0.87	1.09	1.40	1.21
August	-0.19	-0.04	-0.06	0.53	0.61	0.54	0.73	0.86	0.76
September	-0.37	-0.18	-0.21	0.65	0.77	0.66	0.90	1.07	0.92

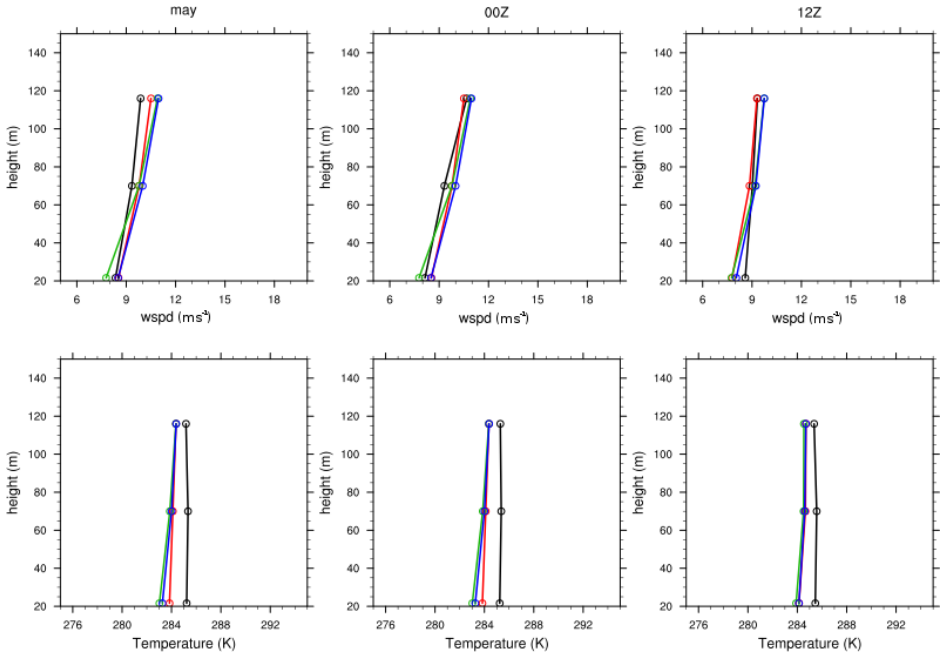

Figure 4.22: Composite vertical profiles for the Egmond aan Zee met mast during May 2006 for a) wind speed and b) temperature. The YSU, MYJ and MYNN PBL schemes are denoted by the red, blue and green lines respectively

PBL scheme. The maximum temperature however, is controlled by both the surface layer scheme and the PBL scheme which are both changed. In spite of the cold temperature bias overall, the maximum temperature is simulated well across each PBL scheme, however, the performance of the model is weaker during the extreme Summer months of June and July.

4.2.2.2 Egmond aan Zee met mast

Summary statistics for the Egmond aan Zee met mast are shown in Tables 4.6 and 4.5, and averaged vertical profiles for May 2006 are shown in Fig. 4.22. Additional profiles for the remaining months can be found in the supplementary material (Figs. A.11-A.14).

Table 4.5: Verification statistics for temperature measured at the Egmond aan Zee meteorological mast during May to September 2006.

Month	BIAS			MAE			RMSE		
	YSU	MYJ	MYNN	YSU	MYJ	MYNN	YSU	MYJ	MYNN
May	-1.03	-1.34	-1.21	1.36	1.56	1.47	1.83	2.03	2.02
June	-1.09	-1.30	-1.38	1.42	1.52	1.61	1.82	1.96	2.11
July	-1.59	-1.72	-1.68	1.95	2.03	2.02	2.52	2.54	2.55
August	0.39	-0.26	0.19	0.65	0.71	0.64	0.85	0.94	0.83
September	-0.83	-1.71	-1.13	1.14	1.84	1.34	1.43	2.31	1.66

Table 4.6: Verification statistics for wind speed measured at the Egmond aan Zee meteorological mast during May to September 2006.

Month	BIAS			MAE			RMSE		
	YSU	MYJ	MYNN	YSU	MYJ	MYNN	YSU	MYJ	MYNN
May	-0.01	0.02	0.09	1.54	1.62	1.46	2.14	2.28	2.06
June	-0.17	0.22	-0.09	1.41	1.60	1.57	1.93	2.14	2.16
July	-0.07	0.18	0.00	1.46	1.55	1.56	1.92	2.10	2.06
August	0.29	0.07	-0.03	1.25	1.35	1.27	1.69	1.90	1.80
September	-0.06	0.13	-0.02	1.23	1.34	1.27	1.70	1.88	1.78

As with the Cabauw tower, all PBL schemes underestimate temperature, although the magnitudes of the error are both smaller and less sensitive to the time of day. The YSU PBL scheme again produces the smallest temperature BIAS, although the differences between the schemes is not as large as on land. In terms of overall performance, in all months apart from August when the MYNN PBL produced marginally better statistics, the YSU PBL scheme again performed the best out of the PBL options tested.

In terms of the vertical temperature profile, unlike those simulated at the Cabauw tower, there is no apparent gain in accuracy with the YSU PBL in the lower part of the model profile during the nocturnal hours. Principally, this is due to the neutral stability of the air column associated with boundary layers over the oceans. The higher heat capacity of the water surface does not allow for much surface cooling during the night and so prevents the formation of a stable nocturnal boundary layer.

The averaged verification statistics for each month from May to September are shown in Table 4.6. As with the onshore results, there are no consistent tendencies to either under or over-estimate wind speed between PBL schemes, unlike the temperature BIAS

errors where each PBL scheme produces negative values. However, the MYJ PBL overestimates wind speed during all tested months. Also, unlike the comparisons with the Cabauw tower, for wind speed the MYJ PBL scheme does not perform as well offshore, as it does in the offshore environment in comparison with the other PBL schemes. Indeed, for MAE, the MYJ PBL achieves the poorest error statistics for all of the PBL schemes, for example, during May the MYJ scored an MAE of 1.22ms^{-1}, compared with 1.31ms^{-1} and 1.24ms^{-1} for the YSU and MYNN PBL schemes at the Cabauw tower which compares with 1.62ms^{-1}, 1.54ms^{-1} and 1.46ms^{1} for the respective schemes at the Egmond aan Zee met mast.

In terms of the wind speed vertical profile there are no consistent differences in model error in terms of time of day. The vertical wind shear across the meteorological mast is represented well, so the degree of model BIAS with height is largely consistent. There are however exceptions such as for example during May, where the YSU PBL scheme overestimates the 21m and 70m wind speed, yet underestimates the 116m. The magnitude of the BIAS however, associated with the YSU scheme is less than $\pm 0.5\text{ms}^{-1}$.

4.3 Heat, momentum and radiation fluxes at Cabauw

Differences between PBL schemes can arise because of the nature of the PBL schemes themselves, of the surface layer schemes which accompany the PBL physics options or because of alterations in incoming solar radiation brought about by differences in cloud cover. Fig. 4.23 shows the averaged 2m temperature and sensible heat flux for the entire land domain. Notably, the PBL scheme which produces the highest 2m temperature is the YSU, yet the land surface averaged sensible heat flux of the YSU scheme is the lowest when compared to all of the other schemes, suggesting that the higher temperature is not attributable to the magnitude of the heat flux alone.

In terms of accuracy, Fig. 4.24 shows that the model simulates the sensible and latent heat fluxes well at Cabauw averaged over May to September 2006. There is however a large overestimation of the maximum sensible heat flux, suggesting that in order to create the cold 2m temperature bias the profile must be too thermodynamically unstable so that there is a greater degree of vertical mixing during the daylight hours. The shape of the vertical profiles are similar to observations, so the temperature bias cannot be attributed

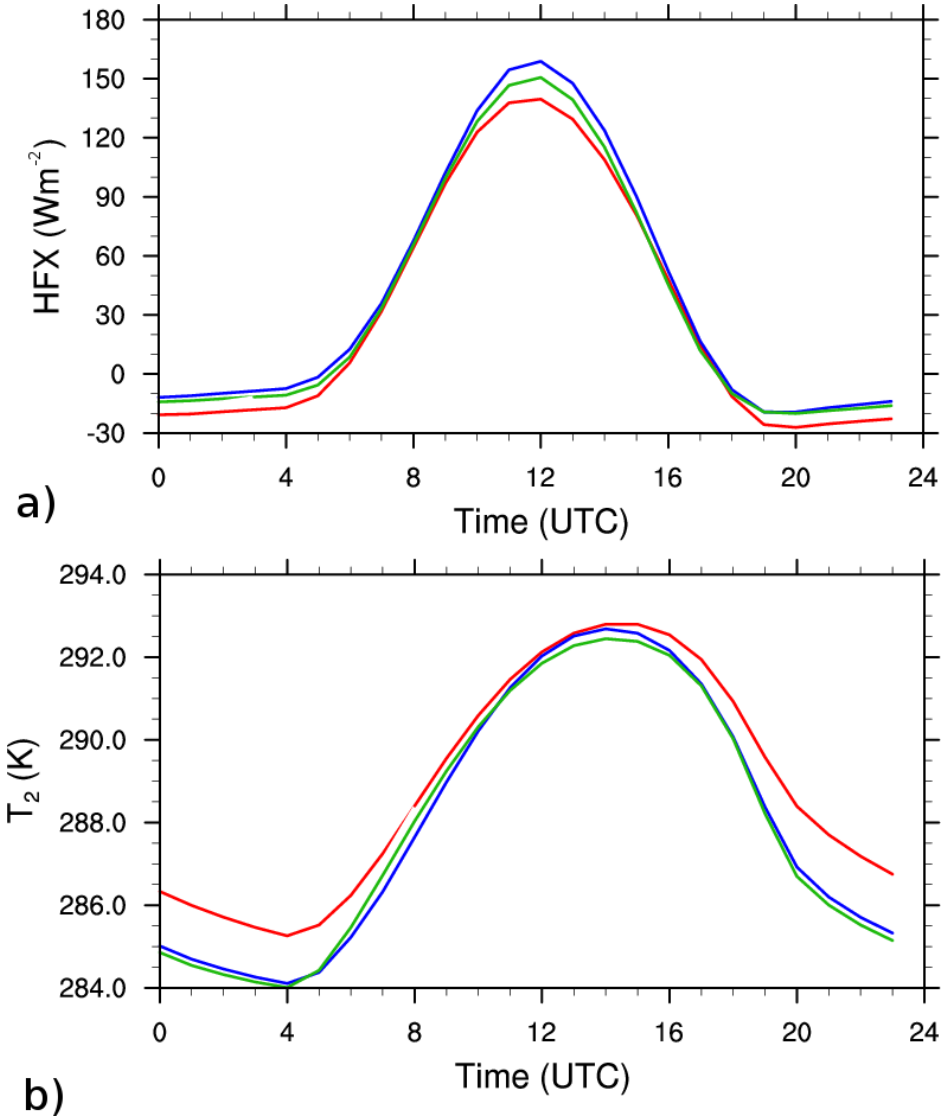

Figure 4.23: Composite time series for all land points during May to September for a) sensible heat flux (Wm^{-2}) and b) 2m temperature (K). The YSU, MYJ and MYNN PBL schemes are denoted by the red, blue and green lines respectively

to intense surface mixing. However, all PBL schemes overestimate the friction velocity during daytime hours. As the surface roughness is too high, the surface layer is more turbulent, thus accounting for the excess sensible heat flux.

The other possible cause for the underestimation of temperature which could not be accounted for by the PBL schemes themselves, is differences in cloud cover. Fig. 4.24 shows the differences in incoming solar radiation between the different PBL schemes. In general, the YSU PBL experiences less incoming solar radiation than the MYJ, by on average $100Wm^{-2}$. A notable exception is over the northern Dutch coast, stretching out to a distance of approximately 150km where there is a region in which the MYJ PBL

receives approximately 50Wm^{-2} less incoming solar radiation than the YSU PBL scheme (Fig. A.6). Between the YSU and the MYJ, there is notably more solar radiation over the sea than over the land for the YSU PBL. This is especially true in the region up to 150km offshore from the Dutch coast, where solar radiation intensity is 100Wm^{-2} greater for the YSU scheme.

Comparison with the incoming solar radiation at the Cabauw observation site, reveals that each PBL scheme significantly overestimates the maximum incoming solar radiation. This would imply that neither cloud cover nor surface heat fluxes are responsible for the majority of the negative temperature biases in the simulations. Instead, it is likely that entrainment within the top of the boundary layer is too high during daylight hours, causing a cooling of the temperature profile through increased vertical mixing from the top of the PBL. Estimates of PBL height can be obtained from the Wattisham wind profiller, however, the PBL height is determined differently for each scheme, and so the method would need to be standardized. Further analysis into the dynamics of each PBL scheme is beyond the scope of this research.

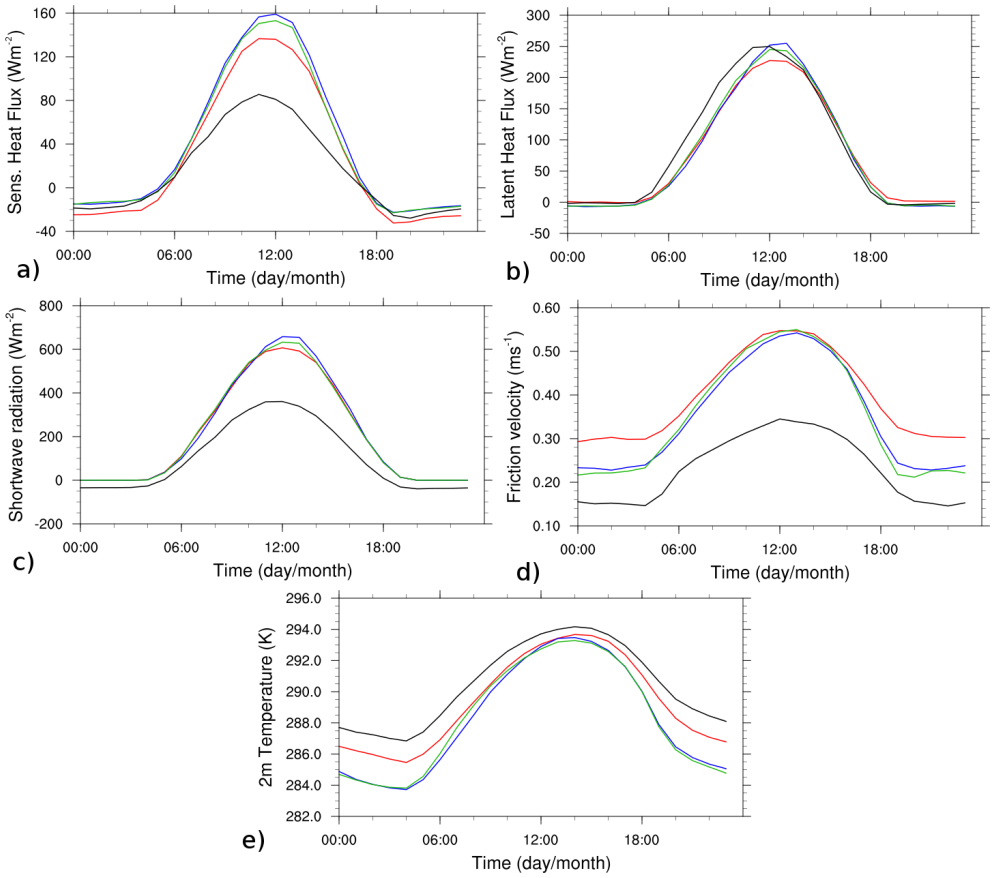

Figure 4.24: Composite time series for Cabauw during May to September 2006 for a) sensible heat flux (Wm^{-2}), b) latent heat flux (Wm^{-2}), c) incoming solar radiation (Wm^{-2}), d) friction velocity (ms^{-1}) and e) 2m temperature (K). The YSU, MYJ and MYNN PBL schemes are denoted by the red, blue and green lines respectively

4.4 Conclusions

In this Chapter, the performance of the WRF model using different PBL schemes has been assessed for both short and long range simulations in an effort to determine the *best case* model set up to form the basis of the sea breeze climatology. The short range simulation was a sea breeze event in which additional sensitivity tests were performed in terms of model horizontal resolution and lead time. Both the Dutch surface meteorological network and the Cabauw tower were used for verification purposes of the high resolution sea breeze simulation. The longer simulations spanned from May to September 2006; a period with exceptionally high temperatures. For these long term simulations, the performance of the model was evaluated both onshore at the Cabauw tower and offshore at the Egmond aan Zee met mast.

In terms of general model performance, the YSU PBL scheme performed the best of the tested schemes and will be used for simulating the sea breeze climatology. All schemes underestimated temperature, especially during the nocturnal hours over the land surface, though the modifications to the nocturnal YSU scheme reduced this BIAS. The daily maximum temperature, however, was simulated well for all schemes, yet there was still a small negative temperature BIAS associated with it.

In the sea breeze simulations, the difference in simulated temperature caused the sea breezes to be triggered at later times than in the observations. The simulated sea breeze also persisted later between 1 and 2 hours later in the evening than in the observations. Despite this, the YSU PBL scheme baseline simulation did not advance the sea breeze far enough inland.

In terms of analysing the impact of the sea breeze on wind energy, it is important to note that 27km horizontal resolution is insufficient to faithfully simulate a sea breeze and so differences between resolutions could be used as a basis for quantifying sea breeze impacts. The most accurate amount of lead time for temperature and humidity is 18 hours without the benefit of analysis nudging.

Finally, the reason for the cold BIAS in the model is likely due to increased vertical mixing at the top of the PBL rather than in the surface physics, confirming that the differences between models are caused by the PBL schemes themselves.

Chapter 5

Using and testing the sea breeze identification method

In Chapters 3 and 4 it has been demonstrated that the choice of PBL scheme strongly affects the typical characteristics of a sea breeze and that overall, the YSU PBL scheme gives the best statistical scores when compared with observations. Here, the simulations are extended to include the complex coastlines of the southern North Sea from May 2002 to September 2012 and the sea breeze identification method performed on 5 different coastlines. The method is tested by using different calculations for the land-sea thermal contrast and varying the gradient wind height. The relative effect of each filter is also analysed. This chapter is organized so that Section 5.1 gives an overview of the study period in terms of the Lamb weather typing and SST anomalies. Section 5.2 presents the results for each individual coastline and Section 5.3 presents the results of the sensitivity analysis. Finally, conclusions are drawn and summarized in Section 5.4 as to the performance of the method and the frequency and distribution of sea breezes.

5.1 Summary of 2002-2012: The study period

In Europe, it is known that during the latter and early years of the 20^{th} and 21^{st} Centuries, air temperatures were warm to the extent that several years were considered to be some of the warmest on instrumental record (Della-Marta *et al.*, 2007; Rebetez *et al.*, 2006). It could therefore be inferred on a simple level that conditions were much more favourable for sea breeze development during this period than during the 1960's, when Simpson *et al.*

(1977) conducted their climatology. Consequently the number of observed sea breezes may be higher than the 76 observed by Simpson *et al.* (1977). However, referring back to Fig. 3.1, many other factors, such as gradient wind strength and orientation with respect to the coastline can influence sea breeze numbers so it should not simply be expected that if a decade is warm during the Spring and Summer months, more sea breezes will form. Furthermore, during a prolonged warm period, the SST rises more quickly and so the minimum land temperature required to stimulate sea breeze development is higher later in the season, than in a year which has Spring and Summer temperatures closer to the climatological average. A brief summary of the decade is now given, highlighting in particular seasons which experienced anomalous weather which may affect sea breeze numbers.

5.1.1 UK Lamb weather variability and frequencies

From January 2002 to December 2012 over the UK, 32% of the days were classified as *Anticyclonic*, 25% were *Cyclonic*, 41% were *Pure Directional* and 2% of days were *Unclassified* flow regimes. With the exception of March, where *Anticyclonic* flow regimes dominate, the most common weather type during the study period is *Pure Directional* (Fig. 5.1a). Two pronounced peaks in anticyclonic weather type days occur during March and September. Two peaks in directional weather types occur in December and May, but otherwise in each month there are on average approximately 12 days of pure directional flow. During the first six months of the year, anticyclonic flow regimes are more frequent than cyclonic, however, this becomes changeable during the latter half of the year. The number of cyclonic days per month on average varies between 6 and 8, but there is also a pronounced trough during September, where the average is reduced to 4. Approximately 6 days per year were *unclassified* flow regimes. However, only on 2 occasions during the 11 year period were any of the *unclassified* flow regimes not occurring between May and September, implying that the slackened pressure gradients associated with the late Spring and Summer months are more conducive to forming *unclassified* flow regimes.

In comparison with the results of Briffa *et al.* (1990), the study period is on average slightly more *Anticyclonic* than between 1861-1980 with 68.2 days of *Pure Anticyclonic* weather types per year compared with 65.5 (compare Table. 5.1 with Table 5.2). This

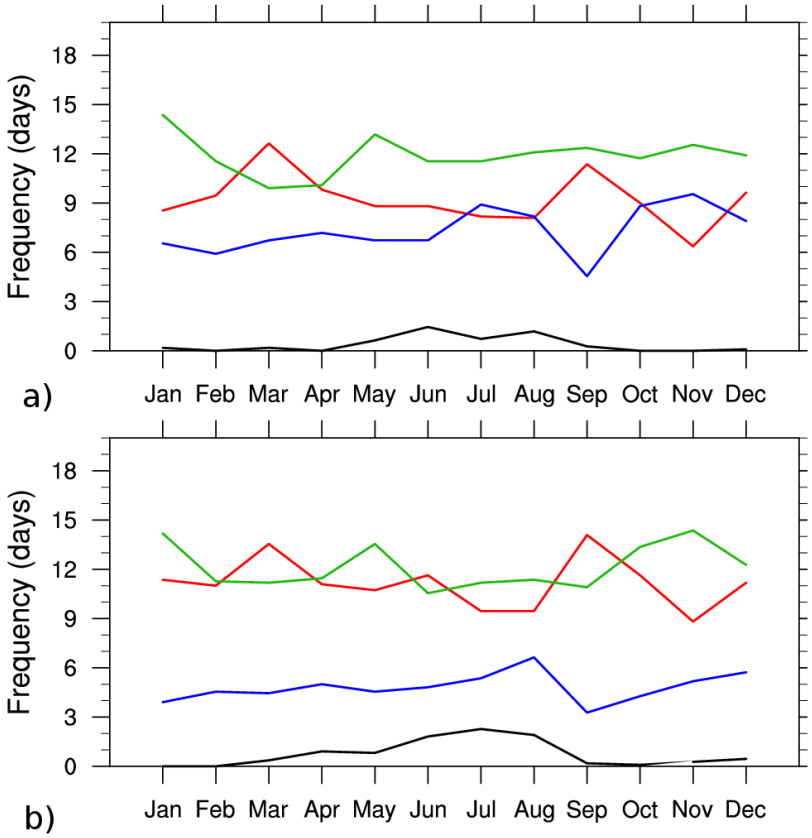

Figure 5.1: Average number of days per month between January 2002 to December 2012 for each class of Lamb weather type for the a) UK and the b) Netherlands. The respective weather types are *Anticyclonic* (red), *Cyclonic* (blue), *Pure Directional* (green) and *Unclassified* (black).

increase is found during the Winter and Spring months only; Summer and Autumn are less *Anticyclonic* than the 1861-1980 average. During the study period, the *Pure Anticyclonic* weather type is the most dominant, whereas the long term climatology diagnoses the *Pure Westerly* type to be the most common. In particular, Briffa *et al.* (1990) note a decline in the more recent decades of the climatology of the *Pure Westerly* weather type which is compensated for by an increase in both the *Pure Anticyclonic* and *Cyclonic* weather type frequencies. Despite covering only a period of 11 years, the Lamb weather types calculated here support a continuation of this trend.

The number of *Unclassified* weather types during the study period is also notably different to the study by Briffa *et al.* (1990). The annual frequency of expected *Unclassified* weather types is approximately half that in the long term climatology. Whereas, in Briffa *et al.* (1990), approximately 4 days per season are *Unclassified*, the 2002-2012 study period contains a maxima in Summer of 4.4 days and a decline in number to between 0.7-1.5 days during the other seasons.

Table 5.1: Means and standard deviations (in parenthesis) of the seasonal and annual frequencies of the Lamb weather types for the period January 2002 - December 2012. The Winter seasons of 2001/2002 and 2012/2013 are not included since they are incomplete.

Weather type	Winter	Spring	Summer	Autumn	Annual
A	19.0 (4.2)	19.7 (7.1)	15.3 (5.8)	15.7 (5.6)	68.2 (8.8)
ANE	0.7 (0.6)	0.5 (0.7)	0.2 (0.1)	0.2 (0.2)	1.4 (1.0)
AE	0.4 (0.6)	0.8 (0.8)	0.4 (0.5)	0.1 (0.2)	1.7 (0.9)
ASE	0.6 (1.1)	1.2 (0.9)	0.5 (0.4)	0.7 (0.8)	3.0 (1.8)
AS	4.3 (2.7)	5.0 (2.3)	4.2 (1.3)	5.2 (1.8)	18.9 (5.0)
ASW	2.2 (1.7)	2.3 (1.6)	2.3 (1.2)	3.0 (1.4)	10.0 (2.5)
AW	3.1 (1.7)	3.2 (1.7)	2.9 (1.9)	3.7 (1.8)	13.1 (3.8)
ANW	1.6 (1.4)	2.0 (1.1)	2.1 (1.2)	1.8 (0.6)	7.5 (2.8)
AN	3.6 (1.9)	3.6 (2.1)	3.5 (1.8)	3.0 (1.2)	13.4 (5.4)
NE	2.8 (2.6)	2.4 (1.6)	2.8 (1.8)	1.8 (1.6)	9.2 (4.0)
E	2.2 (2.1)	3.8 (4.1)	2.6 (1.9)	1.5 (1.6)	9.7 (4.8)
SE	2.7 (3.3)	5.7 (2.3)	4.7 (3.2)	3.2 (2.0)	16.1 (3.9)
S	7.9 (4.6)	7.9 (3.7)	9.6 (4.1)	9.9 (5.9)	35 (10.7)
SW	14.2 (4.8)	11.8 (4.3)	12.1 (4.3)	17.4 (5.8)	56.5 (8.7)
W	15.5 (7.5)	12.5 (5.4)	10.8 (3.5)	14.8 (4.3)	55.2 (10.5)
NW	7.1 (3.0)	7.3 (2.2)	8.5 (3.7)	8.3 (2.3)	32.2 (6.9)
N	6.3 (3.0)	5.8 (4.2)	7.4 (2.3)	4.6 (2.0)	23.5 (9.9)
C	11.9 (5.3)	12.1 (5.2)	13.8 (6.9)	12.9 (5.3)	50.6 (12.0)
CNE	0.6 (1.0)	0.3 (0.4)	1.0 (1.4)	0.7 (0.6)	2.5 (1.8)
CE	0.5 (0.7)	0.6 (0.6)	0.9 (0.8)	0.6 (0.7)	2.5 (1.2)
CSE	0.6 (0.6)	1.2 (1.0)	1.2 (1.1)	0.9 (1.0)	3.9 (1.6)
CS	4.3 (1.4)	5.3 (2.4)	5.1 (1.9)	5.8 (2.4)	20.5 (4.4)
CSW	2.2 (0.9)	2.1 (0.8)	1.8 (0.5)	2.9 (0.7)	9.2 (1.4)
CW	2.0 (1.7)	1.5 (0.8)	1.4 (0.4)	1.9 (0.7)	7.1 (1.9)
CNW	1.3 (0.5)	1.1 (0.6)	1.0 (0.5)	1.2 (0.6)	4.7 (1.2)
CN	2.7 (1.5)	2.3 (1.1)	3.6 (2.3)	3.0 (1.2)	11.4 (3.3)
U	0.7 (0.7)	1.5 (1.4)	4.4 (2.0)	1.0 (0.7)	7.5 (3.1)

The Lamb weather type wind directions largely conform with the expectation that the most dominant wind directions in the British Isles are south westerly and westerly (Fig. 5.2a Earl *et al.*, 2013). Notably, this is less apparent during May, where the frequency distribution of the wind directions is more varied. August also has a higher frequency of north westerly flow, which is approximately equal to the frequency of westerly and south westerly air flows. The degree of dominance of the southerly and south westerly flow regimes is increased during the Autumn and Winter months over the other flow directions, which is expected due to the relative position of the North Atlantic storm track (Earl *et al.*, 2013).

The annual variability of the *Anticyclonic* flow regimes is shown in Fig. 5.3. The

Table 5.2: Means and standard deviations (in parenthesis) of the seasonal and annual frequencies of the Lamb weather types for the period 1861-1980 as for those reported in Briffa *et al.* (1990)

Weather type	Winter	Spring	Summer	Autumn	Annual
A	14.3 (6.1)	17.4 (6.6)	16.9 (7.8)	17.0 (6.8)	65.5 (14.8)
ANE	0.7 (1.0)	1.7 (1.6)	1.4 (1.7)	1.2 (1.6)	5.1 (3.0)
AE	1.8 (2.1)	3.3 (2.6)	2.2 (2.2)	1.9 (2.0)	9.2 (4.3)
ASE	0.8 (1.2)	0.9 (1.1)	0.7 (0.9)	1.0 (1.4)	3.4 (2.2)
AS	1.3 (1.5)	0.9 (1.0)	0.9 (1.0)	1.1 (1.2)	4.1 (2.5)
ASW	1.0 (1.3)	0.5 (0.9)	0.7 (0.9)	0.8 (1.0)	2.9 (2.1)
AW	4.3 (3.5)	3.4 (2.5)	5.2 (2.9)	4.3 (3.0)	17.2 (6.8)
ANW	1.1 (1.2)	1.3 (1.6)	1.8 (1.7)	1.2 (1.3)	5.4 (2.9)
AN	1.4 (1.5)	2.5 (2.1)	2.1 (2.0)	1.6 (1.5)	7.6 (4.0)
NE	0.6 (0.9)	1.3 (1.3)	0.9 (1.4)	0.6 (1.0)	3.4 (2.6)
EE	2.9 (3.1)	5.6 (3.9)	1.8 (1.9)	2.6 (2.4)	12.9 (5.9)
SE	2.0 (2.1)	1.9 (2.1)	0.6 (0.9)	1.6 (1.7)	6.1 (3.4)
SS	4.9 (3.0)	3.9 (2.7)	2.3 (2.3)	4.3 (3.4)	15.4 (5.5)
SW	3.4 (2.9)	1.8 (1.5)	1.9 (1.6)	2.5 (2.1)	9.6 (4.5)
WW	20.9 (8.5)	12.6 (5.6)	16.7 (6.7)	18.2 (7.2)	68.5 (16.1)
NW	3.4 (2.7)	3.2 (2.3)	4.3 (2.8)	3.1 (2.4)	13.9 (6.4)
NN	3.3 (2.6)	5.2 (3.0)	4.4 (2.9)	4.3 (3.2)	17.2 (6.1)
CC	9.5 (5.4)	11.6 (5.1)	14.7 (6.4)	10.8 (4.6)	46.5 (10.8)
CNE	0.3 (0.6)	0.5 (0.7)	0.2 (0.6)	0.3 (0.6)	1.4 (1.3)
CE	0.9 (1.3)	1.3 (1.3)	0.8 (1.1)	1.0 (1.2)	4.0 (2.7)
CSE	0.4 (0.7)	0.6 (0.8)	0.2 (0.5)	0.5 (0.7)	1.7 (1.6)
CS	1.2 (1.3)	1.3 (1.4)	0.9 (1.3)	1.2 (1.2)	4.6 (2.9)
CSW	0.7 (0.9)	0.4 (0.7)	0.5 (0.9)	0.7 (1.2)	2.4 (2.1)
CW	4.0 (2.4)	2.8 (2.1)	4.3 (2.8)	3.9 (2.5)	15.0 (5.5)
CNW	0.7 (0.9)	0.9 (1.0)	1.0 (1.1)	0.7 (0.8)	3.3 (2.0)
CN	1.1 (1.4)	1.5 (2.5)	1.2 (1.3)	1.2 (1.4)	5.0 (3.0)
U	3.3 (2.2)	3.8 (1.9)	3.4 (2.0)	3.5 (2.1)	14.1 (4.1)

year 2008, is largely less *Anticyclonic* than the average of the 2002-2012 study period, with the exception of small positive anomalies during the Winter months. The Summers of 2007 and 2008 were both particularly wet, yet neither show a particularly strong *Cyclonic* anomaly (Fig. 5.4). There is, however, a positive anomaly spanning the Spring and Summer months in 2008 for *Pure Directional* types, suggesting that the rainfall was more frontally driven. The Spring and Autumn of both years are very different, however, in terms of weather typing. During both seasons, 2008 contains large positive *Cyclonic* anomalies, yet, 2007 is largely *Anticyclonic*.

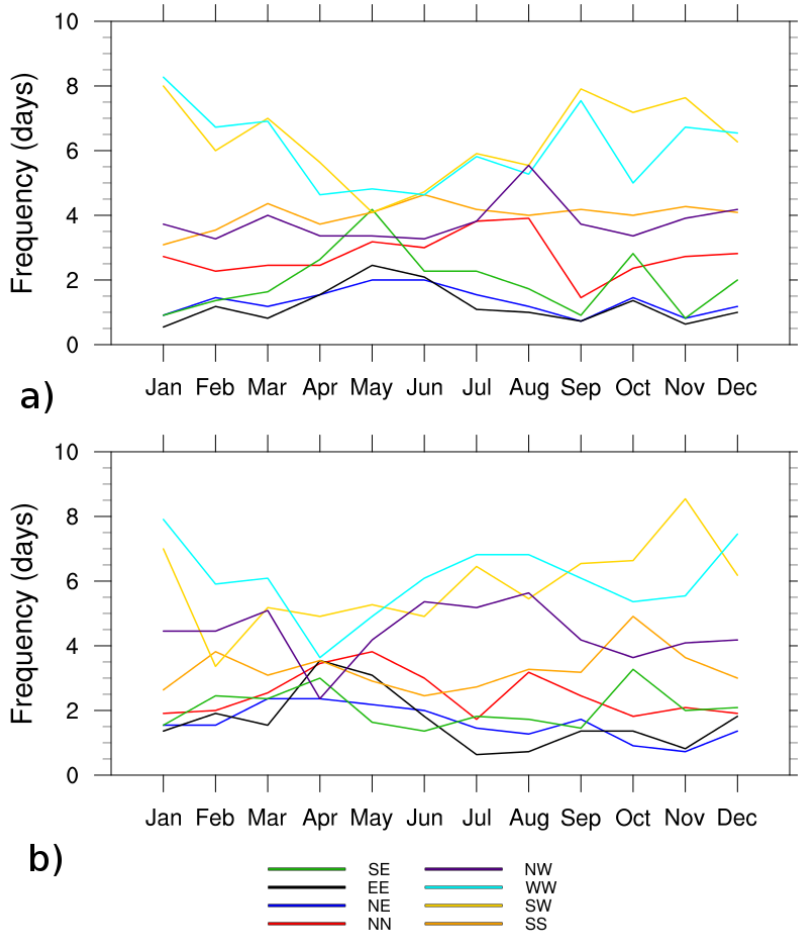

Figure 5.2: Average number of days per month between January 2002 to December 2012 for each class of Lamb weather type wind direction for the a) UK and the b) Netherlands.

Both years 2003 and 2006 were exceptionally warm and a number of European Summer heat-waves caused temperatures to soar, both in the UK and continental Europe, causing a number of heat related deaths (Della-Marta *et al.*, 2007; Rebetez *et al.*, 2006, 2009). June 2006, in the UK, was the most anticyclonic June since 1976, which is reflected by the strong positive anomaly in Fig. 5.3 (Eden, 2006). With exception of August, there is no such positive anomaly in 2003, however, due to the more southerly position of the omega blocking system responsible for the heat-wave, a strong directional anomaly exists, where southerly and easterly gradient winds persist (Rebetez *et al.*, 2009).

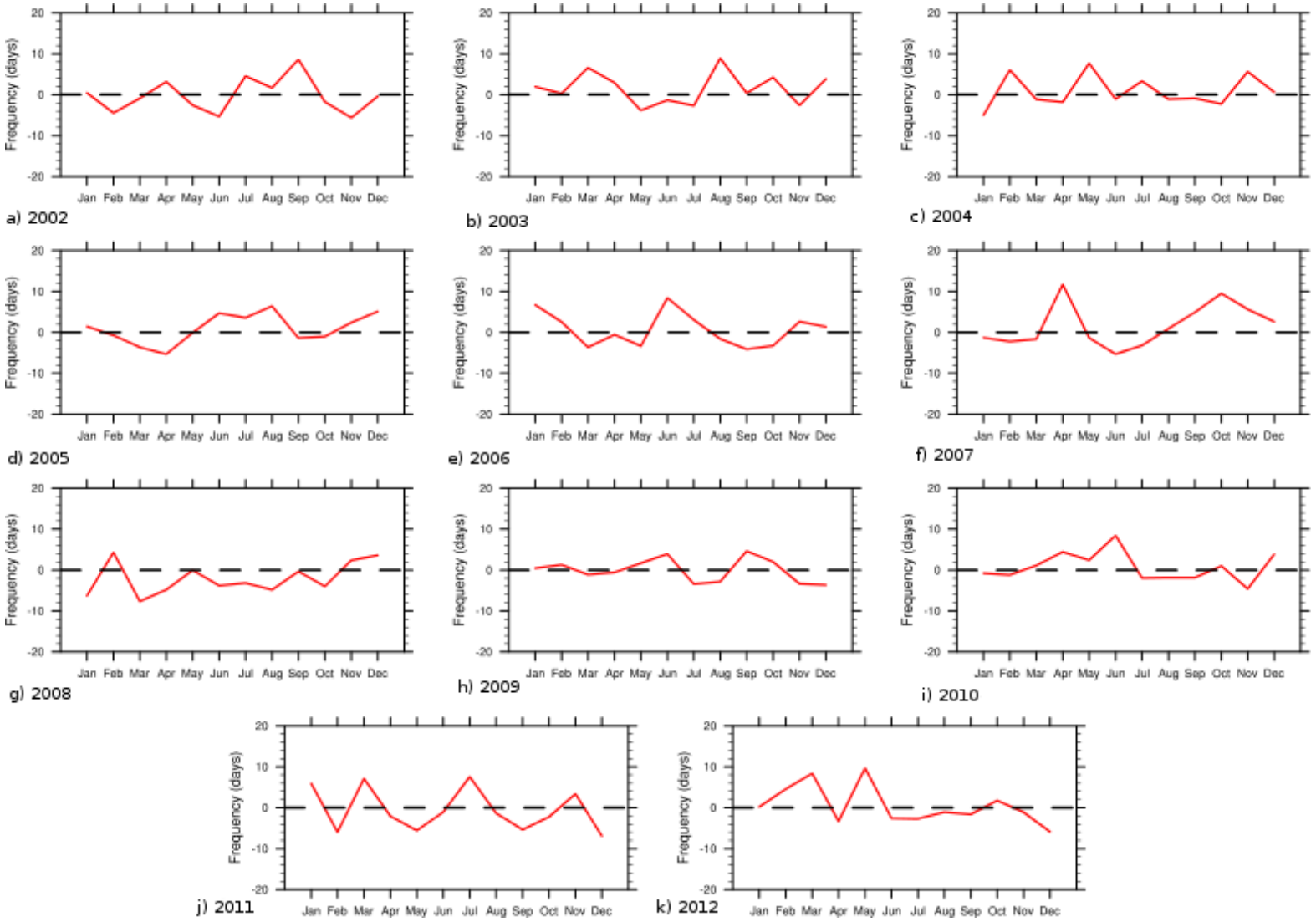

Figure 5.3: *Antiyclonic* flow regime anomaly for each year compared to the January 2002 to December 2012 climatology for the UK.

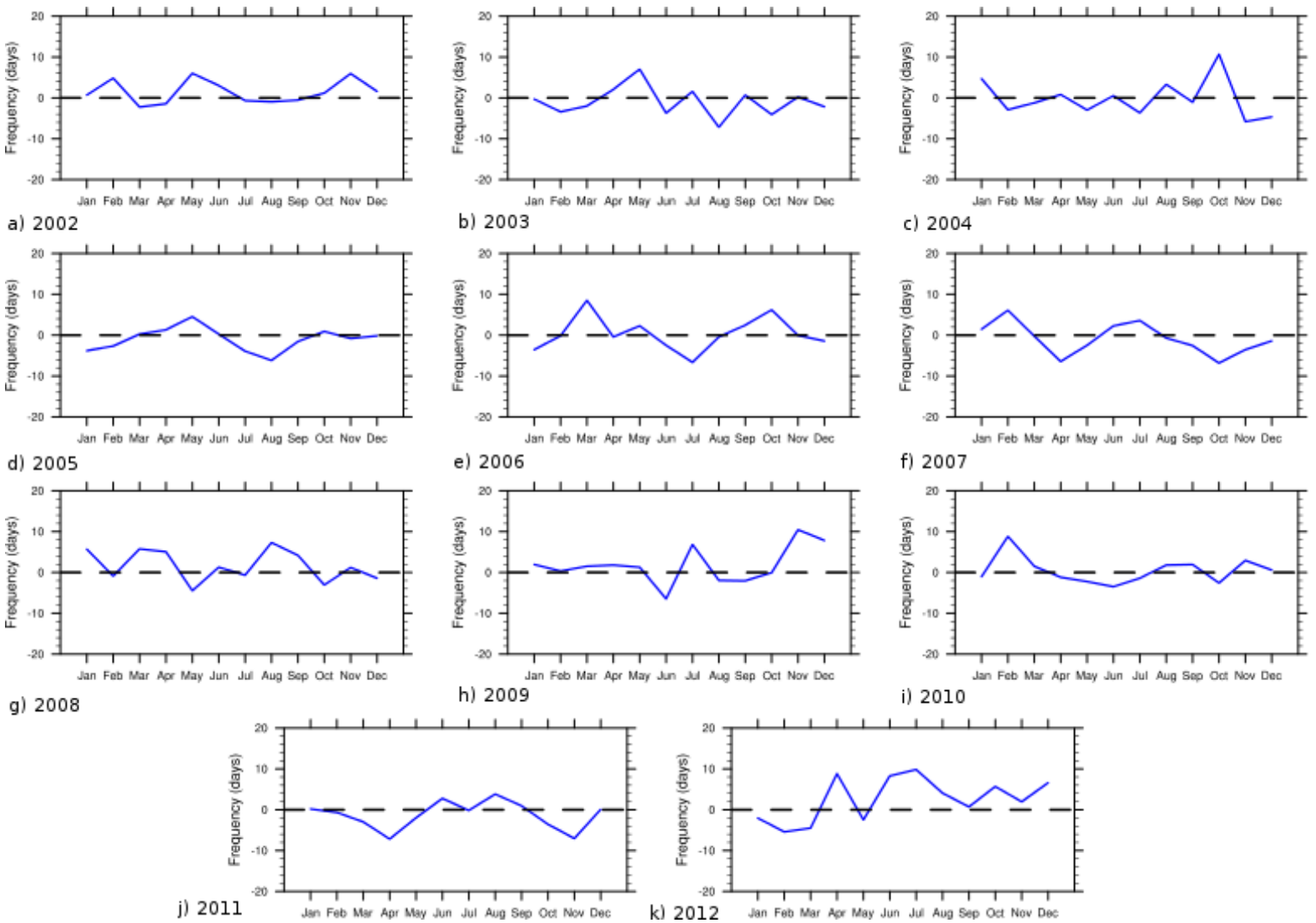

Figure 5.4: *Cyclonic* flow regime anomaly for each year compared to the January 2002 to December 2012 climatology for the UK.

3990

There are a large number of *Anticyclonic* days during the Spring months during the study period. Furthermore, 2003, 2007, 2011 and 2012 show positive *Anticyclonic* anomalies during Spring. It is during these months that the SST is lowest, and so it could be the case that these sea breeze seasons are more pronounced during the Spring months. Sea breezes typically form in the UK during late Spring and early Summer when the land-sea contrast is at a maximum and there are light gradient winds (Simpson, 1994). Strong *Anticyclonic* conditions during these months may be favourable for sea breeze formation but are not the only factor. Light *Pure Directional* weather types and *Unclassified* flow regimes may be sufficient to produce sea breezes but will be sensitive to the coastal orientation.

5.1.2 Lamb weather type frequencies and variability in the Netherlands

The Dutch weather typing as split into percentages identified 38% *Anticyclonic*, 17% cyclonic, 41% *Pure Directional* and 3% *Unclassified* flow regimes between January 2002 to December 2012. Notably, in comparison with the UK, there are significantly more *Anticyclonic* and unclassified regimes, yet overall, although numbers differ, the seasonal cycles are extremely similar between the two areas. Again, there appear to be two maxima in *Anticyclonic* weather types during March and September (Fig. 5.1b). Despite more pure directional days being observed, the dominant weather type repeatedly fluctuates between *Anticyclonic* and *Pure Directional*. On average, approximately 12 days of both *Anticyclonic* and *Pure Directional* weather types occur each month. The number of *Cyclonic* days per month is approximately 4, with a maximum of 7 in August and a minimum of 3 in September. The largest frequency of *Unclassified* days again occur during the Summer months, however, they are present on a much broader temporal range than for the UK. *Unclassified* days, do not have particularly strong gradient winds and are disorganised flow regimes. These are therefore more likely to occur when the pressure gradient is slackened. Consequently, with an increased number of *Anticyclonic* days occurring over the Netherlands relative to the UK, a further increase in *unclassified* flow regimes could also be implied.

Overall, the variability of the frequency in Lamb type wind direction is greater for

Table 5.3: Means and standard deviations (in parenthesis) of the seasonal and annual frequencies of the Lamb weather types for the period January 2002 - December 2012 diagnosed for the Netherlands. The Winter seasons of 2001/2002 and 2012/2013 are not included since they are incomplete.

Weather type	Winter	Spring	Summer	Autumn	Annual
A	19.3 (5.0)	22.0 (7.1)	18.5 (7.0)	19.9 (5.6)	79.3 (10.3)
ANE	0.9 (0.7)	1.0 (0.9)	0.8 (0.7)	0.7 (0.7)	3.3 (2.0)
AE	0.8 (0.6)	1.8 (1.2)	0.4 (0.9)	0.9 (1.2)	4.0 (2.2)
ASE	1.2 (1.3)	0.8 (0.9)	0.5 (0.5)	1.4 (1.5)	3.6 (2.9)
AS	5.8 (2.3)	5.0 (2.0)	4.6 (1.5)	6.9 (3.1)	22.0 (4.8)
ASW	3.2 (1.0)	2.8 (1.4)	2.6 (0.8)	3.9 (2.2)	12.4 (2.6)
AW	4.4 (2.5)	2.5 (1.1)	3.3 (0.9)	3.8 (1.5)	14.6 (4.3)
ANW	2.0 (1.3)	2.1 (1.0)	2.7 (0.9)	2.4 (1.1)	9.2 (2.8)
AN	4.9 (2.1)	5.1 (2.1)	5.1 (1.6)	4.3 (1.9)	19.0 (4.4)
NE	3.7 (3.0)	4.5 (3.2)	2.6 (2.1)	2.5 (1.6)	12.8 (7.3)
EE	4.1 (2.9)	6.5 (4.0)	1.2 (1.9)	3.0 (2.8)	14.4 (6.1)
SE	5.3 (4.5)	4.9 (2.9)	2.4 (2.1)	4.6 (3.0)	16.5 (5.6)
SS	7.5 (4.7)	6.9 (2.2)	6.0 (2.2)	9.3 (4.4)	29.1 (6.3)
SW	13.1 (4.1)	11.9 (3.5)	12.5 (2.5)	17.9 (5.9)	56.0 (10.5)
WW	15.0 (6.9)	10.3 (4.0)	13.9 (4.7)	13.4 (4.0)	55.1 (12.1)
NW	9.2 (3.9)	7.8 (2.7)	11.8 (3.2)	9.0 (3.7)	38.5 (8.7)
NN	4.6 (2.8)	6.8 (3.1)	5.3 (2.8)	3.9 (2.4)	20.2 (5.6)
CC	7.4 (3.6)	7.2 (3.8)	9.5 (2.6)	6.4 (2.8)	29.9 (6.8)
CNE	0.6 (0.4)	0.6 (0.7)	0.5 (0.7)	0.4 (0.5)	1.9 (1.5)
CE	0.8 (1.1)	0.9 (0.6)	0.4 (0.5)	0.5 (0.6)	2.4 (1.7)
CSE	0.9 (1.0)	0.8 (1.0)	0.4 (0.4)	0.6 (0.6)	2.6 (1.0)
CS	4.2 (1.8)	3.6 (1.6)	3.6 (1.6)	4.0 (1.7)	15.2 (3.6)
CSW	1.5 (1.2)	1.8 (1.3)	2.2 (1.4)	2.0 (0.9)	7.4 (2.9)
CW	1.2 (0.6)	1.2 (0.7)	1.8 (0.8)	1.5 (1.1)	5.9 (2.0)
CNW	1.4 (1.0)	1.0 (0.5)	1.5 (0.7)	0.7 (0.6)	4.6 (1.9)
CN	2.6 (1.2)	2.2 (1.1)	2.5 (0.7)	1.5 (0.6)	8.7 (1.9)
U	1.1 (1.2)	3.1 (1.0)	6.9 (2.6)	1.2 (1.0)	12.1 (3.1)

the Netherlands than for the UK (Fig. 5.2b). Throughout the year the westerly and south westerly flow directions dominate, as with the UK, however, there is a larger contribution from north westerly flow regimes. There are maxima in wind direction for the north westerlies during the Summer months of approximately 5 days per month; approximately equal to the number of south westerlies in June and August. The month with the largest variability, corresponding with a drop in the frequency of westerly and south westerly flow regimes, is again April in agreement with the shift in Atlantic storm track as for the UK.

There are a large number of *Anticyclonic* days during the Spring months of the study

period. Furthermore, 2003, 2007, 2011 and 2012 show positive *Anticyclonic* anomalies during Spring (Fig. 5.5). The variability in *Cyclonic* weather types is less than for the UK (Fig. 5.6). For the majority of the study period, the anomaly remains within ± 6 days. The only exception to these limits which could also be significant for the sea breeze season is April 2012, where there is a strong positive *Cyclonic* anomaly of approximately 10 days.

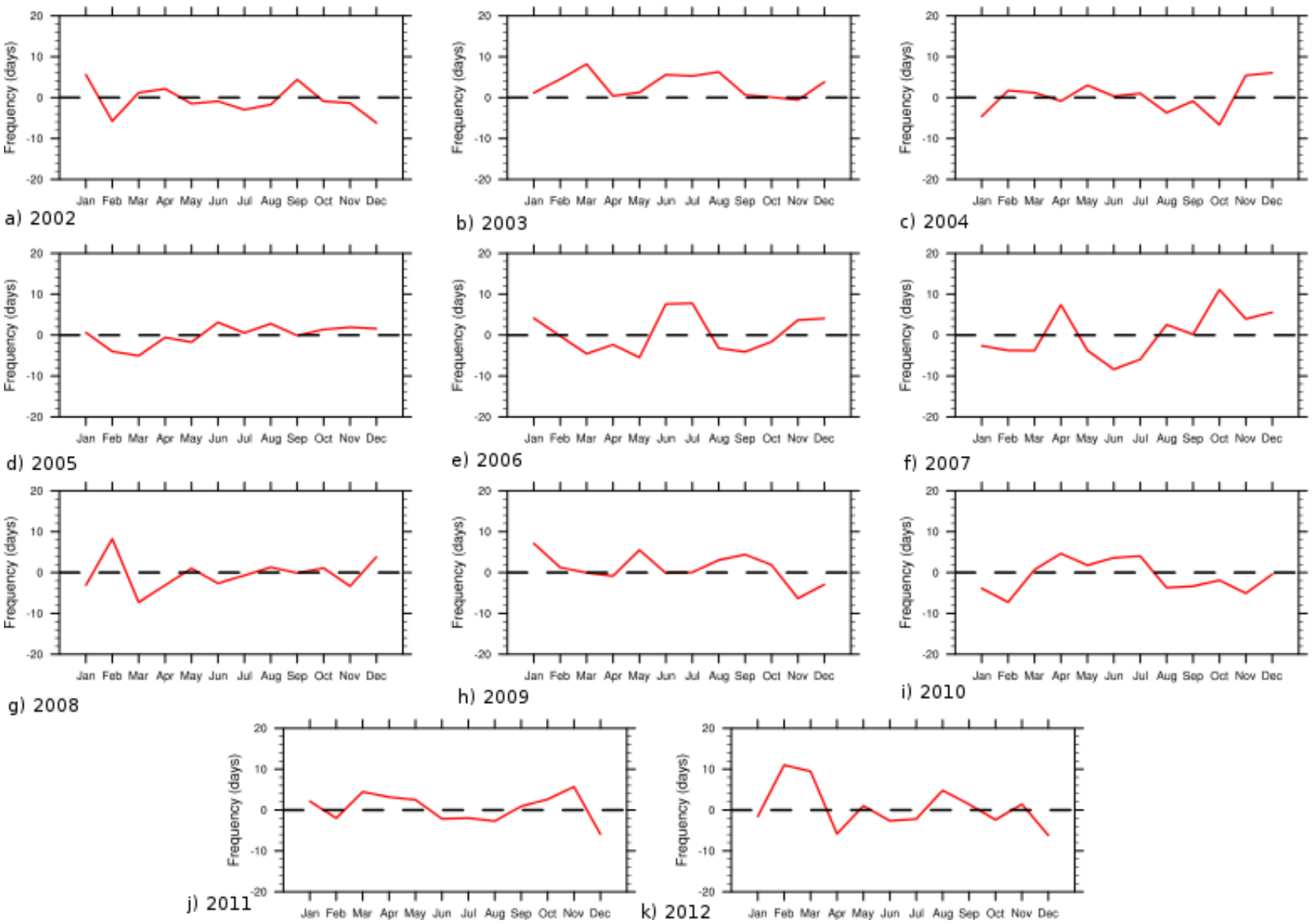

Figure 5.5: *Anticyclonic* flow regime anomaly for each year compared to the climatological average of the period January 2002 until December 2012 for the Netherlands.

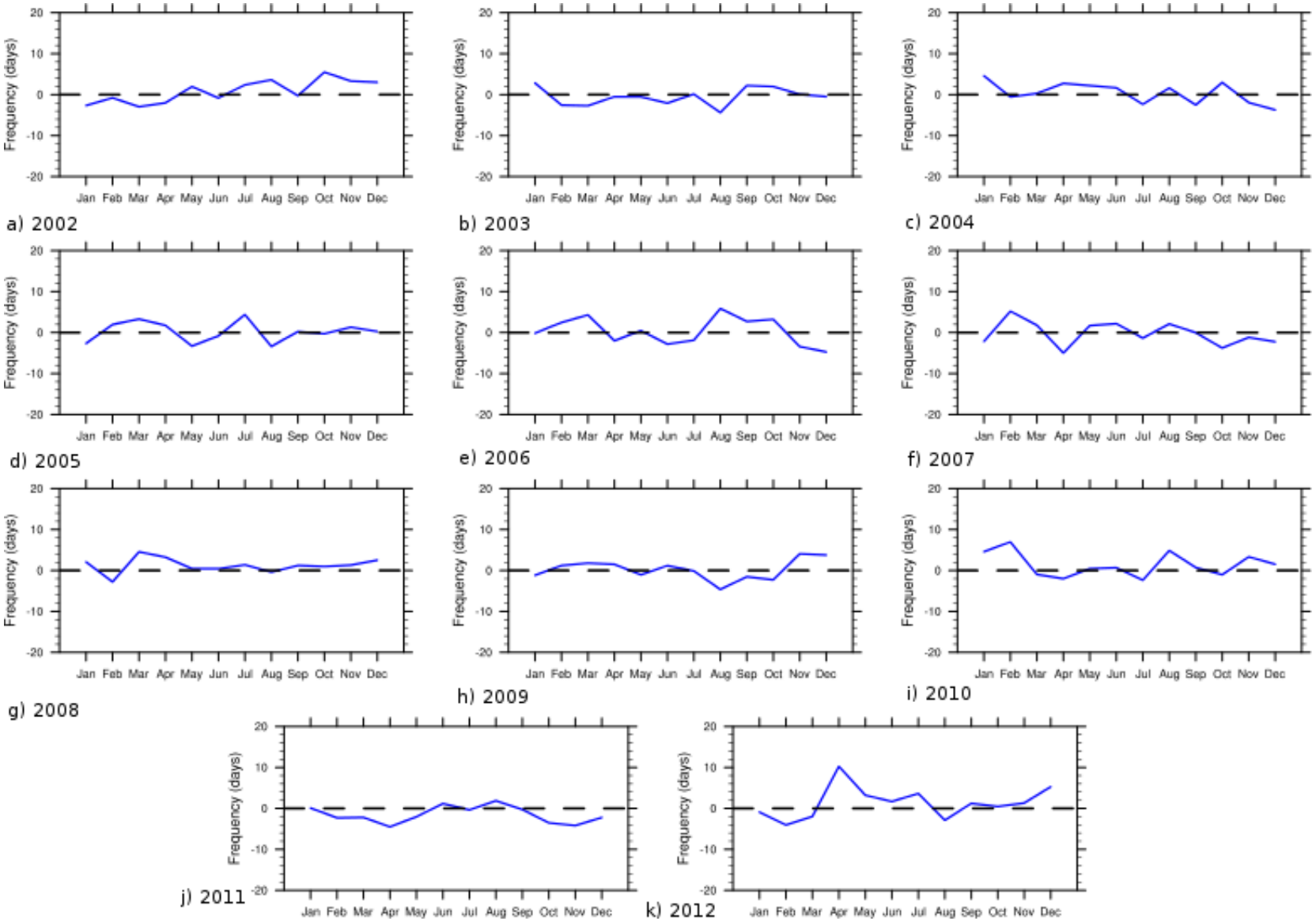

Figure 5.6: *Cyclonic* flow regime anomaly for each year compared to the climatological average of the period January 2002 until December 2012 for the Netherlands.

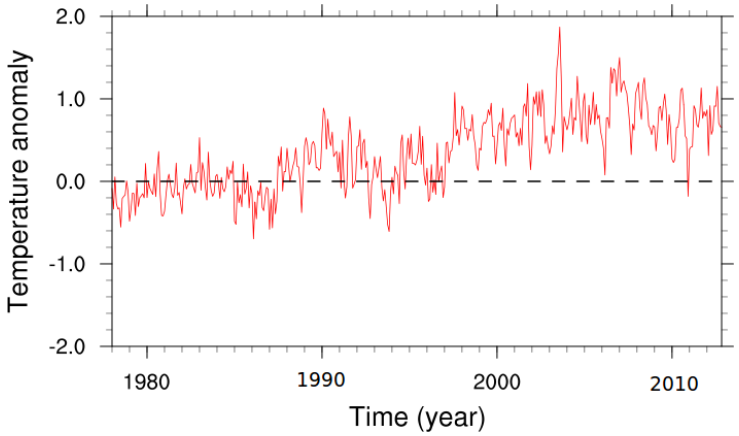

Figure 5.7: Monthly time series of surface temperature anomaly (°) from 1961-1990 of hadCRUT3 averaged over 40-70N and 25W-20E.

5.1.3 Land and sea temperature anomalies

Fig. 5.7 shows the monthly surface temperature anomalies from hadCRUT3 averaged over Europe (40-70N, 25W-20E). Even from such a coarse resolution, the observations clearly show the dominance of the positive temperature anomaly during the early 21^{st} Century. A notable maximum occurs during 2003 and a more prolonged warm episode is also evident during 2006. Only once, during December 2010, does the temperature anomaly become negative during the study period. During Winter 2005, the temperature anomaly is close to zero, and during 2009, there exists a broader trough associated with a prolonged spell of cooler temperatures during the Winter.

The relationship between SST's during early Spring and the strength of the Winter air temperature anomaly could provide an indication as to the level of preconditioning achieved before the start of the sea breeze season. For example, as particularly mild Winter could create a warm Spring SST anomaly and could therefore be detrimental to sea breeze development, even if all of the other criteria are satisfied. However, Fig. 5.8 shows that cold Winters do not coincide with cold SST anomalies. The Winters of 2007 and 2008 are the mildest during the study period and yet they produce negative SST anomalies (Compare Figs. 5.7 and 5.8). There are several plausible explanations.

Mild Winters tend to be associated with a greater degree of westerly flow and stronger wind speeds (Earl *et al.*, 2013). These winds could act to increase the level of vertical mixing in the water column and therefore reduce the SST. Furthermore, stronger winds

promote higher sensible heat fluxes, and so more heat is lost to the atmosphere despite the reduced thermal contrast. In the converse case, cold air over the sea may act to increase the sensible heat flux, but the slackened winds associated with a cold Winter promote stratification of the water column and so the magnitude of the heat loss is less than for a mild Winter.

The other possible cause is that the increased degree of westerly flow implies a greater degree of moisture and therefore cloud cover. This increase in cloud cover decreases the degree of incoming solar radiation and therefore reduces the SST, despite the warmer air temperatures from the westerly flow regimes. It is also plausible that both of these factors may contribute to the colder SST anomalies in the milder Winters.

To summarize the 2002 to 2012 period, the years which are best preconditioned for sea breezes in the southern North Sea because of SST anomalies are 2007 and 2008. However, preconditioning of the SST is not the sole determinant of the formation of sea breezes. High frequencies of cyclonic flow regimes during the Spring and Summer months prevent daytime maximum temperatures from reaching the required values to form a thermal pressure gradient between the land and sea. However, cyclonic regimes early in the sea breeze season, such as in 2003 may suppress the SST and so sea breeze formation occurs later in the season. Other factors, such as the gradient wind strength, prolonged warm weather early in the season and the direction of the gradient wind all need to be considered for sea breeze prediction purposes. The sea breeze climatology for 5 different coastlines will now be presented.

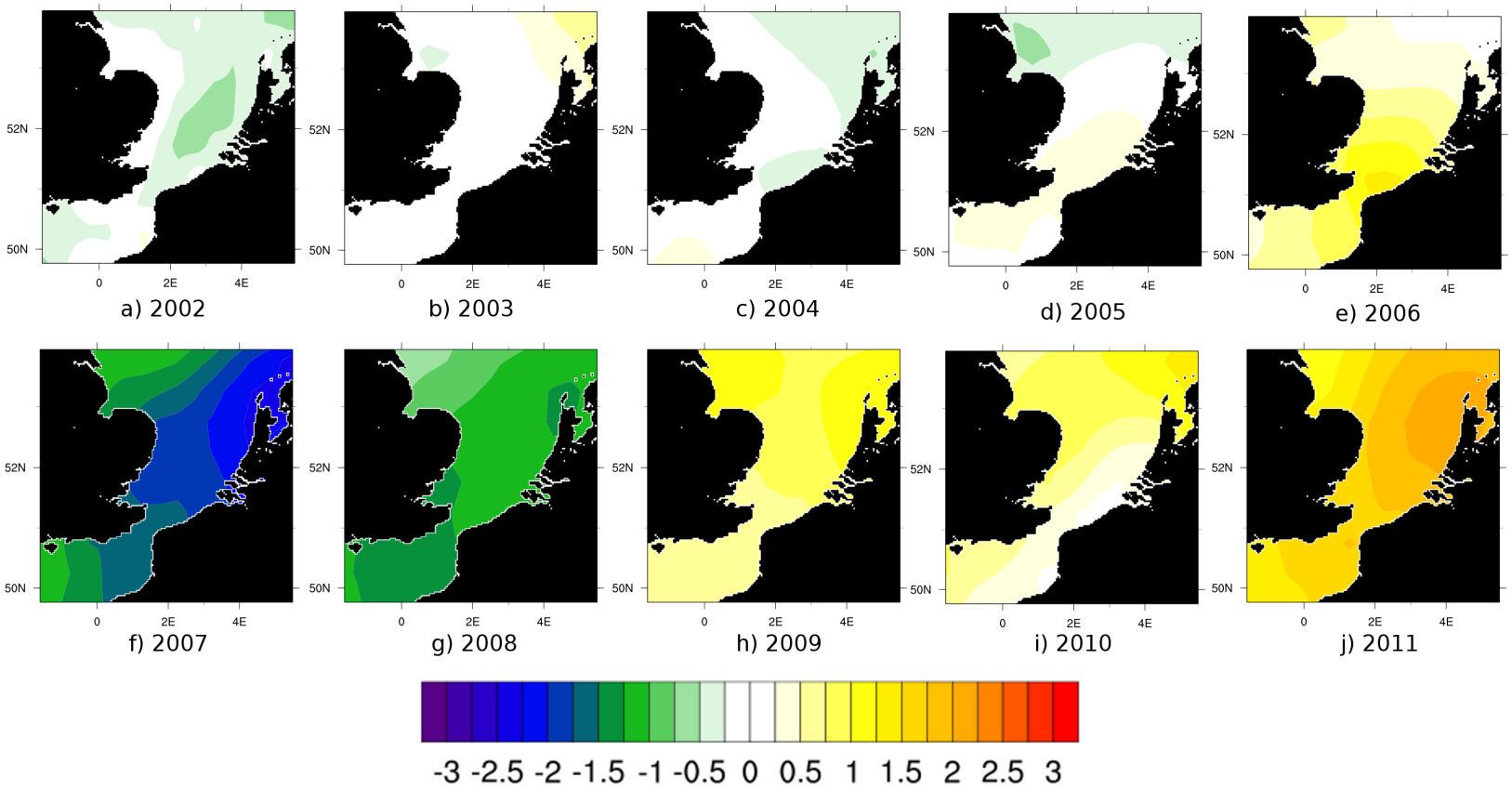

Figure 5.8: Winter (December, January, February) composite SST anomalies from the period 2002-2012. Anomalies are calculated using 1° NCEP Real-Time SST archives and the units are in Kelvin.

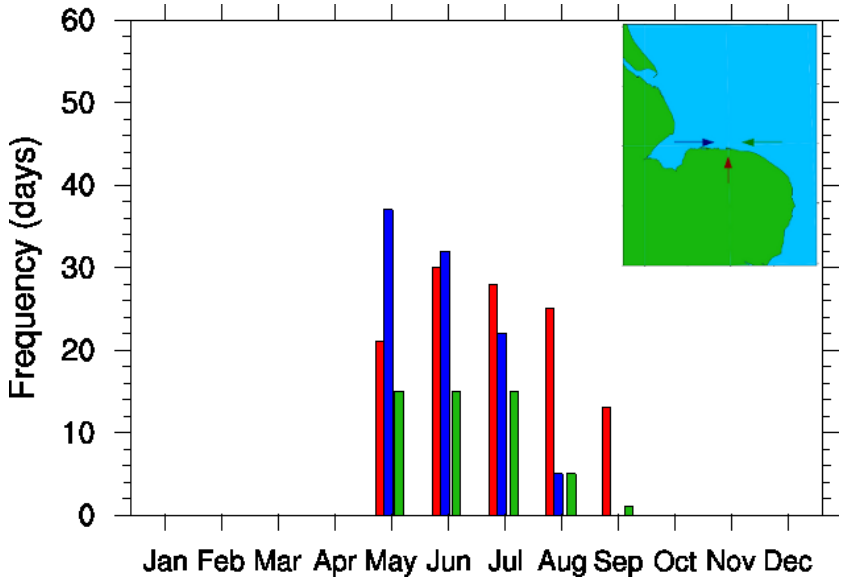

Figure 5.9: Sea breeze frequencies for the period May 2002- September 2012 for the coast of north Norfolk. *Pure*, *corkscrew* and *backdoor* sea breezes are shown in red, blue and green respectively. The orientation of the gradient wind with respect to the coastline for each sea breeze type is shown in the map as arrows of the respective colours

5.2 Results

5.2.1 North Norfolk

The frequencies of each sea breeze type for the study period are shown in Fig. 5.9. In all, 117 *pure*, 96 *corkscrew* and 51 *backdoor* sea breezes were identified. Considering the west-east orientation of the coast, the results of the identification method appear to support the logic of an increase in warm southerly airflow during the summer months (Section 6.1). The distribution of sea breeze events throughout the year agrees well with the climatology of Simpson *et al.* (1977), where sea breezes are most common during late Spring and early Summer, when the land-sea thermal contrast is at a maximum. This confines these sea breeze events to a *season* from May to September. The number of *pure* events predicted are significantly higher than those observed by Simpson *et al.* (1977), however, taking into account the comparatively warm study period (Fig. 5.7) in relation to previous decades, it is not altogether unexpected.

The relative frequencies of the other types of sea breeze also compare well when considering the orientation of the coastline. *Pure* sea breezes are produced with an offshore gradient wind and so, in this case, the flow direction is southerly; a more frequent occurrence during the Summer months (Figs. 5.9 and 5.2). *Corkscrew* sea breezes are the most

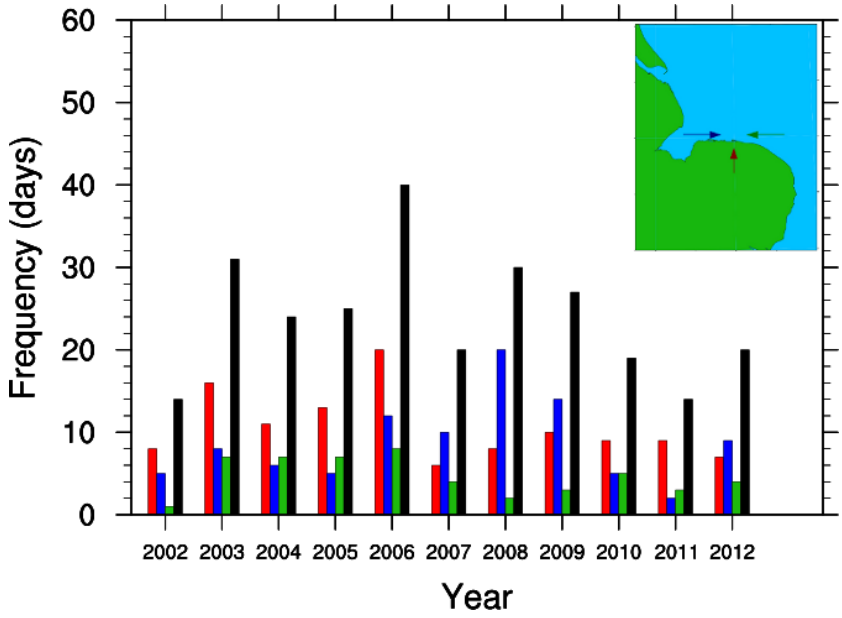

Figure 5.10: Sea breeze frequencies for the period May 2002- September 2012 for the coast of North Norfolk. *Pure*, *corkscrew* and *backdoor* sea breezes are shown in red, blue and green respectively. The total number of sea breezes are shown in black. The map shows the orientation of the gradient wind required to produce each sea breeze type in their respective colours.

common type during late Spring and early Summer, but after July, the numbers markedly drop. August corresponds with a rise in North Westerly Lamb weather type flow directions and for September, a marked rise in frequency of Westerly and South Westerly flow directions. Neither flow regime is conducive to the formation of *corkscrew* sea breezes on the North Norfolk coast. *Backdoor* sea breezes are also more common during Spring and early Summer.

The number of sea breezes per year fluctuates quite substantially, with the impact of heat-waves of 2003 and 2006 clearly being visible as two separate peaks (Fig. 5.10). However, 2008 and 2009, which were not particularly renowned as warm Summers, were predicted 30 and 28 sea breezes respectively. The dominance of the *pure* type sea breeze is apparent up to 2006, but afterwards, there appears to be a decline in *pure* and a rise in *corkscrew* sea breeze numbers. The decline in *pure* sea breeze numbers is associated with a decline in the frequency of southerly flow regimes after 2006. The rise in *corkscrew* sea breeze numbers is associated with increased westerly flow regimes.

The *pure* sea breeze composite centres an anticyclone 10km to the north of the Netherlands, leading to southerly offshore flow on the North Norfolk coast (Fig. 5.11). The

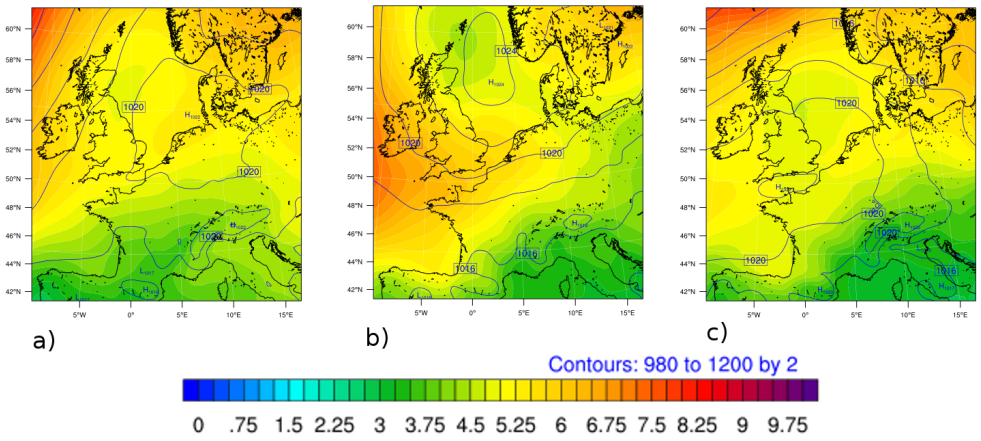

Figure 5.11: 12:00 UTC composite plots of sea level pressure (contours) and its standard deviation (shading) for North Norfolk a) *pure* (117 events), b) *corkscrew* (96 events) and c) *backdoor* (51 events) sea breezes.

anticyclone drags in warm continental air into southern Britain, which causes large temperature differences between the land and sea (Fig. 5.12). Evidence for an offshore calm zone and rotation of the surface wind field to the onshore direction begins as early as 09:00 UTC (Fig. 5.12). The calm zone, initially extending to 15km offshore from the eastern section of the coastline travels westward and progressively becomes detached from the eastern section of the coastline. A secondary calm zone centred in the south east of the Wash, progressively travels north east as the sea breeze forms, so that by 12:00 UTC, a single calm zone is present orientated south west to north east.

Off the coasts of Lincolnshire and East Norfolk, coastal jets are formed from 10:00 UTC which extend approximately 6km offshore in both cases, although the jet off East Norfolk is weaker. Furthermore, the divergence associated with the shore parallel flow forms *corkscrew* sea breezes, denoted by the increased degree of onshore flow extending inland at both the Lincolnshire and the East Norfolk coastlines.

Over time, the easterly component of the 10m flow intensifies and its magnitude increases to the extent that by 13:00 UTC the calm zone is no longer evident. The jets remain and intensify, so that by 15:00 UTC, much of North Norfolk and Lincolnshire experience wind speeds in excess of 8ms^{-1}. The sea breeze inland reaches approximately 15km, as denoted by the line of convergence in Fig. ? and dissipates from east to west entirely by 19:00 UTC. No visible offshore structure is evident for this complex coastline,

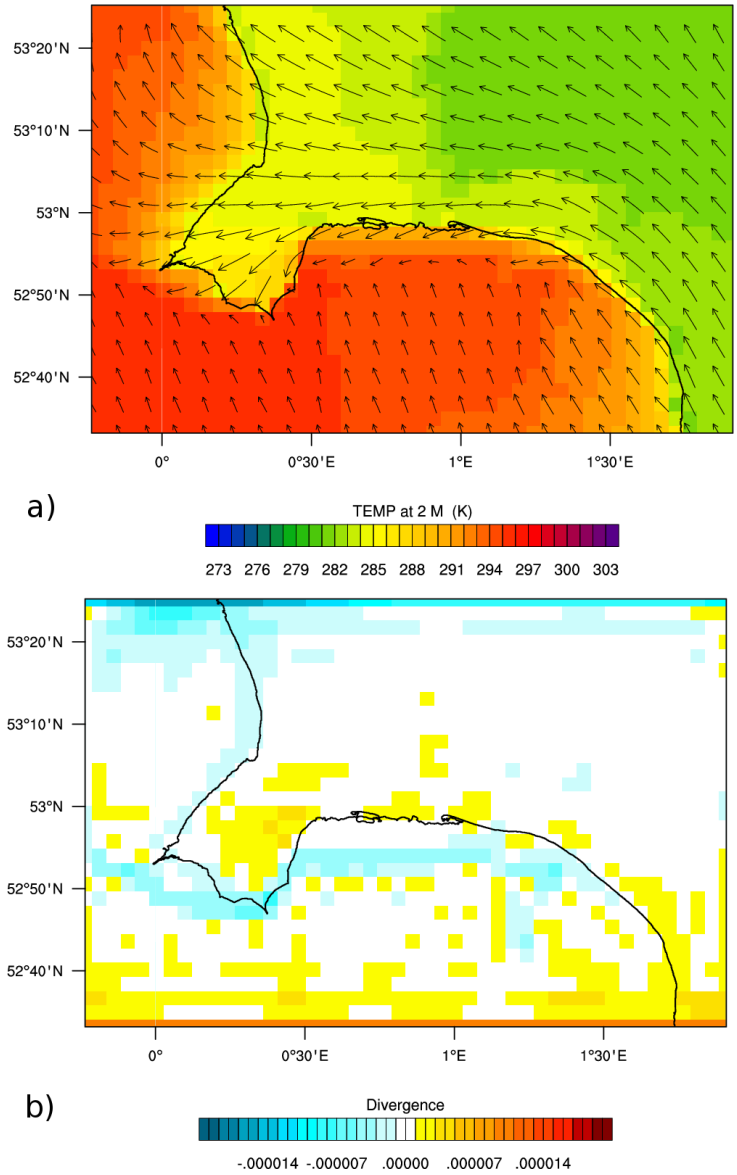

Figure 5.12: Composite plots for the 117 selected *pure* sea breeze days for the coast of North Norfolk at 16:00 UTC. Filled contours in a) denote 2m temperature (K) and b) divergence (s^{-1}).

however the presence of the calm zones in the early stages of *pure* sea breeze development occur precisely in the location of the Lynn and Inner Dowsing wind farm until 13:00 UTC.

A cross-section plotted through 52.5N to 53.5N at constant longitude of 1E reveals the presence of a sea breeze structure (Fig. 5.14), however the surface onshore flow component is weak and does not extend to the offshore environment. Considering the degree of sensitivity of the *pure* sea breeze to the strength of the offshore gradient wind, the presence of the sea breeze signal in the composite is a good indication that the identification

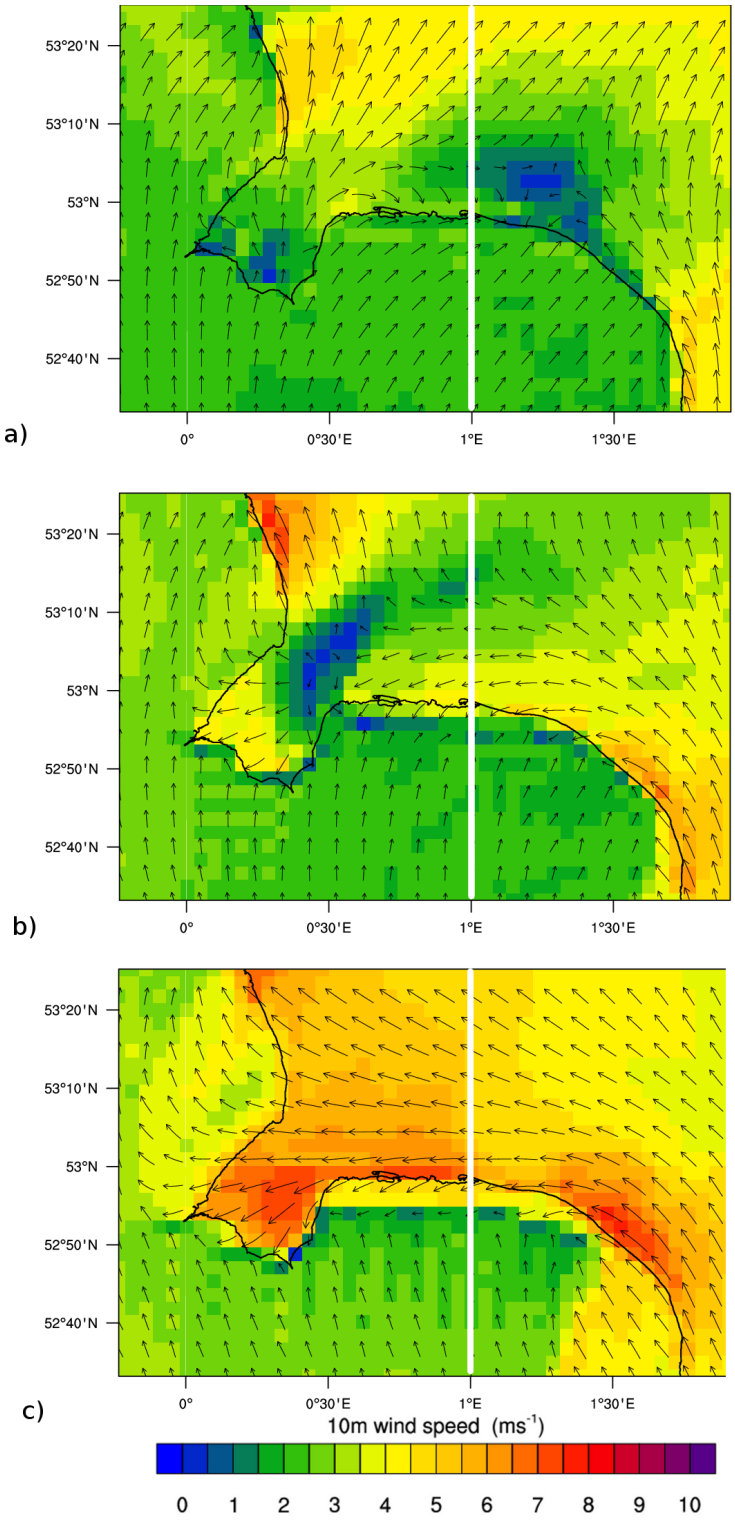

Figure 5.13: Composites of the 117 *pure* sea breeze events identified for North Norfolk by the identification method at a) 09:00 UTC, b) 12:00 UTC and c) 15:00 UTC. Filled contours indicate wind speed and vectors indicate flow direction. The white line indicates the position of the cross-section in Fig. 5.14.

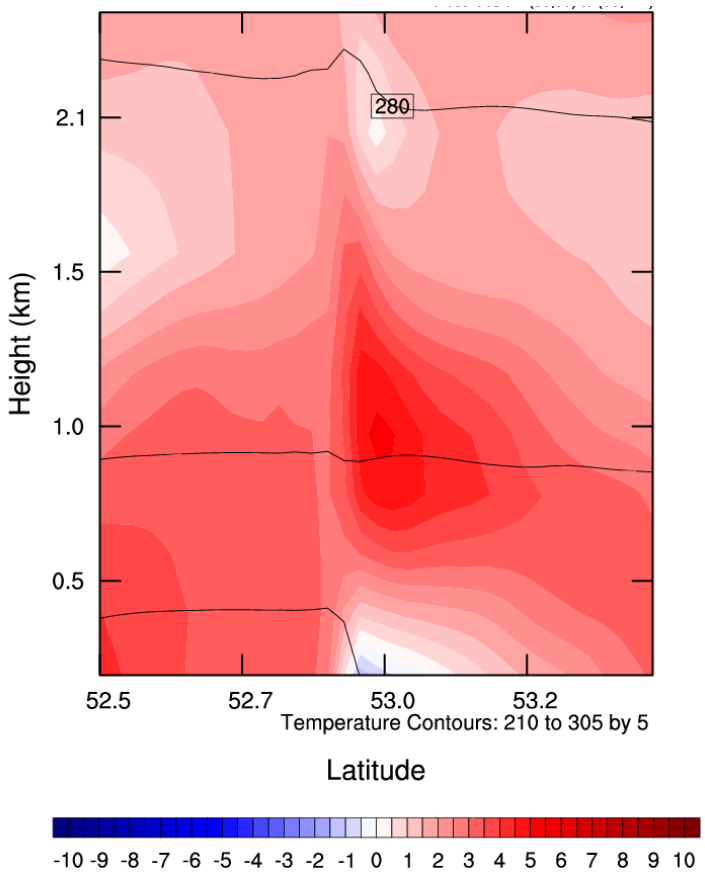

Figure 5.14: Composite cross-section from 52.5N to 53.5N, 1E (Fig. 5.13), at 15:00 UTC of v-wind component on *pure* sea breeze days, where the v component is defined as positive perpendicular offshore. Temperature (K) is also indicated by the solid black lines

method has correctly identified sufficient sea breeze days. Naturally, it is entirely plausible that sea breeze days are incorrectly rejected and so further analysis of the success of the method is covered in Section 6.3.

For the 96 composite *corkscrew* sea breezes predicted for North Norfolk, there is an elongated anticyclone orientated north-south centred approximately 50km to the east of Scotland (Fig. 5.11b). The thermal contrast is much weaker than the *pure* sea breeze type, though a convergence line does form further inland than for the *pure* sea breeze (Fig 5.15). The convergence line is not apparent advancing inland prior to 14:00 UTC, and so it would appear that a frontal region does not occur immediately as the sea breeze is formed.

The composite *corkscrew* results show higher 10m wind speeds over the sea than over the land at 09:00 UTC (Fig. 5.16). The maximum 10m wind speeds are between 7-8ms^{-1} near the coasts of The Wash, Lincolnshire and the Eastern end of North Norfolk. A slight northerly component to the easterly 10m winds make determination of the presence

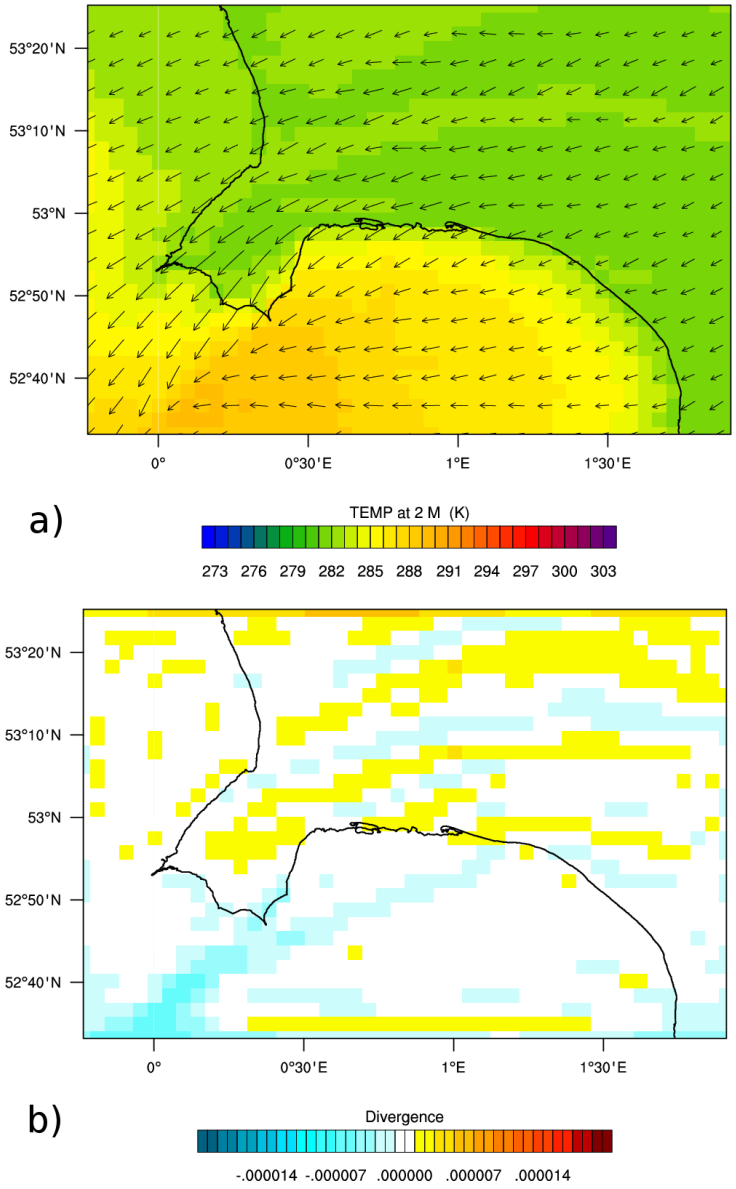

Figure 5.15: Composite plots for the 96 selected *corkscrew* sea breeze days for the coast of North Norfolk at 15:00 UTC. Filled contours in a) denote 2m temperature (K) and b) divergence (s^{-1}).

of a sea breeze difficult from the surface wind speeds alone. However, the northerly wind component does gradually increase as the thermal pressure gradient establishes. Furthermore, the 10m wind field is entirely easterly where the orientation of the North Norfolk coast changes and so, as expected for a *corkscrew* sea breeze, there is the presence of weak divergence at the North Norfolk coast.

The divergence pattern over the southern North Sea has a peculiar wave structure and is associated with low level stratus or coastal fog (Fig. 5.17). By 11:00 UTC the fog has evaporated, but begins to reform and encroach the East Norfolk coast by 16:00 UTC. Considering the orientation of the anticyclone, relative to the North Norfolk coast, the

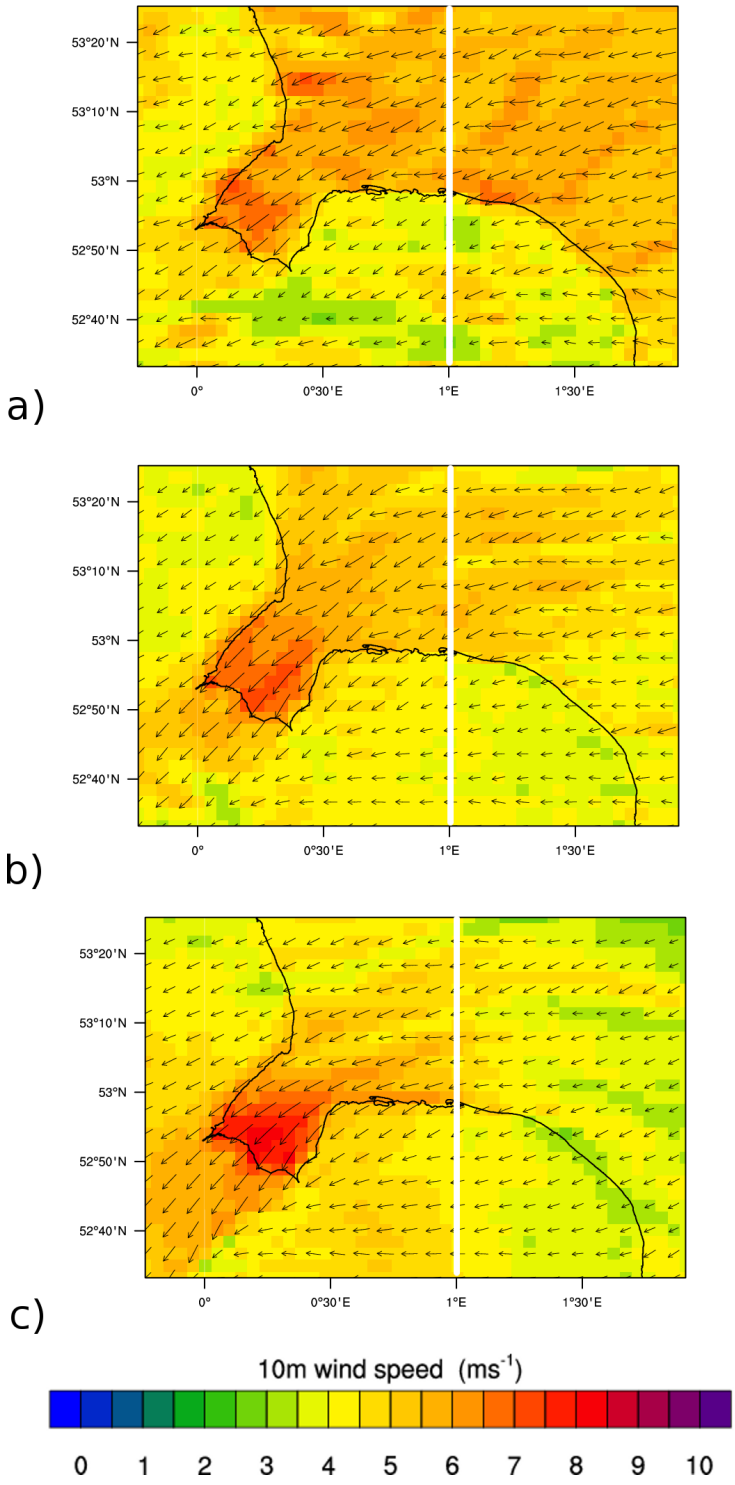

Figure 5.16: Composites of the 96 *corkscrew* sea breeze events identified for North Norfolk by the identification method at a) 09:00 UTC, b) 12:00 UTC and c) 15:00 UTC. Filled contours indicate wind speed and vectors indicate flow direction. The position of the cross-section in Fig. 5.19 is denoted by the white line.

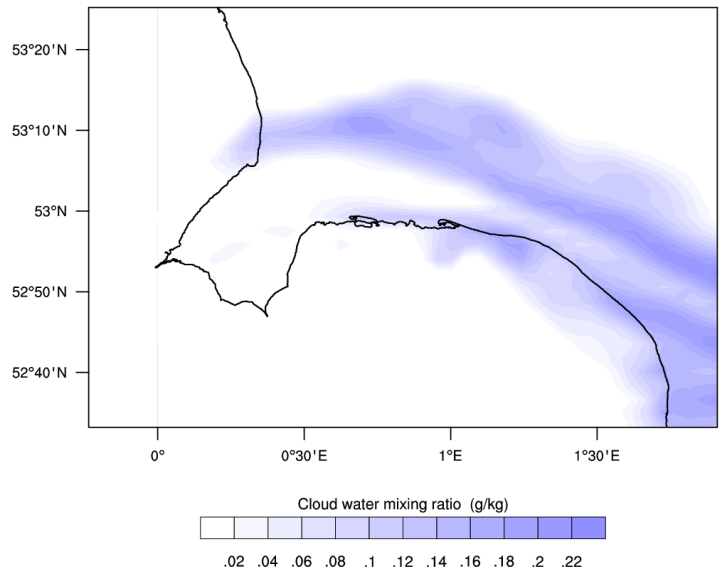

Figure 5.17: Cloud water mixing ratio (gkg^{-1}) composite of the 96 *corkscrew* sea breeze events at 18:00 UTC for the lowest eta level (0.998).

presence of low level stratus can be explained. The Northerly winds associated with the anticyclone bring the cooler air southwards, which then pick up the moisture from the relatively warm sea. It has been noted by Tang (2012) that NWP models over predict the degree of coastal fog and mist in simulations because of a poor representation of the diurnal cycle of the near coast SST. Tang (2012) argues that the SST diurnal cycle can reduce the land-sea thermal contrast on average by 1.5K in open water and that near to a coastal boundary this difference can be as much as 4.5K. It could therefore be inferred that the degree of coastal fog may, in reality be less for *corkscrew* sea breezes, however, the conclusions of Tang (2012) have been drawn from only a single case study, and therefore more research is required in this subject area.

As the 10m wind speed gains strength a line of convergence is formed oriented north-east to south west from the eastern corner of the Wash. By 14:00 UTC a second convergence line is visible and develops to extend the original line to the North East coast of Norfolk. This results in the generation of weak surface instability as denoted by Fig. 5.18.

The cross-section from 52.5N to 53.5N, 1.0E is also less clear than for the *pure* composite, however, a sea breeze structure does exist which is not unlike that for the idealized cases in Section 4.1.3 when considering the variability in gradient wind speed for the 96 *corkscrew* cases (Fig. 5.19).

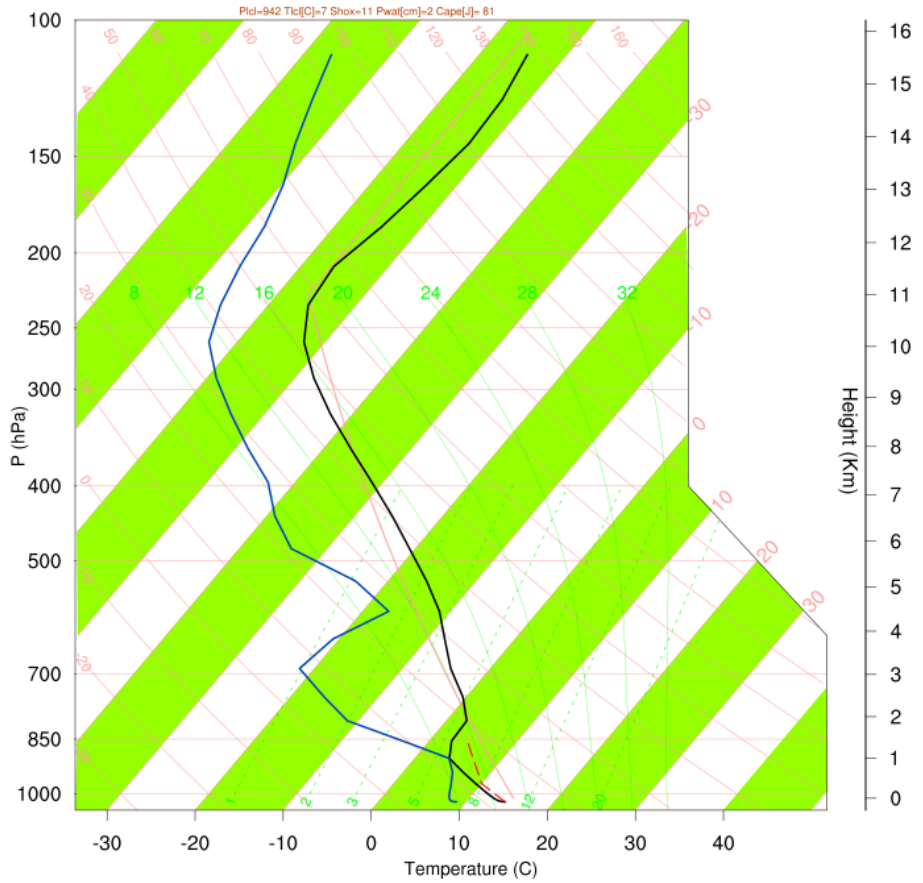

Figure 5.18: Composite Skew-T at 52.67°N and 0.2°E of the 96 *corkscrew* sea breeze types at 15:00 UTC.

The *backdoor* type sea breeze is the least common according to the identification method with 51 occurrences during the 11 year study period. Considering the dominance of the westerly flow regimes in Table 5.1, it initially may be quite surprising that there are so few *backdoor* sea breezes. However, the *backdoor* sea breeze gradient wind threshold of 5ms^{-1} used in stage 3 of the identification method is comparatively small, so it is likely the case that more days are rejected at this stage. Further analysis of the performance of each filter can be found in section 6.3.

The composite of the 51 *backdoor* sea breezes places an elongated anticyclone, centred over the English Channel, producing light westerly winds across the coast of North Norfolk (Fig. 5.11). Unlike the other composites, the *backdoor* sea breeze shows the development of thermal lows over the land surface as early as 09:00 UTC (Fig. 5.20). The Wash develops a calm zone near to the eastern coastline and a maxima in surface flow on the western side, not unlike the dual-coast configuration for *corkscrew* and *backdoor* idealized sea breeze simulations in section 4.2.3 (Fig. 5.21). As time progresses, the

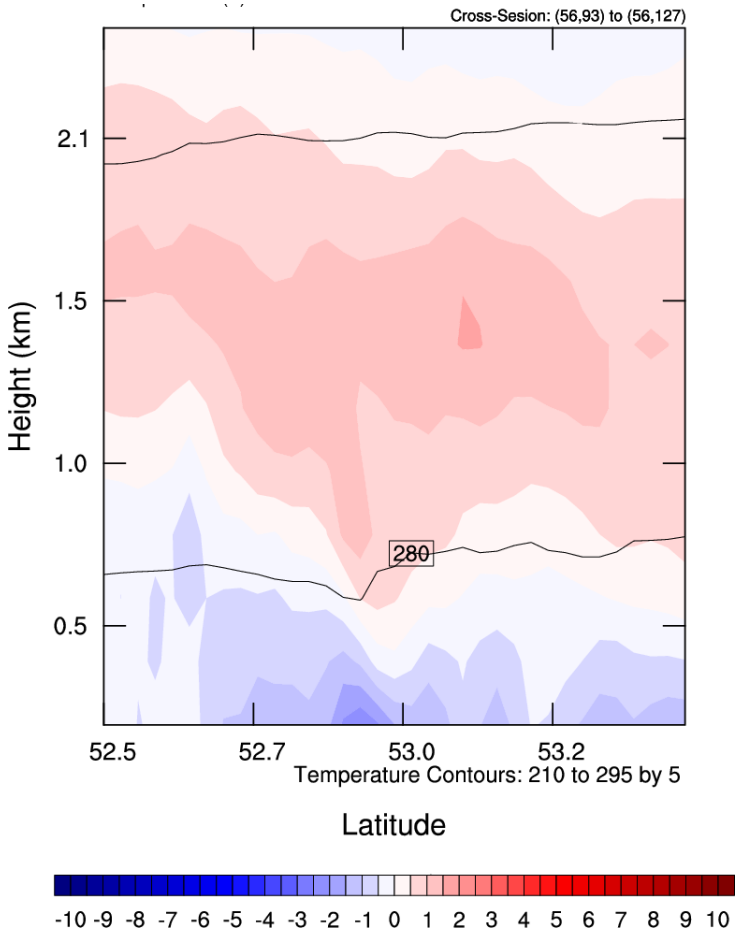

Figure 5.19: Composite cross-section from 52.5N to 53.5N, 1.0E (Fig. 5.16), at 15:00 UTC of v-wind component (ms^{-1}) of the 96 *corkscrew* sea breeze days, where the v component is defined as positive perpendicular offshore. Temperature (K) is also indicated by the solid black lines

winds on the west coast of the Wash and Lincolnshire intensify and a *pure*, *corkscrew* and *backdoor* sea breeze is formed on each of the three coasts of the Wash.

By 11:00 UTC, two calm zones exist, one extending approximately 6km from the eastern coast of the Wash, the other approximately 15km offshore from the coast of North Norfolk. The calm zone in the Wash progressively extends north east towards the second region, while the second region moves north eastwards, producing weak *Cyclonic* rotation. Similarly, the relatively intense winds on the western coast extend their reach to approximately 15km offshore up through the coast of Lincolnshire. As the weak *Cyclonic* circulation travels north east, the 10m wind direction at the coast changes to an easterly and forms a jet. The formation of the jet suppresses the development of the calm zone originating in the Wash by 14:00 UTC. The zone of high wind speed rapidly intensifies and spreads so that by 16:00 UTC, most of the offshore study area has a 10m wind speed of $8ms^{-1}$.

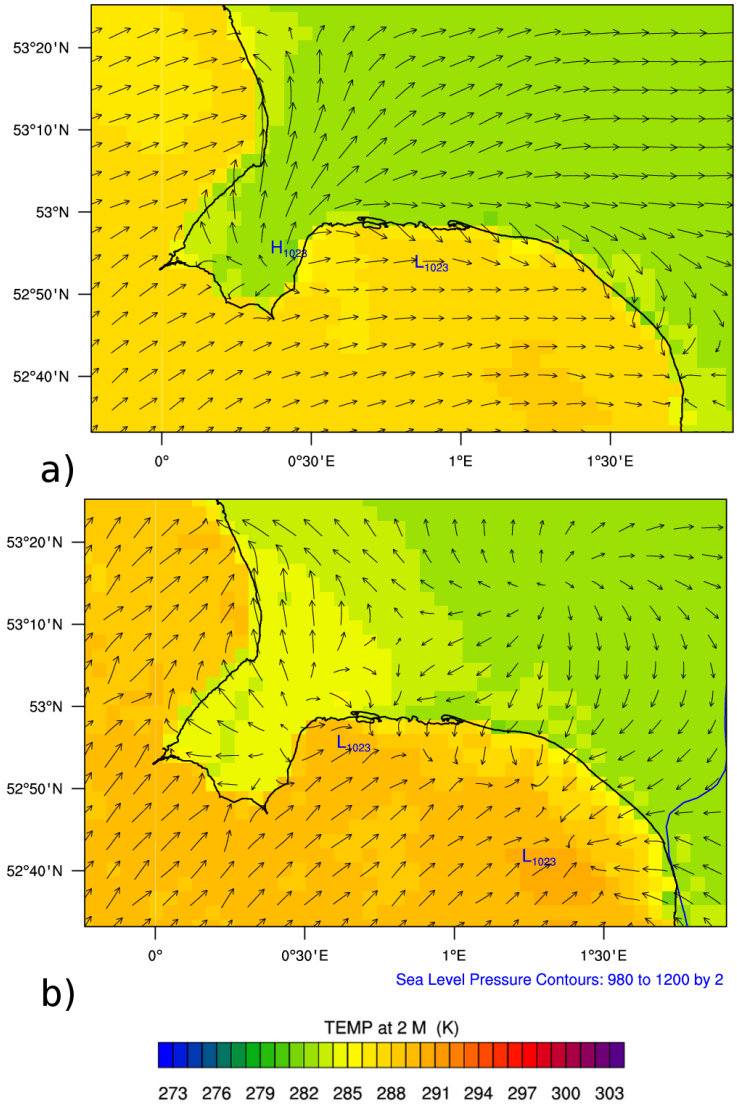

Figure 5.20: Composite of 51 *backdoor* sea breezes at a) 09:00 UTC and b) 12:00 UTC. Filled contours indicate 2m temperature (K) and vectors represent 10m wind speed. Also shown are sea level pressure spot maxima and minima.

Onshore, there are signs of *backdoor* sea breeze development as early as 09:00 UTC and a convergence line initially covers the Wash, North and East Norfolk and parts of Lincolnshire. By 13:00 UTC, the sea breeze advances more rapidly from North East Norfolk, as the position of the body of *Cyclonic* rotation causes air to stream directly into North East Norfolk. Evidence of a sea breeze structure exists for the North coast of Norfolk from 09:00 UTC to 14:00 UTC; until the easterly flow begins to dominate.

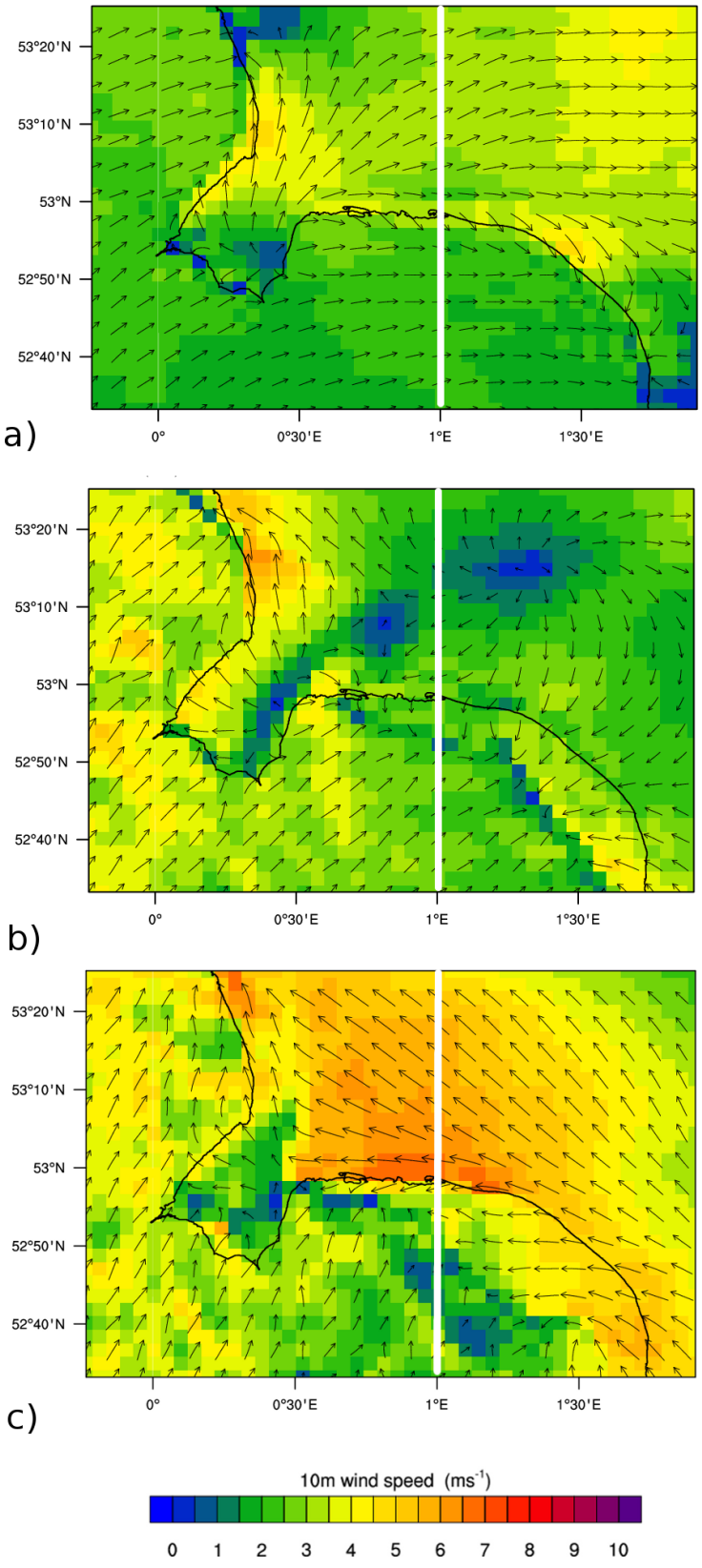

Figure 5.21: Composites of the 51 *backdoor* sea breeze events identified for North Norfolk by the identification method at a) 09:00 UTC, b) 12:00 UTC and c) 15:00 UTC. Filled contours indicate wind speed and vectors indicate flow direction. The position of the cross-section in Fig. 5.22 is depicted as the white line.

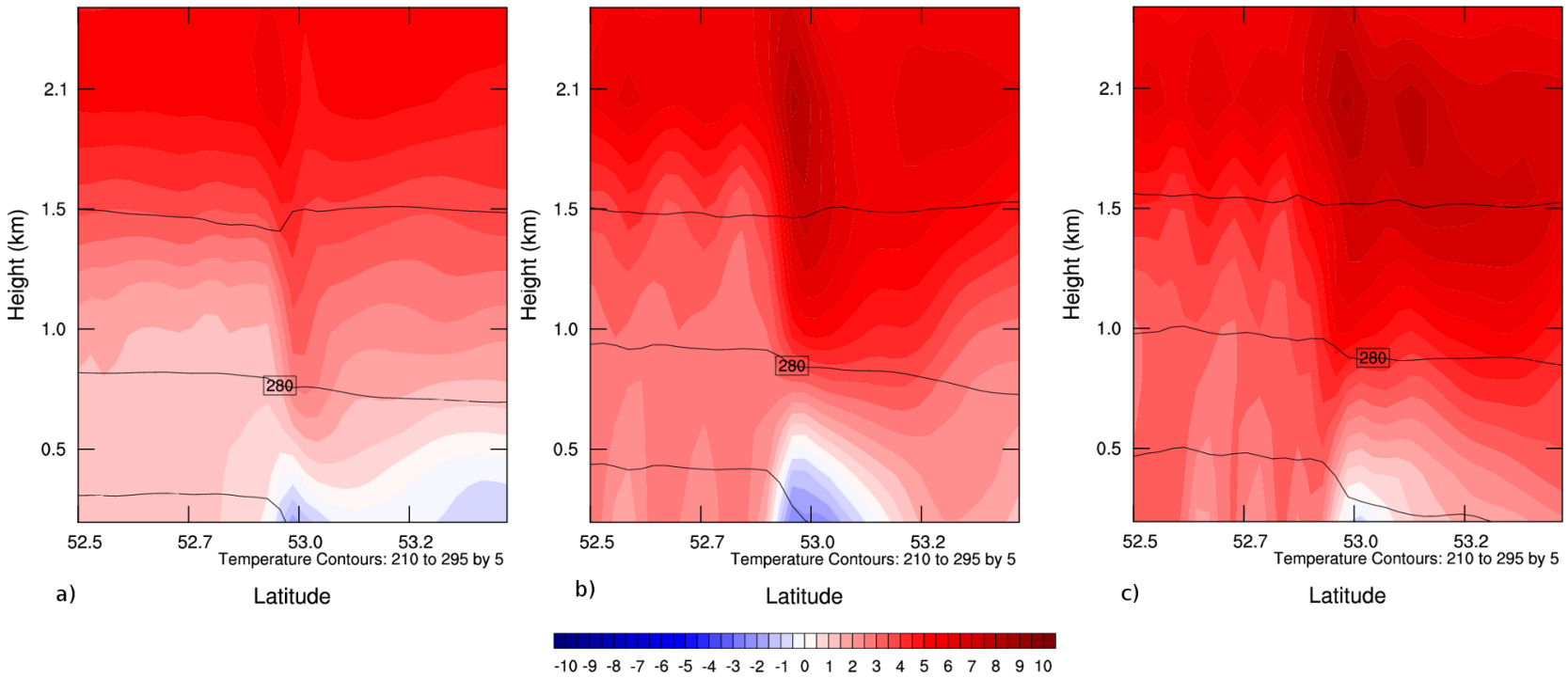

Figure 5.22: Cross-section from 52.5N to 53.5N, 1.0E (Fig. 5.21) at a) 10:00 UTC, b) 12:00 UTC and c) 14:00 UTC of 51 composite *backdoor* sea breeze v-winds (ms^{-1}), where the v component is defined as positive perpendicular offshore. Temperature (K) is also indicated by the solid black lines.

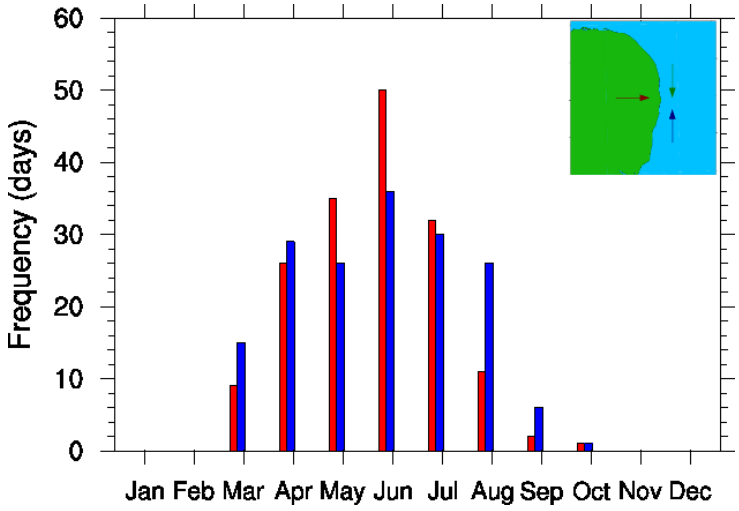

Figure 5.23: Sea breeze frequencies for the period May 2002- September 2012 for the coast of East Norfolk. *Pure*, *corkscrew* and *backdoor* sea breezes are shown in red, blue and green respectively if present.

The impact of using the sea breeze identification method on the North Norfolk coast has not only revealed the inter-annual variability, the seasonality and the characteristics of each sea breeze type, but also the impact of other sea breezes on the coasts of Lincolnshire and East Norfolk. The *corkscrew* sea breeze which forms off the Lincolnshire coast, for example, when a *pure* sea breeze forms off North Norfolk, impacts the windfields of the offshore environment, as well as the *pure* North Norfolk Sea breeze, by the formation of coastal jets. The presence of coastal jets and calm zones, which form with the *pure* sea breeze, both have the potential to impact the Lynn and Inner Dowsing wind farm.

5.2.2 East Norfolk

In contrast to the coast of North Norfolk, East Norfolk sea breeze occurrence is not restricted to the traditional sea breeze season (Fig. 5.23). Traditionally, sea breezes are expected from May to September, though April is sometimes included as part of the season. However, as many as 24 sea breezes are predicted as early as March, and 2 were even predicted to occur as late as October. In all, 166 *pure* and 169 *corkscrew* sea breezes were predicted. No *backdoor* types were predicted for this coastline.

In principle, the lack of *backdoor* sea breezes is logical as in order to produce a *backdoor* sea breeze, there must be a northerly gradient wind. Therefore, it is both unlikely and difficult to create such a flow pattern, where the land-sea thermal contrast is sufficient to trigger a *backdoor* sea breeze.

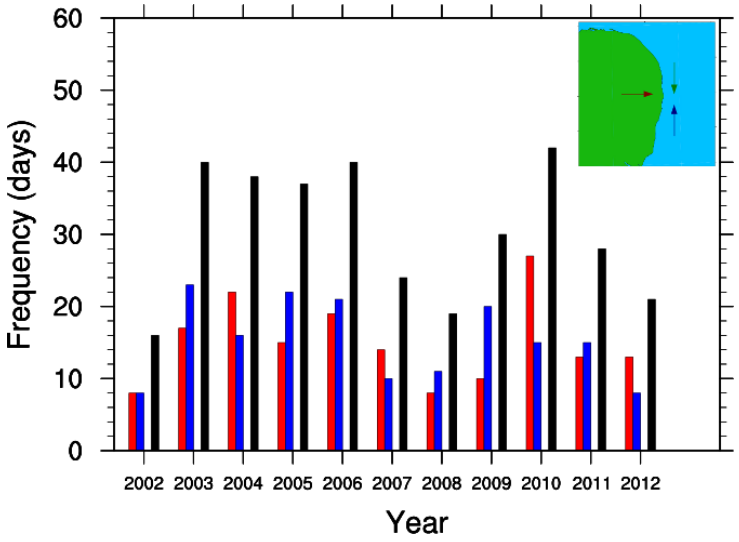

Figure 5.24: Sea breeze frequencies for the period May 2002- September 2012 for the coast of east Norfolk. *Pure*, *corkscrew* and *backdoor* sea breezes are shown in red, blue and green respectively. Shown in black are the total number of sea breezes

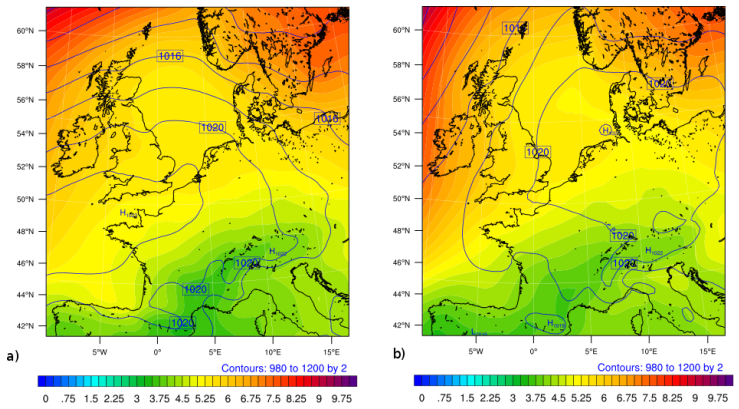

Figure 5.25: 12:00 UTC composite plots of sea level pressure (contours) and its standard deviation (shading) for East Norfolk a) *pure* (166 events) and b) *corkscrew* (169 events) sea breezes.

Intuitively, it may be expected that more sea breezes are experienced in May and June, where the warmer air temperatures have still yet to significantly affect the SST. Since this climatology is over 11 seasons, there is strong inter-annual variability which skews the distribution (Fig. 5.24). Note that there are once again years which produce a high number of sea breezes which do not especially conform with the warmest Summers, for example the 2010, 2005 and 2004 seasons produce a comparable number of sea breezes to 2003 and 2006, despite being, on average, 1K cooler than these warm periods.

The position of the anticyclone for the 166 *pure* sea breezes predicted on the east Norfolk coast is the same as for the *backdoor* type sea breeze predicted for north Norfolk; that is, centred over the English Channel (Fig. 5.25). Indeed, 48 out of the 51 days determined by the identification method to be *backdoor* sea breezes on the coast of North

Norfolk are included in the list of 166 *pure* sea breeze days for East Norfolk.

The composites of the 10m wind speed evolution reveal that, in this case, the *pure* sea breeze causes an increase in wind speed near to the coast as it forms (Fig. 5.26). At 09:00 UTC, a weak offshore flow is evident ranging from 0.5-1.5ms^{-1}. Offshore, the weak flow from the land extends approximately 15km offshore in the North of the region to approximately 50km in the south. At maximum, the 10m wind speed offshore is 3-3.5ms^{-1}, but there is a northerly component which increases towards the southern end of the coast so that the flow direction in the southern extremities of the region is from the north east.

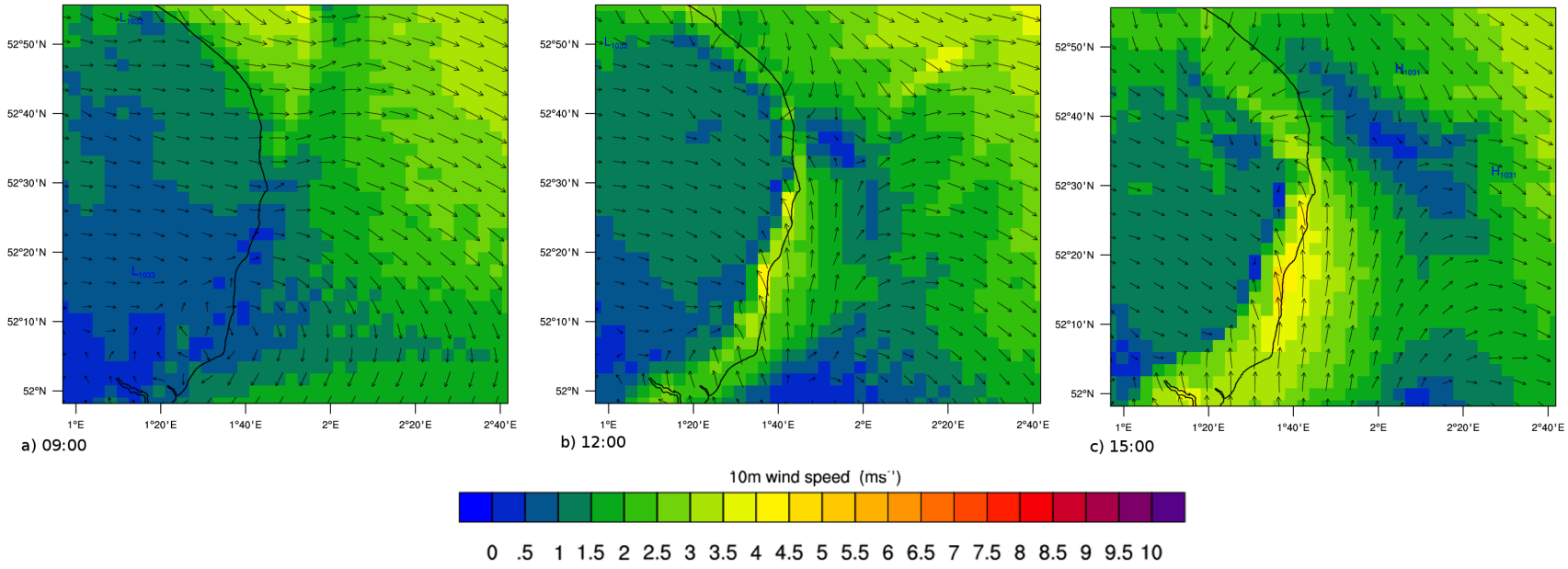

Figure 5.26: Composites of the 166 *pure* sea breeze events identified for East Norfolk by the identification method at a) 09:00 UTC, b) 12:00 UTC and c) 15:00 UTC. Filled contours indicate 10m wind speed (ms^{-1}) and vectors indicate flow direction

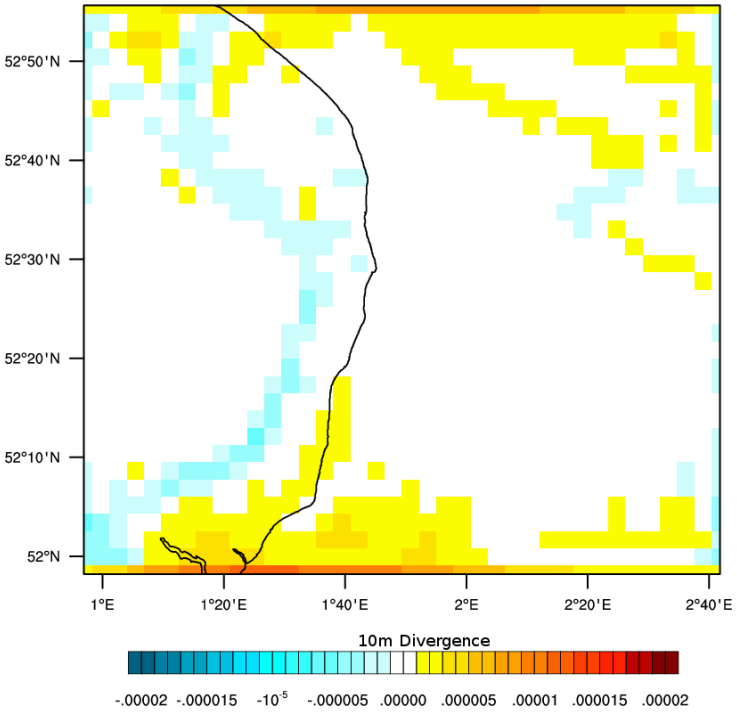

Figure 5.27: Composite of the 166 *pure* sea breeze events forming off East Norfolk. Filled boxes indicate 10m divergence (s^{-1}), with negative regions representing convergence, at 16:00 UTC.

As the *pure* sea breeze forms, the 10m wind speed increases to a maximum of $4ms^{-1}$ in the central part of the coast and extends offshore so that the calm region now lies approximately 20km offshore. Towards the outer extremes, where the increase in 10m wind speed is weaker due to the sea breeze, less offshore advancement is evident and so the calm zone is closer to the coast. By 15:00 UTC, the *pure* sea breeze in the central part of the coast has increased in offshore extent so that two calm zones exist at the upper and lower ends of the North Norfolk coastline, approximately 15km across and at most 20km offshore.

There is more onshore advancement of the sea breeze in the upper and lower extremes of the coastline, where the sea breeze is weaker. This corresponds to the regions where the calm zones are closer to the coast and where the coast itself is orientated differently. The changing orientation of the coast relative to the gradient wind enables the formation of a *backdoor* sea breeze in the northern coast and a *corkscrew* sea breeze on the southern extreme. The relative differences between the different sea breeze onshore advancement are clearly visible as the convergence lines in Fig. 5.27

Similarly for the *corkscrew* sea breeze, the sea level pressure composite is similar in respect to the *pure* type sea breeze forming off the coast of North Norfolk (Fig. 5.25). The

centre of the anticyclone is 10km to the west of Denmark, generating a southerly flow over East Anglia. Of the North Norfolk *pure* type sea breezes, 101 of the 117 days identified were also selected as days producing *corkscrew* sea breezes off East Norfolk. Therefore, the number of *corkscrew* sea breezes forming off the East Norfolk coast is greater than the number of *pure* events forming off North Norfolk, and not identical as what could be inferred from the gradient wind orientation. This is likely due to the $9ms^{-1}$ restriction on gradient wind strength imposed on the *pure* type identification criteria which is not imposed on *corkscrew* types.

In the case of the *corkscrew* composite, the 10m winds are orientated to the north, so that if the type of sea breeze formed were to be judged simply by the surface winds, it would be classed as a *backdoor* type. They are also very weak. Over the land, the 10m wind is calm, and does not become greater than $1ms^{-1}$, with the exception of those parts near to the coast. Over the sea, the 10m wind speed is a stronger as expected, but only reaches speeds of $3ms^{-1}$ on average. The 10m wind speed gradually increases during the day by approximately $4ms^{-1}$ away from the sea breeze. By 10:00 UTC, the sea breeze begins to form at the coast, and consequently the wind speed increases up to 6km offshore to approximately $5.5ms^{-1}$. A convergence line is evident in the southern portion of this coastline but becomes less apparent as the 10m winds move progressively onshore.

5.2.3 Suffolk and Essex

The coast of Suffolk and Essex, once again does not adhere to the traditional sea breeze season (Fig. 5.28). Despite sea breezes occurring between March to September, both the *pure* and the *backdoor* types only occur up until July for this coastline. The month in which most sea breezes occur is June, and there is a significant drop in the number of *corkscrew* sea breezes in May. Also, the number of predicted *corkscrew* circulations are much more dominant over the other types. In all 167 *corkscrew* types were predicted, compared with 46 *pure* and 13 *backdoor* types. The number of *corkscrew* types is explainable due to the dominance of the SW weather type (Table 5.1)

The annual variability does not fluctuate as much as the other coasts, however, after 2008, the number of sea breezes is more erratic (Fig. 5.29). From 2003 to 2007, the number of sea breezes is consistently over 20 per year. The years 2008, 2011 and 2012

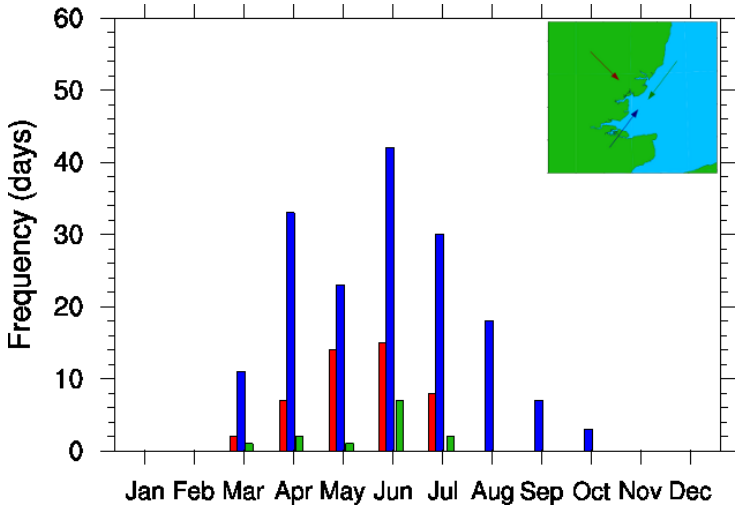

Figure 5.28: Sea breeze frequencies for the period May 2002- September 2012 for the coasts of Suffolk and Essex. *Pure*, *corkscrew* and *backdoor* sea breezes are shown in red, blue and green respectively

all produced less than 20, a reflection of the poor Summers during these years. However, the year experiencing the largest number of sea breezes is 2010 with 32. In East Anglia, the Summer of 2010 was 1K warmer than the 1971-2000 climatological average (NCIC, 2010), however, the SST anomaly was positive also. The land-sea thermal contrast is therefore not the dominant cause of the increased number of sea breezes. It is the positive south westerly anomaly which is present for the Spring and Summer period which consistently keeps the gradient wind in a favourable direction which is responsible. No year produced more than 10 of either *pure* or *backdoor* sea breeze days and the years 2002, 2004, 2008, 2010 and 2011 did not produce any *backdoor* types.

The position of the anticyclone for the *pure* sea breeze is centred almost equivalent for the East Norfolk coast with the exception of the centre being located 10km further to the west, south of Cornwall (Fig. 5.25). Indeed, 41 of the 46 *pure* sea breeze days are also classified as *pure* sea breeze days for East Norfolk.

The 46 *pure* sea breeze days produce a complex wind field pattern than the 166 *pure* sea breezes identified for East Norfolk (Compare Figs. 5.31 and **??**). Note also that *pure* sea breezes are 3 times less frequent on the Suffolk and Essex coasts than on East Norfolk. Such a high degree of *pure* sea breeze frequency variability on two coastlines in close proximity due to the differences in coastal orientation with respect to the gradient wind.

At 09:00 UTC, the 10m offshore wind speed over the land is between 1-3ms^{-1}, whilst

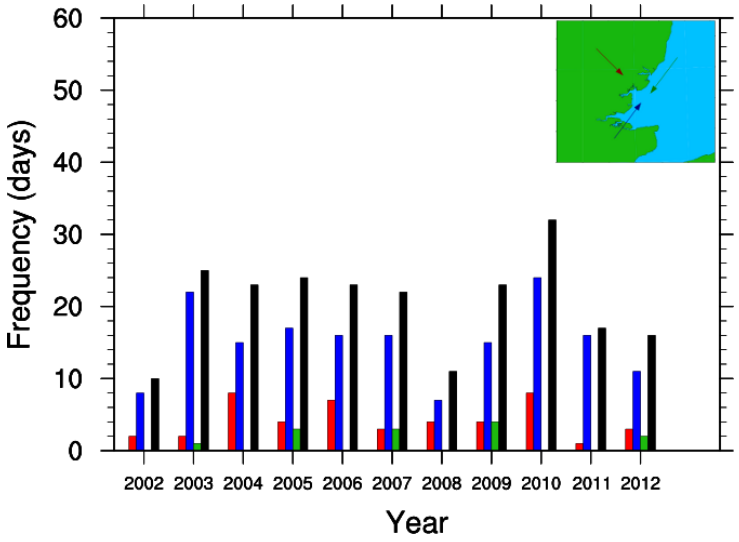

Figure 5.29: Sea breeze frequencies for the period May 2002- September 2012 for the coasts of Suffolk and Essex. *Pure*, *corkscrew* and *backdoor* sea breezes are shown in red, blue and green respectively. Shown in black are the total number of sea breezes

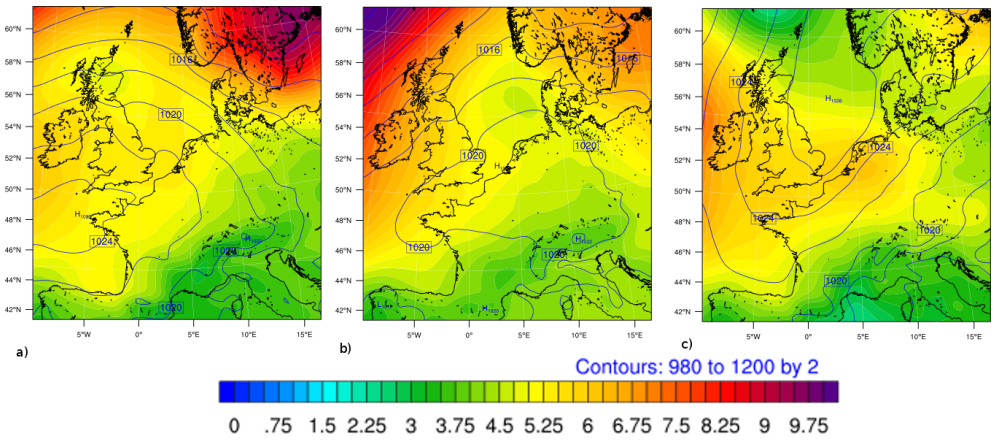

Figure 5.30: 12:00 UTC composite plots of sea level pressure (contours) and its standard deviation (shading) for a) *pure* (46 events), b) *corkscrew* (167 events) and c) *backdoor* (13 events) sea breezes forming off the coast of Suffolk and Essex. The number of *pure*, *corkscrew* and *backdoor* events are 46 and 167 and 13 respectively.

over the sea it ranges between 2-4ms^{-1} where 15km offshore and beyond the wind is south westerly and in the upper range of these values. A region of locally high 10m wind speed is present from the Thames Estuary to the north coast of Kent. By 12:00 UTC, the relatively stronger winds are confined to within 6km of the complex bays and headlands of Essex. A line of convergence is also present at the coast, marking the sea breeze boundary. In contrast to 09:00, the northern coast of Kent is now calm to 3km offshore, and a region of 1-2ms^{-1} 10m wind speed extends 3-15km offshore from the coast of Kent. By 15:00 UTC, the calm zone is confined only to the far eastern 9km of Kent, as both the combination of the sea breeze influence on the Essex coast and the development of a jet

in the Straits of Dover act to reduce the size of the calm zone.

For the 167 *corkscrew* type circulations predicted by the method, the composite in sea level pressure shows the central high pressure in the anticyclone to be within 100km of the Suffolk and Essex coast. As a consequence, the 10m winds are very light and a general flow direction is difficult to determine, however, as with East Norfolk, the 10m wind direction over the southern North Sea is again north easterly.

At 09:00 UTC, Suffolk and Essex are calm inland (Fig. 5.32). The 10m wind speed over the sea also does not reach over $3ms^{-1}$, apart from a small region of the Thames Estuary and the Straits of Dover. By 12:00 UTC, the sea breeze causes the coastal winds to strengthen up to 12km both inland and offshore. A calm region spanning a further 30km offshore covers the width of the Suffolk and Essex coast and only marginally moves offshore so that by 17:00 UTC the *corkscrew* sea breeze has extended offshore a further 9km.

The 12:00 UTC composite sea level pressure for the 13 *backdoor* sea breeze days shows an elongated anticyclone positioned south west of Scandinavia. The relative position of this coast would appear to imply that the gradient winds are rotating towards the onshore direction. Indeed, the onshore component makes the determination of whether a sea breeze is actually present in the profile very difficult to determine. No convergence line forms and the only indication of a sea breeze is the advancement of cooler air inland. In this case, there are very few *backdoor* sea breeze days selected in the climatology. Consequently, if the method selects a day which does not form a sea breeze, then it will have more weight in the average. Further analysis as to the success of the identification method is conducted in section 6.2.

5.2.4 The Netherlands

For the coast of the Netherlands, it could be expected that the sea breeze season may begin earlier than any of the British coasts. Warmer land temperatures could cause the sea breeze season to shift so that it begins earlier in the year and is more prolonged than for the UK, as stronger land-sea contrasts are established earlier in the year. Since also, there are a high number of *corkscrew* types on the coast East Anglia, it may also be expected that there will be more *backdoor* type sea breezes forming.

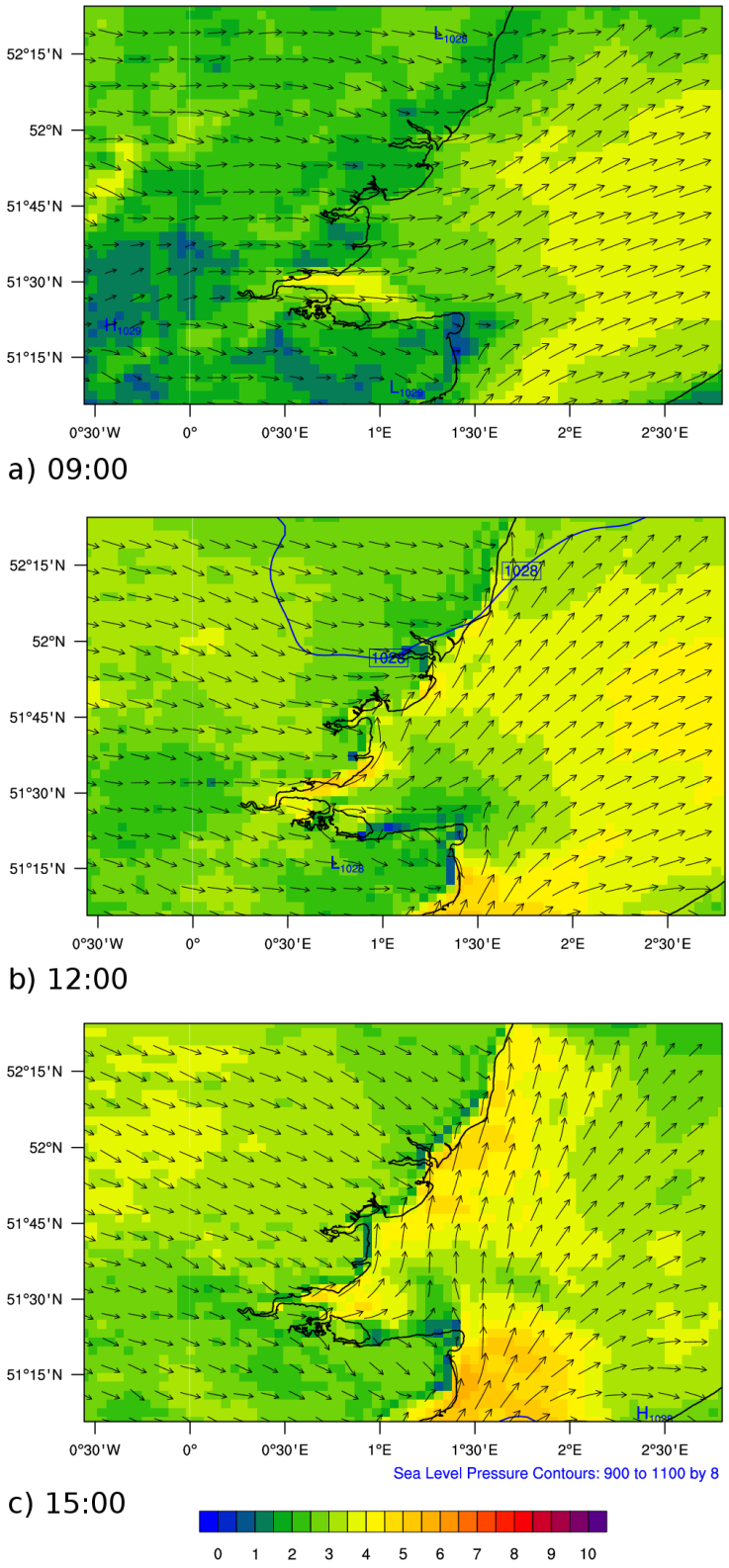

Figure 5.31: Composites of the 46 *pure* sea breeze events identified for Suffolk and Essex by the identification method at a) 09:00 UTC, b) 12:00 UTC and c) 15:00 UTC. Filled contours indicate wind speed (ms^{-1}) and vectors indicate flow direction.

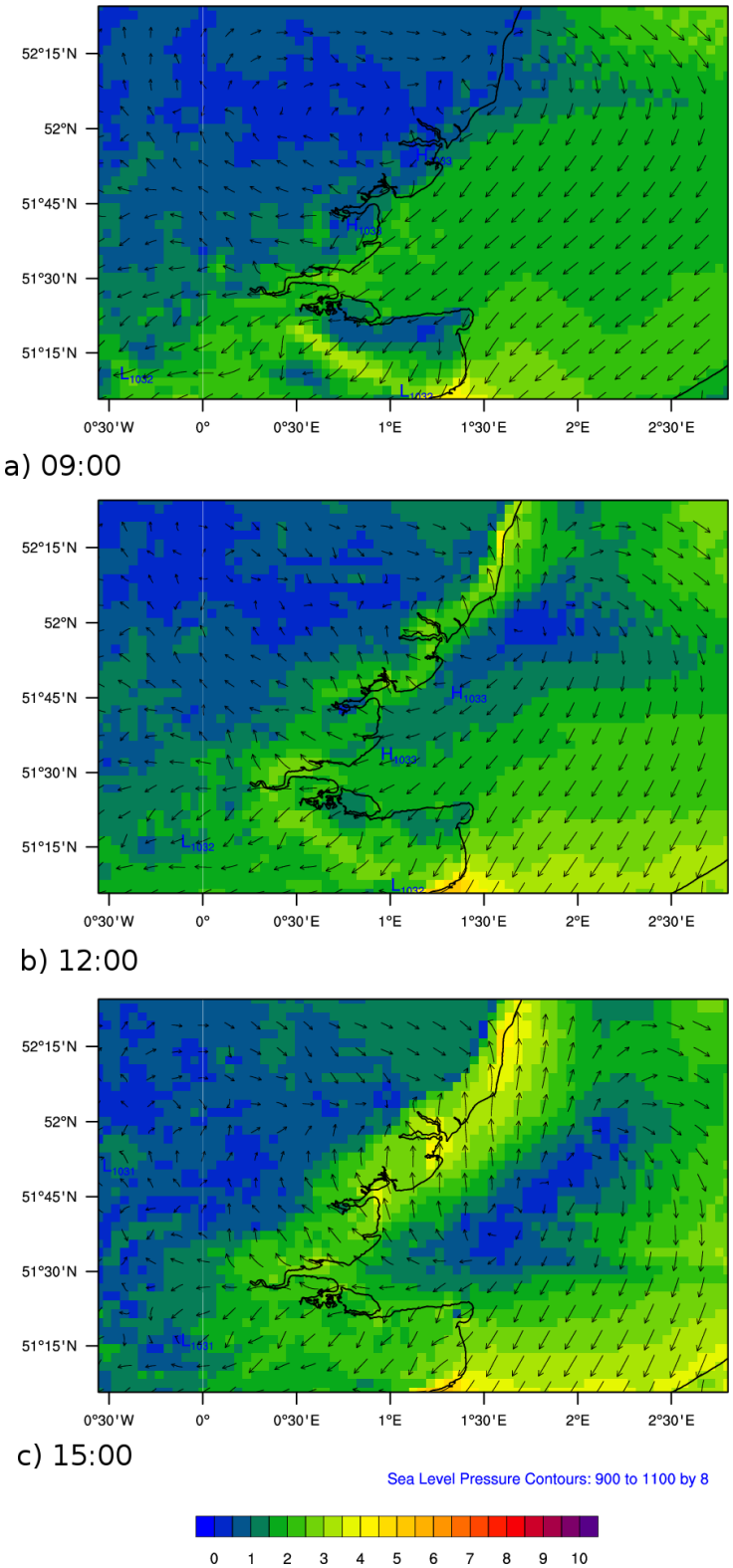

Figure 5.32: Composites of the 167 *corkscrew* sea breeze events identified for Suffolk and Essex by the identification method at a) 09:00 UTC, b) 12:00 UTC and c) 15:00 UTC. Filled contours indicate 10m wind speed (ms^{-1} and vectors indicate flow direction.

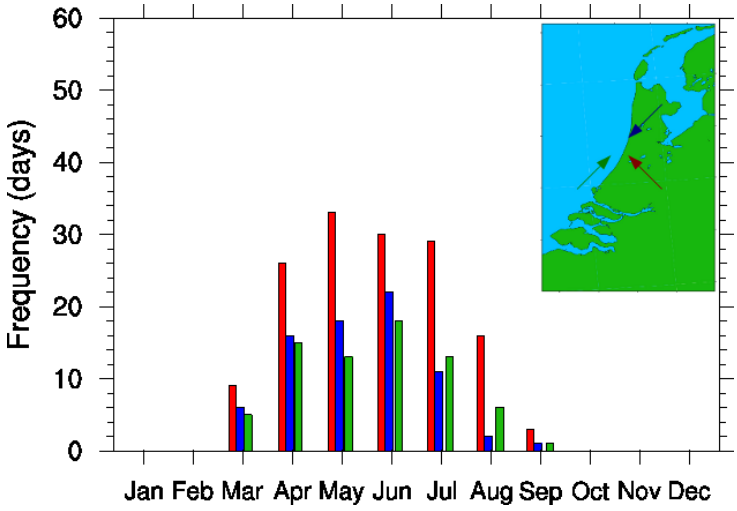

Figure 5.33: Sea breeze frequencies for the period May 2002- September 2012 for the coast of the Netherlands. *Pure*, *corkscrew* and *backdoor* sea breezes are shown in red, blue and green respectively

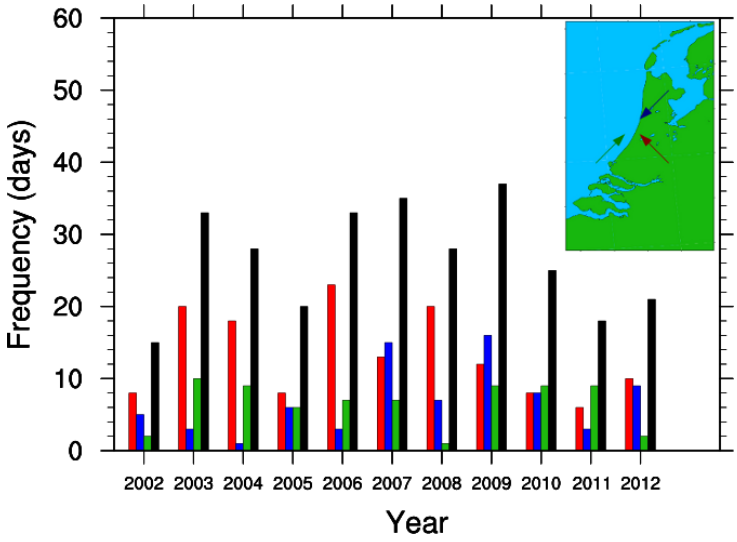

Figure 5.34: Sea breeze frequencies for the period May 2002- September 2012 for the coast of the Netherlands. *Pure*, *corkscrew* and *backdoor* sea breezes are shown in red, blue and green respectively. Shown in black are the total number of sea breezes

In total, there were 146 *pure*, 76 *corkscrew* and 71 *backdoor* sea breezes identified on the Dutch coastline (Fig. 5.34). Sea breezes were identified in all months spanning from March to September and the *pure* type sea breeze is clearly the most dominant in each month. Despite the orientation of the Dutch coast, the numbers of *corkscrew* and *backdoor* circulations are approximately the same. This is likely due to the sensitivity of the *backdoor* type circulation to the strength of the gradient wind speed rather than the frequency of specific flow regimes occurring.

The annual variability of sea breeze frequencies again is high, ranging from 18 in

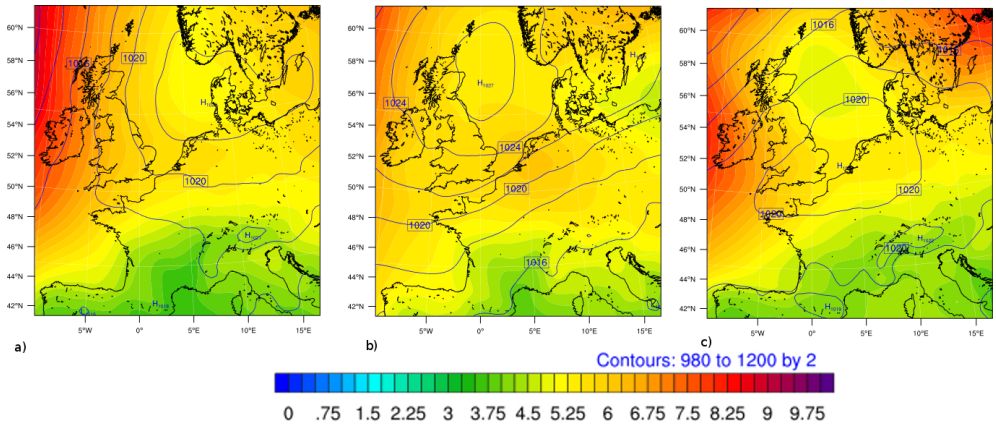

Figure 5.35: 12:00 UTC composite plots of sea level pressure (contours) and standard deviation for a) *pure* (146 events), b) *corkscrew* (76 events) and c) *backdoor* (71 events) sea breezes forming off the coast of the Netherlands.

2011 to 36 in 2009 (Fig. 5.34). Up to 2006, the most dominant type of sea breeze is the *pure* type. Beyond 2006, the distribution between sea breeze types is more equal, which is also a reflection of the nature of the latter Summers with respect to the gradient wind direction.

The sea level composite of the 146 *pure* type sea breeze shows an anticyclone centred 10km off the west coast of Denmark, creating the easterly component of gradient wind necessary to generate the offshore flow (Fig. 5.35). The 10m wind direction at 09:00 UTC is north easterly, due to surface friction and ranges from approximately 2ms^{-1} inland to 4ms^{-1} from 12km offshore (Fig. 5.36). Towards the north west, the wind speed declines as the centre of the anticyclone is neared. By 12:00 UTC, the coastal wind speed has again increased, particularly over the north western coast of the Netherlands and the coasts surrounding Ijsselmeer and Markermeer. By 15:00 UTC the composite *pure* sea breeze has advanced approximately 9km inland whilst the sea breeze at Markermeer has advanced approximately 15km inland. The discrepancy in average inland penetration is a result of the Markermeer sea breeze developing as a *corkscrew* type, due to the relative orientations of the western Dutch and southern Markermeer coasts to the easterly gradient wind. By 16:00 UTC, the *pure* sea breeze off the western coast of the Netherlands has reached approximately 12km inland, whilst the Markermeer sea breeze has advanced over 20km. There is potential, therefore for the sea breezes forming at Markermeer to interact with those forming off the western coast of the Netherlands.

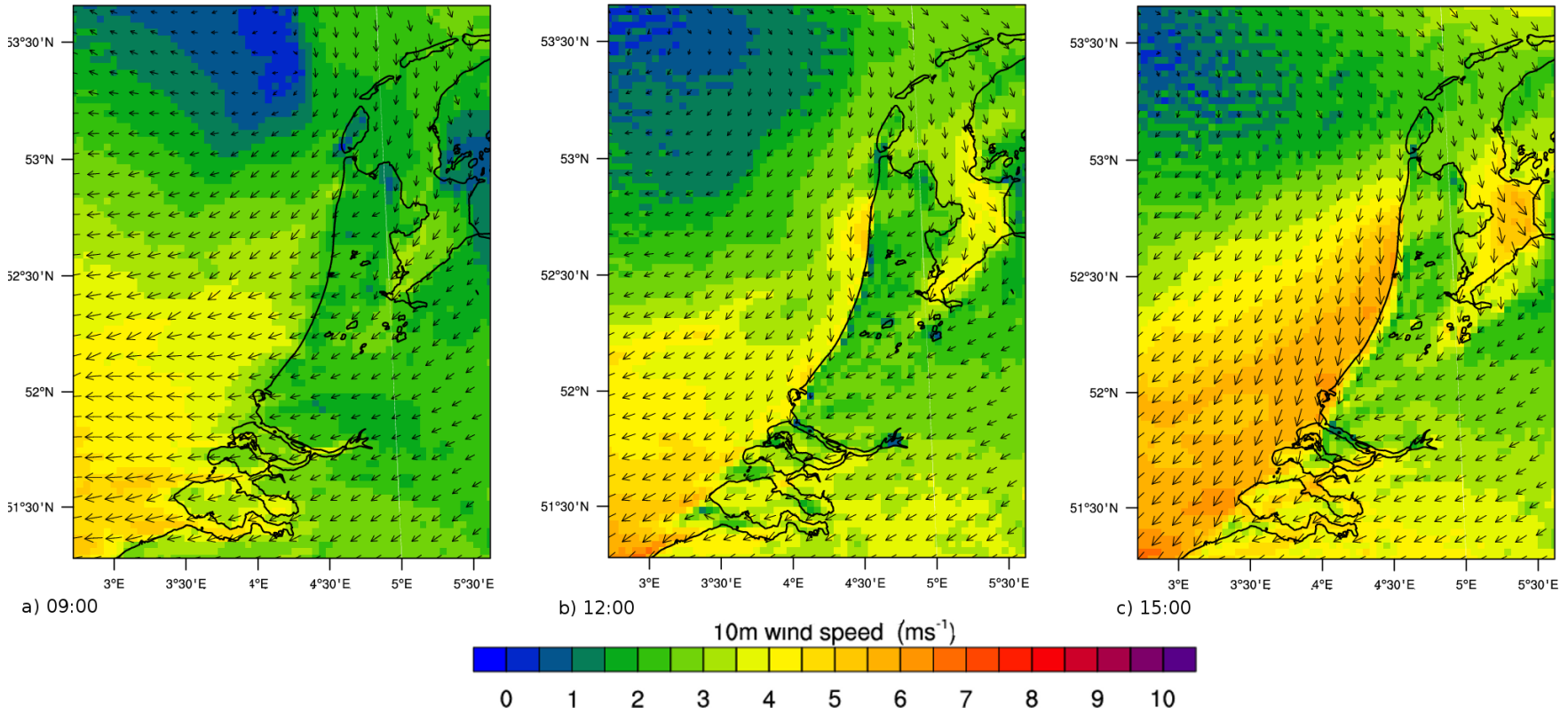

Figure 5.36: Composites of the 146 *pure* sea breeze events identified for North Norfolk by the identification method at a) 09:00 UTC, b) 12:00 UTC and c) 15:00 UTC. Filled contours indicate wind speed (ms^{-1}) and vectors indicate flow direction.

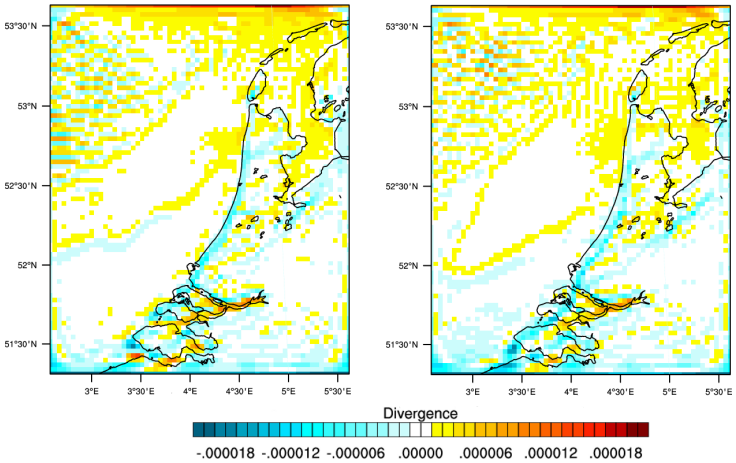

Figure 5.37: Composite of divergence (s^{-1}) for a *pure* sea breeze at a) 13:00 UTC and b) 16:00 UTC

Offshore, the 10m wind speed continues to intensify. Up to 30km offshore, by 16:00 UTC, the wind speed is between 6-7ms^{-1} (Fig. 5.36). Unlike the other coastlines considered so far, there are no calm zones which develop as the sea breeze forms. However, between 30-50km offshore oriented south west to north east a line of divergence and weakening convergence travels steadily southwards. Also, as the sea breeze develops by 13:00 UTC, a larger region of divergence forms to approximately 20km offshore from the north of the Netherlands. The former divergence region is likely the result of the air flowing north east across the Netherlands and not the result of the sea breeze. The combination of its movement southwards and the presence of the divergence line throughout the composite results both support this theory. The developing region of convergence to the north of the Netherlands is likely due to a combination of the sea breeze drawing in air against the general circulation and the airflow over the complex islands to the north.

The 76 *corkscrew* events place the centre of an anticyclone in the composite in sea level pressure approximately 20km to the west of Scotland (Fig. 5.35). The composite gradient wind flow direction does therefore have an offshore component to it. However, the 10m wind field behaves differently to the *pure* composite in several ways. Firstly, the initial wind speed is higher over the sea due to the more westerly position of the anticyclone (Fig. 5.38). Secondly, as the sea breeze begins to form, several jets and calm zones develop. The calm zones are at most 3km away from the coast and form in the lee of the land masses. The jets occur to 12km offshore, reaching speeds of 6ms^{-1}. One jet is located off the coast of north Holland and the other off the western coast of Freisland. The

jets intensify to 8ms^{-1} and move southwards. In the case of the Freisland jet, it moves into Ijsselmeer. By 18:00 any evidence in the 10m wind field patterns have vanished, though the two jets remain present.

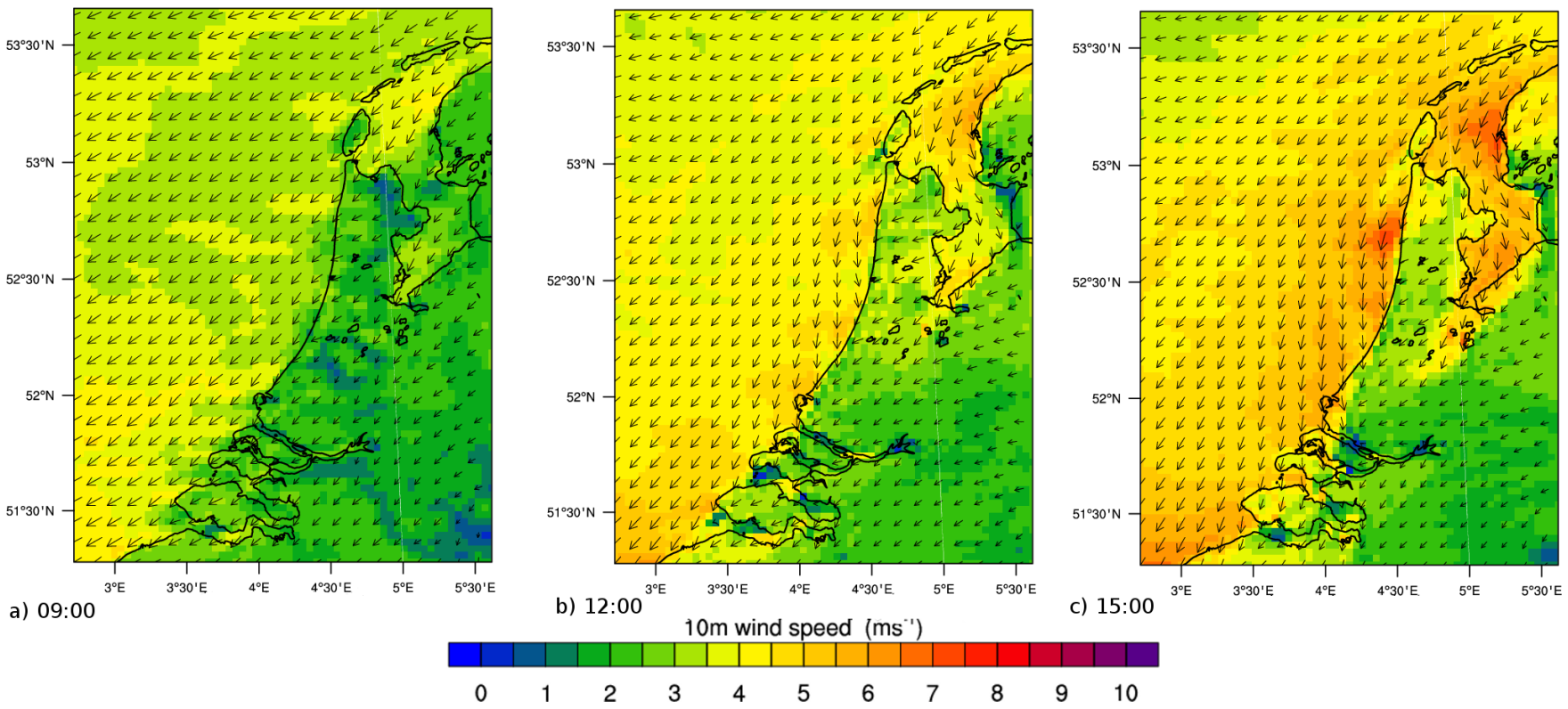

Figure 5.38: Composites of the 76 *corkscrew* sea breeze events identified for the Netherlands by the identification method at a) 09:00 UTC, b) 12:00 UTC and c) 15:00 UTC. Filled contours indicate wind speed (ms^{-1}) and vectors indicate flow direction.

The 71 *backdoor* sea breeze events occur once again in very light wind speeds, owing to the proximate location of the high pressure centre approximately 10km west of the Netherlands. The 10m wind field over the southern North Sea is in the range 2-3ms^{-1} by 09:00 UTC and is calm over the land. Onshore flow begins to develop at 11:00 UTC, and by 12:00 UTC, the composite *backdoor* sea breeze has already advanced 9km inland. The wind speed remains in the range 2-3ms^{-1} and an asymmetry develops, with the advancement of the sea breeze in north Holland advancing to within 3km of Markermeer by 13:00 UTC and therefore impacting the *pure* sea breeze forming there. In contrast, over southern Holland, the sea breeze has only advanced 6km onshore by 13:00 UTC. By 16:00 UTC, the sea breeze in southern Holland has accelerated and has advanced 18km inland, producing 10m wind speeds of 4ms^{-1} across the sea breeze front. The sea breeze continues to advance inland, reaching a maximum of approximately 30km inland.

Offshore, a calm zone is formed to the south of Holland, 10km offshore with a width of approximately 30km by 15:00 UTC and extends north-eastward over time. As a consequence, the region of onshore flow denoting the sea breeze offshore extent is clearly visible, extending to a maximum of 15km offshore. By 17:00 UTC, the 10m winds in the offshore environment have taken on the characteristics of the gradient flow and so the sea breeze is no longer evident offshore.

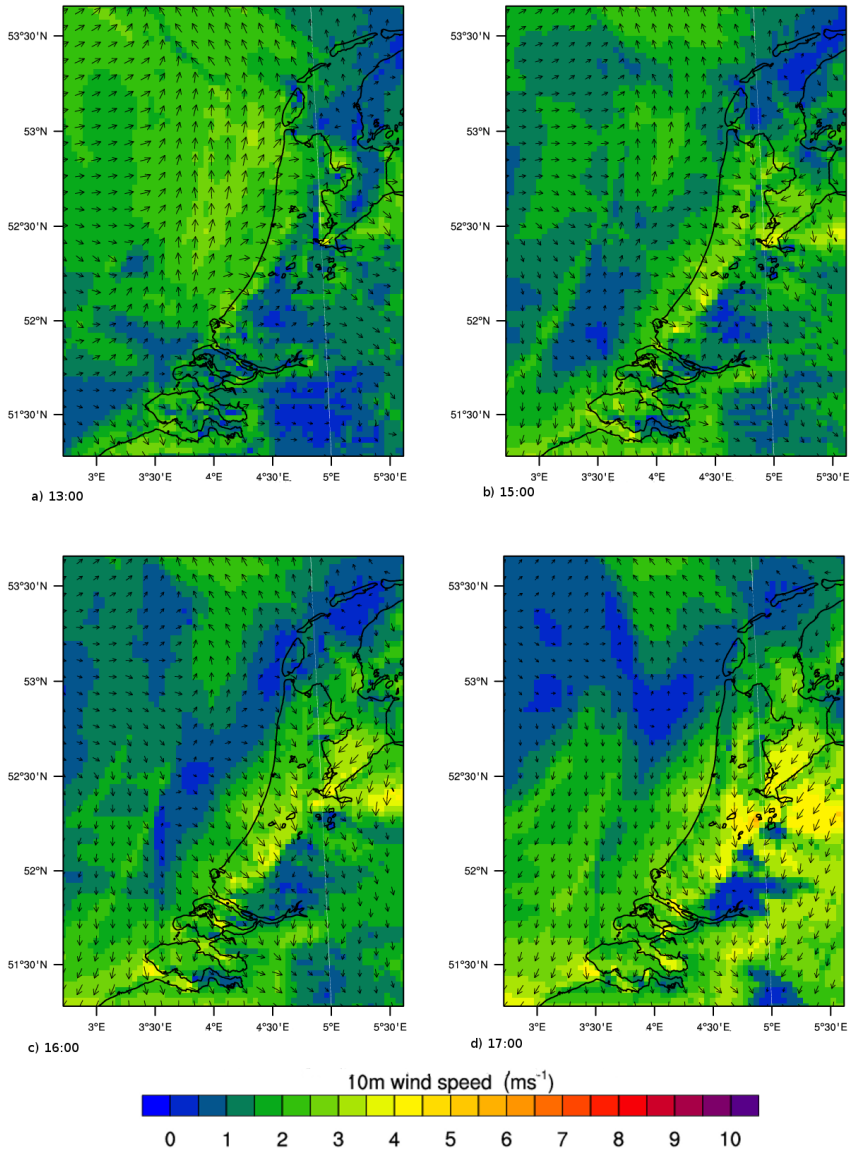

Figure 5.39: Composites of the 71 *backdoor* sea breeze events identified for the Netherlands by the identification method at a) 13:00 UTC, b) 15:00 UTC, c) 16:00 UTC and d) 17:00 UTC. Filled contours indicate wind speed and vectors (ms^{-1}) indicate flow direction.

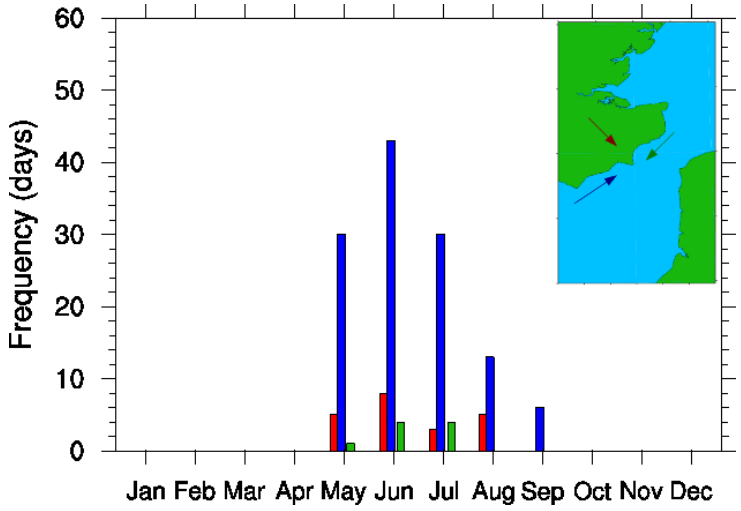

Figure 5.40: Sea breeze frequencies for the period May 2002- September 2012 for the southern coast of Kent. *Pure*, *corkscrew* and *backdoor* sea breezes are shown in red, blue and green respectively

5.2.5 The coast of Kent

The final coast tested is the coast of Kent. In all, 21 *pure*, 122 *corkscrew* and 9 *backdoor* sea breezes were identified (Fig. 5.41). These all occurred between May and September although no *backdoor* sea breezes were identified during either August or September, nor were there any *pure* sea breezes in September. The most dominant month for the generation of all sea breeze types is again June, though much of the monthly variability comes from the number of estimated *corkscrew* sea breezes.

During any one year there were at most 23 sea breezes on the coast of Kent, making it the coastline with the fewest sea breeze events of those tested. By far the poorest year, in terms of generation of sea breezes was 2008, when there were only 4 events (Fig. 5.41). This may be due to a variety of factors. Firstly, the coastline is orientated west-east, so that the days in which warm southerly flow brings higher temperatures to the UK in Summer are discounted as onshore gradient wind days. Secondly, the Kentish coast is a peninsula, which may not reach the higher temperatures. Furthermore, the Straits of Dover are narrow and relatively shallow, promoting higher SST's and therefore weakening the overall temperature gradient.

The composite of the 21 *pure* sea breeze events (Fig. 5.42) shows an anticyclone centred in the southern Atlantic, approximately 300km west of Cornwall, drawing a north-westerly airflow across the Kentish coast. At 09:00, there are three distinct calm zones, with the largest spanning the 30km length of the Straits of Dover (Fig. 5.45). By 12:00

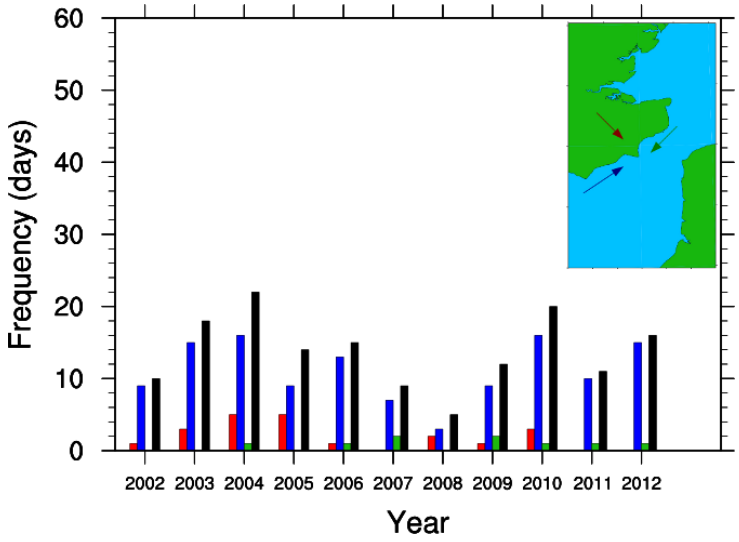

Figure 5.41: Sea breeze frequencies for the period May 2002- September 2012 for the southern coast of Kent. *Pure*, *corkscrew* and *backdoor* sea breezes are shown in red, blue and green respectively. Shown in black are the total number of sea breezes

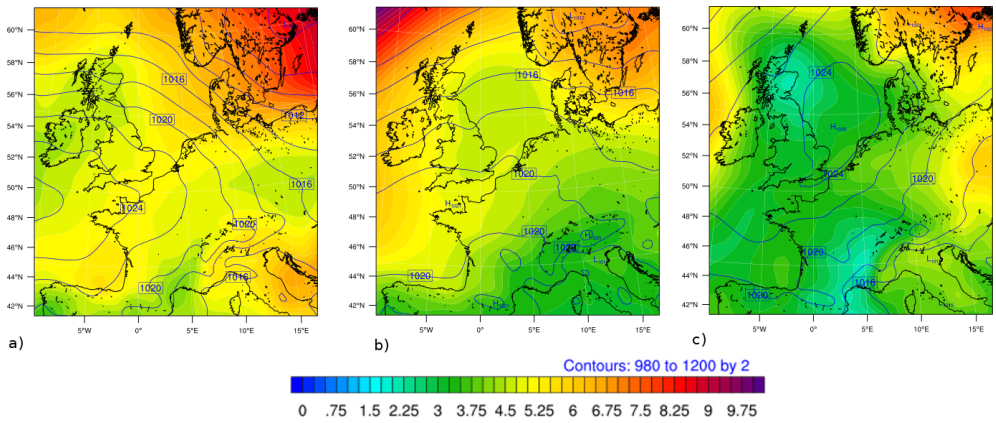

Figure 5.42: 12:00 UTC composite plots of sea level pressure (contours) and standard deviation (shading) for a) *pure* (21 events), b) *corkscrew* (122 events) and c) *backdoor* (9 events) sea breezes forming off the southern coast of Kent.

UTC, these have all but completely phased out by a strengthening coastal jet, as the sea breeze forms. The only calm zone remaining by this point spans the Dover Straits but only to a 3km width. The sea breeze, by 12:00 UTC has penetrated 6km inland and is visible as a convergence line. The acceleration due to the coastal jet spans approximately 20km offshore with a maximum 10m wind speed of approximately 8ms^{-1} in it's core spanning 6km. The jet intensifies and the sea breeze advances inland to a maximum penetration of approximately 20km before subsiding at 18:00 UTC. The maximum width of the jet core is approximately 12km offshore at the point of dissipation.

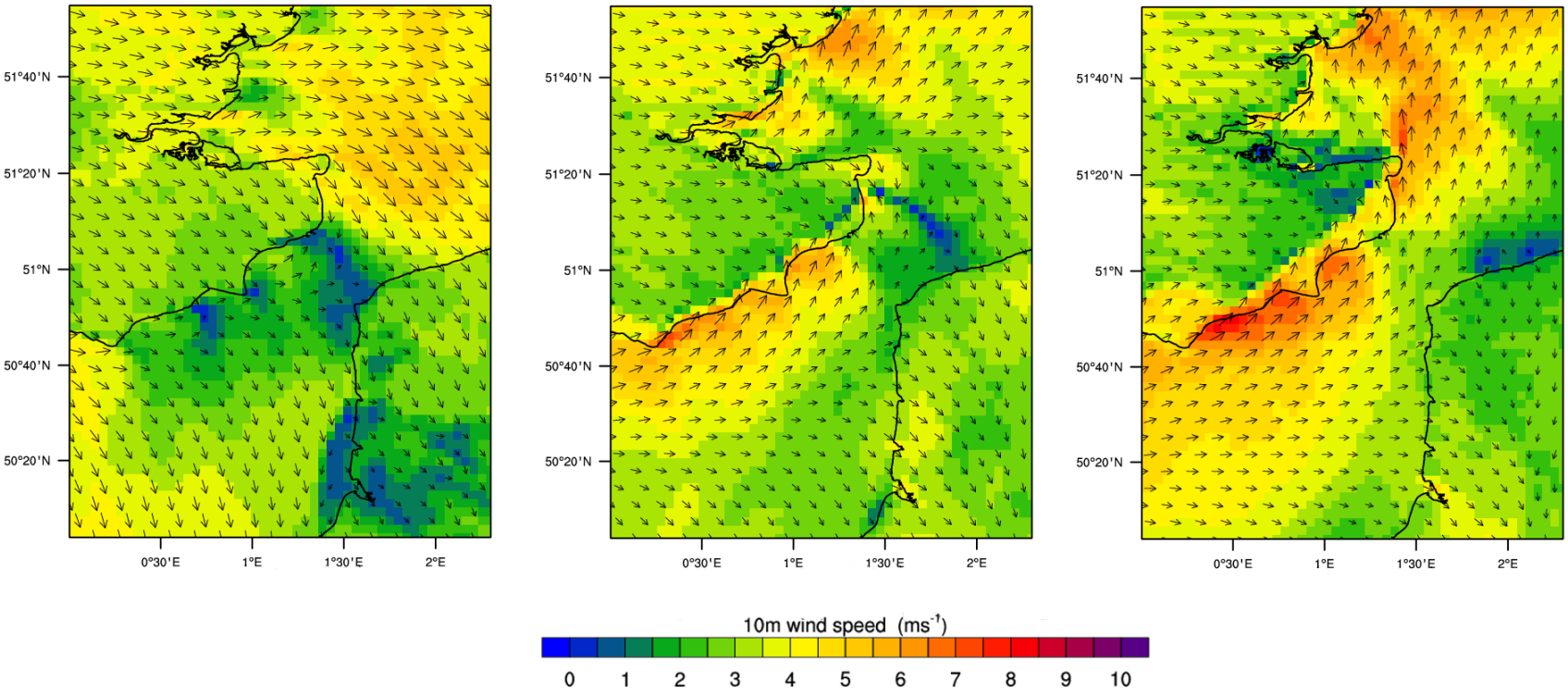

Figure 5.43: Composites of the 21 *pure* sea breeze events identified for the south coast of Kent by the identification method at a) 09:00 UTC, b) 12:00 UTC and c) 15:00 UTC. Filled contours indicate wind speed (ms^{-1}) and vectors indicate flow direction.

The most dominant type of sea breeze forming off the southern coast of Kent is the *corkscrew* sea breeze with 122 days in the 11 year period. The composite of sea level pressure places an elongated anticyclone over the English Channel with a centre approximately 30km off the coast of Normandy. The 10m wind speed is higher than for the *pure* composite at 09:00 UTC both over the sea and over the land. Again, a jet develops at the coast, reaching speeds of 8ms^{-1} in its core. Furthermore, as the sea breeze advances inland, a calm zone is created, to 12km off the northern Kentish coast in which a *pure* type sea breeze develops. By 15:00 UTC the calm zone diminishes and the *pure* type sea breeze has advanced approximately 10km inland. In comparison, the stronger *corkscrew* sea breeze by 15:00 UTC has advanced 15km inland, and by 17:00 UTC, the two sea breezes converge and the *pure* type is forced back to the northern coast of Kent.

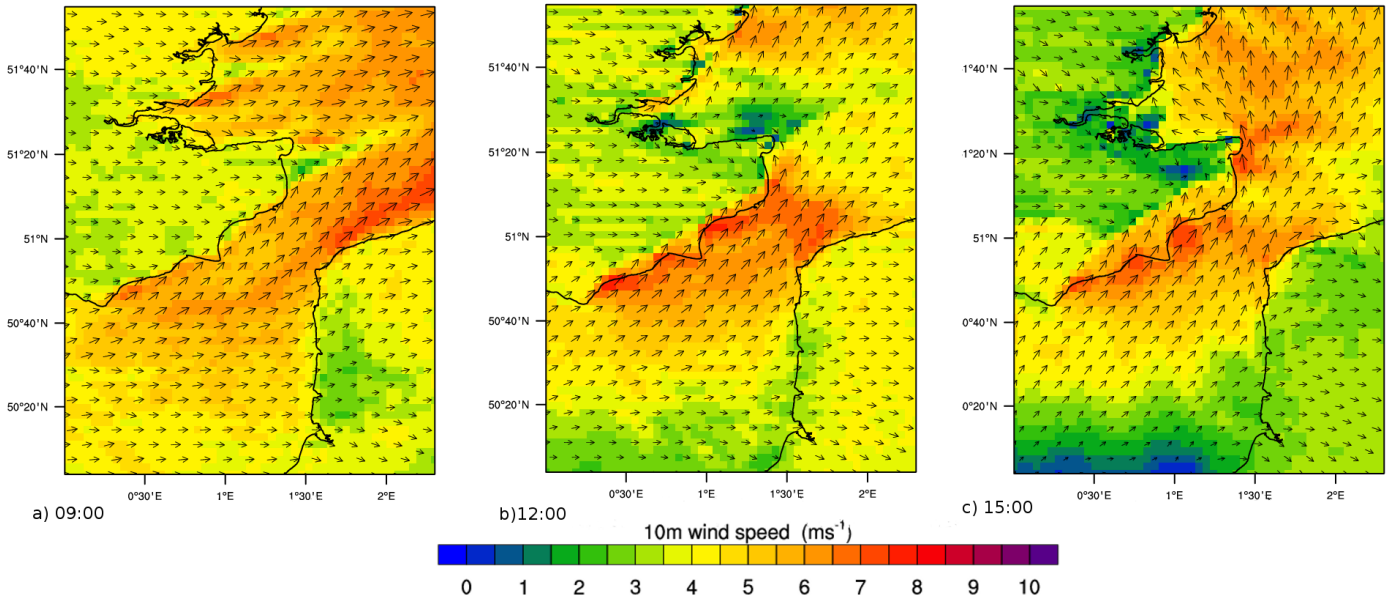

Figure 5.44: Composites of the 122 *corkscrew* sea breeze events identified for the south coast of Kent by the identification method at a) 09:00 UTC, b) 12:00 UTC and c) 15:00 UTC. Filled contours indicate wind speed (ms^{-1}) and vectors indicate flow direction.

Offshore at 17:00 UTC, the coastal jet has weakened both in intensity and scale however a second jet forms off Margate, the far eastern tip of Kent. The 10m winds in the English Channel weaken to approximately 5ms^{-1}.

With only 9 occurrences during the whole climatology, the composite of the *backdoor* sea breeze events on the southern coast reveals the presence of an anticyclone centred 30km north east of Norfolk. The 10m wind speeds are initially low and mostly indeterminate in terms of a general flow direction as a result. The English Channel initially has a weak jet off the coast of Calais, reaching speeds of 4ms^{-1} in its core of 3km. Off the southern coast of Kent, a calm zone extends 15km offshore. By 11:00 UTC, the jet has strengthened and its influence extended to 15km offshore. The calm zone off the southern Kent coast as a result diminishes and the *backdoor* sea breeze rapidly advances inland. Simultaneously, a *corkscrew* sea breeze develops on the northern coast of Kent and similarly advances rapidly, impacting the *backdoor* sea breeze at 11:00 UTC. A narrow jet has also formed, extending 3km offshore along the northern coast of Kent.

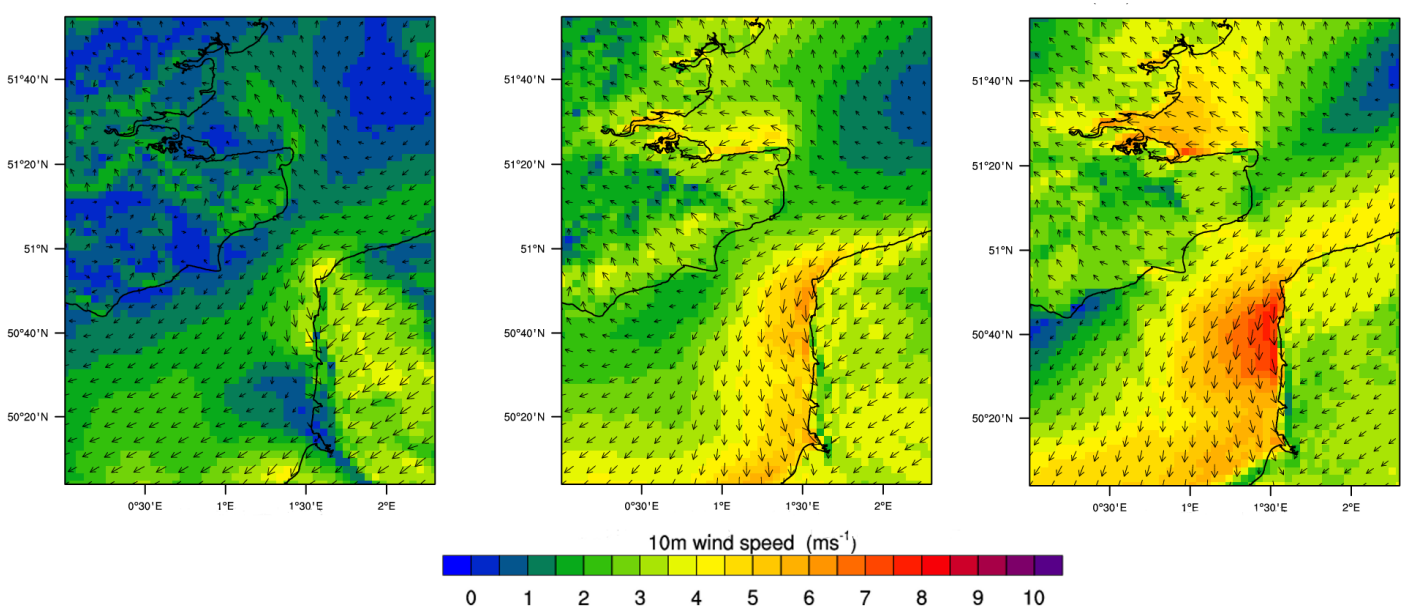

Figure 5.45: Composites of the 9 *backdoor* sea breeze events identified for the south coast of Kent by the identification method at a) 09:00 UTC, b) 12:00 UTC and c) 15:00 UTC. Filled contours indicate wind speed (ms^{-1}) and vectors indicate flow direction.

Table 5.4: Frequency in days of sea breezes for each coastline between May 2002 - September 2012.

Coast	Total *pure*	Total *corkscrew*	Total *backdoor*	Grand total
North Norfolk	117	96	51	264
East Norfolk	166	169	0	335
Suffolk/Essex	46	167	13	226
Netherlands	146	76	71	293
Southern Kent coast	21	122	9	154

The jet forming off the coast of Calais, progressively travels along the French coast, resulting in both an increase in 10m wind speed along the northern section of the Kentish coast and the formation of a calm zone, extending 15km offshore from the southern sector. This lasts for the duration of the composite day.

5.2.6 Summary of sea breeze frequencies and distributions

The frequency of sea breezes is highly variable, both on a spatial and temporal scale. Compared with the observed 12 year climatology of Simpson *et al.* (1977), the 76 *pure* sea breezes observed on the south coast of England agree well with the number of *pure* types predicted for the other coasts. The range in frequency of *pure* type sea breezes is from 46 to 166 forming off the Suffolk/Essex coasts and East Norfolk respectively. East Norfolk also experiences the higher number of *corkscrew* types with 169, corresponding to the highest number of *backdoor* sea breezes forming off the coast of the Netherlands with 71; the strict threshold in gradient wind strength causes a restriction to *backdoor* sea breeze numbers.

The distribution of sea breeze types is strongly dependant on the orientation of the coastline to the gradient wind. In many cases, the formation of a particular type of sea breeze corresponds to a different type on another, for example North and East Norfolk (Table 5.5. Furthermore, the offshore extent is difficult to determine accurately in most cases. The *corkscrew* sea breeze produces a coastal jet which is not captured in the simple 2-Dimensional idealized experiments; an effect which is amplified by the more complex coastlines, such as East Norfolk and Kent.

Calm zones, where formed, are often only present for short periods of time, when the

Table 5.5: The relationship between sea breeze types identified on one coastline with those on others. Values are expressed as percentages of the number of sea breezes occurring on the coastlines in the far left column. The letters *p*, *c* and *b* stand for *pure*, *corkscrew* and *backdoor* sea breezes.

Coast	Type	N. Nfk			E. Nfk		Sfk & Essx			Neth.			Kent		
		p	c	b	p	c	p	c	b	p	c	b	p	c	b
N. Nfk	p	-	-	-	0	86	0	35	0	30	2	12	0	19	2
	c	-	-	-	0	0	0	0	10	40	39	1	0	0	7
	b	-	-	-	94	0	20	61	0	0	0	37	4	49	0
E. Nfk	p	0	0	29	-	-	25	50	0	0	0	17	7	47	1
	c	60	0	0	-	-	0	41	0	31	1	15	0	15	0
Sfk & Essx	p	0	0	22	89	0	-	-	-	0	7	24	52	0	0
	c	25	0	19	50	42	-	-	-	7	0	21	0	38	0
	b	0	77	0	0	0	-	-	-	15	77	0	0	0	31
Neth.	p	24	26	0	0	36	0	8	1	-	-	-	0	3	3
	c	3	49	0	0	3	0	0	13	-	-	-	0	0	5
	b	20	1	27	41	35	4	49	0	-	-	-	0	31	0
Kent	p	0	0	10	57	0	52	0	0	0	0	0	-	-	-
	c	18	0	20	64	14	20	52	0	4	0	18	-	-	-
	b	22	78	0	0	22	0	0	0	44	56	44	-	-	-

sea breeze is forming, or they travel to different locations as the sea breeze extends laterally. For example, the calm zone formed in the composite *pure* sea breeze scenario forming off North Norfolk travels westwards into the Wash as the coastal jet gains strength, eventually covering the location of the Lynn and Inner Dowsing wind farm.

5.3 Sensitivity testing of the method

This section examines the effectiveness of the method in terms of the performance of each filter and the clarity of the composites. During the construction of the identification method, a number of initial sensitivity tests were performed regarding the height of the gradient wind level and the land-sea thermal contrast as outlined in Table 3.1. Firstly, the method is broken down in order to examine the effectiveness of each filter independently. Secondly, the results of altering the gradient wind height to 850hPa, as previously used by Furberg *et al.* (2002), are examined before finally examining the effect of using differing temperature measurements.

5.3.1 Filter breakdown

Between the 1st May 2002 to 30th September 2012, 35% of days were rejected by the first filter acting over the UK. For the Netherlands, the percentage decreased to 25% or 974 days. The second filter, removing days in which the gradient wind direction rotated by more than 90° in any one direction rejected the least number of days, filtering just 35 or 54 days for the UK and the Netherlands respectively. This accounts for 1% of the number of days which passed stage 1.

Filters 3 and 4 are more localized and so show more variability between coasts. In all cases, the size of the box for which gradient wind speed is the same. The reason for the differences between the number of rejected days resides with the coastal orientation. As discussed in, for example, Earl *et al.* (2013) and in Section 6.1, the dominant wind direction for the UK and Western Europe is westerly. In this case, the only coastline which approximately facing this quadrant is the coast of the Netherlands, resulting in approximately 70% more days being rejected when compared to the other coastlines. Overall, the filter removes approximately 53% of the 2437 days which pass stage 2 for the British coastlines and approximately 70% of 2811 days which pass stage 2 for the Dutch coast.

The final filter, calculating the land-sea thermal contrast, has variations both in terms of the size of the land and the sea averaging box. Due to the constraints of the space available in proximity to the target coastline, there are coastlines which have a significantly larger land averaging box than the sea. Suffolk and Essex, for example, has a land averaging box which is approximately three times the size of the sea. Conversely, the coast of East Norfolk has an averaging box which is approximately equal to the sea. Owing to the different heat capacities of land and water, it could be expected that the fluctuations of the temperature of the land are greater and therefore the effects of averaging over a smaller grid box is larger for variations in land grid box size, rather than sea. However, the size of the averaging boxes implicitly constrains the maximum temperature, and if the size of the land surface has dictated the size of the averaging box then this is a reflection of the conditions of the target coastline. For example, the Dutch land averaging box is constrained by Markermeer and the southern islands. The continental effect also assures higher land surface temperatures, and combined with a smaller averaging box allows the

Table 5.6: Percentage number of days rejected by each stage of the identification method using 2m air temperature to determine thermal contrast and 925hPa height for gradient wind. Thresholds for *pure* and *backdoor* sea breezes were $9ms^{-1}$ and $5ms^{-1}$ respectively. The total number of days passed through the filter method is 3806 (1^{st} May 2002 to 30^{th} September 2012). Each abbreviation stands for North Norfolk (N. Nfk), East Norfolk (E. Nfk), Suffolk and Essex (SFK/E), the Netherlands (Ned) and South Kent (S. Kent).

Stage	N. Nfk	E. Nfk	Sfk/E	Ned	S. Kent
1. Weather type	35	35	35	25	35
2. Flow direction	1	1	1	1	1
3. Wind thresholds	52	53	54	69	54
4. Thermal contrast	69	70	80	65	83

filter to reject fewer days. Note that the number of rejected days for filter 4 acting on the Dutch coast is a third smaller than for the other coastlines. Percentages vary from 65% for the Dutch coast to 83% on the southern coast of Kent which passed stage 3 that were rejected by the last filter **??**.

Both the coasts of Kent and the Netherlands have particularly small averaging grid boxes for the thermal contrast, yet the number of rejected days are very different. The SST averaging box is approximately 2° further north and cooler for the Dutch coast than for southern Kent. This, combined with the continental effect of the land strengthens the average land-sea thermal contrast and so the filter does not reject as many days. Conversely, southern Kent has a much smaller land surface to boost thermal conductivity as the coast is positioned on a peninsula. Furthermore the more southerly position of the sea averaging box is in a region with warmer SST's and is in close proximity to mainland Europe, promoting warmer temperatures by advection off the mainland. Consequently, the average land-sea thermal contrast is lowered.

The average number of days passed by each filter does vary each month (Fig 5.46). It is immediately apparent from Fig. 5.46 that filter 4 is less effective during the months of April to July as the land temperatures are climatologically warmer. Therefore the necessary 5K temperature difference between the land and sea is consistently met during these months.

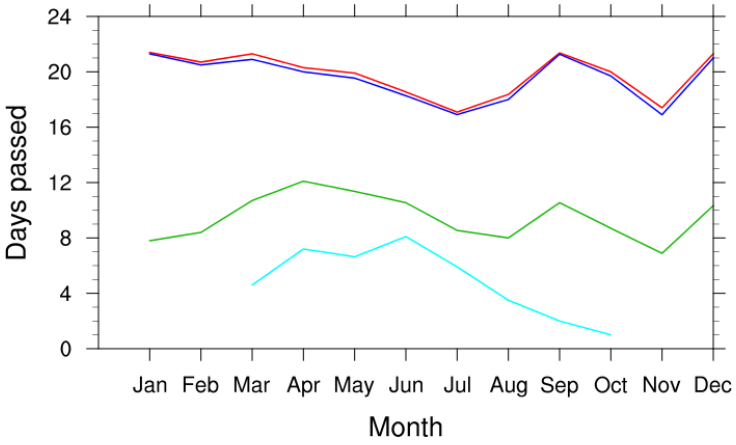

Figure 5.46: Average number of days per month passed by each stage of the filter method when set to the CLIM specifications for North Norfolk between March 2002 to September 2012. That is, using 925hPa height to calculate gradient wind, using 2m temperature only to calculate the thermal contrast and setting the *pure* and *backdoor* thresholds to 9ms^{-1} and 5ms^{-1} respectively. Filters 1,2,3 and 4 are shown in red, blue, green and cyan respectively.

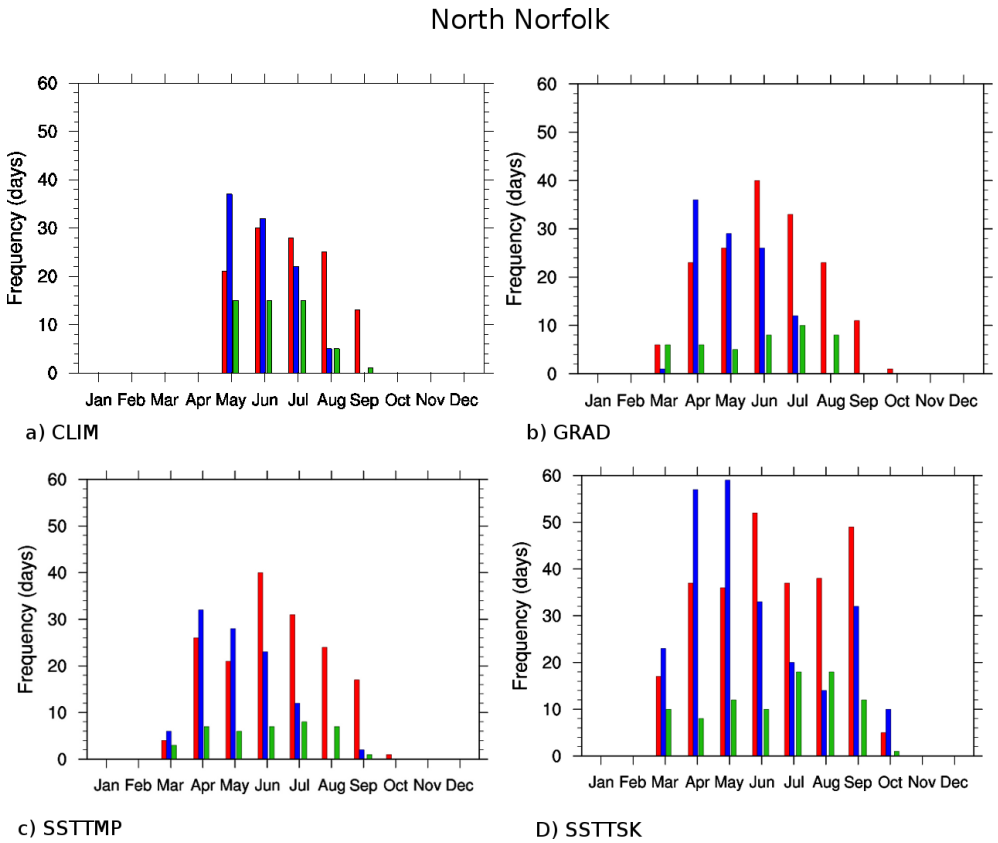

Figure 5.47: Frequency of sea breeze types calculated using the identification method for the coast of North Norfolk over the period March 2002 to September 2012 for each individual sensitivity test. In each case, red, blue and green bars represent *pure*, *corkscrew* and *backdoor* sea breezes respectively. The CLIM test (a) uses 925hPa height for calculating gradient wind speed and direction, and *pure* and *backdoor* thresholds of 9ms^{-1} and 5ms^{-1} respectively. To calculate the land-sea thermal contrast the CLIM test uses 2m temperature. The GRAD test is as CLIM but uses a gradient wind height of 850hPa. The SSTTMP (c) is as CLIM but uses SST and 2m temperature for the land-sea contrast. Finally, the SSTTSK (d) experiment is as CLIM but uses SST and skin temperature for the land-sea thermal difference.

Table 5.7: Number of days rejected by each stage of the identification method for the coast of North Norfolk under different sensitivity experiments. The CLIM test defines the set-up used for the climatology, that is, using 2m temperature for both the land and sea measures, 925hPa gradient wind heights and *pure* and *backdoor* sea breeze thresholds of 9ms^{-1} and 5ms^{-1} respectively. The GRAD test uses the same configuration as the CLIM with the exception that the gradient wind height is increased to 850hPa. The SSTT2 experiment is the same configuration as the GRAD but uses SST and 2m temperature for the sea and land temperatures respectively. Similarly, the SSTSTK test uses skin temperatures to calculate the thermal contrast. All other settings for the SSTSTK experiment are the same as for the GRAD.

Stage	CLIM	GRAD	SSTT2	SSTTSK
1. Weather type	1334	1334	1334	1334
2. Flow direction	35	35	35	35
3. Wind thresholds	1266	1364	1364	1364
4. Thermal contrast	807	758	767	465
Sea breeze frequencies				
pure	117	280	164	271
corkscrew	96	200	103	248
backdoor	51	94	39	89

5.3.2 Gradient wind height sensitivity

Increasing the gradient wind height to 850hPa, hereafter the GRAD experiment, results in an increase in the number of sea breezes (Table 5.7). The number of *pure* sea breezes forming off the North Norfolk coast rises to 280 with the higher gradient wind reference height, compared with 117. Similarly, the number of *corkscrew* and *backdoor* sea breezes is again more than doubled from 96 and 51 sea breezes respectively to 200 and 94 with the higher gradient wind reference. The length of the sea breeze season is also significantly longer for the coast of North Norfolk, spanning from March until October. Aside from the number of *backdoor*, which is lower for the higher gradient wind height, there is an increase in frequency in the number of sea breezes per month. April shows the sharpest rise in sea breeze numbers, as for a gradient wind height of 925hPa there were no events but when it is increased to 850hPa, over 60 sea breeze events are predicted. However, the increase in predicted *pure* sea breeze numbers reduces the performance of the method to the extent that no sea breeze is recognisable in the composite, indicating that the increase in numbers are *false alarms* and so are detrimental to the methodology. The *corkscrew* and *backdoor* composites however retain the sea breeze structure in the composite, though they are much less distinct.

5.3.3 Temperature measure sensitivity

Similar to the gradient wind height sensitivity experiment, the number of sea breezes predicted for the SSTTSK, where both land and sea surface skin temperatures are used, is at least twice the magnitude of the CLIM experiment (Table 5.7). The SSTT2 experiment, where the land temperature is taken from the 2m temperature field, however only predicts *pure* type sea breeze frequencies to be higher than the CLIM experiment. Indeed, the number of *backdoor* sea breezes in the SSTT2 experiment is lower than for the CLIM with 39 compared to 51 events. However, the composite does not show any evidence of a forming *backdoor* sea breeze, regardless of fewer numbers. Similarly, the composites for the *pure* and *corkscrew* sea breeze types for both the SSTT2 and SSTTSK experiments are also poor in comparison to the CLIM.

On examination of the individual filters, it would appear that the land-sea temperature filter is made largely ineffective when using skin temperatures in the SSTTSK experiment, suggesting that the threshold of 5K is too low and would need to be adjusted accordingly if skin temperatures are to be used in the method. Using SST and 2m temperature as a basis for calculating the thermal contrast does not significantly alter the effectiveness of the filter as only 9 extra days are rejected by the stage between the GRAD and SSTT2 experiments. The filter responsible for the reduction in performance of the method is the height of the gradient wind.

5.4 Summary

In this chapter, the sea breeze identification method has been tested on 5 different coastlines, varying in both complexity and orientation, during the period Mar 2002 - September 2012. Sea breeze annual and monthly frequencies have been examined, as well as the composite wind fields in the offshore environment. Finally, the method has been examined by looking at the performance of each individual filter and various sensitivity experiments have been performed to look at the effects on the method both in terms of quality and sea breeze frequencies.

It is found that sea breezes are highly variable in terms of annual frequencies, season length and type distribution. The number of sea breezes is not solely dependant on the

magnitude of the air temperature of the Summer months; the heat-waves of 2003 and 2006 do not produce the highest number of sea breezes. The numbers can however be *preconditioned* in favour of sea breeze development by a particularly mild and wet Winter. The higher wind speeds increase the degree of mixing in the Ekman layer of the water column and consequently decrease the SST anomaly. Even so, if the SST is *preconditioned*, the orientation of the target coastline and the degree to which the land surface is warmed can limit the number of sea breeze events.

The two filters which account for the most number of rejections are days in which the daytime Lamb weather type is *Cyclonic* and the strength and direction of the gradient wind. This again suggests that the land-sea thermal contrast is not the most important factor. This is due to the contrast being sufficient to cover much of the annual temperature variability of the Summer months and so very few days are rejected during this time. The land-sea temperature filter increases in relative contribution during the Spring and Autumn months as the mean temperature drops, and so the Annual variability produces more days in which the thermal contrast is insufficient to generate sea breezes.

A factor that is not considered in the idealized simulations which plays an important role in the offshore wind fields is the generation of coastal jets where the gradient wind is orientated to produce *corkscrew* sea breezes. These are particularly apparent when the coastline contains complex bays and headlands. Offshore calm zones are created for the *pure* sea breeze simulations, however, their duration and extent are a function of the complexity of the target coastline.

Varying the thermal contrast measure and the height of the gradient wind can have a significant effect on the frequency of the sea breezes. However, these deviations from the method used in the climatological study significantly reduce the effectiveness of the identification method, by reducing the clarity of the sea breezes in the composite imagery, stressing the importance of choosing the correct thresholds and methodology.

In terms of wind energy, the most significant implication relates to predictability. The high degree of annual, regional and monthly variability of meteorological phenomena present a hazard to wind power forecasters, depending on the contribution of a single event. Also, the method highlights the importance of being able to distinguish between

different sea breeze types and what the effect is on the offshore wind field. For example, a *pure* sea breeze forming off the North Norfolk coast occurs in conjunction with a *corkscrew* sea breeze off the coast of Lincolnshire which acts to produce a jet over the Lynn and Inner Dowsing wind farm. Conversely. a *corkscrew* sea breeze forming off the coast of Essex also forms in conjunction with a *pure* sea breeze off the northern coast of Kent. The result is the creation of an offshore calm zone in one of the major wind farm regions in the southern North Sea.

Chapter 6

Assessing the impact of sea breezes on offshore wind energy

This Chapter utilizes the sea breeze climatology constructed in Chapter 6 in order to determine the impact of different sea breeze types on offshore wind energy. Although attention is given to all 5 coastlines, particular emphasis is given to the Netherlands and North Norfolk coasts where offshore mast and turbine observations are available for verification. Ways in which the sea breeze spatially impacts offshore wind power are explored, by firstly differencing the 27km and 3km domains from the sea breeze climatology in Section 6.1. Sea breeze composite data are compared to the observations at the Egmond aan Zee mast to show the temporal variations associated with each sea breeze type. In Section 6.2, by using the 2009 sea breeze season, the effects of the 2-way interactive nesting are removed by using a single independently run 27km domain and differencing from the 3km. The resultant power predictions and wind speeds are compared to observations at both Lynn wind farm and the Egmond aan Zee mast. Finally in Section 6.3, sea breeze days are compared against those which fail the identification method on account of an insufficient thermal contrast.

6.1 Horizontal resolution differences

6.1.1 Spatial sea breeze impact on capacity factor

From Section 1.1.3.1, capacity factor is defined as the ratio of power produced to the theoretical maximum power output for a given time period. Fig. 6.1 shows the result of subtracting the total capacity factor of the 3km domain from the re-gridded 27km domain for different sea breeze types forming off the North Norfolk coast. Overall, each sea breeze type adds overall to wind power generation potential to a distance of 30km offshore on the days concerned. The magnitude of this increase to capacity factor is between 3-5%. Notably for the composite of the *pure* sea breeze type, there is a narrow region, of approximately 6km, where the overall effective contribution of the *pure* sea breeze at 3km resolution is approximately equal to the 27km resolution. This occurs off the coast of North Kent, where the orientation of the gradient wind also implies the formation of *pure* sea breezes (Fig. 6.1a). However, the region is not evident for *pure* sea breezes forming off the East Norfolk coast, suggesting that the individual characteristics of each coastline play an important role in determining the sea breeze contribution (Fig. 6.2a).

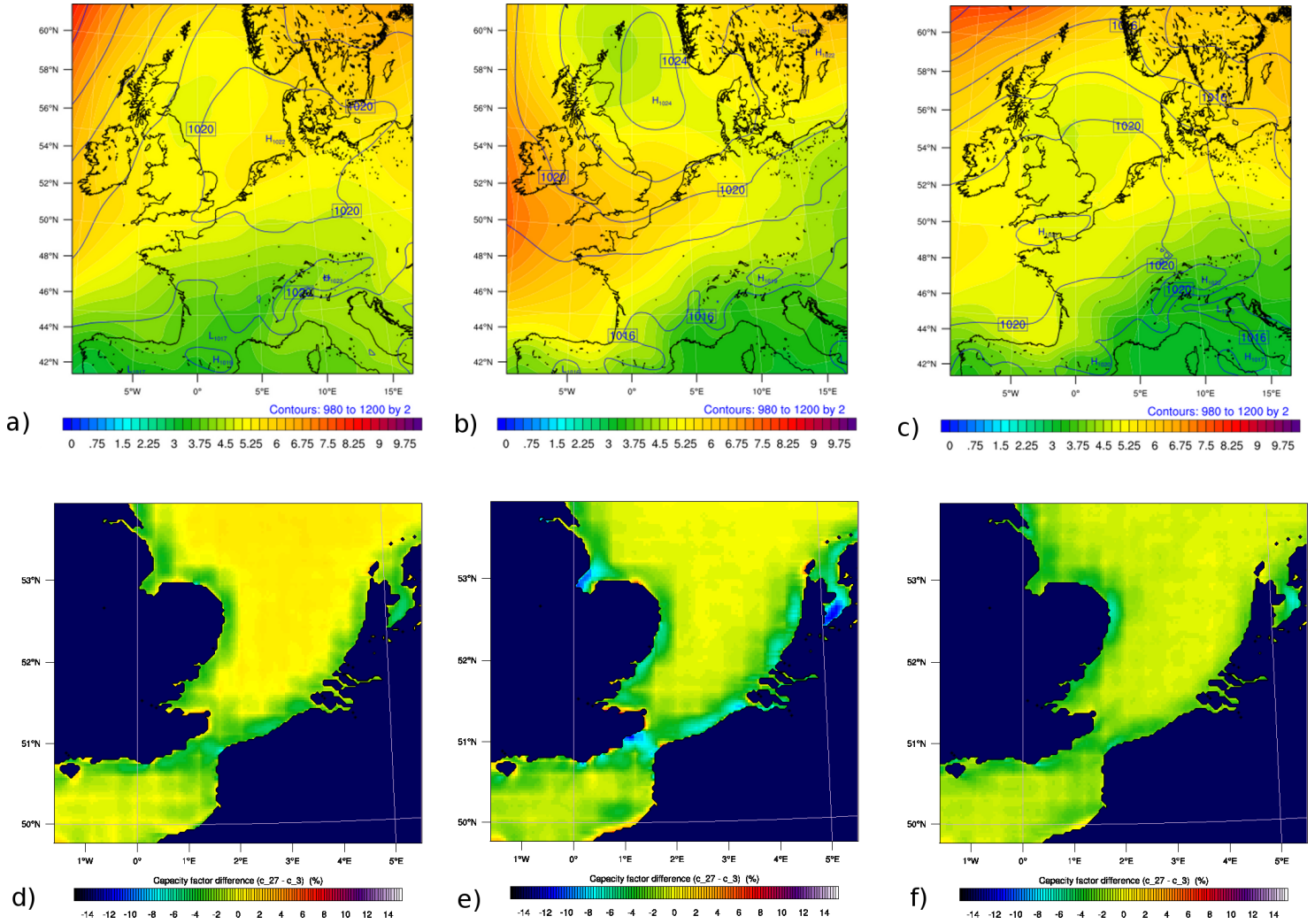

Figure 6.1: Composite sea level pressure and standard deviation for the 117 *pure* (a), 96 *corkscrew* (b) and 51 *backdoor* (c) sea breeze events forming off the North Norfolk coast between May to September 2002-2012. Composite differences in capacity factor between the 3km domain subtracted from the 27km, where the 27km domain is interpolated to the 3km grid, for the respective sea breeze types (d-f). The capacity factor is determined for each sea breeze composite for a period of 1 day.

One potential issue with this methodology is that, in addition to the poor representation of the sea breeze by the single 27km resolution domain (Section 5.1.2.1; Fig 5.11), the coastline is also poorly resolved. This implies that the differences in capacity factor observed here are not solely attributable to the simulations with and without a sea breeze. This is especially true as the differences between simulations are within 27km, or one grid square, of the coastline. Unlike the case study in Section 5.1, the nesting configuration is 2-way interactive, where information is passed back to the 27km resolution domain, and so the 27km resolution simulations will have some representation of a sea breeze. However, the coastal jet over The Wash in the *corkscrew* sea breeze composite for the North Norfolk coast (Fig. 6.1e) is evident when the 2-way interactive nests are differenced, suggesting that components of the sea breeze are not all resolved in the process of 2-way nesting at the coarser resolution (Fig. 6.1b). The contributions of 2-way nesting to the capacity factor differences will be examined further in Section 7.2.

The *corkscrew* sea breeze shows a greater degree of variability than other sea breeze types, both in terms of the magnitude of the capacity factor differences and the spatial variation of these differences for each coastline (Figs 6.1; 6.2; A.15; 6.3; A.16). The *corkscrew* sea breeze has distinct regions where the presence of the sea breeze causes a reduction in capacity factor, the magnitudes of which are as high as 5%, such as up to 6km offshore from North Norfolk (6.1e). A strong contribution of greater than 10% is present in the eastern Wash, and further extends to the coast of Lincolnshire; including the location of the Lynn and Inner Dowsing wind farm for the North Norfolk *corkscrew* sea breeze composite (Figs. 3.13; 6.1). For the coast of the Netherlands (Fig. 6.3), it is noticeable that the *corkscrew* sea breeze composite contributes the most to the overall capacity factor difference when compared to the other sea breeze types.

In terms of overall contribution to wind energy, it is necessary to consider not only the magnitude of the sea breeze contributions, but also whether or not the general wind field, without the presence of the sea breeze, would be of sufficient strength to overcome the cut-in threshold. Assuming a 3.6MW turbine operating over a 24hr period. The composite capacity factors of each of the sea breeze types can be derived from the composite 80m model level windfields. For all coastlines, *backdoor* sea breeze favouring synoptic conditions produce capacity factors of approximately 10% in the offshore environment

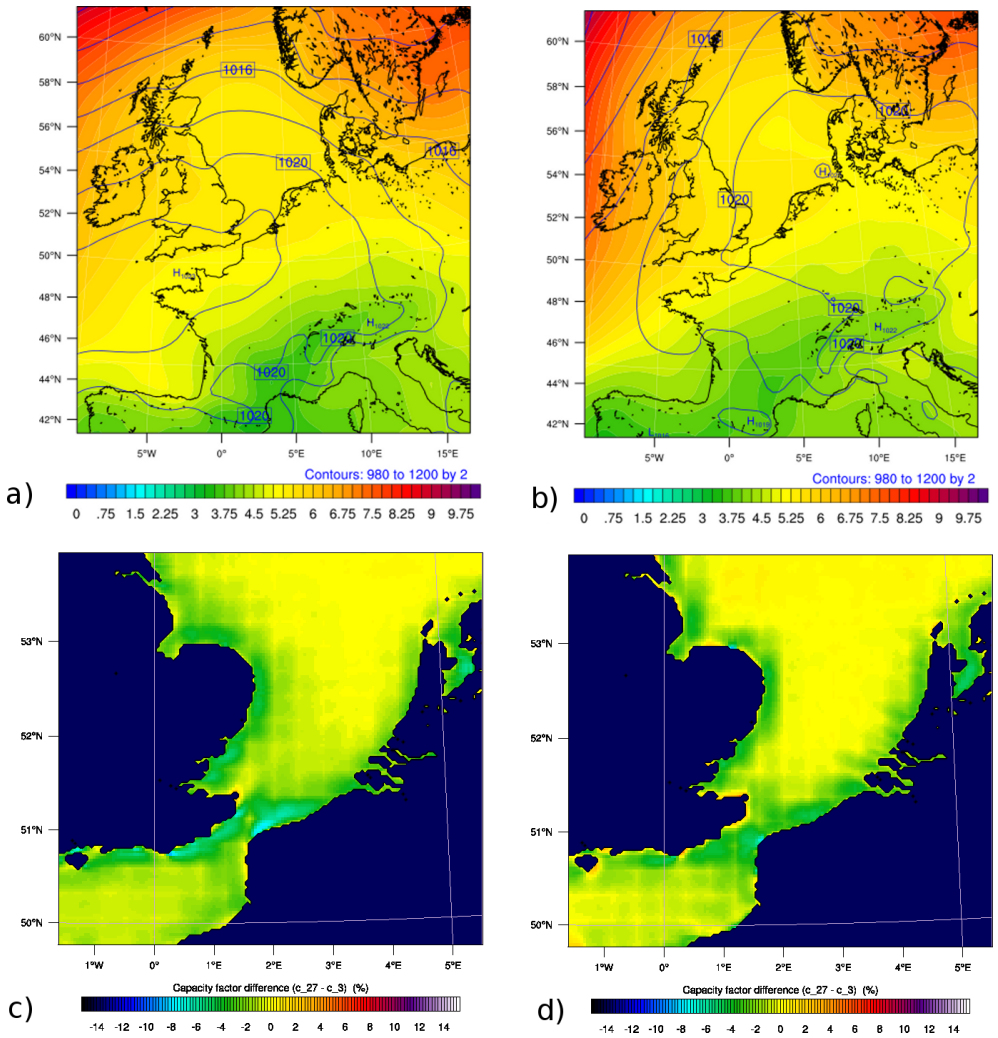

Figure 6.2: Composite sea level pressure and standard deviation for the 166 *pure* (a) and 169 *corkscrew* (b) sea breeze events forming off the East Norfolk coast between May to September 2002-2012. Composite differences in capacity factor between the 3km domain subtracted from the 27km, where the 27km domain is interpolated to the 3km grid, for the respective sea breeze types (d-e). The capacity factor is determined for each sea breeze composite for a period of 1 day.

(eg. Fig. 6.4); that is in 24 hours, for average *backdoor* sea breeze conditions, the amount of power which can be generated by a 3.6MW turbine is equivalent to that same turbine operating at capacity for 2.4 hours.

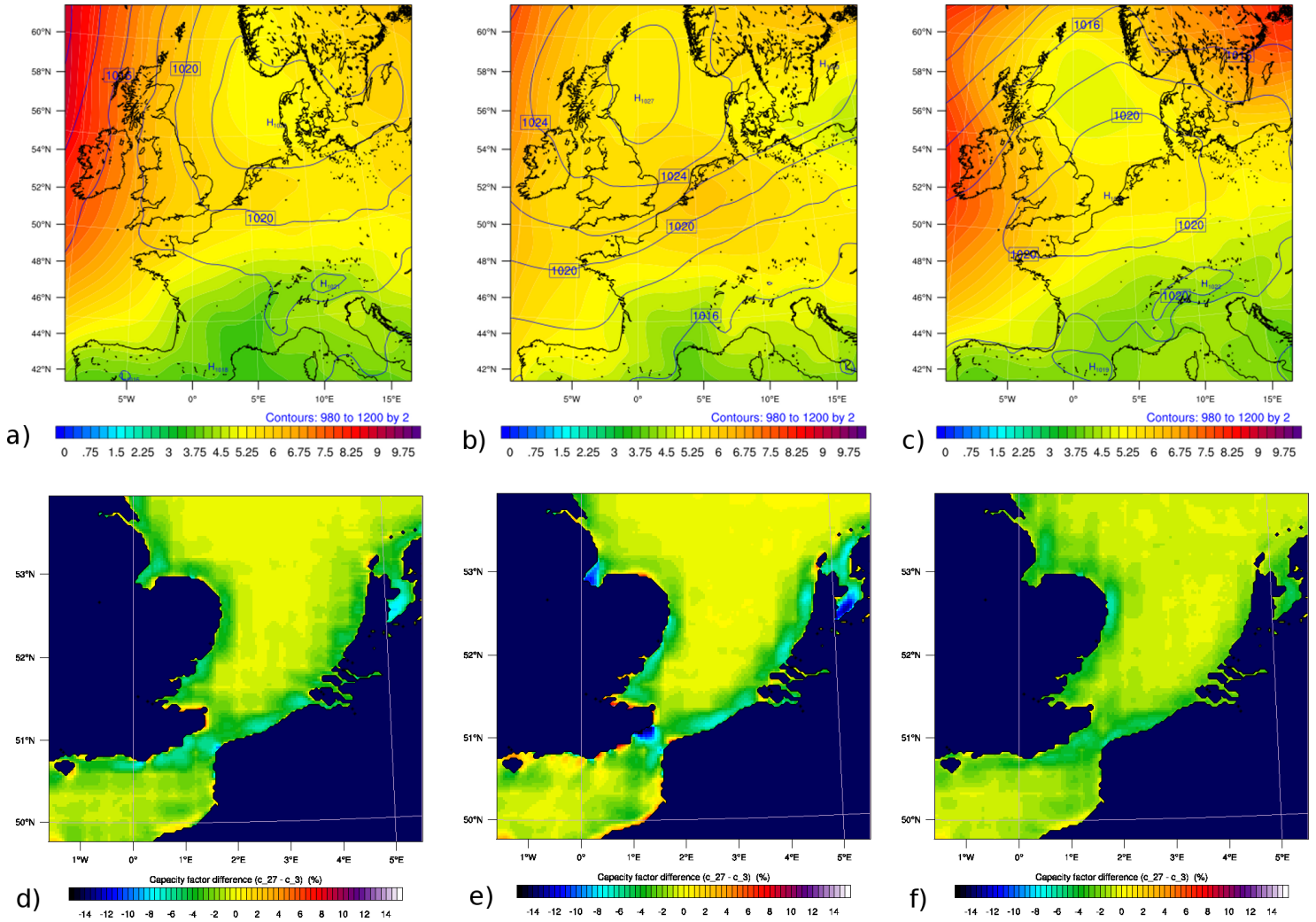

Figure 6.3: Composite sea level pressure and standard deviation for the 146 *pure* (a), 76 *corkscrew* (b) and 71 *backdoor* (c) sea breeze events forming off the Netherlands coast between May to September 2002-2012. Composite differences in capacity factor between the 3km domain subtracted from the 27km, where the 27km domain is interpolated to the 3km grid, for the respective sea breeze types (d-f). The capacity factor is determined for each sea breeze composite for a period of 1 day.

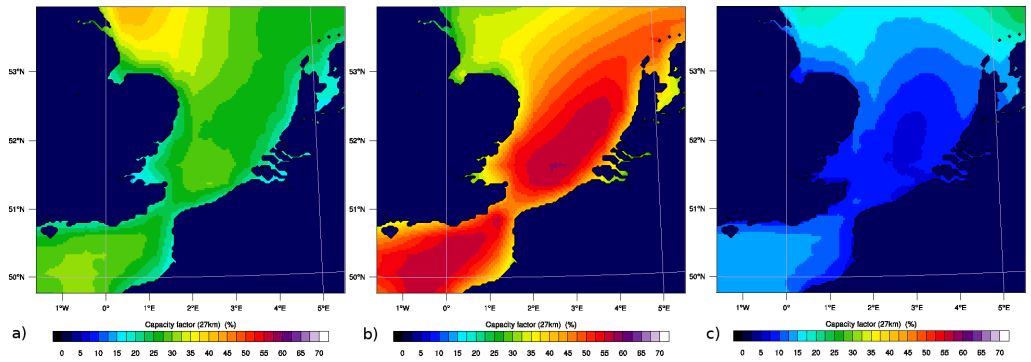

Figure 6.4: Capacity factor composites of a) *pure* (117 events), b) *corkscrew* (96 events) and c) *backdoor* (51 events) sea breeze events forming off the North Norfolk coast. The capacity factors are calculated for the composite 3km simulation results over a 24 hour period assuming a 3.6MW turbine.

In contrast, typical composite capacity factor variations of conditions favouring *corkscrew* sea breeze development reach as high as 60%, especially up to 100km off the coast of the Netherlands and in the English Channel (eg. Fig. 6.4b). The typical open water capacity factor for *pure* sea breeze events is approximately 30% (Fig. 6.4a). In both the *pure* and the *backdoor* composites, the magnitudes of the capacity factor are related to the thresholds of 9ms^{-1} and 5ms^{-1} used in filter 3 of the identification method.

The result of comparing the 27km with the 3km composite sea breeze days shows that, in general, the sea breeze can cause net increases in capacity factor by, on average, 5% to 30km offshore. However, differences due to improved resolution of the coastline cannot be ruled out as a contributing factor. Furthermore, additional information obtained by the 3km simulation is transferred back to the 27km during the process of 2-way interactive nesting.

Wind energy forecasters are not solely interested in the overall wind energy contribution for a given sea breeze day. They are also interested in short term sudden variations in power production, known as *ramp up* and *ramp down* events. Short sudden changes in power production can be very costly to the wind energy industry as can the generation of surplus energy. The next section explores the temporal evolution of each sea breeze type and compares the simulated results against observations made at the Egmond aan Zee met mast.

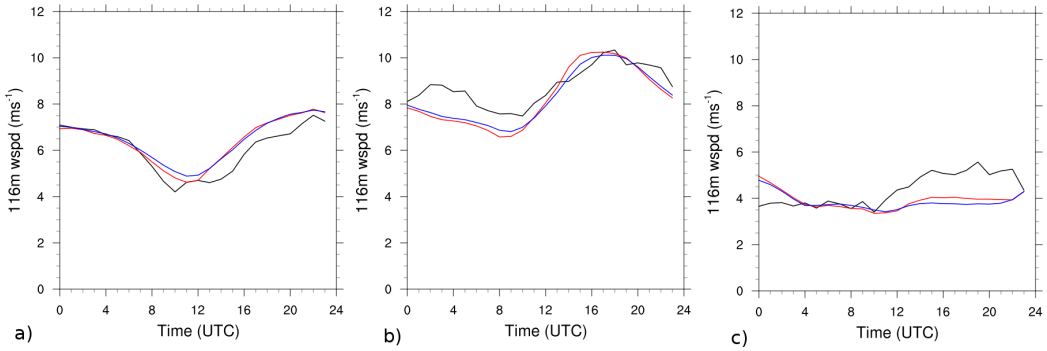

Figure 6.5: Composite wind speed diurnal cycle of a) 77 *pure*, b) 52 *corkscrew* and c) 34 *backdoor* sea breeze events at 116m compared with the respective 116m wind speed measurements at the Egmond aan Zee met mast (black), 18km offshore from the Dutch coast. All sea breeze events occurred during 2005-2010, the operational period of the meteorological mast. Red and blue lines represent the simulated composite WRF output using 3km and 27km horizontal resolution respectively.

6.1.2 Temporal sea breeze contributions to wind energy

Whilst a current typical offshore 3.6MW wind turbine hub height is between 70-80m, modern 8MW designs are approximately 100m tall. Hence any comparisons with the Egmond aan Zee met mast are given at the 116m height, rather than at either 70m or 21.6m (Section 2.1.3). Fig. 6.5 shows the composite time series of the *pure*, *corkscrew* and *backdoor* sea breeze events forming off the Dutch coast. The time series also compare the 3km and the 27km simulation data.

Firstly, it is apparent that the composite *backdoor* sea breeze is not as well captured as the other two sea breeze types at the mast location. At 10:00 UTC, the observations show an increase in 116m wind speed of 1.6ms^{-1} to above typical turbine cut-in speed. The model has both a weaker increase in 116m wind speed, associated with the *backdoor* sea breeze, of only 0.6ms^{-1} and a later arrival time of 11:00 UTC. The magnitude of the increase in model wind speed is not sufficient to surpass the cut-in threshold of 4ms^{-1}, although it is important to note that cut-in wind speeds as low as 2ms^{-1} are possible with vertical axis turbines (Islam *et al.*, 2013).

The establishment of the thermal pressure gradient in the case of the *pure* sea breeze causes a drop in power output by over 60% (Fig. 6.6). The minimum recorded wind speed, between 10:00-14:00 UTC, is approximately equal to the turbine cut-in speed of 4ms^{-1}. Note that the cut-in speed is the same for both the 3.6MW turbine and the 8MW as only vertical axis wind turbines are able to generate power in lower wind speeds (Islam *et al.*, 2013). These have not yet been implimented in the offshore environment. Once formed,

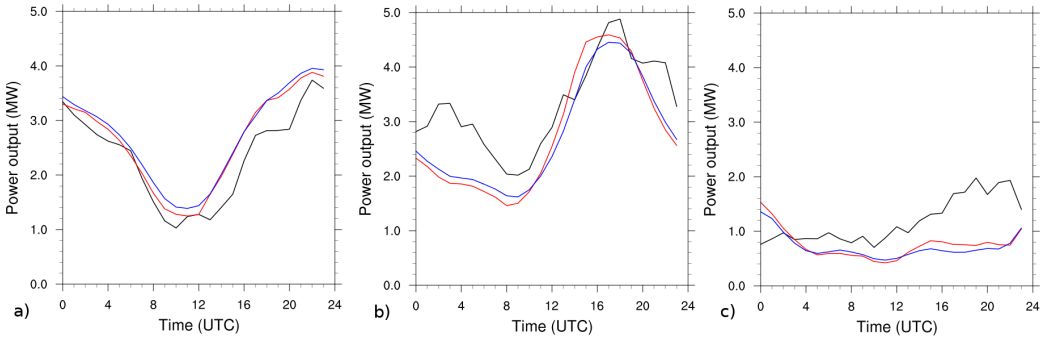

Figure 6.6: Composite wind power diurnal cycle of a) 77 *pure*, b) 52 *corkscrew* and c) 34 *backdoor* sea breeze events, 18km offshore from the Netherlands coast. Measurements of 116m wind speed were observed at the Egmond aan Zee met mast and were converted into wind power estimates using a theoretical 8MW turbine with blades of radius 80m (black). All sea breeze events occurred during 2005-2010, the operational period of the meteorological mast. Red and blue lines represent the simulated composite WRF output using 3km and 27km horizontal resolution.

upon arrival at the offshore meteorological mast, the sea breeze restores the predicted power output to over 2MW. The difference between the 27km and the 3km resolutions is small, implying that whilst the sea breeze is not represented well on land for the single case study in Section 5.1.2.1, the 2-way interactive nesting is sufficient to reduce much of the differences between resolutions at 18km offshore (Compare Figs. 3.13 and 6.5).

The largest contributor to wind energy in terms of both total power gain and the magnitude of the diurnal power fluctuations is the *corkscrew* sea breeze (Fig. 6.6). During a single day, the average variation in power output is approximately 3MW. In this case, the *corkscrew* sea breeze produces an overall gain in wind energy of approximately 2MW, however, this includes the full diurnal cycle and therefore an overestimation of the total power gained.

The hypothetical wind turbine used here is based on current projections as to average turbine size by 2020 (EWEA, 2013a), that is, 8MW with rotor blades of 80m radius and a hub height of 116m. Currently, the most common offshore wind turbine is rated 3.6MW with a hub height and blade radius of 70m and 60m respectively (EWEA, 2013a). Fig. 6.7 shows the composite wind power time series of all sea breeze types on the Netherlands coast for the 3.6MW turbine. Note that the magnitude of the rise in power output associated with the sea breeze is less for the 3.6MW model than for the taller 8MW taller turbine. This therefore implies that the sea breeze will have a greater effect on the power output of the next generation turbines. This effect is greatest in the *corkscrew* sea breezes but is also evident in the *pure* and *backdoor* types.

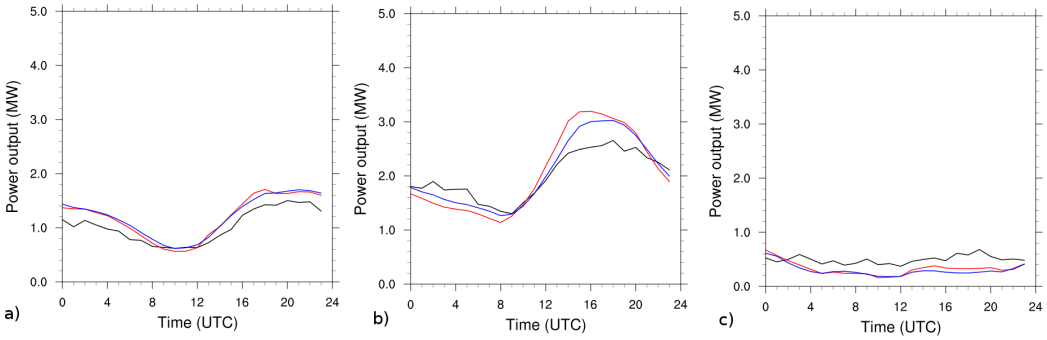

Figure 6.7: Composite wind power diurnal cycle of a) 77 *pure*, b) 52 *corkscrew* and c) 34 *backdoor* sea breeze events, 18km offshore from the Netherlands coast. Measurements of 70m wind speed were observed at the Egmond aan Zee met mast and were converted into wind power estimates using a theoretical 3.6MW turbine with blades of radius 60m (black). All sea breeze events occurred during 2005-2010, the operational period of the meteorological mast. Red and blue lines represent the simulated composite WRF output using 3km and 27km horizontal resolution.

In summary, in terms of potential significance to wind power prediction, the *corkscrew* sea breeze both shows the most variability throughout the day and produces the most amount of power. Both the *pure* and the *corkscrew* types of sea breeze show a marked decline in power output prior to sea breeze onset, however, on arrival of the sea breeze the contribution of the sea breeze is greater than the original decline. This pattern is more marked for larger turbines, suggesting that *pure* and *corkscrew* sea breeze days will likely have a greater effect in the future. *Backdoor* sea breezes form at lower wind speeds and so are not associated with large power fluctuations. However, some turbine types, such as the vertical axis wind turbine, operate at lower cut-in speeds than the more widely used horizontal axis and so it is plausible that the *backdoor* sea breeze will have a greater affect should the vertical axis type be modified for the offshore environment (Islam *et al.*, 2013).

Currently, only the composite effect of all events have been examined over the period of one day for each sea breeze type. Consequently, whilst the contribution of the sea breeze can be assessed on a given day, its relative importance in terms of the overall effect over a season has not yet been determined. In the following section, the 2009 North Norfolk sea breeze season is examined and model results compared against observations at Lynn wind farm. Furthermore, the consequence of comparison with the 2-way nesting interaction is explored as single 27km resolution simulations are conducted for the sea breeze season and compared to the equivalent 2-way nested results.

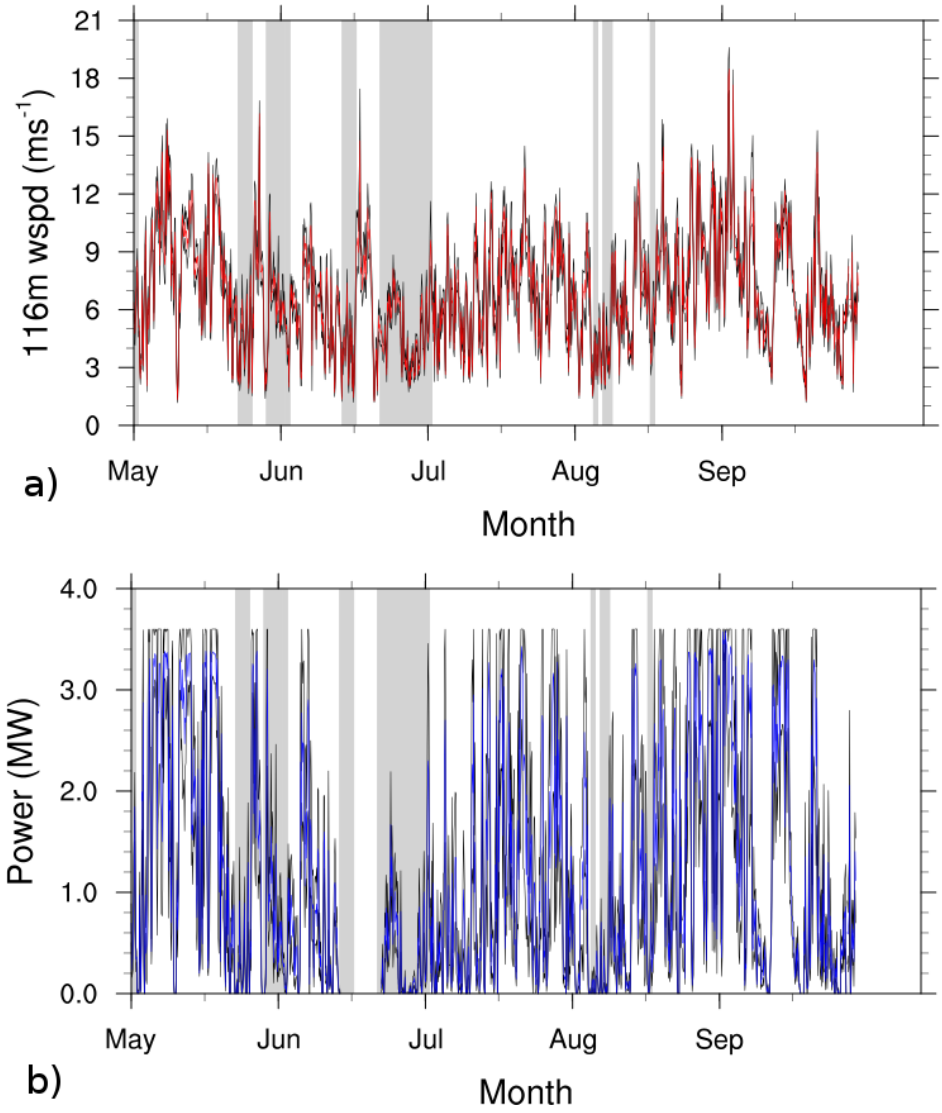

Figure 6.8: Time series of averaged a) hub height (80m) wind speed and b) average power production per turbine for the Lynn wind farm for the 2009 sea breeze season. The black lines denote $\pm$ the standard deviation across the farm. Shaded vertical lines denote sea breeze events.

6.2 The 2009 North Norfolk sea breeze season

Referring back to Fig. 6.10, the year in which the highest frequency of sea breeze events occur on the North Norfolk coast but after the construction of the Lynn and Inner Dowsing wind farm in 2008, is 2009. Fig. 6.8 shows the time series of averaged hub height wind speed and standard deviations for the 27 wind turbines at Lynn wind farm. For this period, Lynn wind farm is chosen as a complete record exists of wind turbine data for the whole season unlike Inner Dowsing where a large proportion of observations in May were not recorded. Shaded regions denote the 27 sea breeze days as determined by the selection method for North Norfolk.

In total, 10 *pure*, 14 *corkscrew* and 3 *backdoor* sea breezes were identified in the 2009 season. The turbine averaged total capacity factor of the 5 month period is 31.0%. In this season, sea breezes account for 1.96% of the total capacity factor for the 5 month period. The *corkscrew* sea breeze events were responsible for generating the most capacity with 1.44% followed by *pure* sea breezes with 0.43% and *backdoor* types with 0.10%.

For the Dutch coast, the 2009 sea breeze season produced 37 sea breezes, including 12 *pure* types, 16 *corkscrew* and 9 *backdoor* sea breezes. The total capacity factor for the season is 55.6%, with *pure*, *corkscrew* and *backdoor* sea breezes accounting for 0.57%, 2.25% and 0.37% respectively. In this case, the capacity factor is determined from a theoretical turbine of height 80m, blade radius of 60m and with an efficiency operating at the Betz limit, whereas for North Norfolk the capacity factors are from observations at the wind farm. Also note that compared to the turbines operating at the Egmond aan Zee wind farm, they are 10m taller.

6.2.1 Spatial differences in capacity factor between nesting methods

In Section 7.1.1, the method of differencing the 27km and 3km domains was used to determine spatial differences in capacity factor, assuming that the 27km resolution was unable to simulate the sea breeze. However, the presence of 2-way interactive nesting allowed information between the two resolutions to be transferred, causing an underestimation of the capacity factor of the sea breeze itself. In this section, single 27km WRF simulations are used in the differencing process for the 2009 sea breeze season so that no interaction takes place between nests. The results are compared against the equivalent 2-way nested simulations.

Fig. 6.9 shows the differences between using the single 27km resolution domain and the 2-way interactively nested 27km domain when applied to the 10 *pure*, 14 *corkscrew* and 3 *backdoor* sea breezes forming off the coast of North Norfolk. Immediately apparent are the differences in spatial scales of the capacity factor differences between the two methods, implying that a large proportion of the differences are removed by the 2-way nesting process. Within 30km of any coastline in the 3km domain, the differences between the 3km and the 27km resolutions are similar between nesting methods in terms of spatial distribution, but the magnitudes of the contributions of the 2-way interactive differencing

method are up to 10% less for all sea breeze types (eg. Fig. 6.9. These can be attributed to differences with and without a sea breeze or differences due to resolving the coastline at both resolutions.

In the single 27km domain case for the 10 *pure* sea breeze events over North Norfolk in 2009, capacity factor differences are as high as 20%, with a maximum spanning approximately 50km offshore from the Humber estuary and another up to 100km north east of East Anglia. The spatial scale of these contributions, unlike for the 2-way case, is within range of the proposed Round 3 developments (Compare Figs. 6.9 and 1.1).

For North Norfolk, the positive contributions in The Wash attributed to the *corkscrew* sea breeze are highlighted in the 2-way differencing method (Fig. 6.9c and e). Also, the two regions of equal capacity factor 6km offshore from north-east Norfolk and the Lincolnshire coast are captured in both methods. However, contributions of up to 15% extend up to 60km offshore from the Netherlands and up to 20% offshore from Southern Kent are also present in the single 27km domain comparison, but the magnitude of the contribution in the 2-way method only reaches at most 10%.

For the 3 *backdoor* sea breezes forming off the North Norfolk coast, the capacity factor difference associated with the sea breeze is 3%, though the *pure* sea breeze forming off Lincolnshire forms a contribution of approximately 15% to a distance of 30km offshore which partly affects North Norfolk. Similarly, the contributions in the *pure* sea breeze case for North Norfolk are also predominantly caused by the type of sea breeze forming off Lincolnshire coast. The synoptic situation for the *pure* case over North Norfolk implies the formation of a *corkscrew* sea breeze off of Lincolnshire which results in the high capacity factor differences (Fig. 6.1a).

In the case of the Netherlands, the 16 *corkscrew* sea breeze events contribute the most to the capacity factor reaching magnitudes of 15% up to 60km offshore. In comparison, the 9 *backdoor* sea breezes contribute less than 2% to a distance of approximately 12km offshore. For the 10 *pure* sea breeze events which form off the coast of the Netherlands in 2009, although the differences span a similar horizontal extent to the *corkscrew* composite, the magnitude of the contribution is lower, reaching a maximum of approximately 10%.

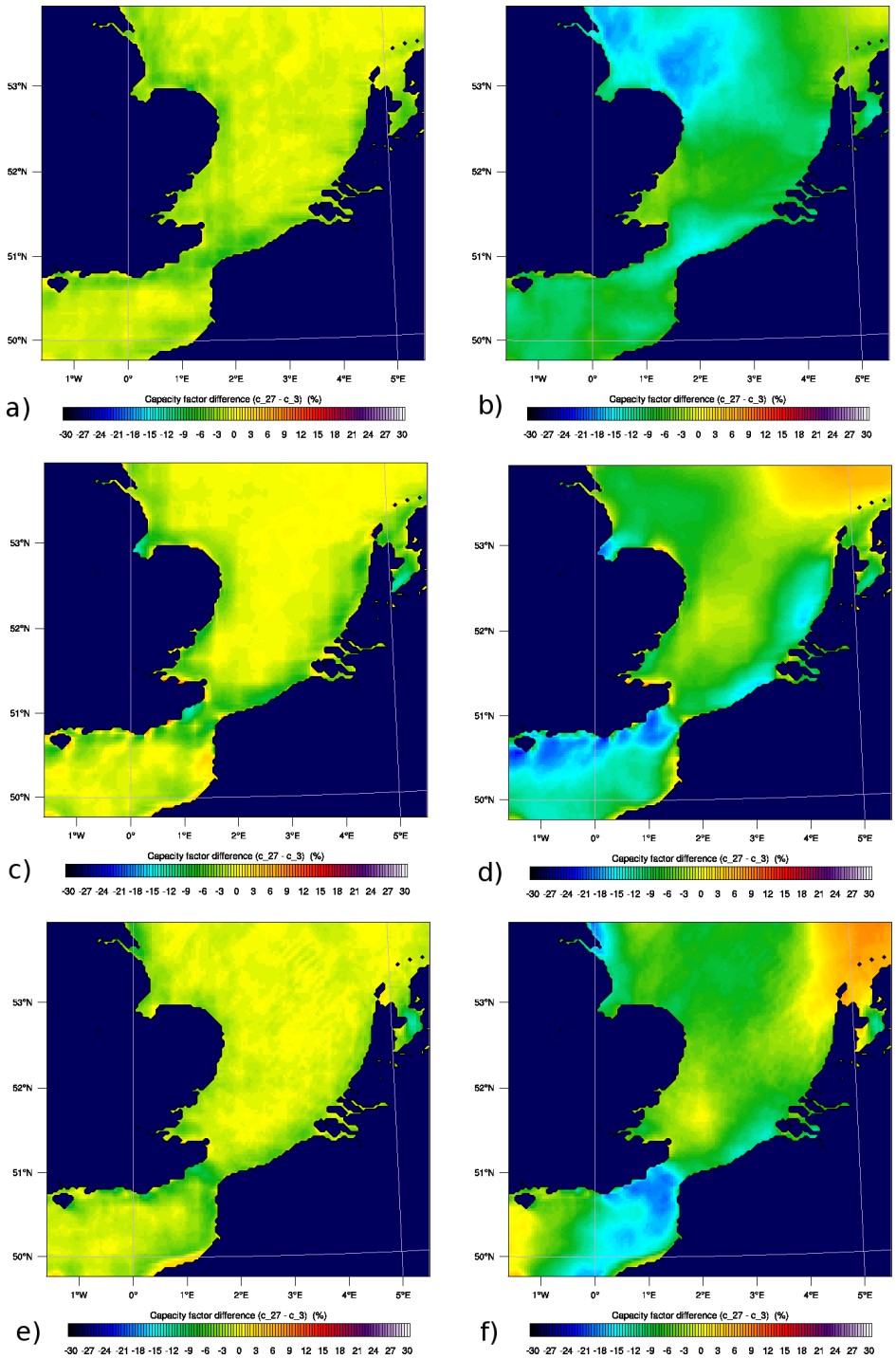

Figure 6.9: Composite capacity factor differences between the 27km and the 3km resolution domains for the (a,b) 10 *pure*, (c,d) 14 *corkscrew* and (e,f) the 3 *backdoor* sea breeze events forming off the coast of North Norfolk in 2009. The left hand side (a,c,e) plots show the differences between the 2-way interactively nested domains and the right hand side plots (b,d,f) show the differences between two independent 27km and 3km domains. Before differencing, the 27km domain is interpolated onto the 3km using bilinear interpolation.

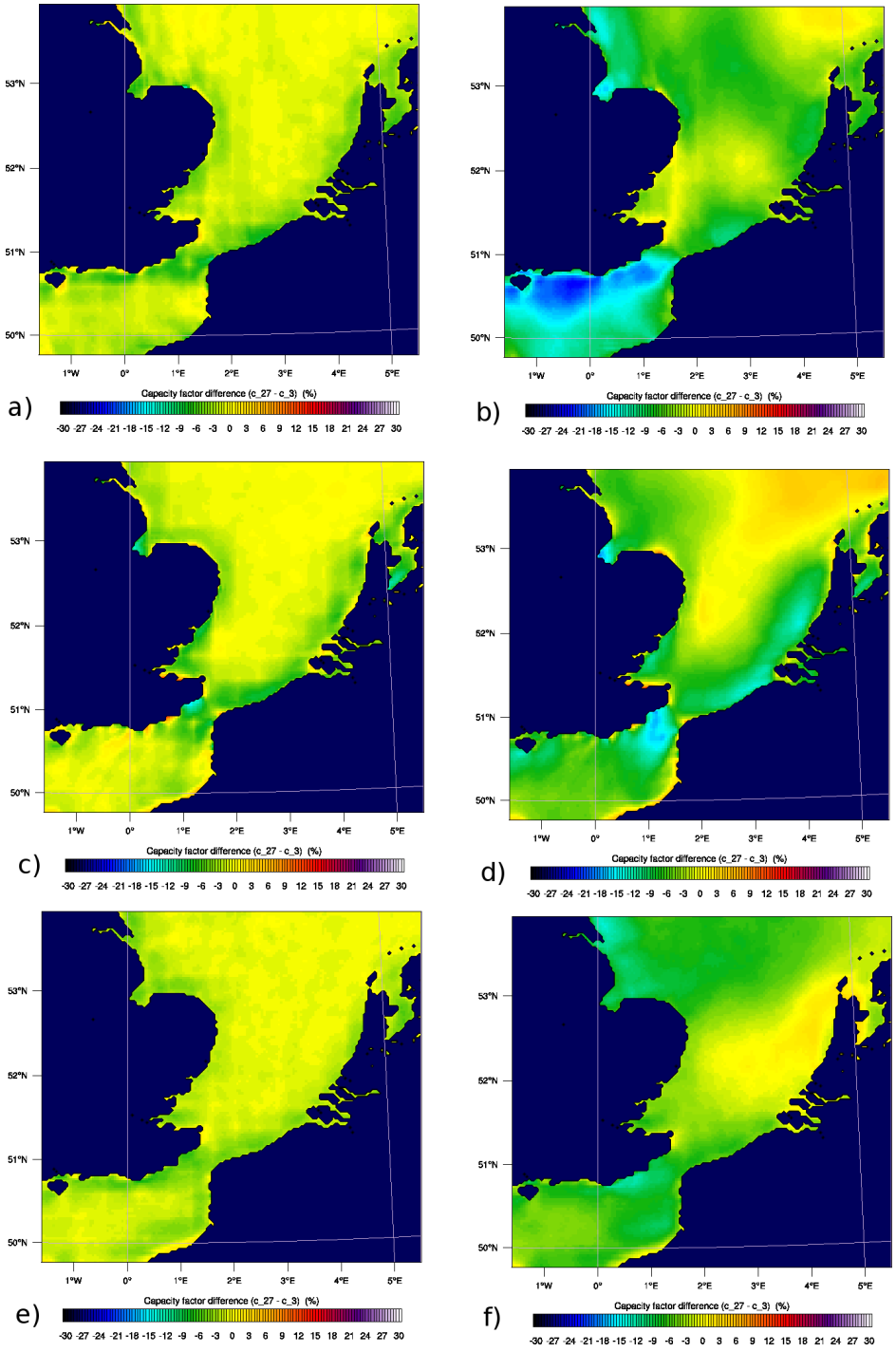

Figure 6.10: Composite capacity factor differences between the 27km and the 3km resolution domains for the (a,b) 10 *pure*, (c,d) 16 *corkscrew* and (e,f) the 9 *backdoor* sea breeze events forming off the coast of the Netherlands in 2009. The left hand side (a,c,e) plots show the differences between the 2-way interactively nested domains and the right hand side plots (b,d,f) show the differences between two independent 27km and 3km domains. Before differencing, the 27km domain is interpolated onto the 3km using bilinear interpolation.

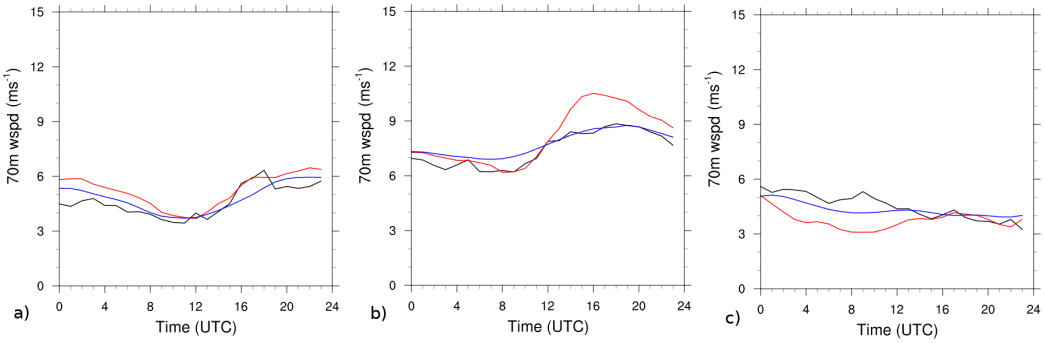

Figure 6.11: Composite 70m wind speed time series of a) 10 *pure*, b) 16 *corkscrew* and c) 9 *backdoor* sea breeze events which occurred during the 2009 Dutch sea breeze season. Red and blue lines represent the simulated composite WRF output using 3km and 27km horizontal resolutions without 2-way nesting. The black line represents the observations made and averaged over all the respective types of sea breeze at the Egmond aan Zee mast situated 18km offshore.

6.2.2 Temporal differences at the Egmond aan Zee met mast

The composite time series of 70m wind speed for the 10 *pure*, 16 *corkscrew* and 9 *backdoor* sea breeze events in the 2009 sea breeze season for the Egmond aan Zee met mast are shown in Fig. 6.11. In this sub-set of events, the differences between the resolutions are revealed by comparison with the single re-gridded 27km domain. Both the 27km and the 3km resolutions agree well with the observations.

In the *pure* sea breeze composite, the increase in wind speed due to the arrival of the sea breeze at 15:00 UTC is captured by the 3km simulations but not in the 27km, though the diurnal cycle is well resolved. However, the *corkscrew* sea breeze is better captured by the 27km horizontal resolution simulations. The *corkscrew* sea breeze in the 3km results is approximately 2ms^{-1} too strong on arrival at the mast. Similarly, the diurnal cycle is again well captured by both resolutions for the 9 *backdoor* sea breeze events, though there is no rise in observed wind speed associated with the arrival of the *backdoor* sea breeze, suggesting that for this sub-set of days, the *backdoor* sea breeze does not extend the 18km offshore to the mast.

The composite power output for each sea breeze type (Fig. 6.12) again emphasises the effect of propagating errors in wind speed compared with power values. The 2ms^{-1} error in the *corkscrew* composite equates to a power difference of 1MW. Due to instrument malfunction at 116m height for the selection of sea breeze days identified, the theoretical wind turbine is the equivalent to the 70m 3.6MW turbine used in Fig. 6.7. Note therefore that this magnitude of error relates to current turbines and not the larger 8MW machines

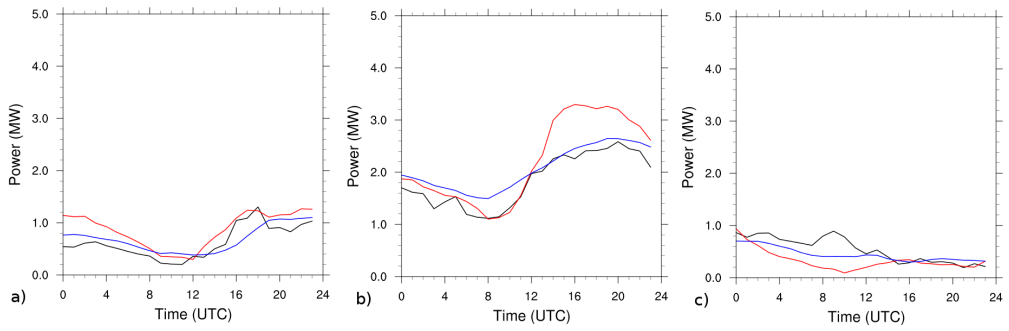

Figure 6.12: Composite wind power time series of a) 10 *pure*, b) 16 *corkscrew* and c) 9 *backdoor* sea breeze events which occurred during the 2009 Dutch sea breeze season. Measurements of 70m wind speed were observed at the Egmond aan Zee met mast and were converted into wind power estimates using a theoretical turbine with blades of radius of 60m and a power rating of 3.6MW (black). Red and blue lines represent the simulated composite WRF output using 3km and 27km horizontal resolution.

which would produce a larger wind power error with an equivalent wind speed error.

In the case of the *backdoor* sea breeze, the mast is too far offshore to to capture the sea breeze. In the next section, observations at Lynn wind farm are compared to equivalent model results. Lynn wind farm is situated 5-9km offshore from the Lincolnshire coast and so more sea breeze events are likely to reach the site.

6.2.3 Temporal differences at the Lynn wind farm

Compared with Fig. 6.5, the differences between the 27km and the 3km resolution without 2-way interactive nesting are more apparent in the composite time series for each sea breeze type (Fig. 6.13). Furthermore, with the exception of the *backdoor* sea breeze type, the coarse resolution performs as well as, if not better than the 3km. However, it is important to note that the position of the anemometers behind the turbine implies that the wind speeds are underestimated. Also, the simulated wind speeds are interpolated to 80m height and so it is plausible that the linear interpolation used is a source of error.

Similarly, the temporal evolution of the wind power generated at Lynn wind farm for each composite sea breeze type is better estimated by the 27km resolution simulations without the 2-way interactive nesting (Fig. 6.14). This is likely due to the differences between the methods of calculating the wind power. In the case of both model results, a theoretical wind turbine is used which is operating at the Betz limit and so power is overestimated, compared to the observations. Fig. 6.15 shows that when the observed wind speed is converted into wind power using the same hypothetical wind turbine as the

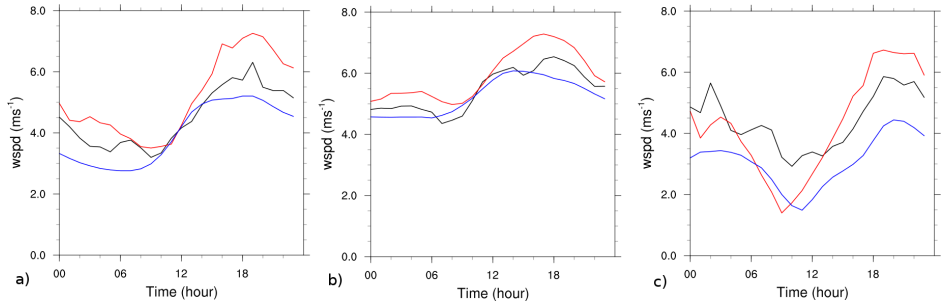

Figure 6.13: Composite time series of 80m wind speed at the Lynn wind farm of the a) 10 *pure*, b) 14 *corkscrew* and c) 3 *backdoor* sea breeze events in the 2009 sea breeze season. In each case, the black line represents the wind speed averaged over the 27 turbines at Lynn wind farm. The red and blue lines represent the 3km and 27km domains respectively. There is no 2-way interactive nesting in the model results.

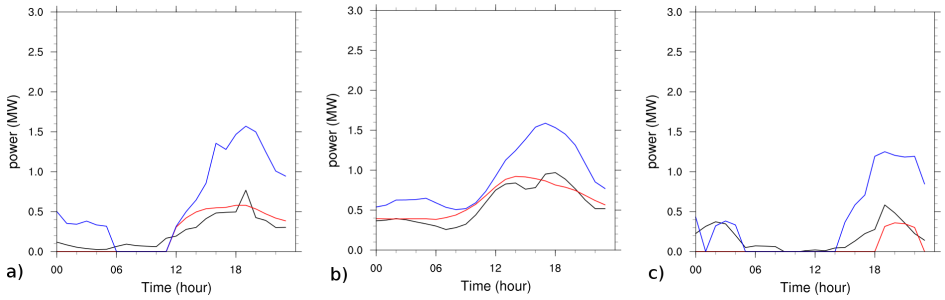

Figure 6.14: Composite time series of wind power production at the Lynn wind farm of the a) 10 *pure*, b) 14 *corkscrew* and c) 3 *backdoor* sea breeze events in the 2009 sea breeze season. In each case, the black line represents the wind power averaged over the 27 turbines at Lynn wind farm. The red and blue lines represent the 3km and 27km domains respectively. There is no 2-way interactive nesting in the model results. The conversion to wind power in the model results uses a hypothetical 3.6MW wind turbine with a hub height of 80m and a blade radius of 60m

model results, the power output is in better agreement with the 3km composite simulation.

In terms of the temporal evolution of wind power, both the *pure* and *backdoor* sea breezes contain periods where the simulated wind speed drops below the cut-in ($4 ms^{-1}$) wind speed and no power is produced. In the case of the observations, however, this does not occur for the *pure* composite although the power output is near negligible. The duration of this period for the *pure* sea breeze events is approximately 5 hours, while the thermal pressure gradient establishes and cancels out the gradient wind before the sea breeze establishes. For the composite of the 3 *backdoor* simulations, this period lasts for 9 hours for the 3km resolution simulation and only 2 hours in the observations. The 27km resolution does not pass the cut-in wind speed until 18:00 UTC.

To summarize, in the relatively active 2009 sea breeze season, sea breeze days contributed approximately 6% of the total capacity generated for both the Lynn and Egmond aan Zee wind farms. *Corkscrew* sea breeze days account for approximately 70% of the

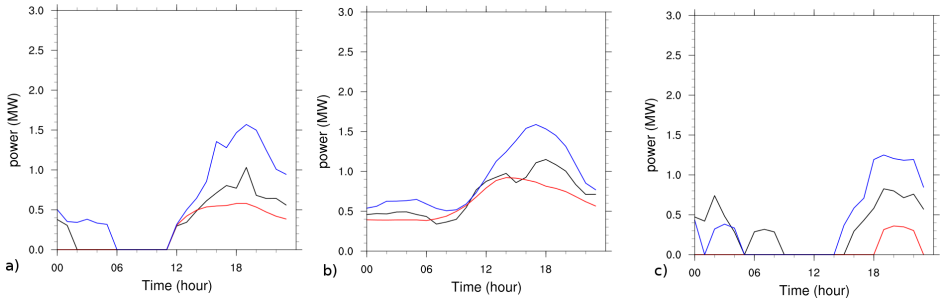

Figure 6.15: Composite time series of wind power production at the Lynn wind farm of the a) 10 *pure*, b) 14 *corkscrew* and c) 3 *backdoor* sea breeze events in the 2009 sea breeze season. In each case, the black line represents the wind speed averaged over the 27 turbines at Lynn wind farm and converted into power using a hypothetical wind turbine. The red and blue lines represent the 3km and 27km domains respectively. There is no 2-way interactive nesting in the model results. The hypothetical wind turbine is rated 3.6MW with a hub height of 80m and a blade radius of 60m

total sea breeze contribution, again for both the Lynn and Egmond aan Zee wind farms. Only the hub height wind speed of the *corkscrew* sea breeze events does not fall below the cut-in speed during any time of day for the results at the Lynn wind farm in the 2009 season. For the *pure* sea breeze, this occurs during the morning hours when the thermal pressure gradient is reducing the strength of the gradient wind. In the *backdoor* case, the duration of negligible power is much longer than in the *pure* case.

The effect of the 2-way interaction causes estimates of sea breeze impact on wind energy to be significantly underestimated, both in terms of spatial extent and overall magnitude of the capacity factor differences. This is especially true in open water, where the complexities of the coastline do not add a further dimension to uncertainty. Conducting single 27km horizontal resolution simulations for all sea breeze seasons will remove the effect of the 2-way nesting, however, problems still exist with the poor representation of the coastline in the 27km domain. In Section 7.3, this complication is removed as days which pass the selection method are compared against those which fail because of an insufficient temperature contrast.

6.3 Comparison against failed sea breeze days

One of the key issues highlighted so far is that the true contribution of the sea breeze is masked by the resolution of the coastline, the presence of the 2-way nesting and the land sea temperature contrast. This next methodology uses the composite of the days which are rejected by the identification method on the basis of an insufficient, but positive,

temperature contrast. This eliminates the issues regarding resolution differences and 2-way nesting interactions. The use of the composite smooths any associated day to day weather patterns. Naturally, the pressure patterns and associated wind speeds are not going to be identical, however, it is by definition a direct comparison between an average day which produces a sea breeze and one which does not. Days which included a negative temperature contrast between land and sea are not included as the composite imagery produced a land breeze of comparable strength to the sea breeze (Fig. A.17).

Whilst these Winter features are interesting and are not well documented in the literature, further investigation is beyond the scope of this project, and for the purposes of the methodology, the inclusion of a potential second coastal phenomena in the *non sea breeze event* composite would impact the conclusions. However, it is important to note that this *Winter land breeze* phenomena may very well impact offshore wind power production where conditions are similar to the Spring and Summer sea breeze events. Such an investigation would have both scientific benefits and potential benefits to the wind energy industry.

In agreement with the results presented so far, the *backdoor* sea breeze does not produce any significant contributions to wind energy as the background wind field is simply too low until the sea breeze forms to surpass the cut-in threshold. This is especially the case with the *backdoor* sea breeze forming off the coast of Suffolk and Essex, where much of the influence on capacity factor is due to *corkscrew* sea breezes forming off the Dutch coast (Fig. 6.16).

Corkscrew sea breezes on average enhance the capacity factor by between 8-10% up to approximately 60km offshore, (Fig. 6.17). In light gradient wind speeds, as is the case with the *corkscrew* events off the Dutch coast in Fig. 6.16, the extent of the capacity factor contributions due to the sea breeze reach 100km offshore. The result is again sensitive to the choice of coastline. For example, *corkscrew* sea breezes forming off the Dutch coastline on average create a contribution of approximately 10% to between 60km offshore, whereas *corkscrew* sea breezes off the Suffolk and Essex coastlines only extend to 20km offshore and contribute at most 7% (Fig. 6.17). In particular, the magnitude of the offshore extent is proportional to the available fetch perpendicular to the coastline A notable exception to this is for North Norfolk, where no such increase in capacity factor

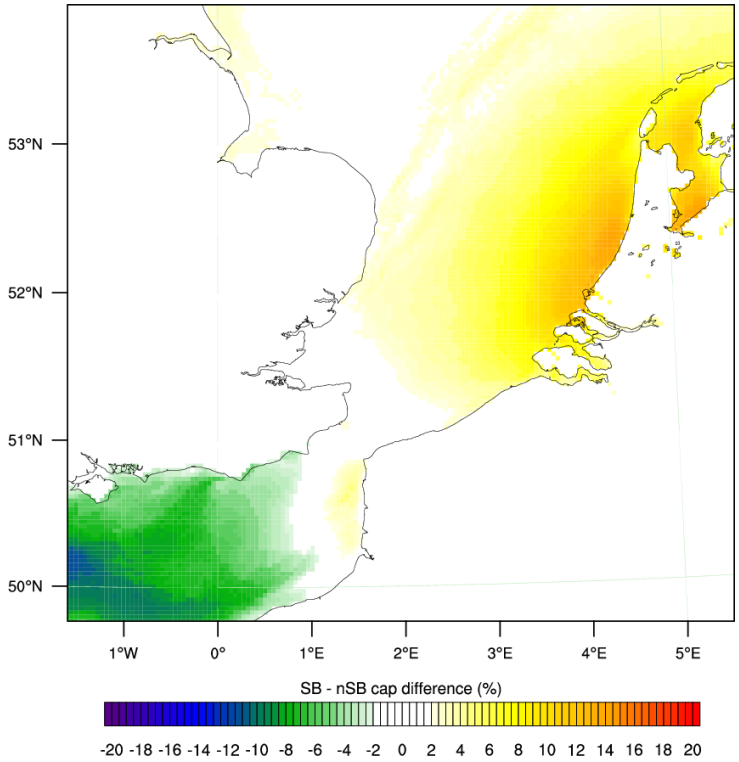

Figure 6.16: Composite capacity factor difference of the 13 *backdoor* sea breezes (SB) forming off the coast of Suffolk and Essex with the 18 days which were rejected (nSB) on the basis of a temperature contrast less than 5K but greater than 0K.

is evident. This is likely due to the influence of the adjacent Lincolnshire coast forming its own circulations.

For example, in the case of the *pure* sea breeze forming off North Norfolk, the *corkscrew* sea breeze forming off the Lincolnshire coast interacts and masks the influence of the *pure* sea breeze (Fig. 6.18). The *pure* sea breeze does not affect the daily total capacity factor for any of the other coastlines within 10km of the coast. However, it is quite apparent that days which form *pure* sea breezes have a lower 80m wind speed, compared to those which fail because of a poor land-sea thermal contrast. As a result, capacity factor differences further offshore than 10km from a *pure* sea breeze forming coastline are negative. This is true for all coastlines apart from the Netherlands which do not show any appreciable differences in capacity factor. The result agrees with the time series results in as much as the *pure* sea breeze compensates for the decline in wind speed before onset (Fig. 6.19).

Ahead of the advancing sea breeze, there is a calm region associated with a drop in power production at both the sea-ward and the land-ward edges of the circulation. This is most striking in the *pure* sea breeze composite for Southern Kent (Fig. 6.20). Not only is there evidence of sea breezes forming on different coastlines, but there is also a clear

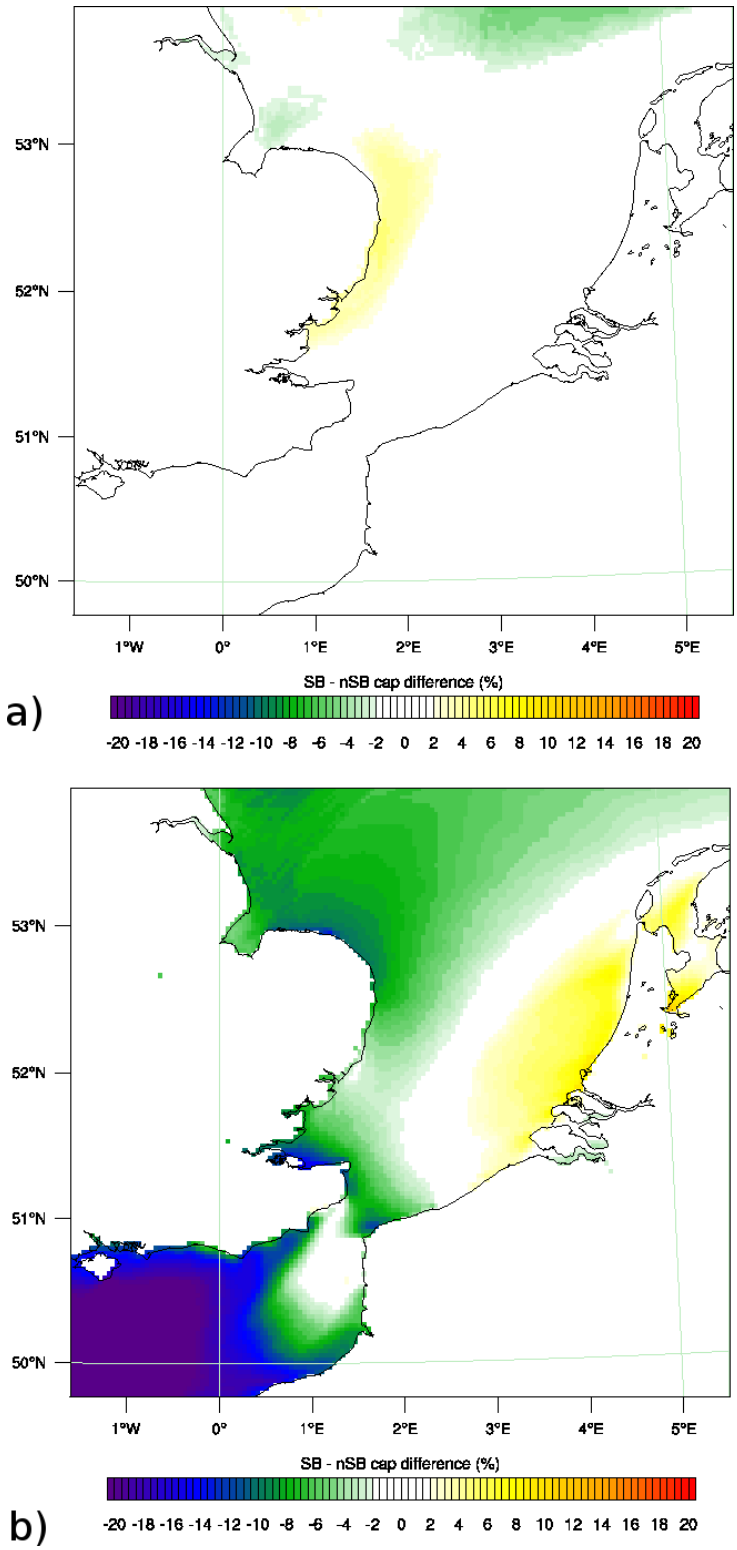

Figure 6.17: Composite capacity factor differences between both the 167 and 76 *corkscrew* sea breeze events (SB) forming off the coasts of a) Suffolk and Essex and b) the Netherlands respectively. The differences were calculated from the days which failed the selection method on the account of a positive land-sea contrast of less than 5K (nSB). For Suffolk and Essex, the number of failed days were 580 and for the coast of the Netherlands this number was 190.

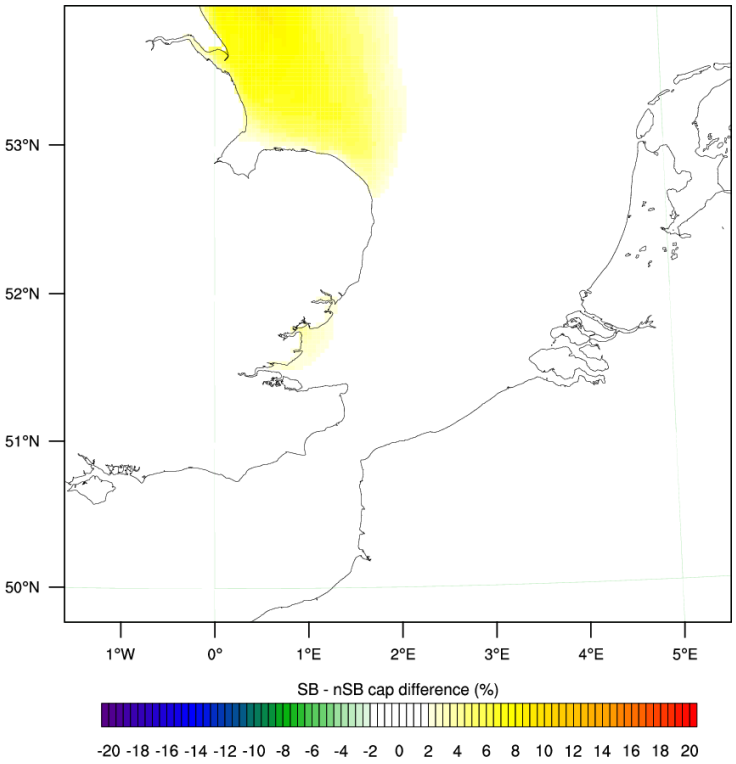

Figure 6.18: Composite capacity factor difference of the 117 *pure* sea breezes (SB) forming off the coast of North Norfolk with the 335 days which were rejected on the basis of a temperature contrast less than 5K but greater than 0K (nSB).

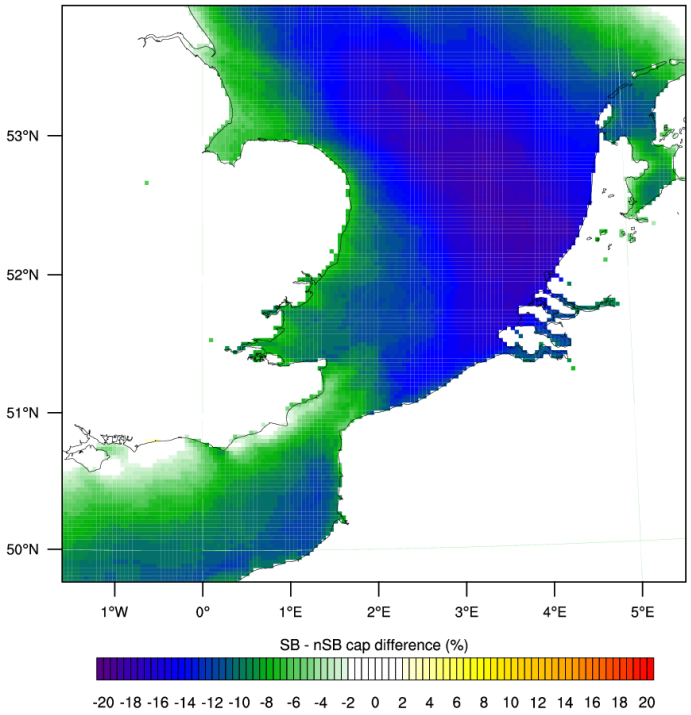

Figure 6.19: Composite capacity factor differences between the 21 *pure* sea breezes forming off the coast of Southern Kent with the 143 days which were rejected on the basis of a land-sea temperature contrast greater than 0K but less than 5K.

indication of the sea breezes influencing the wind fields of coastlines on the opposing side of the southern North Sea and English Channel. Furthermore, this gives a good indication that many of the days were correctly rejected as not producing sea breezes.

6.4 Summary and conclusions

The sea breeze climatology formulated in Chapter 6 has been used to determine the potential impact of each sea breeze type on wind energy. Results have been compared against offshore observations at the meteorological mast at Egmond aan Zee and at Lynn wind farm. Several methods have been used in order to try and quantify the spatial impact of the sea breeze. Firstly, simple differencing with the 3km grid was performed where the 27km domain was first interpolated onto the 3km grid. This method produced spatial differences in capacity factor up to approximately 30km offshore, where all sea breezes contribute to the overall capacity factor on average between 3-5%. Spatial complexities between coastlines caused subtle differences in capacity factor, especially near to complex coastlines. However, the impact of the 2-way nesting, shown through comparison with a single 27km domain for the 2009 sea breeze season, caused the magnitude and the extent of the differences to be significantly underestimated.

A comparison with the Egmond aan Zee meteorological mast revealed that the largest potential contribution to wind power production is from *corkscrew* sea breezes. Furthermore, both the *corkscrew* and *pure* sea breezes produce a marked drop in power production before the onset of the sea breeze, which is associated with the establishment of the thermal pressure gradient. The *ramp down* period is emphasised when the calculations are carried out for the modern turbines. These are predicted to be in operation by 2020.

An analysis of the Lynn wind farm observations revealed that in the 2009 sea breeze season, sea breeze days contributed 1.96% to the overall capacity factor for the season. Comparative results at the Egmond aan Zee mast revealed that in the same season, sea breeze days were accountable for generating 3.19%. In relative terms, this is equivalent to 6% of the total capacity factor for the season, 70% of which were produced on *corkscrew* sea breeze days. *Backdoor* sea breezes occur during very light wind speed conditions, though, some turbines not currently in use in the offshore environment have a lower cut-in speed and so there is potential for an increase of this in the future.

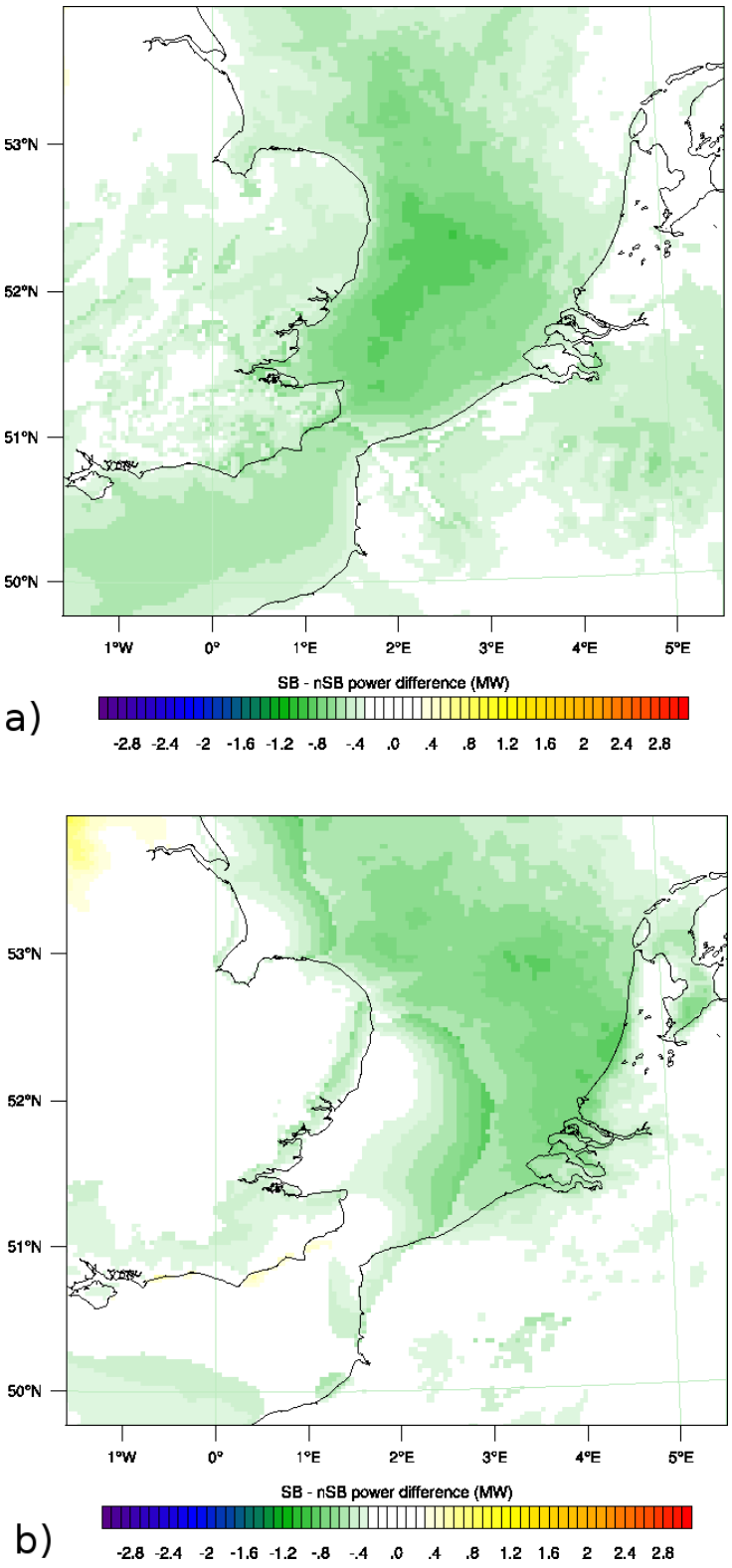

Figure 6.20: Wind power differences between the 21 *pure* sea breezes forming off the coast of Southern Kent with the 143 days which were rejected on the basis of a land-sea temperature contrast greater than 0K but less than 5K. The power curve used for the calculations matches those specifications of an 80m 3.6MW turbine operating at the Betz limit. The times shown are 06:00 UTC (a) and 13:00 UTC (b).

The effects of both the 2-way nesting and resolution differences at the coast were eliminated by the use of composites of days which failed the selection method on account of an insufficiently positive land-sea temperature contrast. Days in which a negative thermal contrast revealed a strong land breeze which could also impact wind farm regions. This is poorly studied and needs to be investigated further. *Corkscrew* sea breezes can potentially affect Round 3 sites depending on the fetch and orientation of the coastline forming the sea breeze.

The effect of *pure* sea breezes is negligible near to the coastline, however, the presence of the calm zone ahead of the sea breeze causes a reduction of power offshore which could potentially affect the proposed Round 3 farms.

Overall the results presented here confirm that the sea breeze can have potential to affect the offshore wind energy industry, both in terms of the projects currently constructed and the proposed Round 3 farms. Also, the types of sea breeze have different effects on capacity factor. For example, the *pure* sea breeze causing a loss in capacity factor offshore and the *corkscrew* sea breeze contributing overall. These results can become more important in the future as turbines become larger.

Chapter 7

Conclusions and recommendations

The rapid expansion of the wind energy industry, particularly in the southern North Sea, has created a pressing need to enhance our understanding of the wind climate in the offshore environment both from a resource and a predictability standpoint. Furthermore, it is within this environment that our basic understanding of coastal phenomena, including the sea breeze, is lacking. In particular, very little attention has been given to the lesser known sea breeze *types*, where the type is defined from the orientation of the gradient flow with respect to the coast. With the aid of high resolution modelling, this study aimed to further understand the behaviour of the sea breeze offshore and to quantify the impact the sea breeze has on current and future wind farms in the southern North Sea. In order to achieve this, several steps were undertaken which yielded many interesting results for a variety of additional user communities, namely practising sailors, operational weather forecasters and those in the atmosphere-ocean research community.

Firstly, using 2-dimensional idealized WRF simulations, the different sea breeze type characteristics were examined (Chapter 3). The simulations were extended to include a second coastline so as to be more representative of the southern North Sea and the results compared to the single coast cases. Sensitivity tests included varying the gradient wind strength and direction, the SST and choice of PBL scheme. In Chapter 4, the PBL schemes in Chapter 3 were again used to simulate the southern North Sea, but this time using realistic coastlines and initial conditions, both for the 2006 sea breeze season and for a single case study in 2012. The WRF simulations were verified against observations from the Dutch surface meteorological network and from two masts: the Cabauw tower

and the Egmond aan Zee offshore mast. These results then informed the selection of the best model set up for the construction of a sea breeze climatology.

A unique WRF simulated 11-year sea breeze climatology was constructed for 5 different coastlines in the southern North Sea using a filter method designed to incorporate all sea breeze types (Chapter 5). Sea breezes on each coast were examined in terms of frequencies, annual variation and composite wind characteristics. The results from the climatology were subsequently used by a variety of means to determine the impact of the sea breeze on wind energy (Chapter 6).

A summary of the results is now presented, initially in the form of answers to the hypotheses first proposed in Chapter 1. In Section 7.2, the relevance of the results and recommendations to different audiences is presented. Finally in Section 7.3, future useful extensions to the project are proposed.

7.1 Answers to the hypotheses

7.1.1 Sea breeze types each have distinct characteristics of their own

True. The idealized WRF simulations presented in Chapter 3 revealed that the different sea breeze types do have their own characteristics. A summary of these can be found in Tables 3.1-3.4. In particular, *pure* sea breezes are often associated with offshore calm zones which are enhanced by the presence of an opposing coastline associated with mainland Europe. For idealized simulations using the YSU PBL scheme, the calm zones span up to 30km and are eliminated entirely for gradient wind speeds greater than 10ms^{-1}. In the climatology, the extent, presence and duration of calm zones is dependant on the coastline considered, for example, the 117 *pure* sea breeze events which form off the North Norfolk coast produced two distinct calm zones up to 15km offshore, whereas no calm zones were formed in the case of the 146 *pure* events which formed off the Dutch coast due to the exposure, or fetch, of the offshore environment.

In contrast, the *corkscrew* sea breeze is often associated with the formation of coastal jets. This is especially the case in Southern Kent where jets are produced as a result of

the sharp changes in coastal orientation. The orientation of the gradient wind responsible for forming the 117 *pure* sea breeze events off the coast of North Norfolk also created *corkscrew* sea breezes off the coasts of Lincolnshire and East Norfolk. These jets encroached on the *pure* sea breeze system on the North Norfolk coast. *Corkscrew* sea breezes also have a different response to gradient wind strength than a *pure* sea breeze. Increasing the offshore gradient wind strength in the idealized *pure* sea breeze simulations resulted in later onset times, a weakening of the circulation, and less advancement in either the onshore or offshore directions. At a gradient wind speed of 9ms^{-1} for the dual-coast idealized simulations, the *pure* sea breeze is unable to form, yet for the same shore-parallel gradient wind strength associated with the *corkscrew* sea breeze, the divergence has allowed the circulation to advance up to 100km inland.

The *backdoor* sea breeze forms under weaker gradient wind conditions than the other two types of sea breeze. This is often due to the impact of other sea breezes on the circulation, for example, in the dual-coast idealized simulations, where a shore-parallel gradient wind using the YSU PBL scheme of 5ms^{-1} caused the *corkscrew* sea breeze on the western coast to prevent the *backdoor* sea breeze on the eastern coast from forming. This is also evident in the sea breeze climatology, where the wind energy analysis of the impacts of the 13 *backdoor* sea breezes on the Suffolk and Essex coasts revealed the influence of *corkscrew* events off the Netherlands coast.

7.1.2 There is a minimum horizontal resolution required to simulate the sea breeze

Unresolved. The presence of the 2-way interactive nesting in the WRF climatology simulations had a significant effect on reducing the difference in results between resolutions apart from within 27km, or one grid cell, of the coastline. In the single onshore case study presented in Section 5.1, there was a significant reduction in skill at horizontal resolutions coarser than 9km, suggesting that the minimum required resolution to simulate sea breezes was 9km. However, the composites of the sea breeze events at both Lynn and Egmond aan Zee wind farms, shown in Section 7.2, revealed that the skill of both the 3km and the 27km resolutions were comparable.

Intuitively, unless there was an unknown component of the model which was creating

errors close to the coastline, it may be expected that increasing resolution should improve accuracy of the results. However, this is not the case for the 2009 sea breeze events studied in Section 7.2. This remains a source of uncertainty. There are, however, several possible explanations. Firstly, the comparison is only with two model grid points for sub-sets of 27 and 35 events at Lynn and Egmond aan Zee wind farms respectively. It may be the case that these events at these locations are simulated inaccurately, and so the best estimate is from the coarser resolution for these cases. The sub-set of events may also not be large enough to smooth out any errors of particularly poorly simulated events, and so the composites may be biased towards these errors.

There is also the possibility that higher resolution in a marine environment does not improve the accuracy of a simulation as much as over the land due to homogeneity of the sea surface. Further investigation is required and suggested methods are proposed in Section 8.3.

7.1.3 Sea breeze systems can interact on coastlines across the southern North Sea

True. Early single coast idealized simulations revealed that the spatial scale of the sea breeze is sufficiently large to have the potential to traverse the southern North Sea (Fig. 4.3). Furthermore, the addition of the second coastline provided further evidence as *corkscrew* sea breezes forming on the western coast were able to traverse the 100km domain and restrict the formation of *backdoor* sea breezes on the eastern.

From the climatological results, this effect was evident for *backdoor* sea breeze events forming off the coast of Suffolk and Essex (Fig. 7.14). The offshore extent of the coincident *corkscrew* sea breeze forming off the Dutch coast was sufficient to extend to within 10km of the Suffolk and Essex coast. Although the *pure* sea breeze does not extend as far offshore as the *corkscrew* sea breeze, the influence of the calm zones ahead of the circulation does extend sufficiently offshore from, for example, the south coast to reach northern France.

7.1.4 A sea breeze identification method can be designed which produces coherent composite events with realistic characteristics

True. For each coastline and sea breeze type, the identification method produced composites which clearly show the development of distinctly different sea breeze types (Chapter 5). The diurnal wind cycles of each composite at the Egmond aan Zee mast shown in Chapter 6 are also different for each sea breeze type. Because of the clear sea breeze signal in the composites, some of which embrace in the order of 100 events, confidence in the ability of the identification method to capture sea breeze events is justified.

7.1.5 Sea breeze climatology is independent of coastal orientation in a given region

False. Referring to Table 5.4, it can clearly be seen that this is not the case, and that the frequency of sea breezes is strongly dependent on the orientation of the coastline, a significant new finding previously undocumented. Furthermore, the degree of this frequency variability between coastlines can be greater than a factor of two, for example, from May 2002 to September 2012 154 sea breezes formed off the southern coast of Kent whereas 335 sea breezes in total formed off East Norfolk (Table 5.4). In conjunction with the coastal orientation, the dominant flow regimes and gradient wind directions are also important. Around the coasts of Britain and the Netherlands, this combination leads to a high degree of sea breeze inter-annual variability which is different for each coastal orientation (Fig. 6.46).

The coastal orientation with respect to the prevailing flow regimes also contributes to the length of the sea breeze season. For example, the sea breeze season of East Norfolk is three months longer (March - October) than that of North Norfolk (May - September) despite these coasts being located adjacent to one another (Fig. 5.47). Furthermore, *pure* sea breezes forming off the coast of North Norfolk are significantly affected by *corkscrew* sea breezes forming off the coast of Lincolnshire.

7.1.6 Sea breezes have an important impact on wind energy generation in the Southern North Sea

True. Sea breezes have an impact in terms of the temporal evolution of wind power generation on a sea breeze day over a spatial scale of relevance to Rounds 1,2 and 3 of the UK offshore wind energy program. Furthermore, the effects are likely to increase as the power rating of offshore wind turbines increases (Figs. 7.6 and 7.7).

Corkscrew sea breezes contribute the most to wind energy, due to the formation of coastal jets enhancing the coastal wind speed (Fig. 6.15). Within the *pure* sea breeze circulation, the increase in wind power associated with the arrival of the sea breeze is counteracted by the development of offshore calm zones (Fig. 6.18). Further offshore, beyond the offshore extension of the *pure* sea breeze, the calm zone has a detrimental effect on wind power production, suggesting more relevance to the Round 2 and 3 developments that are further than 10km offshore.

In terms of the overall contribution of the sea breeze to wind energy in a given season, in 2009, it was found that 6% of the total wind energy capacity factor between at both Lynn (May - September) and Egmond aan Zee (March - October) wind farms were generated on sea breeze days. Approximately 70% of this was purely attributable to *corkscrew* sea breeze days. The *backdoor* sea breeze was only responsible for 5% of the sea breeze contribution as associated wind conditions were often too low to exceed the turbine cut-in threshold speed. Given that 2009 was a year which produced a marginally above average number of sea breezes, these estimates are likely to be above what is to be expected for any given sea breeze season. Nevertheless, the values here represent a significant contribution to the overall capacity of a season.

7.2 Recommendations

There are a number of relevant audiences for whom the results presented here are of value. Obviously for the wind energy industry, knowing that different sea breezes will affect power production in different ways, and knowing how frequently they occur on a given coastline provides important insight. This is not just from an operational forecasting perspective where unanticipated power shortfalls and surpluses can be very costly. Also

of significance, if a coastline is to be modelled for wind energy purposes, either for an existing farm or one which is in planning, it is clearly not enough to simply analyse one coastline in detail since it is entirely possible for the wind climate to be influenced by a sea breeze forming off another, as in the case of *corkscrew* sea breezes forming off the coast of the Netherlands influencing the coast of East Norfolk. Knowledge about the sea breeze climate for multiple coasts is therefore key to any southern North Sea wind farm including those proposed in Round 3. Furthermore, simply positioning wind farms further offshore, as is the case with the Round 3 farms, does not necessarily mean that the wind speeds are always going to be higher, such as in the case of the 169 *corkscrew* sea breeze events forming off the coast of East Norfolk.

For the weather forecasting community, as highlighted in Section 7.1.1, knowledge of sensitivity to model setup is always vital with regard to overall forecast performance and the potential need for human forecaster intervention. For example, the effect of having a 2m temperature cold bias on the timing of a sea breeze and the differences between sea breeze characteristics between PBL schemes will impact a forecaster's perception of when and whether a sea breeze may form (Chapter 4). Greater forecaster awareness of the different sea breeze types and how one type on a particular coastal orientation may impact another can follow as a direct addition to the forecaster knowledge base. For example, 60% of days which produce a *pure* sea breeze on the North Norfolk coast will also lead to a coincident *corkscrew* sea breeze on the East Norfolk coast. Also, by highlighting how varied the sea breeze season is with respect to specific coasts and in terms of inter-annual variability, this research will change some perceptions of the physics and characteristics of the sea breeze circulations.

Other communities, such as those in sailing, will be affected by the offshore jets and calm zones produced in *corkscrew* and *pure* sea breeze conditions. Although the terms *corkscrew* and *backdoor* sea breezes were originally coined by the sailing community, improved knowledge of the degree of expected sea breeze type variability for each coastal orientation and of what can be expected when a certain type of sea breeze forms on one coast of a different orientation will nevertheless be of use to both hobbyists and competition sailors. For example, if a sailing event were to take place off the North Norfolk coast and the gradient wind was offshore, the *pure* sea breeze which initially forms will

generate calm regions between 09:00 and 12:00, subsequently the *corkscrew* sea breezes forming over Lincolnshire and East Norfolk will generate coastal jets and dominate the offshore windfield.

For the atmosphere-ocean research community, a number of new findings are of consequence, especially the distinction between the different sea breeze type characteristics. Most existing studies are only concerned with the *pure* sea breeze type, though as shown in Chapter 3 and Fig. 6.5, notably different diurnal wind cycles are produced for each different sea breeze type. A climatology of all sea breeze types has not been previously created for the southern North Sea. As far as the author is aware, there are no existing identification methods which exist for making the distinction between different sea breeze types. Also, the testing of an identification method on several coastlines, rather than on an individual coast, highlighting regional coast-to-coast variations, is not something which has previously been tested. The behaviour of the different PBL schemes in simulating sea breeze characteristics highlights possible reasons for discrepancies between previous simulations of sea breeze offshore extents. Also, there is the expectancy that at higher resolution, the forecast will be more accurate. However, the verification at the offshore sites in Chapter 6 imply that this is not always the case. Whilst the analysis conducted is not conclusive, the results do warrant further investigation.

7.3 Future research

There are a number of issues which have resulted from this research which warrant further investigation. Firstly, the lack of improvement between model resolutions when examining the offshore environment. As stated previously, the verification conducted is by no means exhaustive or conclusive, and so further work is required in verifying against offshore resources. Although not always in ideal positions to study sea breezes, there are 4 offshore buoys and a mast present in the North Sea which warrant further investigation. The Meteomast IJmuiden is located 85km offshore from IJmuiden. Like the Egmond aan Zee mast, it has 3 levels where observations are taken. However, it is also equipped with a lidar to examine windfields at greater height and at much finer vertical resolution than a mast. The mast could also be of use for further examination of the performance of the PBL schemes since there was no conclusive evidence that one scheme was more

favourable than another. Additionally, to eliminate the effect of the 2-way interactive nesting, 27km simulations should be run for the whole climatology period to conduct a more rigorous analysis as to the effect of changing resolution offshore.

Whilst the Lynn and Inner Dowsing wind farm is used in comparison with the sea breeze climatology off the North Norfolk coast, the incorporation of the Lincolnshire and North Kent coasts into the sea breeze climatology will complement the results, although some Lincolnshire sea breeze days are included in the North Norfolk sea breeze climatology. Furthermore, sea breezes forming off the North Kent coast will likely impact the London array and Thanet wind farms and so creating a sea breeze climatology for North Kent will be beneficial to these wind farms.

The *Winter land breeze* which was revealed from analysing the composite of days which did not pass the sea breeze identification method on the basis of an insufficient land-sea thermal contrast presents an additional avenue for further study (Section 6.3). This feature is not well documented and could easily be further examined using a modified version of the identification method. The strength of the feature is surprisingly comparable to the sea breeze and potential therefore exists for an impact on offshore wind energy in a similar manner.

Finally, the range of sea breeze characteristics could be explored in relation to the composite imagery. This will provide a greater idea as to the range of possible windfields expected for each sea breeze type, rather than the composite effect explored here.

Appendix A

Data and tools

In this chapter, each resource used in the present study is described. First, the observational resources are explained, including two meteorological masts, the Dutch surface meteorological network, and the Lynn and Inner Dowsing wind farms. Secondly, the WRF numerical model is described, including the use of SST and lateral boundary conditions to drive the model.

A.1 Observational resources

There are numerous types of observation used in the present study in order to form a comparison to any numerical simulations (Fig. A.1). These can be split into two distinct categories. These are surface observations, or observations taken at one height, or profiles, which can either take the form of a mast or a full atmospheric sounding. These are now described.

Table A.1: Types of observation used in the present study and corresponding numbers for Fig. A.1.

Number	Name	Type	Number	Name	Type	Number	Name	Type
1.	Valkenburg	surface	12.	Leeuwarden	surface	23.	Cabauw	mast
2.	IJmuiden	surface	13.	Marknesse	surface	24.	Giltze-Rijen	surface
3.	De Kooy	surface	14.	Deelen	surface	25.	Herwijen	surface
4.	Schiphol	surface	15.	Lauwersoog	surface	26.	Eindhoven	surface
5.	Vlieland	surface	16.	Heino	surface	27.	Volkel	surface
6.	Berkhout	surface	17.	Vlissingen	surface	28.	Ell	surface
7.	Hoorn	surface	18.	Westdorpe	surface	29.	Maastricht	surface
8.	De Bilt	surface	19.	Wilhelminadorp	surface	30.	Arcen	surface
9.	Soesterberg	surface	20.	Hoek van Holland	surface	31.	Egmond aan Zee	mast
10.	Stavoren	surface	21.	Woensdrecht	surface	32.	Lynn and I. Dowsing	wind farm
11.	Lelystad	surface	22.	Rotterdam	surface	33.	Herstmonceux	sounding

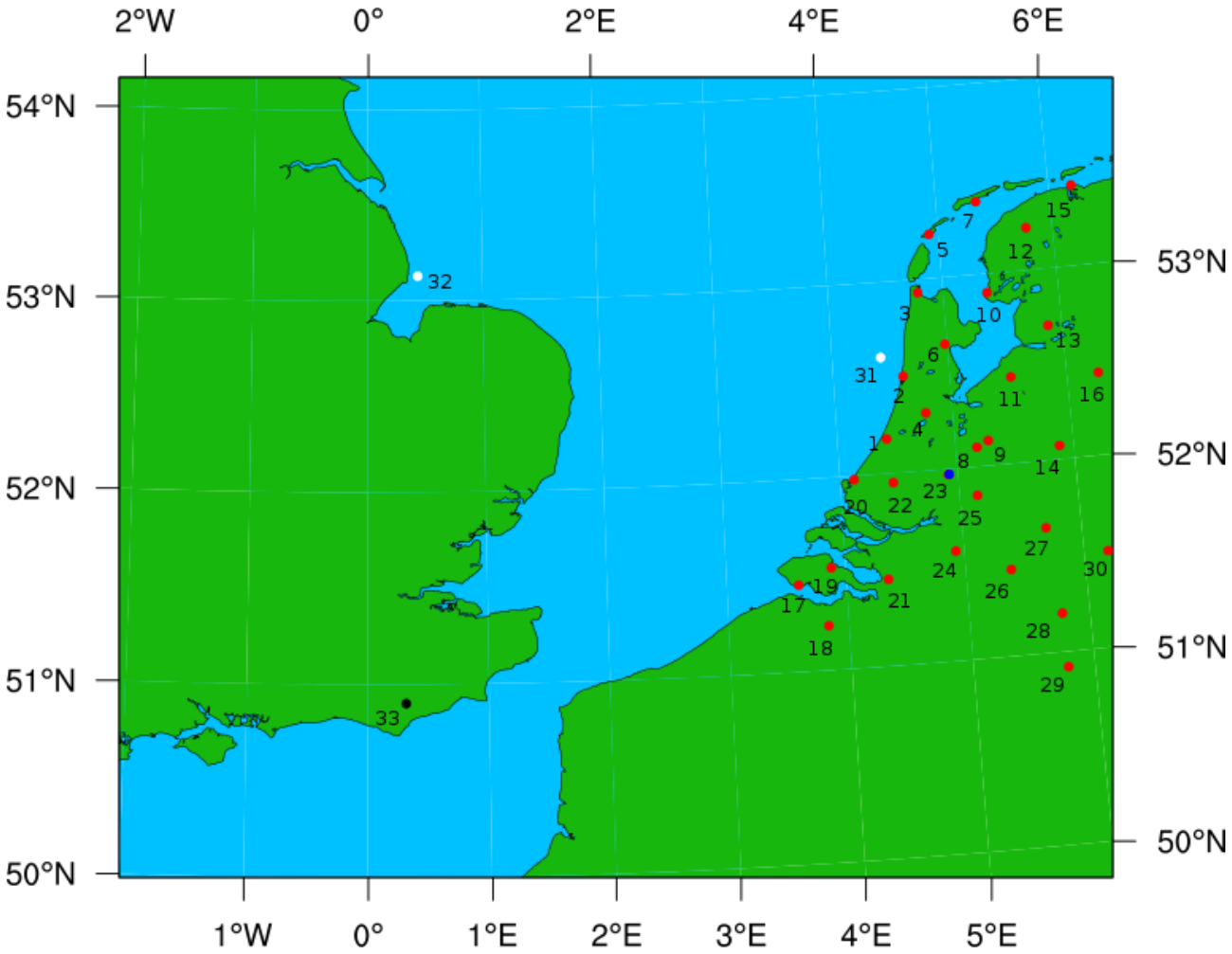

Figure A.1: Lambert conformal projection of observations used in the present study. The blue and black circles show both the Cabauw tower and the Herstmonceux radiosonde station. Shown in red, are the locations of the Dutch surface observation network. Finally, the white spots indicate the locations of the offshore observations. The numbers on the map correspond with the numbers in Table A.1

A.1.1 The Dutch Surface observational Network

The Dutch surface meteorological network has been built and maintained since 1905 by the Royal Netherlands Meteorological Institute and consists of 36 stations, each observing hourly values of pressure, wind direction, wind speed, temperature and dew point temperature. Detailed meta-data for each station can be found at `http://www.knmi.nl/klimatologie/metadata/stationslijst.html`. The resolution of the stations is much greater than in eastern England and so offer an opportunity to study the sea breeze in greater detail as it penetrates inland. In this study, observations from 30 of the 36 stations are used as the remaining 6 are outside the region of interest (Fig. A.1).

In practice, the data observed at the surface stations are assimilated in Royal Netherlands Meteorological Institute (KNMI)'s operational High Resolution Limited Area Model (HIRLAM) for forecasting weather and climate. The data are not gap-filled, although various quality control checks are undertaken:

1. Site surveys are undertaken twice a year to ensure that measurements are being recorded in conditions which agree to the World Meteorological Organization's (WMO) standards.

2. Before usage, each sensor is calibrated and evaluated. KNMI uses a fixed calibration constant for each type of instrument so that the user does not have to adjust for individual instruments

3. Each sensor is connected to the KNMI sensor Interface (SIAM). On operation, this checks for consistency between readings, for example that maximum temperature is greater than minimum and that minimum temperature is less than average temperature. The system also checks for any sudden jumps between successive measurements of a given instrument.

4. Once in the central database, data are subject to further quality control by a forecaster where sensor reports can be checked and discarded if necessary. Data are again subject to consistency checks and spatial variations.

A.1.2 The Cabauw tower

The Cabauw tower forms part of the Cabauw Experimental Site for Atmospheric Research (CESAR). The tower is located at 51.97°N 4.93°E (Fig. A.1; Table A.1) and has been in operation since the 26th October 1972. Despite being situated over 50km away from the North Sea, sea breezes are known to reach Cabauw (Tijm pers. comm.; Tijm *et al.*, 1999; Tijm and Van Delden, 1999), and so, in terms of validating model simulations for both sea breeze events and for general performance, the tower is fit for purpose.

It consists of 7 levels ranging from 1.5, 10, 20, 40, 80, 140, 200m A.2. Temperature and dew point temperature are recorded at all levels at a temporal resolution of 10s. Similarly, wind speed and direction are recorded at the same temporal resolution but on 6 levels. These levels are identical to temperature but the level at 1.5m is excluded. Although measurements are recorded below 20m, they are not in undisturbed flow and so these measurements are observed from two other nearby masts at the CESAR site.

At each height, there are two instruments fitted to either side of a boom. Both instruments are continually recording, though only the one which is in the most undisturbed flow is used for data logging purposes. This naturally varies through time because of wind direction changes and so this is accounted for during post processing. The data are subject to the same SIAM system as the surface network but also undergo gap filling, following the method of Beljaars and Bosveld (1997). A continuous record of gap-filled observations from present dating back to the 1st January 2001 are freely available online at `http://www.cesar-database.nl/ShowCategories.do`.

A.1.3 The Egmond aan Zee meteorological mast

The Egmond aan Zee wind farm consists of 36 wind turbines with a capacity of 3MW each. Located 10-18km offshore of the Netherlands (Fig. A.1; Number 31), the farm was the first large scale project to be completed by NordzeeWind; a joint venture between Shell wind energy and Nuin Duurzame Energie. Part of the project involved the construction of a meteorological mast, built to record wind speed, wind direction, temperature and water characteristics both before during and after the construction of the wind farm.

The mast was originally erected in 2003 and continued to operate until the end of December 2010, where turbines were in operation from the 1st January 2007. Data are

Figure A.2: The 213m Cabauw tower, located at 51.97°N 4.93°E (Fig. A.1). Image from IAMU (2012)

available from July 2005 and are freely available at `http://www.noordzeewind.nl/kennis/rapporten-data/`. The mast, located at 52.6°N, 4.38°E is positioned at the south western side of the wind farm, so that the dominant wind direction is least disturbed by the turbines. Booms are located at 21.6, 70 and 116m, corresponding to the rotor heights and sweep area of the blades. Three booms are located at each height oriented at 300° (NW), 60° (NE) and at 180° (S) with sonic and acoustic anemometers are used so that wake effects can be isolated and filtered out. The data are recorded in 10 minute intervals and checked at the end of each month by the supplier for quality.

A.1.4 Lynn and Inner Dowsing offshore wind farm

The Lynn and Inner Dowsing wind farms were developed simultaneously as part of round one, and have been operational since May 2008. Operated as a single farm by Centrica,

it consists of 54 turbines, 27 at Lynn and 27 at Inner Dowsing, each with a power rating of 3.6MW. Hub height of each turbine is 80m and cut-in and cut-out speeds are 4ms^{-1} and 25ms^{-1} respectively. The rated wind speed, the speed in which the power output is at maximum, is 13.5ms^{-1}. Since construction, the average capacity factor of the farms is between 30-35% (4COffshore, 2013).

Wind speeds are measured at hub height for each turbine by a cup anemometer, situated behind the rotor, so there is likely interference from wake effects. The anemometers are not subject to the same quality control methods as the other sources. Therefore, quality control checks against neighbouring turbines must be carried out first.

A.1.5 HADcrut3 dataset

HADcrut3 is a 5° dataset of global historical temperature anomalies with respect to 1961-1990. It consists of land surface data from the CRUTEM3 and SST data from the HadSST2 datasets. A comprehensive discussion of the dataset is available in (Brohan *et al.*, 2005). For the purposes of this project, the data are solely used by way of showing the evolution of temperature anomalies during the study period (Section 6.1).

A.1.6 Satellite imagery

Satellite imagery is used from the Moderate Resolution Imaging Spectroradiometer (MODIS) aboard the 2 Earth Orbiting System (EOS) satellites (Section 5.1). The scanner has 36 channels, where the visible and infra-red imagery are operating at a spatial resolution of up to 250m, 16 times higher than other scanners, such as AVHRR and SeaWIFS, making it ideal for visualizing cloud streets associated with sea breeze development. Imagery are available from the Dundee Satellite Recieving Station at `http://www.sat.dundee.ac.\ac{UK}/auth.html`.

A.1.7 Radiosonde ascents

Radiosondes ascents from Herstmonceux station (Fig. A.1: Number 33) are used to initialize idealized experiments described in Section 3.1. They are launched twice a day (at midnight and midday), sampling pressure, temperature and humidity at regular intervals, giving an indication of the full thermodynamic profile of the atmosphere.

A.2 Modelling resources

A.2.1 The Global Forecasting System (GFS) final analysis

The Global Forecasting System (GFS) Final Analysis is freely available to download at `http://rda.ucar.edu/datasets/ds083.2/`. Output is at 1° spatial resolution and 6 hourly temporal resolution from the 30th July 1999 at 18:00 UTC until present. The GFS FNL analysis is different to a standard real-time analysis as production is delayed by an hour so that more observations can be assimilated.

During the data availability period a number of diagnostic variables are added to the output of the analysis such as PBL height and latent heat flux in 2007. For detailed metadata, see National Centers for Environmental Prediction (2000). Impotatantly for this project, the number of soil layers increased from 2 to 4 on the 31st May 2005, from which there was a brief period of 36 hours where the quality of the soil data were questionable.

These data are supported for use with the WRF model and have been widely used in sea breezes and WRF modelling studies (eg. Challa *et al.*, 2009; Tie *et al.*, 2009; Papanastasiou *et al.*, 2010)

A.2.2 NCEP real time SST archive

SST input is derived from the NCEP real time SST archives which span between the 1st January 2001 until present. The analyses are derived through a combination of ship, buoy, satellite derived SST and satellite derived sea ice coverage. Data are freely available to download at `http://polar.ncep.noaa.gov/sst/oper/Welcome.html`.

The output of the analyses are daily with a horizontal resolution of 0.5°. Each satellite SST observation is first averaged onto the 0.5° grid with night and day observations separated. Bias errors associated with the satellite observations is removed using the same technique in the 7-day Reynolds-Smith climatological analysis (Reynolds *et al.*, 2007). The use of satellite retrievals has varied throughout the dataset. Between the 5th June 2001 and the 6th May 2004, the NOAA-16 AVHRR data were used when a switch to NOAA-17 occurred. NOAA-18 and NOAA-19 were substituted on the 23rd September 2008 and September 14th 2010.

Any late observations which do not make it into the previous analysis but are less than

36 hours old are used in the following day. Regarding sea ice, if the ice cover exceeds 50% then the surface temperature is estimated using:

$$t(S) = -0.0575S + 0.0017S^{1.5} - 0.0002S^2 \tag{A.1}$$

where S is salinity in psu.

Regarding verification of the analyses, 5 parallel runs are computed but with a subset of buoys withheld. Each buoy which passes quality control is used for verification purposes in one of the parallel runs but is also be assimilated in the other 4. Bias, standard deviation of the bias and root mean squared error is calculated for each of the parallel runs and then averaged over all runs to produce a series of ensemble statistics. The statistics are then sub-divided into 33 different regions. As with the GFS FNL analysis, the data are supported for use with the WRF model and have been proven to give realistic results (eg. Shimada and Ohsawa, 2011).

A.3 The WRF Model

The (WRF) model is a mesoscale model designed to be able to have both forecasting and research capabilities (Skamarock and Klemp, 2008). Contributors to the model include the National Center for Atmospheric Research (NCAR), the National Oceanic and Atmospheric Administration (NOAA), the Air Force Weather Agency (EFWA), the Naval Research Laboratory, the University of Oklahoma and the Federal Aviation Administration (FAA). It has been widely used in meso-scale modelling applications, including sea breeze simulations (eg. Borge *et al.*, 2008; Papanastasiou *et al.*, 2010; Lin *et al.*, 2008). Furthermore, WRF has a high degree of flexibility, offering a wide range of model physics and set-up options, giving the user more control with model design.

The model consists of two dynamical cores; the Advanced Research WRF (ARW) and the Non-Hydrostatic Mesoscale Model (NMM). Both are Eularian mass solvers and operate with terrain-following vertical coordinates and identical physics options, though there are differences in horizontal grid staggering and equation solving methods that distinguish between the two cores (Skamarock and Klemp, 2008). Research has shown that there is little superiority between either core, but there is a tendency for the NMM to be used

more so with forecasting applications (Bernardet *et al.*, 2010; Gallus and Bresch, 2006). For the purposes of this research, version 3.3.1 is used in conjunction with the ARW dynamical core. For a detailed explanation of the model formulation see Skamarock and Klemp (2008), however, because of the importance of simulating the PBL for sea breeze and wind energy applications and for their role in the project, 3 different PBL schemes and are now described.

A.3.1 PBL physics

The region of the atmosphere which is affected by surface friction is known as the PBL. Since both the scale of the sea breeze and wind turbine operating heights are within the PBL, accurately simulating this region is a high priority. Accurately resolving the PBL involves parametrizing the sub-grid scale eddies and therefore the need to solve the turbulence closure problem (Stensrud, 2007). WRF has several PBL physics options used to achieve this. For the purposes of this study, the Yonsei State University (Hong and Pan, 1996), Mellor-Yamada Janjic (Mellor and Yamada, 1982; Janjic, 1990) and the Mellor-Yamada-Nakanishi and Niino (Nakanishi, 2001) PBL schemes (herein after YSU, MYJ and MYNN respectively) are used. These particular schemes are chosen as examples of the two different types of turbulence closure models and a further example of more complex PBL scheme.

A.3.1.1 YSU first order non-local PBL scheme

The first to consider is the YSU PBL. Principally this is a first order non-local scheme; where turbulent mixing is carried out over the whole of the PBL depth in order to represent mixing by large scale eddies. However, the YSU PBL is based on the local *K profile* approach, in which the degree of mixing over time is directly proportional to the second derivative of a model variable with respect to height,

$$\frac{\partial C}{\partial t} = \kappa_c \frac{\partial^2 C}{\partial z^2}, \tag{A.2}$$

where *C* represents a heat or momentum variable and κ_c is the eddy diffusivity coefficient. The YSU scheme makes two additions to this formulation;

$$\frac{\partial C}{\partial t} = \left[\kappa_c \left(\frac{\partial C}{\partial z} - \gamma_c\right) - (\overline{w'c'_h}) \left(\frac{z}{h}\right)^3\right] \tag{A.3}$$

The first addition is γ_c which represents the correction by non-local eddies. The second is the entrainment flux term, $-\overline{(w'c')_h}(\frac{z}{h})^3$, which gives an explicit treatment to the entrainment process. The height of the PBL is diagnosed from the surface upwards, where the bulk Richardson number first exceeds a particular threshold (Hong *et al.*, 2006). In the initial formulation, this threshold was set to 0, however, Hong and Kim (2008) note that for a stable PBL the scheme produced too little vertical mixing, and so the critical Richardson number was increased to 0.25 over the land.

$$Ri = \frac{\frac{g}{\bar{\theta}}\frac{\partial \bar{\theta}}{\partial z}}{\left[\left(\frac{\partial \bar{u}}{\partial z}\right)^2 + \left(\frac{\partial \bar{v}}{\partial z}^2\right)\right]} \tag{A.4}$$

A.3.1.2 MYJ local 1.5 order TKE PBL scheme

The second PBL scheme to consider is the MYJ 1.5 order Turbulent Kinetic Energy (TKE) local scheme. Turbulence is closed in this scheme using the TKE equation,

$$\frac{d\left(q^2/2\right)}{dt} - \frac{\partial}{\partial z}\left[l_m q S_q \frac{\partial}{\partial z}\left(\frac{q^2}{2}\right)\right] = P_s + P_b + \epsilon \tag{A.5}$$

where on the left hand side, q is twice the kinetic energy, l_m, the master eddy mixing length and S_q is an empirical constant. On the right hand side, the production of TKE by shear, buoyancy and eddy dissipation are represented by P_s, P_b and ϵ respectively. These are determined from;

$$P_s = -(\overline{u'v'})\frac{\partial u}{\partial z} - (\overline{v'w'})\frac{\partial v}{\partial z} \tag{A.6}$$

$$P_b = \beta_1 g(\overline{u'\theta'_v}) \tag{A.7}$$

$$\epsilon = \frac{q^3}{B_1 l_m} \tag{A.8}$$

where B_1 and β_1 are constants. The master length, l_m is defined as the average distance an eddy travels before it exchanges momentum with surrounding eddies. In the MYJ scheme, it takes the mathematical definition;

$$l_m = l_0 \frac{kz}{kz + l_0} \tag{A.9}$$

where *k* is the von Karman constant and l_0 equates to;

$$l_0 = 0.23 \frac{\int_0^z zq \, \mathrm{d}z}{\int_0^z q \, \mathrm{d}z} \tag{A.10}$$

In this scheme, the height of the PBL is determined where q falls below $0.001 \mathrm{m}^2\mathrm{s}^{-2}$

A.3.1.3 MYNN 1.5 order TKE scheme

The final PBL scheme is the 1.5 order MYNN TKE scheme. This is similar in many ways to the MYJ PBL with the exception of the definition of l_m. Here, the inclusion of the surface (l_s), turbulent (l_t) and buoyancy (l_b) length scales give a more explicit treatment of the stability of the PBL;

$$\frac{1}{l_m} = \frac{1}{l_s} + \frac{1}{l_t} + \frac{1}{l_b} \tag{A.11}$$

Here, the value of l_s is dependent on z, normalized by the Monin-ObUKhov length, *L*, where;

$$L = -\frac{u_*^3 \overline{\theta_v}}{kg(\overline{w'\theta_v'})_s} \tag{A.12}$$

and;

$$l_s = \begin{cases} kz/3.7 & \text{if stable } (z/L > 1) \\ kz(1 + 2.7(z/L)) & \text{if neutral } (0 \geq z/L < 1) \\ kz(1 - 100(z/L))^{0.2} & \text{if unstable } (z/L < 0) \end{cases} \tag{A.13}$$

$$l_t = 0.23 \frac{\int_0^\infty zq \, \mathrm{d}z}{\int_0^z q \, \mathrm{d}z} \tag{A.14}$$

$$l_b = \left[1 + 5 \left(\frac{q_c}{l_t N}\right)^{0.5}\right] \frac{q}{N} \tag{A.15}$$

Whilst in any WRF sensitivity experiments conducted, it is stated that the PBL scheme is the only scheme being tested, in actuality, the surface physics schemes need to be

changed to be compatible with the PBL schemes. All three schemes use a form of Monin-ObUKhov similarity theory, where heat, moisture and momentum fluxes are represented by a series of dimensionless relationships (Foken, 2006). The MM5 similarity scheme is used with the YSU PBL and Eta similarity is used in conjunction with the TKE schemes, LYJ and MYNN.

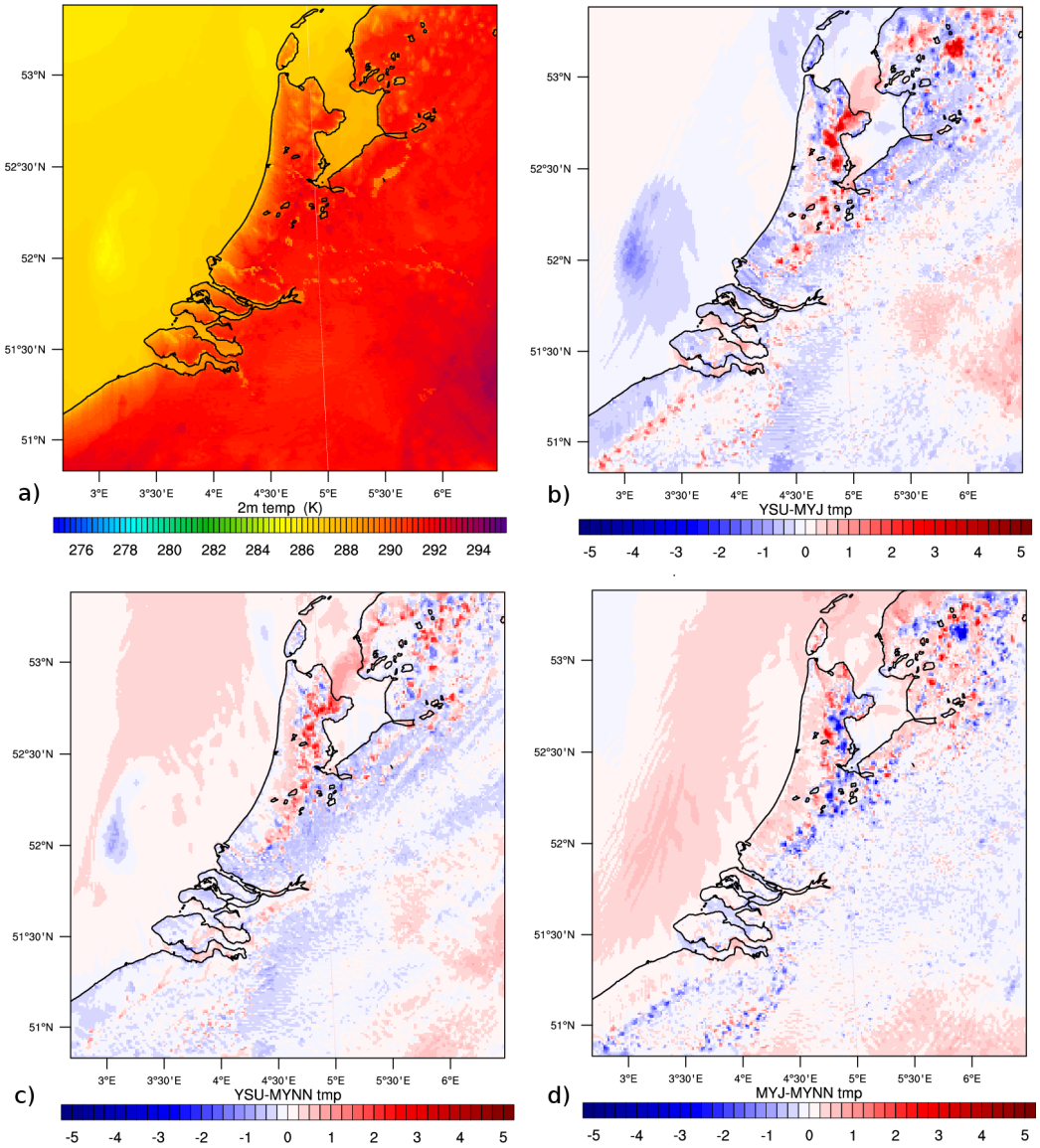

Figure A.3: a) 2m temperature at 12:00 UTC on the 19^{th} June 2012 using the baseline simulation with the YSU PBL. The differences between b) YSU and MYJ, c) YSU and MYNN and d) MYJ and MYNN are also shown for 12:00 UTC baseline simulations.

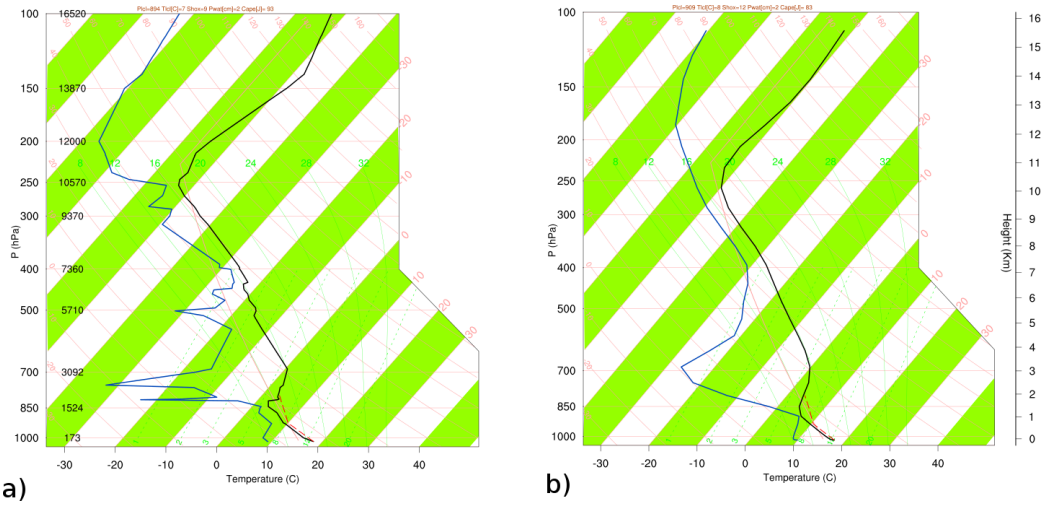

Figure A.4: Observed (a) and simulated (b) thermodynamic profiles at De Bilt for 12:00 UTC on the 19th June 2012. The simulated profile is the YSU baseline simulation taken from the nearest land model point.

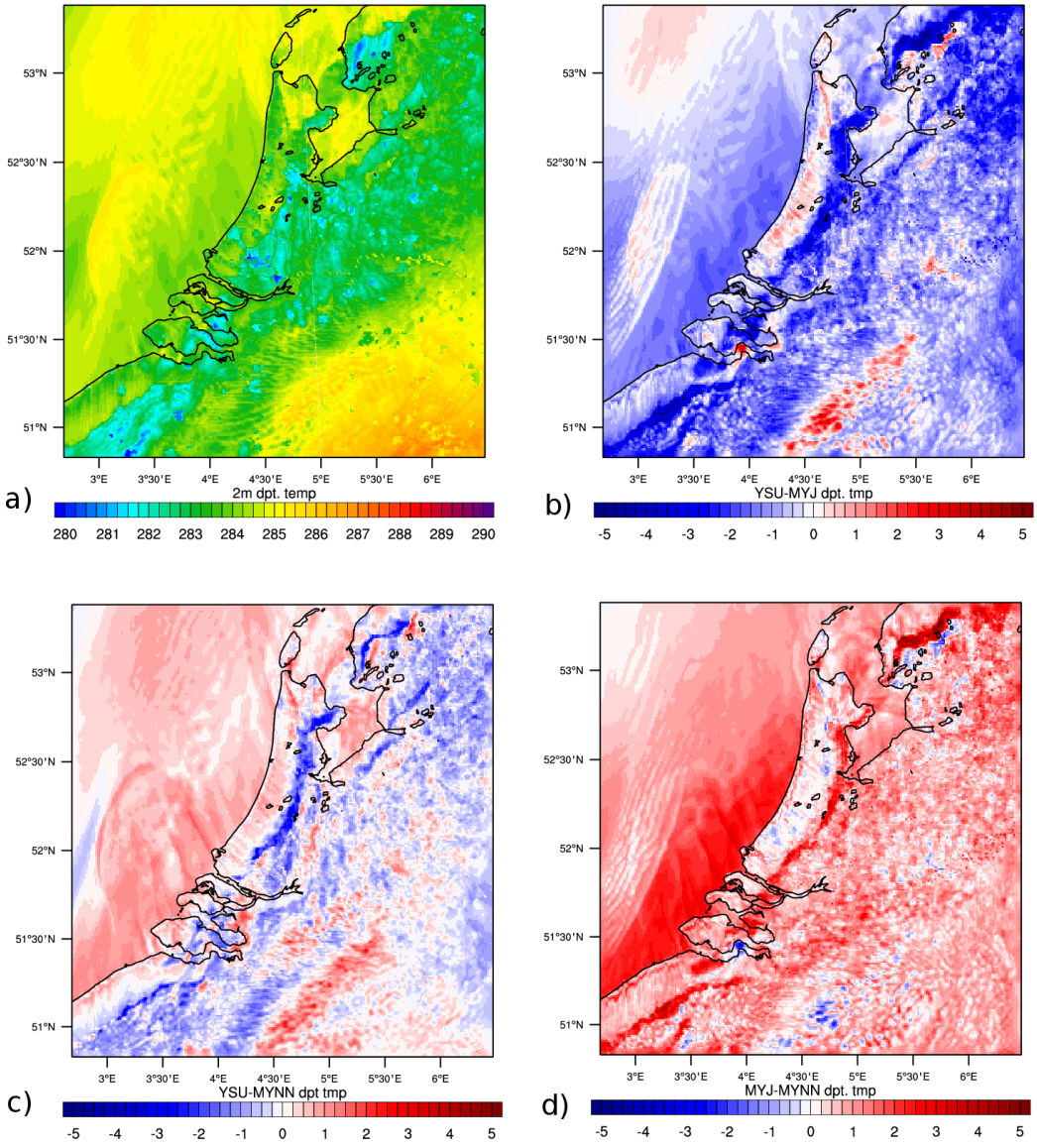

Figure A.5: a) 2m dpt. temperature at 15:00 UTC on the 19^{th} June 2012 using the baseline simulation with the YSU PBL. The differences between b) YSU and MYJ, c) YSU and MYNN and d) MYJ and MYNN are also shown for 15:00 UTC baseline simulations.

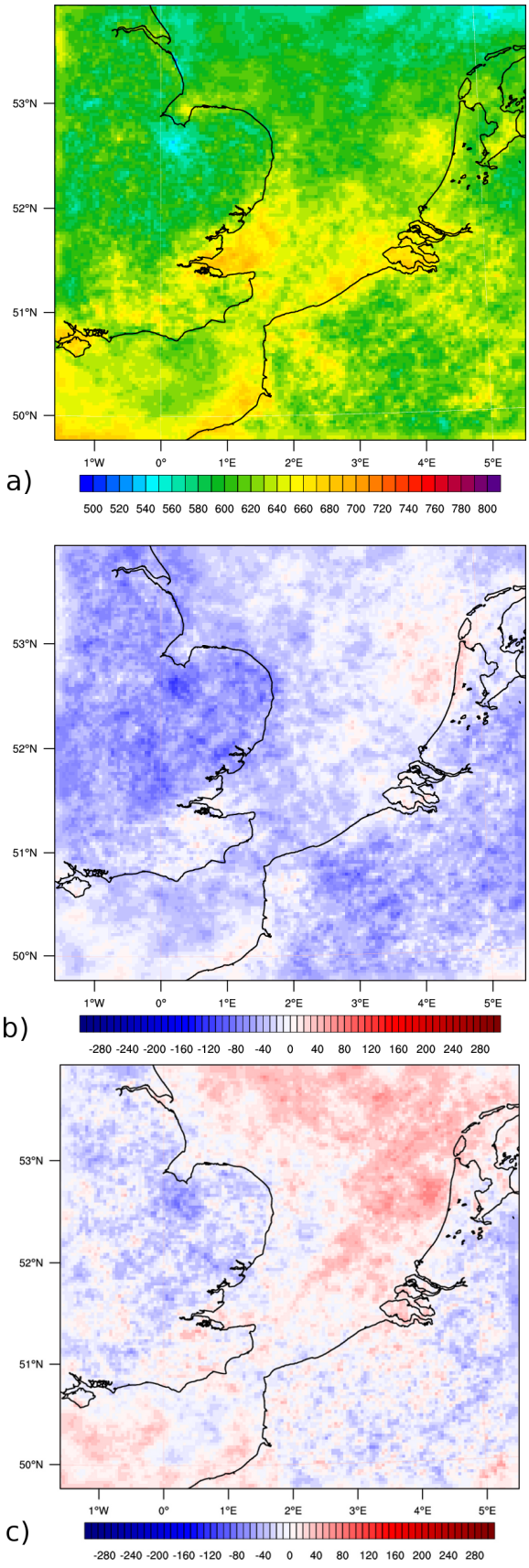

Figure A.6: a) Composite sensible heat flux at 12:00 UTC for May to September 2006 using the the YSU PBL. The differences between b) YSU and MYJ, c) YSU and MYNN and d) MYJ and MYNN are also shown for 12:00 UTC.

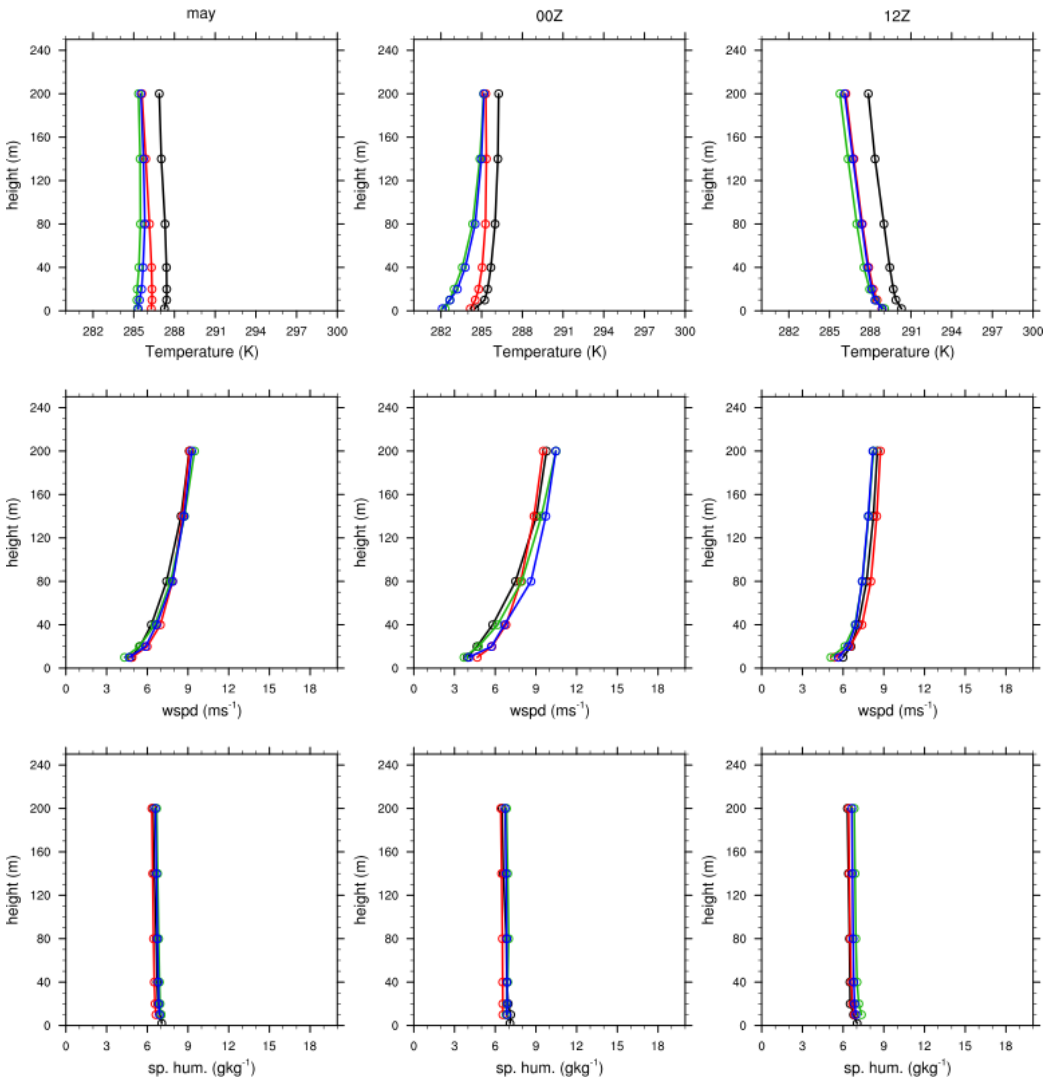

Figure A.7: Vertical profiles of temperature, wind speed and specific humidity averaged for May 2006, at 00:00 UTC and at 12:00 UTC of YSU (red), MYJ (blue) and MYNN (green) PBL schemes for the nearest model grid point to the Cabauw tower. Observations are shown in black.

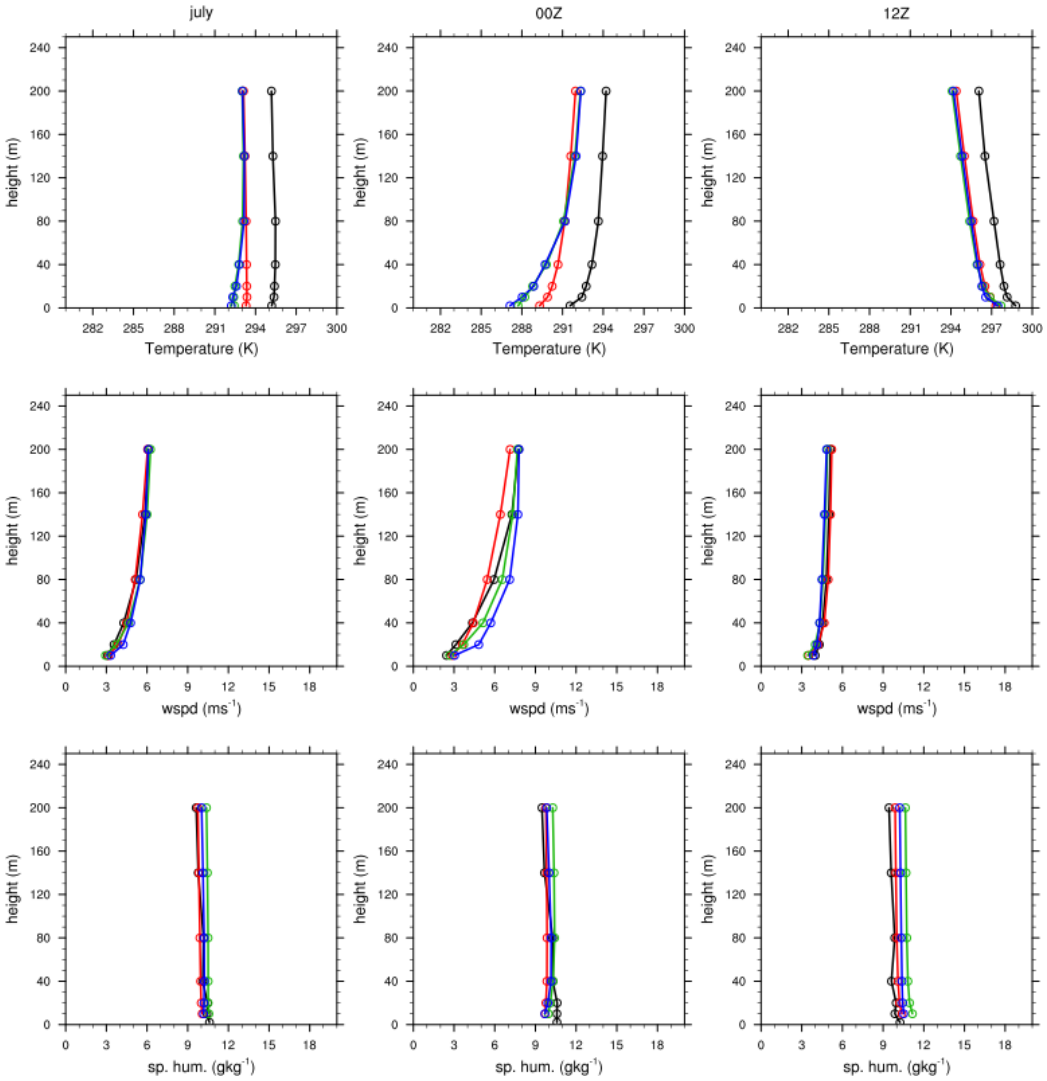

Figure A.8: Vertical profiles of temperature, wind speed and specific humidity averaged for July 2006, at 00:00 UTC and at 12:00 UTC of YSU (red), MYJ (blue) and MYNN (green) PBL schemes for the nearest model grid point to the Cabauw tower. Observations are shown in black.

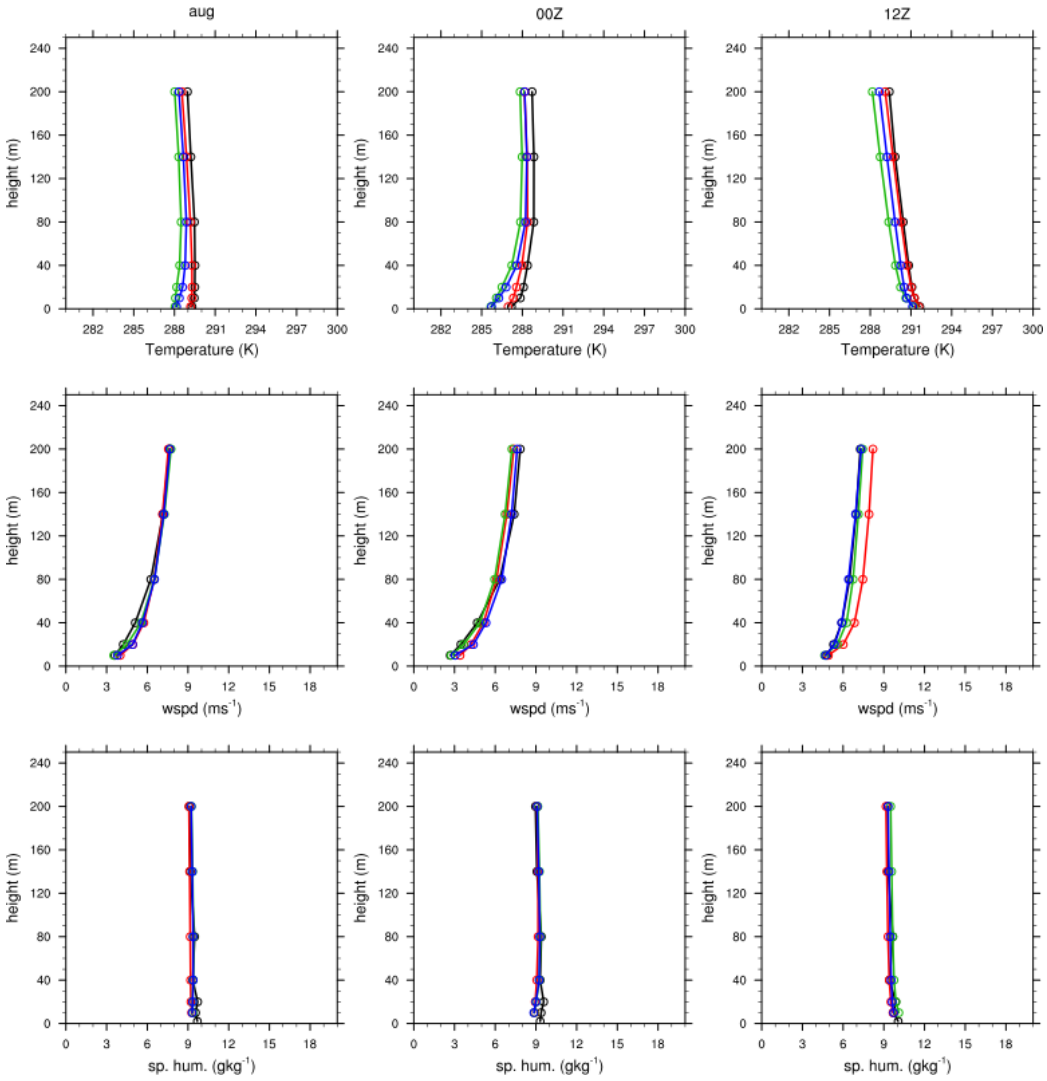

Figure A.9: Vertical profiles of temperature, wind speed and specific humidity averaged for August 2006, at 00:00 UTC and at 12:00 UTC of YSU (red), MYJ (blue) and MYNN (green) PBL schemes for the nearest model grid point to the Cabauw tower. Observations are shown in black.

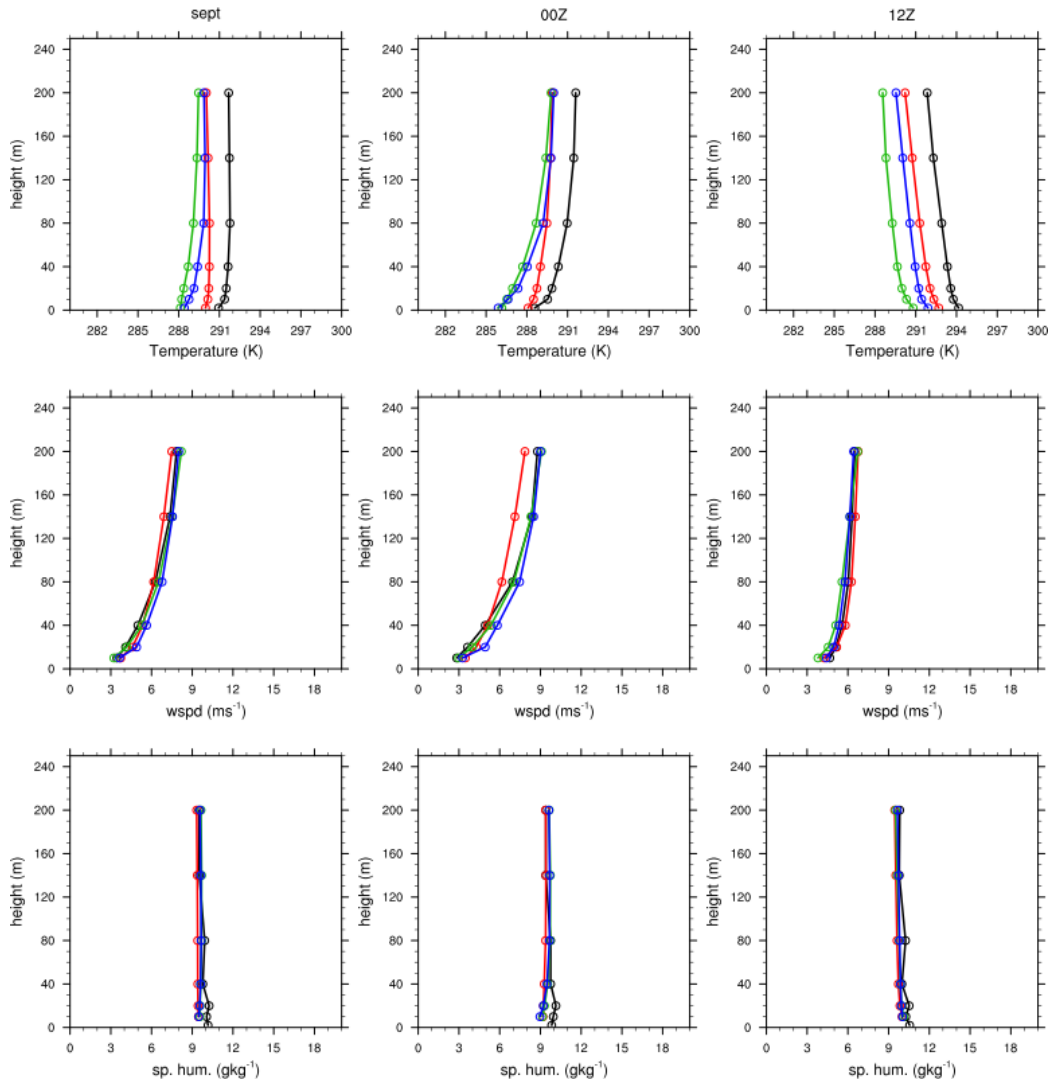

Figure A.10: Vertical profiles of temperature, wind speed and specific humidity averaged for September 2006, at 00:00 UTC and at 12:00 UTC of YSU (red), MYJ (blue) and MYNN (green) PBL schemes for the nearest model grid point to the Cabauw tower. Observations are shown in black.

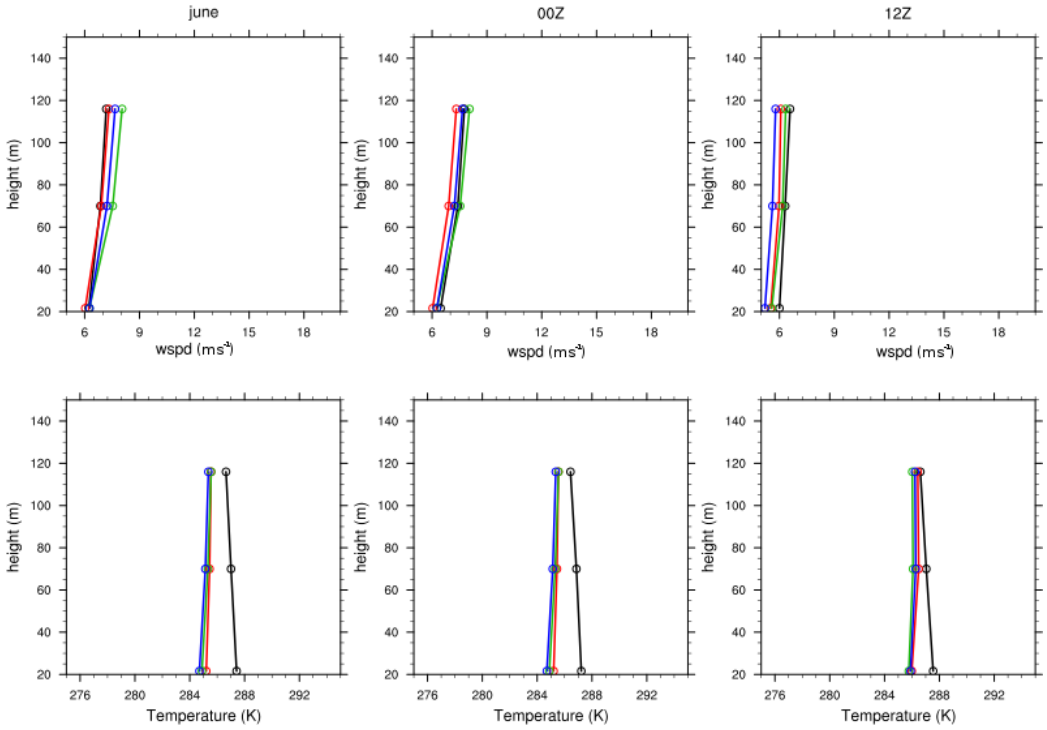

Figure A.11: Composite vertical profiles for the Egmond aan Zee met mast during June 2006 for a) wind speed and b) temperature. The YSU, MYJ and MYNN PBL schemes are denoted by the red, blue and green lines respectively

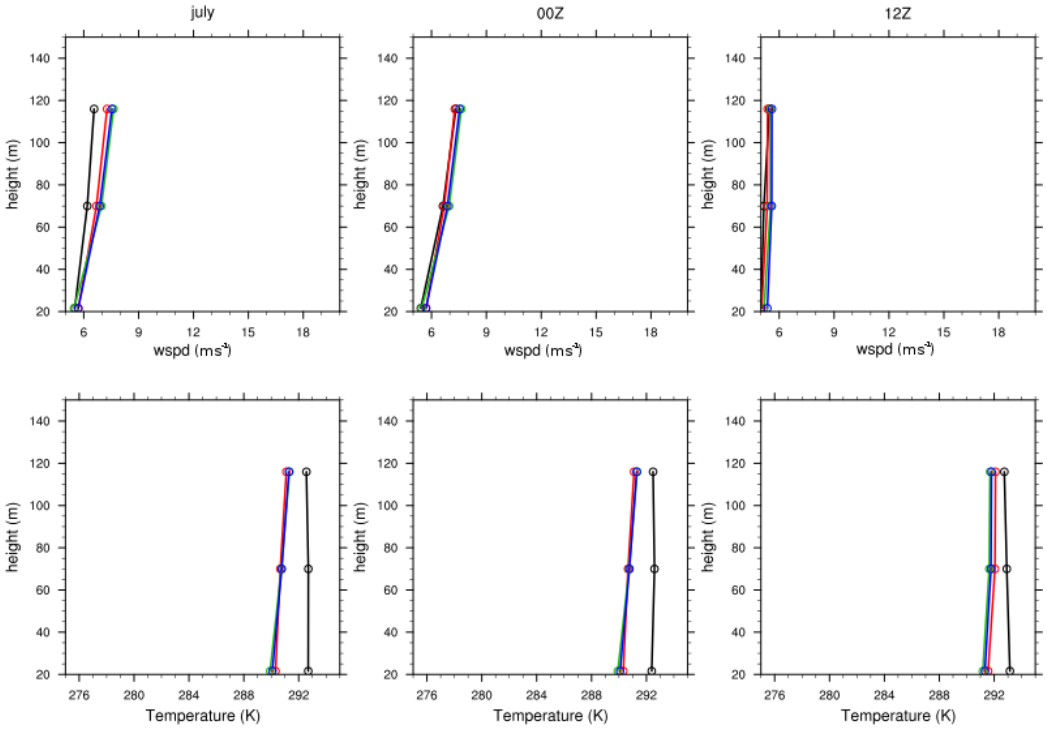

Figure A.12: Composite vertical profiles for the Egmond aan Zee met mast during July 2006 for a) wind speed and b) temperature. The YSU, MYJ and MYNN PBL schemes are denoted by the red, blue and green lines respectively

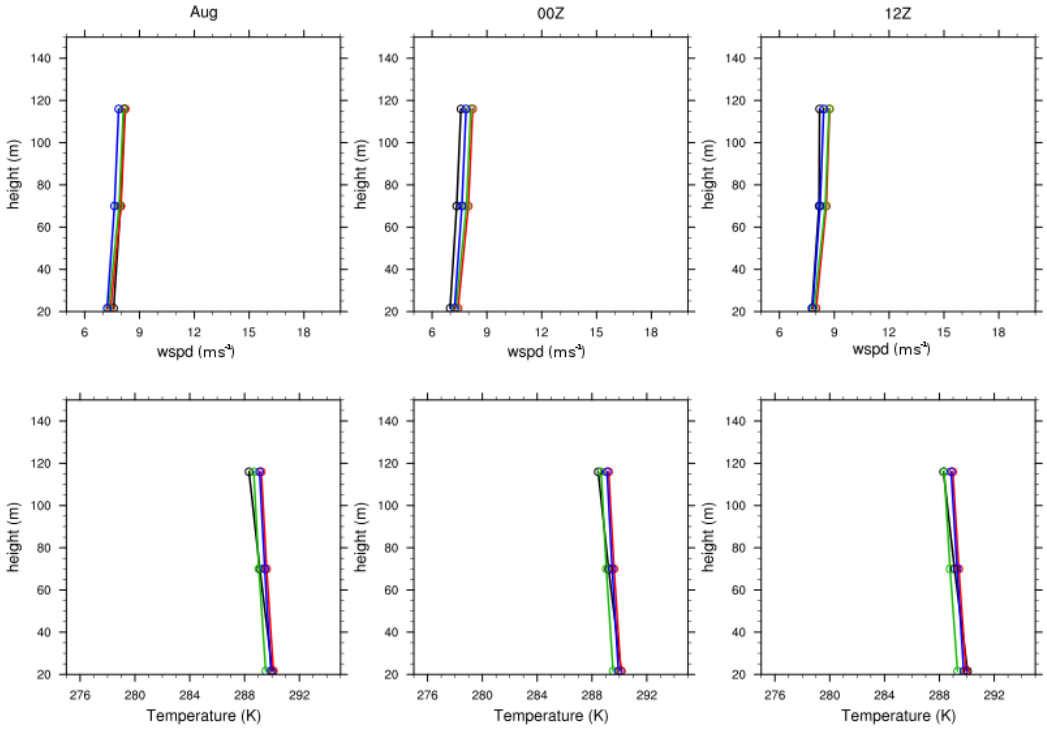

Figure A.13: Composite vertical profiles for the Egmond aan Zee met mast during August 2006 for a) wind speed and b) temperature. The YSU, MYJ and MYNN PBL schemes are denoted by the red, blue and green lines respectively

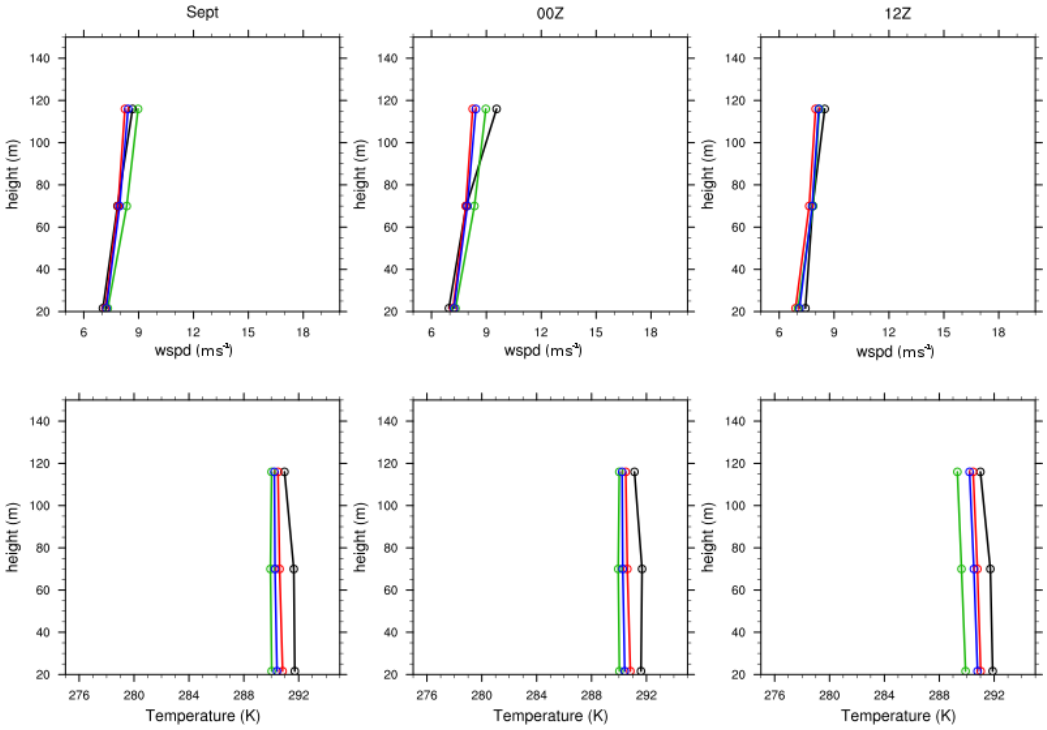

Figure A.14: Composite vertical profiles for the Egmond aan Zee met mast during September 2006 for a) wind speed and b) temperature. The YSU, MYJ and MYNN PBL schemes are denoted by the red, blue and green lines respectively

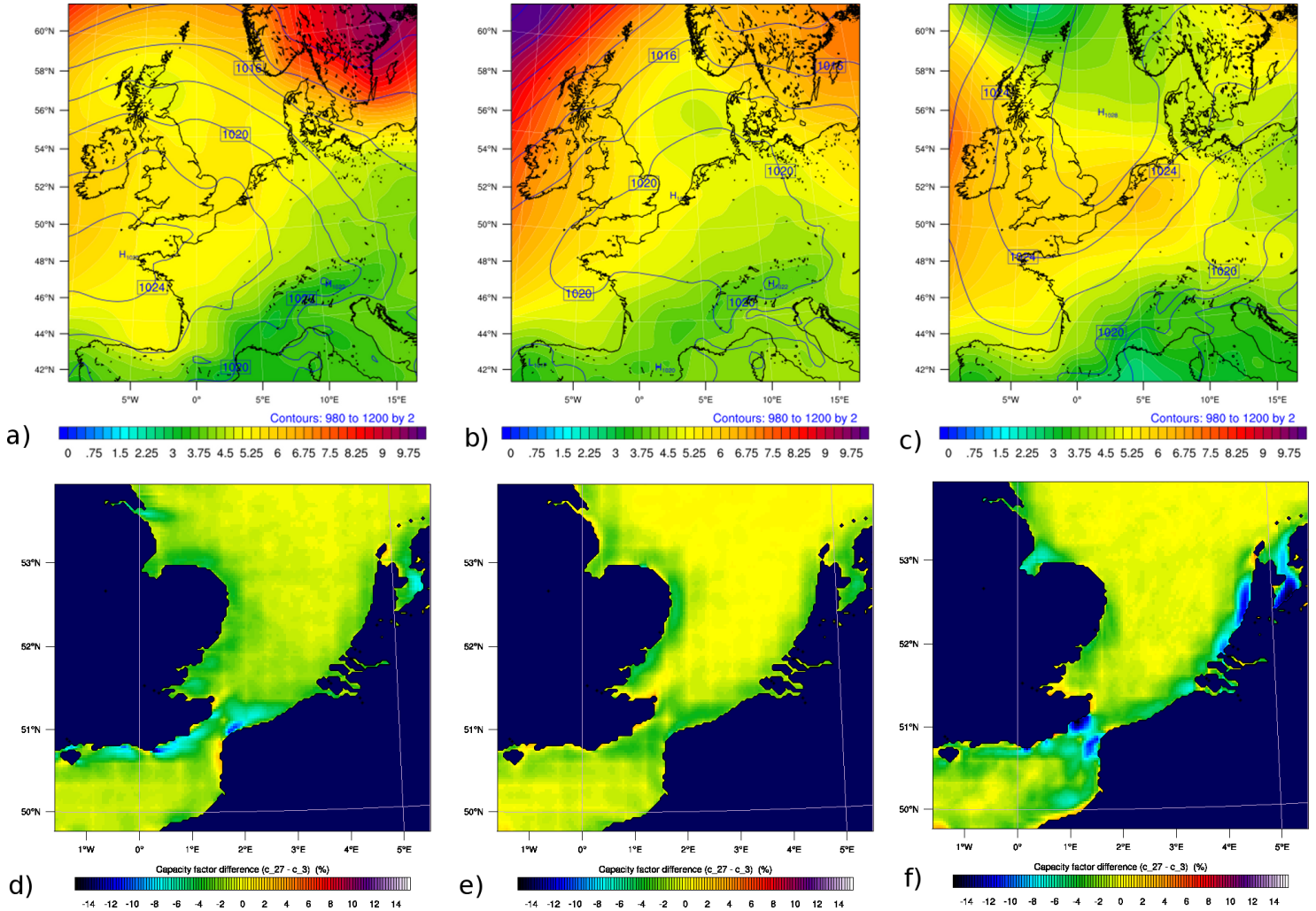

Figure A.15: Composite sea level pressure and standard deviation for the 46 *pure* (a), 167 *corkscrew* (b) and 13 *backdoor* (c) sea breeze events forming off the coasts of Suffolk and Essex between May to September 2002-2012. Composite differences in capacity factor between the 3km domain subtracted from the 27km, where the 27km domain is interpolated to the 3km grid, for the respective sea breeze types (d-f).

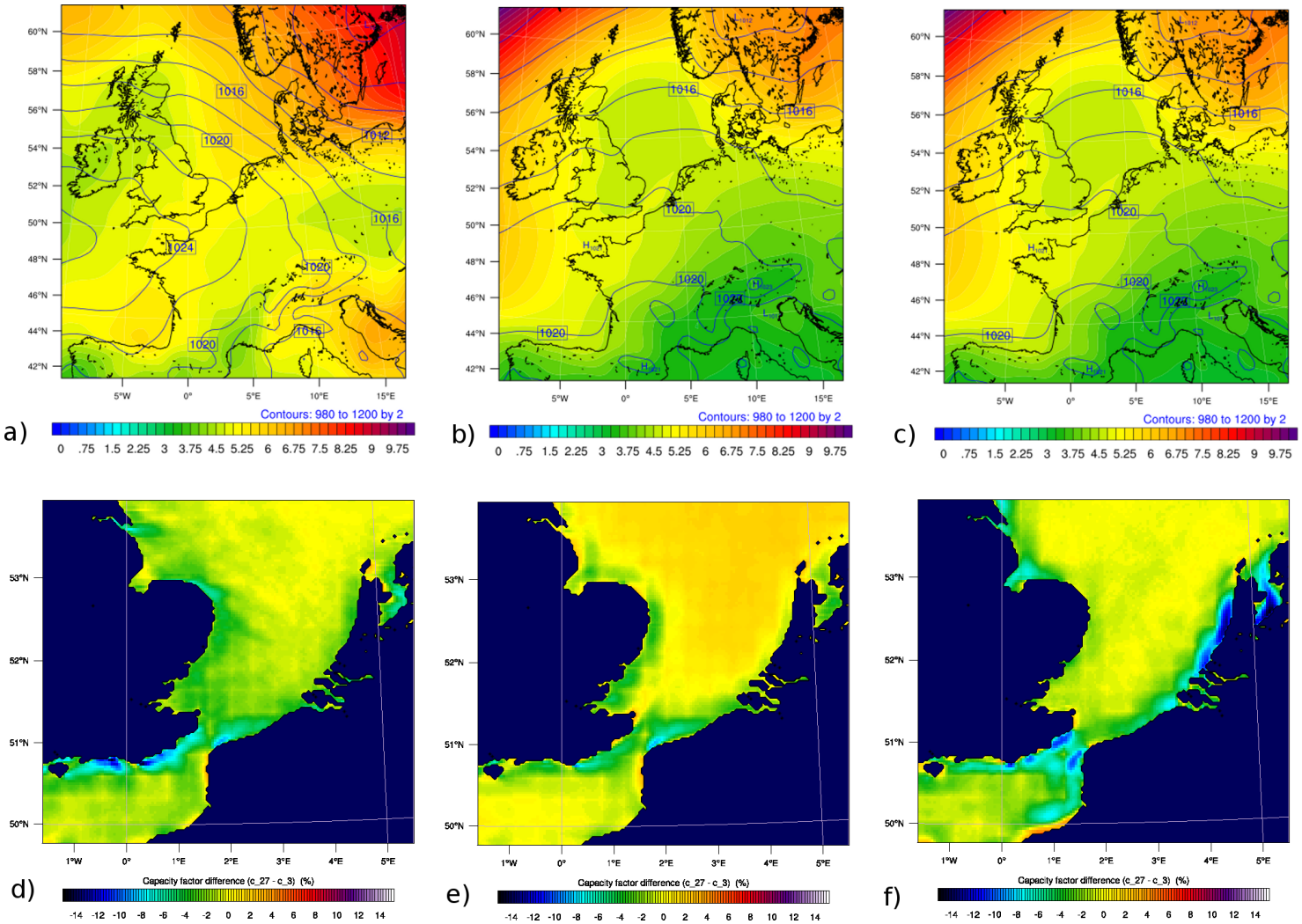

Figure A.16: Composite sea level pressure and standard deviation for the 21 *pure* (a), 122 *corkscrew* (b) and 9 *backdoor* (c) sea breeze events forming off the southern coast of Kent between May to September 2002-2012. d-f) Composite differences in capacity factor between the 3km domain subtracted from the 27km, where the 27km domain is interpolated to the 3km grid, for the respective sea breeze types.

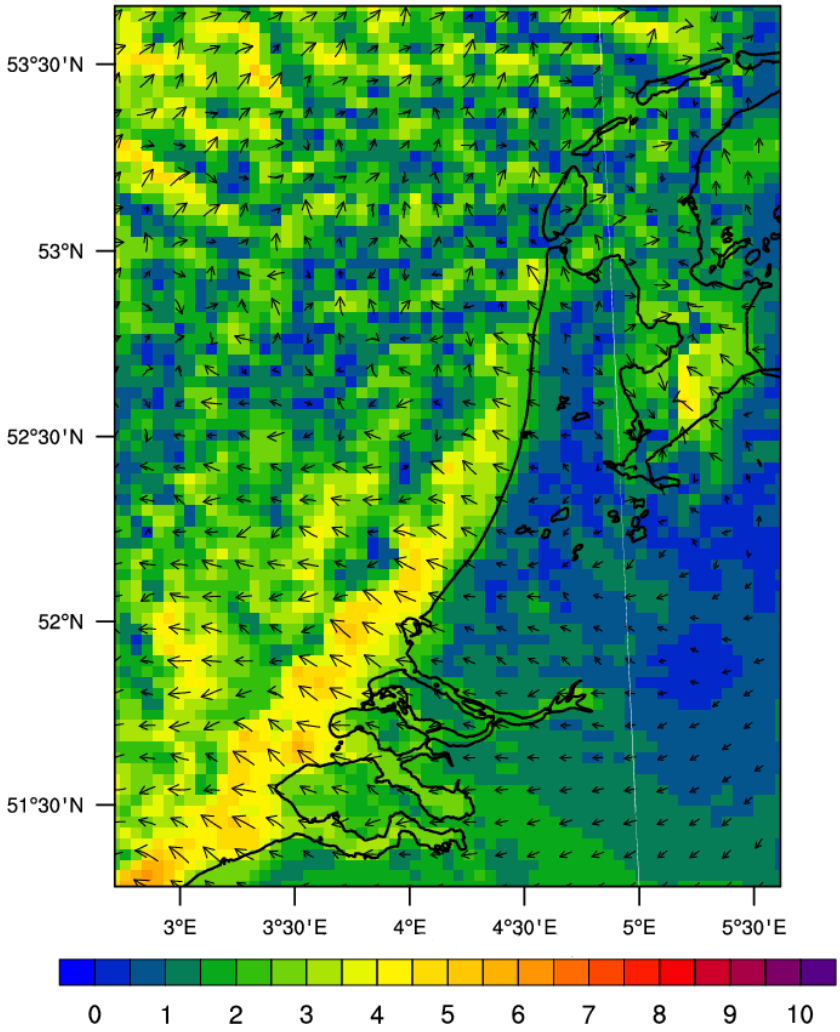

Figure A.17: Composite 10m wind speed (ms^{-1}) at 12:00 UTC of 111 failed *pure* sea breeze events which did not pass the thermal contrast filter during November - February 2002-2012

References

4COffshore (2013), Offshore wind farms, Online, http://www.4coffshore.com/windfarms/.

Abbs, D. J., and W. L. Physick (1992), Sea-breeze observations and modelling: a review, *Australian Meteorological Magazine*, *41*, 7–19.

Adams, E. (2006), Four ways to win the sea breeze game, *Sailing world*, *6*, 1–4.

Allen, M. R., D. J. Frame, C. Huntingford, C. D. Jones, J. A. Lowe, M. Meinshausen, and N. Meinshausen (2009), Warming caused by cumulative carbon emissions towards the trillionth tonne, *Nature*, *458*(7242), 1163–1166.

Antonelli, M., and R. Rotunno (2007), Large-Eddy Simulation of the Onset of the Sea Breeze, *Journal of the Atmospheric Sciences*, *64*, 4445–4457.

Arritt, R. W. (1987), The effect of water surface temperature on lake breezes and thermal internal boundary layers, *Boundary-Layer Meteorology*, *40*(1-2), 101–125.

Arritt, R. W. (1989), Numerical modelling of the offshore extent of sea breezes, *Quarterly Journal of the Royal Meteorological Society*, *115*, 547–570.

Arritt, R. W. (1993), Effects of the Large-Scale Flow on Characteristic Features of the Sea Breeze, *Journal of Applied Meteorology*, *32*(1), 116–125.

Atkinson, B. W. (1981), *Meso-scale atmospheric circulations*, Academic Press.

Azorin-Molina, C., and D. Chen (2009), A climatological study of the influence of synoptic-scale flows on sea breeze evolution in the Bay of Alicante (Spain), *Theoretical and Applied Climatology*, *96*(3), 249–260.

Azorin-Molina, C., S. Tijm, and D. Chen (2011), Development of selection algorithms and databases for sea breeze studies, *Theoretical and Applied Climatology*, *106*, 531–546, 10.1007/s00704-011-0454-4.

Barthelmie, R. J., M. S. Coutney, J. Hjstrup, and S. Larsen (1996), Meteorological aspects of offshore wind energy: Observations from the Vindeby wind farm, *Journal of Wind Engineering and Industrial Aerodynamics*, *62*, 191–211, filed under wind energy studies.

Beljaars, A. C. M., and F. C. Bosveld (1997), Cabauw Data for the Validation of Land Surface Parameterization Schemes, *J. Climate*, *10*(6), 1172–1193.

Berg, L. K., and S. Zhong (2005), Sensitivity of MM5-simulated boundary layer characteristics to turbulence parameterizations, *Journal of Applied Meteorology*, *44*(9), 1467–1483.

Bernardet, L., J. Wolf, L. Nance, A. Loughe, B. Weatherhead, E. Gilleland, and B. a. Brown (2010), Comparison between WRF-ARW and WRF-NMM objective verification scores.

Biggs, W. G., and M. E. Graves (1962), A lake breeze index, *Journal of Applied Meteorology*, *1*, 474–480.

Bigot, S., and O. Planchon (2003), Identification and characterization of sea breeze days in northern France using singular value decomposition, *International Journal of Climatology*, *23*(11), 1397–1405.

Bilgili, M., A. Yasar, and E. Simsek (2011), Offshore wind power development in Europe and its comparison with onshore counterpart, *Renewable and Sustainable Energy Reviews*, *15*(2), 905 – 915.

Borge, R., V. Alexandrov, J. José del Vas, J. Lumbreras, and E. Rodríguez (2008), A comprehensive sensitivity analysis of the WRF model for air quality applications over the Iberian Peninsula, *Atmospheric Environment*, *42*(37), 8560–8574.

Borne, K., D. Chen, and M. Nunez (1998), A method for finding sea breeze days under stable synoptic conditions and its application to the Swedish west coast, *International Journal of Climatology*, *18*(8), 901–914.

Breton, S.-P., and G. Moe (2009), Status, plans and technologies for offshore wind turbines in Europe and North America, *Renewable Energy*, *34*(3), 646 – 654.

Briffa, K. R., P. D. Jones, and P. M. Kelly (1990), Principal component analysis of the Lamb Catalogue of Daily Weather Types: Part 2, seasonal frequencies and update to 1987, *International Journal of Climatology*, *10*(6), 549–563.

Brohan, P., J. J. Kennedy, I. Harris, S. F. B. Tett, and P. D. Jones (2005), Uncertainty exstimates in regional and global observed temperature changes: a new dataset from 1850, *Journal of Geohysical Research*, *111*(D12106), 10:1029/2005JD006548.

Capon, R. A. (2003), Wind speed-up in the Dover Straits with the Met Office New Dynamics Model, *Meteorological Applications*, *10*(3), 229–237.

Challa, V. S., J. Indracanti, M. K. Rabarison, C. Patrick, J. M. Baham, J. Young, R. Hughes, M. G. Hardy, S. J. Swanier, and A. Yerramilli (2009), A simulation study of mesoscale coastal circulations in Mississippi Gulf coast, *Atmospheric Research*, *91*(1), 9 – 25.

Cheng, F.-Y., S.-C. Chin, and T.-H. Liu (2012), The role of boundary layer schemes in meteorological and air quality simulations of the Taiwan area, *Atmospheric Environment*, *54*(0), 714 – 727.

Christiansen, M. B., and C. B. Hasager (2005), Wake effects of large offshore wind farms identified from satellite SAR, *Remote Sensing of the Environment*, *98*, 251–268.

Clarke, R. H. (1983), The morning glory, *Weatherwise*, *36*(3), 134–137.

Clarke, R. H. (1984), Colliding sea-breezes and the creation of internal atmospheric bore waves: two-dimensional numerical studies, *Australian Meteorological Magazine*, *32*, 207–226.

Clarke, R. H. (1989), Sea-breezes and waves: the ”Kalgoorlie sea-breeze’ and the ”Goondiwindi breeze’, *Australian Meteorological Magazine*, *37*(2), 99–107.

Clarke, R. H., R. K. Smith, and D. G. Reid (1981), The morning glory of the Gulf of Carpentaria: an atmospheric undular bore, *Monthly Weather Review*, *109*(8), 1726–1750.

Cleantech (2010), Jefferies CleanTech Review.

Costa, A., A. Crespo, J. Navarro, G. Lizcano, H. Madsen, and E. Feitosa (2008), A review on the young history of the wind power short-term prediction, *Renewable and Sustainable Energy Reviews*, *12*(6), 1725 – 1744.

Crosman, E., and J. D. Horel (2012), Idealized Large-Eddy Simulations of Sea and Lake Breezes: Sensitivity to Lake Diameter, Heat Flux and Stability, *Boundary-Layer Meteorology*, *144*, 309–328, 10.1007/s10546-012-9721-x.

Crosman, E. T., and J. D. Horel (2010), Sea and Lake Breezes: A review of Numerical Studies, *Boundary-Layer Meteorology*, *137*, 1–29.

Damato, F., O. Planchon, and V. Dubreuil (2003), A remote-sensing study of the inland penetration of sea-breeze fronts from the English Channel, *Weather*, *58*(6), 219–226.

Della-Marta, P. M., M. R. Haylock, J. Luterbacher, and H. Wanner (2007), Doubled length of western European summer heat waves since 1880, *Journal of Geophysical Research: Atmospheres*, *112*(D15), D15,103.

Dorland, C., R. Tol, and J. Palutikof (1999), Vulnerability of the Netherlands and Northwest Europe to Storm Damage under Climate Change, *Climatic Change*, *43*(3), 513–535.

Earl, N., S. Dorling, R. Hewston, and R. von Glasow (2013), 1980-2010 variability in UK surface wind climate, *J. Climate*, –(0894-8755), –.

EC (2009), Directive 2009/28/EC of the European Parliament and of the council: on the promotion of the use of energy from renewable sources and amending and subsequently repealing directives 2001/77/EC and 2003/30/EC, *Official journal of the European Union*, *140*, 16–62.

Eden, P. (2006), Weather log: June 2006, warmest and driest locally since 1976, *Weather magazine*, *61*, 10–14.

EWEA (2013a), *The European offshore wind industry - key trends and statistics 2012*, Tech. rep., European Wind Energy Association.

EWEA (2013b), *Wind in power. 2012 European statistics*, Tech. rep., EWEA.

Fichet, A. D., H. Quenol, O. Planchon, and J. Douvinet (2010), Analysis of local wind systems in the Caen region (Lower Normandy, France), *International Journal of Climatology*, *30*(9999), 406–417.

Finkele, K. (1998), Inland and offshore propagation speeds of a sea breeze from simulations and measurements, *Boundary-Layer Meteorology*, *87*, 307–329.

Foken, T. (2006), 50 Years of the Monin-Obukhov Similarity Theory, *Boundary-Layer Meteorology*, *119*(3), 431–447.

Foley, A. M., P. G. Leahy, A. Marvuglia, and E. J. McKeogh (2012), Current methods and advances in forecasting of wind power generation, *Renewable Energy*, *37*(1), 1 – 8.

Furberg, M., D. G. Steyn, and M. Baldi (2002), The climatology of sea breezes on Sardinia, *International Journal of Climatology*, *22*(8), 917–932.

Gahmberg, M., H. Savijarvi, and M. Leskimen (2010), The influence of synoptic scale flow on sea breeze induced surface winds and calm zones, *Tellus*, *62A*, 209–217.

Gallus, W. A. J., and J. F. Bresch (2006), Comparisons of Impacts of WRF Dynamic Core, Physics package, and initial conditions on warm season rainfall forecasts, *Mon. Wea. Rev.*, *134*, 2632–2641.

Galvin, J. (2006), Considering sea-breezes and their inland penetration in south Devon, *Weather*, *61*(7), 192–193.

Garratt, J. (1994), Review: the atmospheric boundary layer, *Earth-Science Reviews*, *37*(12), 89 – 134.

Golding, B., P. Clark, and B. May (2005), The Boscastle flood: Meteorological analysis of the conditions leading to flooding on 16 August 2004, *Weather*, *60*(8), 230–235.

Goodwin, W. W. (1906), The Battle of Salamis, *Harvard Studies in Classical Philology*, *17*, 75–101.

Haydon, F. S. (1941), Aeronautics in the Union and Confederance Armies, baltimore: Johns Hopkins.

Hong, S.-Y., and S.-Y. Kim (2008), Stable boundary layer mixing in a vertical diffusion scheme, in: *18th symposium on boundary layers and turbulence*.

Hong, S. Y., Y. Noh, and J. Dudhia (2006), A new vertical diffusion package with an explicit treatment of entrainment processes, *Monthly Weather Review*, *134*(9), 2318–2341.

Hong, S. Y., and H. L. Pan (1996), Nonlocal boundary layer vertical diffusion in a medium-range forecast model, *Monthly Weather Review*, *124*(10), 2322–2339–.

Hu, X.-M., J. W. Nielsen-Gammon, and F. Zhang (2010), Evaluation of three planetary boundary layer schemes in the WRF model, *Journal of Applied Meteorology and Climatology*, *49*, 1831–1844.

Huhne, C., C. Jones, A. Foster, and F. Ewing (2011), *UK Renewable Energy Roadmap*, Tech. rep., Department of Energy and Climate Change.

Hunt, J. C. R., A. Orr, J. W. Rottman, and R. Capon (2004), Coriolis effects in mesoscale flows with sharp changes in surface conditions, *Quarterly Journal of the Royal Meteorological Society*, *130*(603), 2703–2731.

IAMU (2012), Atmospheric H2 and effects of a hydrogen economy, online.

Islam, M., S. Mekhilef, and R. Saidur (2013), Progress and recent trends of wind energy technology, *Renewable and Sustainable Energy Reviews*, *21*(0), 456 – 468.

James, P. M. (2007), An objective classification method for Hess and Brezowsky Grosswetterlagen over Europe, *Theoretical and Applied Climatology*, *88*, 17–42.

Janjic, Z. I. (1990), The step-mountain coordinate: physical package, *Monthly Weather Review*, *118*(7), 1429–1443–.

Jenkinson, A., and F. Collison (1977), An initial climatology of gales over the North Sea, *Synoptic Climatology Branch Memorandum*, *62*, 18.

Jiang, Q. (2012), A linear theory of three-dimensional land-sea breezes, *Journal of the Atmospheric sciences*, *69*, 1890–1909.

Jones, P. D., M. Hulme, and K. R. Briffa (1993), A comparison of Lamb circulation types with an objective classification scheme, *International Journal of Climatology*, *13*, 655–663.

Kaldellis, J. K. (2012), *Comprehensive Renewable Energy. Volume 2: Wind energy*, Elsevier LTD.

Klemp, J. B., and D. K. Lilly (1978), Numerical Simulation of Hydrostatic Mountain Waves, *Journal of Atmospheric Sciences*, *35*, 78–107.

Krogsaeter, O., J. Reuder, and G. Hauge (2011), WRF and the marine planetary boundary layer, 12th Annual WRF users' workshop.

Kundzewicz, Z., U. Ulbrich, T. bracher, D. Graczyk, A. Krager, C. Leckebusch, Gregor, L. Menzel, I. Piaskwar, M. Radziejewski, and M. Szwed (2005), Summer Floods in Central Europe - Climate Change Track?, *Natural Hazards*, *36*(1-2), 165–189.

Lapworth, A. (2005a), Collision of two sea-breeze fronts observed in Wales, *Weather*, *60*(11), 316–318.

Lapworth, A. (2005b), The diurnal variation of the marine surface wind in an offshore flow, *Quarterly Journal of the Royal Meteorological Society*, *131*(610), 2367–2387.

Lin, C.-Y., F. Chen, J. Huang, W.-C. Chen, Y.-A. Liou, W.-N. Chen, and S.-C. Liu (2008), Urban heat island effect and its impact on boundary layer development and land-sea circulation over northern Taiwan, *Atmospheric Environment*, *42*(22), 5635 – 5649.

Maddaloni, J. D., A. M. Rowe, and G. C. van Kooten (2009), Wind integration into various generation mixtures, *Renewable Energy*, *34*(3), 807 – 814.

Matthews, H. D., N. P. Gillett, P. A. Stott, and K. Zickfeld (2009), The proportionality of global warming to cumulative carbon emissions, *Nature*, *459*(7248), 829–832–.

Mellor, G. L., and T. Yamada (1982), Development of a turbulence closure model for geophysical fluid problems, *Reviews of Geophysics & Space Physics*, *20*(4), 851–875.

Miller, S. T. K., B. D. Keim, R. W. Talbot, and H. Mao (2003), Sea Breeze: Structure, Forecasting and Impacts, *Reviews of Geophysics*, *41*, 1011.

Moore, G. W. K., and I. A. Renfrew (2005), Tip Jets and Barrier Winds: A QuikSCAT Climatology of High Wind Speed Events around Greenland, *J. Climate*, *18*(18), 3713–3725.

Nakanishi, M. (2001), Improvement of the Mellor-Yamada Turbulance closure model based on large-eddy simulation data, *Boundary-Layer Meteorology*, *99*, 349–378.

National Centers for Environmental Prediction, National Weather Service, N. U. D. o. C. (2000), NCEP FNL Operational Model Global Tropospheric Analyses, continuing from July 1999.

NCIC (2010), UK seasonal weather summary: summer 2010, *Weather*, *65*(10), 271–271.

Orr, A., J. Hunt, R. Capon, J. Sommeria, D. Cresswell, and A. Owinoh (2005), Coriolis effects on wind jets and cloudiness along coasts, *Weather*, *60*(10), 291–299.

Papanastasiou, D., D. Melas, and I. Lissaridis (2010), Study of wind field under sea breeze conditions; an application of WRF model, *Atmospheric Research*, *98*(1), 102 – 117.

Peterson, E. L., N. G. Mortenson, L. Landberg, J. Hjstrup, and H. P. Frank (1998a), Wind Power Meteorology. Part I: Climate and Turbulance, *Wind Energy*, *1*, 2–22.

Peterson, E. L., N. G. Mortenson, L. Landberg, J. Hjstrup, and H. P. Frank (1998b), Wind Power Meteorology Part II: Sitings and Models, *Wind Energy*, *1*, 55–72.

Porson, A., D. G. Steyn, and G. Schayes (2007a), Formulation of an Index for Sea Breezes in Opposing Winds, *Journal of Applied Meteorology and Climatology*, *46*(8), 1257–1263.

Porson, A., D. G. Steyn, and G. Schayes (2007b), Sea-breeze scaling from numerical model simulations, Part I: Pure sea breezes, *Boundary-Layer Meteorology*, *122*, 17–29.

Potter, C., and M. Negnevitsky (2006), Very short-term wind forecasting for Tasmanian power generation, *Power Systems, IEEE Transactions on*, *21*(2), 965–972.

Qian, T., C. C. Epifanio, and F. Zhang (2009), Linear theory calculations for the sea breeze in a background wind: The equatorial case, *Journal of the Atmospheric Sciences*, *66*, 1749–1763.

Rebetez, M., O. Dupont, and M. Giroud (2009), An analysis of the July 2006 heatwave extent in Europe compared to the record year of 2003, *Theoretical and Applied Climatology*, *95*, 1–7.

Rebetez, M., H. Mayer, O. Dupont, D. Schindler, K. Gartner, J. P. Kropp, and A. Menzel (2006), Heat and drought 2003 in Europe: a climate synthesis, *Ann. For. Sci.*, *63*(6), 569–577.

RenewableUK (2013), Offshore wind energy, Online, http://www.renewableuk.com/en/renewable-energy/wind-energy/offshore-wind/index.cfm.

Reynolds, R. W., T. M. Smith, C. Liu, D. B. Chelton, K. S. Casey, and M. G. Schlax (2007), Daily high-resolution blended analysis for sea surface temperature, *Journal of Climate*, *20*, 5743–5496.

Rotunno, R. (1983), On the linear theory of the land and sea breeze, *Journal of the atmospheric sciences*, *40*, 1999–2009.

Savijarvi, H., and M. Alestalo (1988), The Sea Breeze over a lake or Gulf as the function of the prevailing flow, *Beitr. Phys. Atmosph.*, *61*, 98–104.

Sha, W., T. Kawamura, and H. Ueda (1993), A Numerical Study of Nocturnal Sea Breezes: Prefrontal Gravity Waves in the Compensating Flow and Inland Penetration of the Sea-Breeze Cutoff Vortex, *J. Atmos. Sci.*, *50*(8), 1076–1088.

Shimada, S., and T. Ohsawa (2011), Accuracy and Characteristics of Offshore Wind Speeds Simulated by WRF, *SOLA*, *7*, 21–24.

Shin, H. H., and S.-Y. Hong (2011), Intercomparison of Planetary Boundary layer parameterizations in the WRF model for a single day from CASES-99, *Boundary-Layer Meteorology*, *139*, 261–281.

Simpson, J. E. (1969), A comparison between laboratory and atmospheric density currents, *Quarterly Journal of the Royal Meteorological Society*, *95*, 758–765.

Simpson, J. E. (1972), Effects of the lower boundary on the head of a gravity current, *Journal of Fluid Mechanics Digital Archive*, *53*(04), 759–768.

Simpson, J. E. (1994), *Sea breeze and local winds*, Cambridge University Press.

Simpson, J. E. (1996), Diurnal Changes in Sea-Breeze Direction, *J. Appl. Meteor.*, *35*(7), 1166–1169.

Simpson, J. E., D. A. Mansfield, and J. R. Milford (1977), Inland penetration of sea-breeze fronts, *Quarterly Journal of the Royal Meteorological Society*, *103*(435), 47–76–.

Sinden, G. (2005), *Wind power and the UK wind resource*, Tech. rep., Environmental Change Institute, University of Oxford.

Skamarock, W. C., and J. B. Klemp (2008), A time-split nonhydrostatic atmospheric model for weather research and forecasting applications, *Journal of Computational Physics*, *227*(7), 3465–3485.

Snyder, B., and M. J. Kaiser (2009), A comparison of offshore wind power development in europe and the U.S.: Patterns and drivers of development, *Applied Energy*, *86*(10), 1845 – 1856.

Steele, C. J., S. R. Dorling, R. von Glasow, and J. Bacon (2013), Idealized WRF model siensitivity simulations of sea breeze types and their effects on offshore windfields, *Atmospheric Chemistry and Physics*, *13*, 443–461.

Stensrud, D. J. (2007), *Parameterization schemes: keys to understanding numerical weather prediction models*, Cambridge University Press.

Steyn, D. (2003), Scaling the Vertical Structure of Sea Breezes Revisited, *Boundary-Layer Meteorology*, *107*(1), 177–188.

Steyn, D. G., and D. A. Faulkner (1986), The climatology of sea-breezes in the Lower Fraser Valley, B. C., *Climatological Bulletin*, *20*, 21–39.

Stull, R. B. (1988), *Boundary Layer Meteorology*, Kluwer Academic Publishers.

Sweeney, C. P., P. Lynch, and P. Nolan (2013), Reducing errors of wind speed forecasts by an optimal combination of post-processing methods, *Meteorological Applications*, *20*(1), 32–40.

Tang, Y. (2012), The Effect of Variable Sea Surface Temperature on Forecasting Sea Fog and Sea Breezes: A Case Study, *J. Appl. Meteor. Climatol.*, *51*(5), 986–990.

Thomas, C. D., A. Cameron, R. E. Green, M. Bakkenes, L. J. Beaumont, Y. C. Collingham, B. F. N. Erasmus, M. F. de Siqueira, A. Grainger, L. Hannah, L. Hughes, B. Huntley, A. S. van Jaarsveld, G. F. Midgley, L. Miles, M. A. Ortega-Huerta, A. T. Peterson, O. L. Phillips, and S. E. Williams (2004), Extinction risk from climate change, *Nature*, *427*(6970), 145–148.

Tie, X., F. Geng, L. Peng, W. Gao, and C. Zhao (2009), Measurement and modeling of O3 variability in Shanghai, China: Application of the WRF-Chem model, *Atmospheric Environment*, *43*(28), 4289–4302–.

Tijm, A. B. C., and A. J. Van Delden (1999), The role of sound waves in sea-breeze initiation, *Quarterly Journal - Royal Meteorological Society*, *125*, 1997–2018.

Tijm, A. B. C., A. J. van Delden, and A. A. M. Holtslag (1999), The inland penetration of sea breezes, *Contributions to Atmospheric Physics*, *72*, 317–328.

Tsunematsu, N., H. Iwai, Y. Murayama, M. Yasui, and K. Mizutani (2009), The formation of sharp multi-layered wind structure over tokyo associated with sea-breeze circulation, *Scientific Online Letters on the Atmosphere*, *5*, 1–4.

Webster, E. W. (2013), *Aristotle's Meteorology (English translation)*, eBook@Adelaide.

Xie, B., J. C. H. Fung, A. Chan, and A. Lau (2012), Evaluation of nonlocal and local planetary boundary layer schemes in the WRF model, *Journal of Geophysical Research: Atmospheres*, *117*(D12), 1–26.

Yerramilli, A., C. V. Srinivas, H. P. Dasari, F. Tuluri, L. D. White, J. M. Baham, J. H. Young, R. Hughes, C. Patrick, M. G. Hardy, and S. J. Swanier (2009), Simulation of atmospheric dispersion of elevated releases from point sources in mississippi gulf coast with different meteorological data, *International Journal of Environmental Research and Public Health*, *6*(3), 1055–1074.